



Advanced interfaces for biomedical engineering applications in high- and low field NMR/MRI

Zur Erlangung des akademischen Grades eines

DOKTORS DER INGENIEURWISSENSCHAFTEN (Dr.-Ing.)

von der KIT-Fakultät für Maschinenbau des
Karlsruher Instituts für Technologie (KIT)
angenommene

DISSERTATION

von

M. Sc. Erwin Fuhrer

Tag der mündlichen Prüfung: 16.07.2019

Hauptreferent: Prof. Dr. Jan G. Korvink

Korreferent: Prof. Dr. Jürgen Hennig

Karlsruher Institut für Technologie
Institut für Mikrostrukturtechnik
Hermann.-v.-Helmholtz Platz 1
76344 Eggenstein-Leopoldshafen

Abstract

The central theme of this dissertation is Magnetic resonance (MR) safety and compatibility of devices. In the general public, this issue is famous in connection with commercial implants. Hazards, resulting from interactions between the MR system and the implant, restrict many patients from undergoing MR examinations. MR compatibility, however, not only plays an important role in design and labelling of implants, but also in MR hardware development. Within this work both topics, implant interactions and hardware design are addressed.

The first part addresses MR interactions of implants. Results from an extensive literature research unveil the urgent need for resilient data, that enable a deeper understanding of MR triggered vibrations of implants. This is especially true for vibrations within viscoelastic environments, such as the brain. An MR probe is developed, which enables quantitative high-precision measurements of vibrations during standard MR acquisitions. By using an amplitude and frequency controlled external current supply, the transfer functions of implant-like structures in viscoelastic environments are precisely determined. Based on the acquired data, a correlation between vibration amplitudes and sequence timing parameters is established and experimentally validated. A key finding is, that these penetrative structures vibrate underdamped within brain-like environments. Furthermore, a new classification number is introduced, which strives to classify the implant interaction for vibration, while providing an easy transfer to any MR system. This classification number indicates the normalized induced torque and facilitates a straightforward calculation of the maximum expected torque on any MRI unit.

Another type of research, *in-situ* high-field NMR/MRI of biological samples, requires novel probes as well as improved MR compatible cell seeding substrates. A novel probe is developed featuring very flexible interfacing. The final version is equipped with two RF channels and a gradient interface for liquid-cooled gradients. It is benchmarked with standard NMR/MRI experiments yielding a linewidth of 0.5 Hz and a comparable SNR to commercial probes. The advantage is its feed-through system, which is integrated in the mechanical frame. This offers a simple method for customised augmentation of the probe using additional electrical, optical and fluid supply lines. On that basis, custom-designed, sophisticated high-field NMR/MRI experimental setups are realisable in short time. This

is without the necessity of tailored, expensive probes. Two measurement examples are presented, in which the probe is applied in an oil-water flow experiment and in a hydrogen-based hyperpolarisation experiment. Furthermore, a novel, MR compatible carbon scaffold is introduced, which was tested successfully for cell growth and MR imaging. MRI is used as an analysis tool to investigate and confirm the preservation of morphology during pyrolysis. The fabrication protocol is applicable to other precursor polymers which paves the way to a variety of lithographically patterned 3D scaffolds.

Zusammenfassung

Das zentrale Thema dieser Dissertation ist die Magnetresonanz(MR)-Sicherheit und MR-Kompatibilität von Bauelementen. Der Öffentlichkeit bekannt ist diese Thematik im Zusammenhang mit kommerziellen Implantaten. Die Gefahren, die sich aus den Wechselwirkungen zwischen dem MR-Tomografen (MRT) und dem Implantat ergeben, hindern viele Patienten daran, eine Untersuchung mittels MRT durchführen zu lassen. MR-Kompatibilität spielt jedoch nicht nur beim Design und der Kennzeichnung von Implantaten eine wichtige Rolle, sondern auch bei der Entwicklung von Bauelementen für die MR-Hardware. Beide Themen, Implantatinteraktionen und Hardware-Design, bilden fundamentale Aspekte dieser Arbeit.

Der erste Teil befasst sich mit MRT-Wechselwirkungen von Implantaten. Die Ergebnisse einer umfangreichen Literaturrecherche zeigen, dass dringend belastbare Daten benötigt werden, um die durch MRT ausgelösten Schwingungen von Implantaten besser verstehen zu können. Dies gilt insbesondere für Vibrationen in viskoelastischen Umgebungen wie dem Gehirn. Im Rahmen dieser Arbeit wird ein neuartiges Messsystem vorgestellt, mit dem sich Schwingungen bei Standard-MRT-Aufnahmen und mit hoher Genauigkeit quantitativ messen lassen. Durch die Verwendung einer amplituden- und frequenzgesteuerten externen Stromversorgung werden die Übertragungsfunktionen implantatartiger Strukturen in viskoelastischen Umgebungen präzise bestimmt. Basierend auf den erfassten Daten wird eine Korrelation zwischen den resultierenden Schwingungsamplituden und den Zeitparametern der Aufnahmesequenz hergestellt und experimentell verifiziert. Eine wichtige Erkenntnis ist, dass die untersuchten Strukturen ein unterdämpftes Verhalten zeigen und damit resonant schwingen können. Darüber hinaus wird eine neue Kennzahl eingeführt, anhand derer die Wechselwirkung des Implantats auf Vibrationen klassifiziert werden können. Die Kennzahl gibt das normierte induzierte Drehmoment an, und ermöglicht eine einfache Berechnung des maximal zu erwartenden Drehmoments auf jedem MRT-System. Somit können die zu erwartenden Maximalamplituden unkompliziert und für jedes System direkt ermittelt werden.

Eine anderes Forschungsgebiet, die *in-situ*-Kernspinspektroskopie und -MRT von biologischen Untersuchungsobjekten im Hochfeld, erfordert eine neuartige MR-Messsonde sowie verbesserte MR-kompatible Substrate für die Zellkultivierung. Eine MR-Sonde mit

flexibler Schnittstelle wurde entwickelt. Die endgültige Version ist mit zwei HF-Kanälen und einer Gradientenschnittstelle für flüssiggekühlte Gradienten ausgestattet. Ein Leistungsbewertung wurde mittels Standard-NMR/MRT-Experimenten durchgeführt, die eine Linienbreite von 0,5 Hz und ein mit kommerziellen Messsystem vergleichbares Signal-Rausch-Verhältnis ergaben. Der Vorteil liegt in dem integrierten Durchführungssystem innerhalb des mechanischen Rahmens. Dies bietet eine einfache Methode, zur spezifischen Erweiterung der Messsonde unter Verwendung zusätzlicher elektrischer, optischer und fluidischer Versorgungsleitungen. Auf dieser Basis können spezifische, komplexe experimentelle Hochfeld-NMR/MRT-Aufbauten in kurzer Zeit realisiert werden, ohne Bedarf nach maßgeschneiderten, teuren Sonden. Als Referenz werden zwei Messaufbauten präsentiert, bei ersterem wird die Sonde für ein Öl-Wasser-Fluidikexperiment und bei dem zweiten, in einem wasserstoffbasierten Hyperpolarisationsexperiment eingesetzt. Darüber hinaus wird ein neuartiges, MR-kompatibles 3D-Zellsubstrat basierend auf Kohlenstoff vorgestellt, das erfolgreich auf Zellwachstum und MR-Bildgebung getestet wurde. Die MRT dient des Weiteren als Analysewerkzeug, um die Erhaltung der Morphologie während der Pyrolyse zu untersuchen und zu bestätigen. Das Herstellungsprotokoll ist auf andere Vorläuferpolymere anwendbar, die den Weg zu einer Vielzahl von lithografisch strukturierten 3D-Gerüsten ebnet.

Nomenclature

Abbreviations

Abbreviation	Meaning
2D & 3D	Two dimensional & three dimensional
ADC	Analog-Digital-Converter
CNR	Contrast-to-noise ratio
CW	Continuous-Wave
COG	Center of gravity
CuSO ₄	Copper(II) sulfate
DAQ	Data acquisition system
DOF	Degree of freedom
FA	Flip angle
FID	Free Induction Decay
FFT	Fast Fourier Transform
GRE	Gradient Echo
LNA	Low-noise amplifier
MEMS	Microelectromechanical systems
MRI	Magnetic Resonance Imaging
NEMS	Nanoelectromechanical systems
NMR	Nuclear Magnetic Resonance
NSCs	Neural Stem Cells
RF	Radio frequency
SA:V	Surface area to volume ratio
SE	Spin Echo
SNR	Signal-to-noise ratio
TE	Echo Time
TR	Repetition time
TPSR	Torque per slew rate

Symbols

Symbol	Description	Unit
S	Spin number	1
\vec{m}	Magnetic dipole moment	kg m s^{-1}
\mathbf{B}_0	Static magnetic field	T
\mathbf{B}_1	RF magnetic field	T
G	Shear modulus	Pa
M_0	Net magnetization	A s^{-1}
M_z	Longitudinal magnetization	A s^{-1}
M_T	Transverse magnetization	A s^{-1}
G_i	Gradient fields ($i \in \{x, y, z\}$)	T m^{-1}
μ_r	Relative permeability	1
χ_V	Volume susceptibility	1
SAR	Specific absorption rate	W kg^{-1}
T	Temperature	K
T_1	Spin-lattice relaxation time	s
T_2	Spin-spin relaxation time	s

Constants

Symbol	Value	Unit	Description
c	$299.792 \cdot 10^6$	m s^{-1}	Speed of light
γ_n	$42.577 \cdot 10^6$	Hz T^{-1}	Gyromagnetic ratio of ^1H
k_B	$1.381 \cdot 10^{-23}$	J K^{-1}	Boltzmann constant
μ_0	$4\pi \cdot 10^{-7}$	H m^{-1}	Vacuum permeability
ϵ_0	$8.854 \cdot 10^{-12}$	F m^{-1}	Vacuum permittivity
e	$1.602 \cdot 10^{-19}$	C	Elementary charge
h	$6.626 \cdot 10^{-34}$	J s^{-1}	Planck's constant
g	9.81	m s^{-1}	Gravitational acceleration of earth

Contents

Abstract	i
Zusammenfassung	iii
Nomenclature	v
1 Introduction	1
1.1 Motivation	1
1.2 Outline	3
1.3 Main results	3
2 Theoretical background	5
2.1 Nuclear magnetic resonance and its applications	5
2.1.1 Nuclear magnetism	5
2.1.2 Excitation, transverse magnetization and dynamics of magnetization vector and signal amplitude	9
2.1.3 Nuclear magnetic resonance spectroscopy	12
2.1.4 Magnetic resonance imaging	14
2.2 MR hardware & probes	21
2.2.1 Electromagnetic fields in NMR/MRI	21
2.2.2 Magnets, probes and probeheads	22
2.2.3 RF electronics	24
2.2.4 Materials and shapes in NMR/MRI	27
2.3 Image postprocessing	31
2.3.1 Digital image representation	31
2.3.2 Segmentation by thresholding	32
2.4 Fundamental methods of vibration analysis	35
2.4.1 Coupled resonator with 2 DOF	35
2.4.2 Basic formulae for torsion	37
2.4.3 Beam theory	39
Part I Low field probe for MR safety applications	43
3 State-of-the-art: MR safety	45
3.1 Types of MR interactions and hazards	45
3.1.1 Overview of interactions and hazards	45

3.1.2	Force	47
3.1.3	Induced voltage	51
3.1.4	Heating	52
3.1.5	MR artifacts	54
3.2	Development of MR safety concepts, technical specifications and standards	57
3.3	Vibration of implant substructures	59
3.3.1	The fundamental problem	59
3.3.2	Studies about induced torque of implants or implant-like structures	60
3.3.3	Studies about mechanical tissue-implant interactions	60
3.3.4	Studies about gradient-induced force for micro-robot propulsion . .	61
3.4	Conclusion	61
4	Low-field probe for MRI and vibration analysis	63
4.1	Concept	64
4.1.1	Measurement using a high-speed camera	64
4.1.2	Measurement using MRI	65
4.1.3	Measurement of laser beam deflection	65
4.2	Optical unit	67
4.2.1	Laser module	67
4.2.2	Detection unit	68
4.3	Amplifier circuit	71
4.4	Mechanical design and assembly	72
4.4.1	Front end	72
4.4.2	MRI module	74
4.4.3	Full integration	75
4.5	Software: Control and acquisition interface	75
4.5.1	Position computation	77
4.5.2	Timing parameters and computation of Fourier transform	80
4.6	Benchmarking	82
4.6.1	Optical detection	82
4.6.2	MR imaging test	84
4.7	Conclusion	85
5	Vibration analysis of implant substructures	87
5.1	Theoretical analysis and simulation of viscoelastic vibration	87
5.1.1	Model description	87
5.1.2	Analysis of static case	90
5.1.3	Analysis of transfer function and resonances	91
5.2	Characterisation of viscoelastic gels	93
5.3	Results from viscoelastic vibration tests	94
5.3.1	Static measurements	95
5.3.2	Dynamic measurements	96
5.3.3	MRI vibration measurements	98
5.4	Torque measurements of real electrodes	99
5.5	Conclusions	102

Part II High field probe for bioengineering applications	105
6 Flexible high-field probe for in-situ measurements	107
6.1 Design- and Manufacturing	107
6.1.1 Design and construction	108
6.2 Benchmarking	113
6.2.1 NMR measurements	113
6.2.2 MR experiments	114
6.3 Experiments	115
6.3.1 Oil droplet measurements	115
6.3.2 Hyperpolarisation experiments using parahydrogen (SABRE)	117
6.4 Conclusions	118
6.5 Outlook	119
7 Evaluation of substrates for in-situ cultivation	121
7.1 Methods	122
7.1.1 Cryogel fabrication, pyrolysis and cell culturing	122
7.1.2 Porosity analysis using MRI	123
7.1.3 MRI imaging of fixed cell cultures	127
7.1.4 Postprocessing	127
7.2 Experimental results	130
7.2.1 Porosity measurements and analysis of scaffold morphology	130
7.2.2 MR imaging of cell clusters	132
7.3 Conclusions	133
Part III Conclusions and Outlook	135
8 Conclusion	137
8.1 Should patients with brain implants undergo MRI?	137
8.2 Do penetrative implant-like structures experience resonant vibration in brain-like environment?	138
8.3 Can we develop a flexible probe for different applications?	139
8.4 Can we develop an MR compatible substrate for biomedical research applications?	140
Bibliography	141
Publications	153
A Appendix	157
A.1 Derivation of equations for MR interactions	157
A.2 Matlab code for laser vibration	160
A.3 3D anaglyph of scaffolds and cell clusters	170

1 | Introduction

1.1. Motivation

In the general public the most famous technique which exploits the phenomenon of Nuclear Magnetic Resonance (NMR) is Magnetic Resonant Imaging (MRI). Physicians worldwide benefit from MRI by obtaining astonishing morphological images of interior body organs which facilitate profound diagnosis. Research and technical developments within the last two decades expedited this technique far beyond standard grey scaled morphological images. Nowadays novel MR based acquisition techniques support the medical diagnostic procedure to a great extent. A list of examples includes measurement and mapping of localised temperature, mechanical properties of tissue, velocity of fluids and even cinematic MRI which means the acquisition of movies, for example a beating heart. Undoubtedly, the most famous and advanced acquisition technology beyond standard MRI is functional Magnetic Resonance Imaging (fMRI) which enables the visualisation of spatially encoded brain activity maps. From this viewpoint it is astonishing that there are still disadvantages within the clinical application of MRI. One of these major drawbacks is widely known: People with implants are most often excluded from MRI due to the risk of serious hazards. Widely known within this context are the warning icons in the vicinity of MR units which restrict carriers of pacemakers or other active implants to cross a certain point to avoid close proximity. Most often, however, it is exactly these patients which would benefit the most from MRI because treatment with implants and clinical surveillance oftentimes complement each other. The question remains why the integration of active implants into the MR environment is such a complicated challenge? The answer can be found in the working principle of both technologies.

MRI is based on the simultaneous interplay of three types of electromagnetic fields and the difference of these fields lies in their magnitude and frequency. Unfortunately, the fundamental working principle of active implants is based on electromagnetism, too. Combining both techniques leads to adverse interactions most often with high risk for the patient. Since both techniques are based on electromagnetism complete decoupling to suppress these interactions remains a major challenge. A reason is that the implant materials and structures interact with the three types of fields in various ways which leads

to a variety of phenomena such as heating, forces, induction and image artefacts.

Very similar challenges exist in a different engineering field, the development of hardware for NMR research and industrial applications. A closer look at the origin of these interactions reveals that for all materials and structures that are placed inside the NMR environment undesired interactions occur. For example, all materials interact with a static magnetic field such that they distort the field homogeneity. To conduct high-end NMR, advanced sensors were developed, so called probeheads, specialized for maximum signal-to-noise-ratio (SNR) and multi-frequency transmission while providing greatest possible field homogeneity for an optimal spectral resolution. In these cases, the electrical and mechanical interfaces including the NMR sensors are placed in close vicinity to the sample. Only the precise knowledge of the interactions of the NMR hardware with the electromagnetic fields allow the production of these high-end products. State-of-the art ultra high field probe and probeheads, however, are most often designed for specific applications such as flow measurements, solid-state or liquid-state NMR and do not support additional connections for advanced controlling or sensing of the sample. In recent years, however, an increasing demand for in-situ measurements has developed, especially for biological samples in ultra-high fields (9.4 T or higher). These types of measurements require precise control over a vast range of parameters such as temperature, oxygen level or pH-Value. Therefore, augmentation of sensors and controllers as well as their interconnection is required to facilitate these sophisticated in-situ measurements.

A combination of both fields was demanded for the initial scope of this research work, which started with the design of NMR probes for applications in MR compatibility testing. Embedded in a highly collaborative large-scale project¹ we were interested in current technology of MR compatibility of implants. With the progression of the research work different aspects and open scientific question emerged which constitute the guidelines for this research. The four main questions are:

1. Should patients with brain implants undergo MRI?^[EF01]
2. Do penetrative implant-like structures experience resonant vibration in brain-like environment?
3. Can we develop a flexible probe for different applications?
4. Can we develop an MR compatible substrate for biomedical research applications?

An option to pave the way for answering the first question lies in an extensive literature review, which was a result of the collaborative work, in which all aspects of MR safety, instrument technology and hazardous cases allow the reader to understand the

¹One goal of the project BrainLinks-BrainTools (BLBT) aimed to develop novel active brain implants. Our collaboration investigated the potential of reaching MR compatibility for these novel implants.

bigger picture and additionally highlights remaining open questions. One result of this review, is the raise of question two and the fact, that there is a lack of knowledge and data, about hazardous amplified vibrations of penetrative implants within the brain during MRI. NMR Probe design generally, is a process to develop a product for very specific tasks, which in the context of building probes for different MR compatibility tests raised the questions if one can build one probe for different application purposes. It has large advantages since probe development is an expensive process which requires many resources. High modularity offers a way to become cost efficient by using resources efficiently. One type of applications is the use of NMR/MRI capabilities in cell biology research. The demands for cell culture scaffolds for applications within the NMR environment and the required MR compatibility are very similar to the MR compatibility issues in active implants. Having MR completable 3D scaffold opens a new experimental tool for biologists.

1.2. Outline

The thesis is structured in 8 chapters and consists of two main parts followed by the conclusions. After the introduction in chapter one, chapter two represents an overview of different theoretical concepts that find application within the presented research work. This is followed by Part I which encompasses the chapters three to five. In chapter three the summary of MR interactions is presented with a focus on vibrations in the last section. Subsequently in chapter four the measurement setup for the gradient vibration experiment is presented. Part I closes with chapter five, which focuses on the presentation of the theoretical analysis and experimental result. Part II of this monograph is a detailed description of the probe development for ultra-high field MRI. This includes chapter six with a detailed analysis of the probe design and development and chapter seven in which various application are discussed. This thesis is concluded in chapter eight with a brief summary and an outlook for future work.

1.3. Main results

The research conducted within this PhD project has led to four main publications (two published and two under review) with a contribution as first author or shared first authorship.

- **Should patients with brain implants undergo MRI?**

Published in Journal of neural engineering, 2018^[EF01].

Authorship status: Shared first authorship together with J. Erhardt.

Contributions: Collecting and evaluation of required literature together with J. Erhardt. Contribution to writing the manuscript and lead in preparation of figures.

Content: A review work of the current state-of-the-art of MR safety with focus on Cochlear implants and Deep Brains stimulation electrodes. It includes a summary of the MR interactions and an synopsis of the history of the development of the implant and MR technology.

- **Gradient-induced mechanical vibration of neural interfaces during MRI.**

Published in IEEE Transactions on biomedical engineering^[EF05].

Authorship status: First author.

Contributions: Involvement in conceiving the idea and the measurement principle. Implementation of experimental realisation and data processing. Lead in writing the manuscript and preparation of figures.

Content: Methods and results of the investigation of mechanical transfer function of implant-like structures within brain-like viscoelastic environment. The systems were found to be strongly damped but not under-damped.

- **Glassy Carbon Microelectrodes Minimize Induced Voltages, Mechanical Vibrations and Forces and Artifacts in Magnetic Resonance Imaging.**

Accepted by Microsystems and Nanoengineering^[EF06].

Authorship status: Shared first authorship together with S. Nimbalkar.

Contributions: Performing the experiments for vibration analysis and induction measurements including data processing and preparation of related figures. Conducting the MR acquisition of high-field artefact experiments as well as data processing. Contributions in editing final manuscript.

Content: The torque induced in electrode ground planes through gradient switching, is quantified. A novel classification number is introduced.

- **3D carbon scaffolds for neural stem cell culture and Magnetic Resonance Imaging.**

Published in Advanced Healthcare Materials, 2018^[EF02].

Authorship status: First authorship.

Contributions: Performing the MR experiments and MR-based porosity analysis as well as data visualisation and post-processing. Contributions to writing the manuscript.

Content: This work encompasses the transformation of 3D hydrogels to carbon gels, and using MRI as the method to analyse porosity. Reconstructed 3D data supports the visualisation of distributed cell clusters within the 3D scaffold.

Contributions to three more published articles are detailed in the publication list.

2 | Theoretical background

Within this chapter the fundamental technological and physical concepts are introduced which are most relevant for the presented work. Section one is focused on the working principle on how to acquire an NMR signal, where does it originate from, how can we manipulate the spins and what information can be extracted from the NMR signal. The fundamental strategies to acquire an MR image and the concepts of signal and contrast are stated. It will be highlighted why the signal quality of NMR is extremely sensitive to the magnetic field environment. On that basis, options and constraints from an engineering viewpoint in order to design sophisticated NMR hardware will be derived and presented in the second section. In addition to the fundamentals of NMR, an introduction to image post-processing will be given which found a strong impact in two application chapters of this thesis. Moreover, a short overview of beam theory will be given to introduce the work being conducted on vibration analysis of implants. The topics presented in this introduction are mostly derived from the following excellent textbooks:

- **NMR:** Spin dynamics from M. Levitt^[89]
- **MRI:** From picture to proton from D. W. McRobbie^[104]
- **Probeheads:** NMR probeheads for from J. Mispelter^[105]
- **Image Processing:** Digital Image Processing from D. Sundararajan^[145]
- **Electrodynamics:** Classical Electromagnetics from J. D. Jackson^[70]
- **Mechanics:** Technische Mechanik 4: Hydromechanik from D. Gross et al.^[58]

2.1. Nuclear magnetic resonance and its applications

2.1.1. Nuclear magnetism

The terminology Nuclear Magnetic Resonance (NMR) reveals the fundamental objects and principles involved in the technology of NMR/MRI. "Nuclear Magnetic" means that the exploited effect originates from the magnetic moment of atomic nuclei. Every atomic nucleus consists of a certain number of protons and neutrons (both together form the group of nucleons). A special case is the nucleus of hydrogen (^1H), which consists of a single proton. Protons and Neutrons itself are composite particles that belong to the group of fermions, the group of half integer spin particles. The total spin number S of an atomic

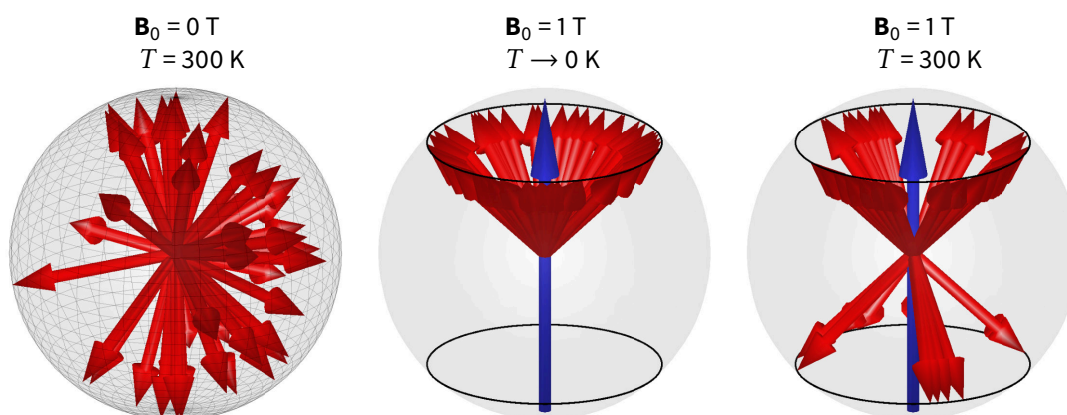


Figure 2.1.: Spin orientations (red vectors) at different magnetic fields \mathbf{B}_0 (blue vector) and temperatures T .

nucleus depends on the number and the energy states of the involved nucleons and can have the following values:

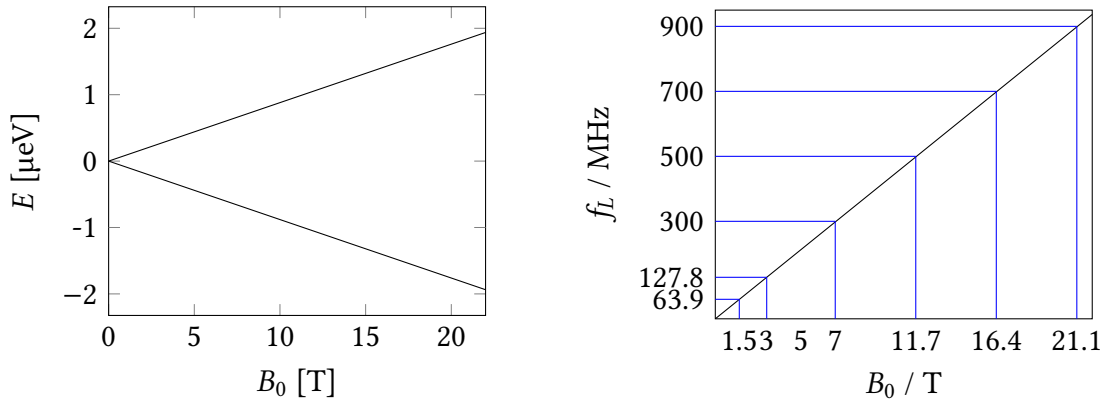
$$S = 0, \frac{1}{2}, 1, \frac{3}{2}, 2, \frac{5}{2}, \dots \quad (2.1)$$

The hydrogen isotope (^1H), a spin half nucleus, is the most important nucleus in NMR. Nuclei with a non-zero spin angular momentum $S \neq 0$ possess a magnetic moment \vec{m} . This magnetic moment \hat{m} is proportional to the spin momentum \hat{S} with the proportionality constant γ :

$$\hat{m} = \gamma \hat{S} \quad (2.2)$$

The **gyromagnetic ratio** γ , describes the ratio of magnetic moment to angular momentum of a nucleus and therewith is unique for each nucleus. Both, spin angular momentum and the magnetic momentum are vector quantities and if both vectors are aligned parallel then γ has a positive value, if they are antiparallel then γ has a negative value. How are the magnetic moments oriented in an ensemble of nuclei? If we look at spin half nuclei (e.g. ^1H) under the absence of a magnetic field we find that the magnetic moments are oriented randomly and the energy levels are degenerated¹ as indicated in figure 2.1. If we, in contrast, apply a static homogeneous magnetic field (\mathbf{B}_0) along the z-direction (per convention), then the magnetic moment starts to precess around the \mathbf{B}_0 -vector. Unlike in classical mechanics the spin orientation in an external potential is discretised which results in discrete energy levels. Knowing the energy levels reveals the frequency which allows to trigger energy transitions and furthermore enables to determine the population statistics at a given temperature. Classically, the potential energy of a magnetic particle

¹This is true under the assumption there is no spin-spin interaction. In reality there is spin-spin coupling and the absence of any external magnetic field opens another realm of NMR, the so called zero field NMR.



(a) Zeemann Splitting of ^1H nucleus w.r.t. magnetic field \mathbf{B}_0 (b) Linear dependence of the Larmor frequency w.r.t. magnetic field \mathbf{B}_0

Figure 2.2.: Zeeman splitting and Larmor frequency with respect to the static magnetic field \mathbf{B}_0 . Indicated are some of the most common field strengths for research MR units and their corresponding Larmor frequency for ^1H .

within a magnetic field can be calculated by the dot product of the magnetic field vector \vec{B}_0 and the magnetic moment $\vec{\mu}$ as given in equation 2.3.

$$E_{pot} = -\vec{m} \cdot \vec{B}_0 \quad (2.3)$$

By combining equation 2.2 and 2.3 we obtain the energy difference for the discrete energy levels. For example, hydrogen as spin half particle has a two-fold degenerate spin state and the resulting energy difference in a certain \mathbf{B}_0 -field is:

$$\Delta E = E_2 - E_1 = -\gamma \left(-\frac{\hbar}{2} \right) B_0 - \left(-\gamma \frac{\hbar}{2} B_0 \right) = \gamma \hbar B_0 \quad (2.4)$$

From the last term the factor γB_0 equals the **Larmor frequency** ω_L :

$$\omega_L = \gamma B_0 \quad (2.5)$$

This is a very fundamental result for NMR, because energy transitions between the discrete states are triggerable only at the resonance condition ω_L^2 . The existence of specific frequencies in NMR is a direct consequence of the quantum nature, because the signals originate from transitions between discrete energy levels.

The energy splitting of spin systems in external magnetic fields is called the Zeeman effect. In figure 2.2a the dependence of the energy levels of ^1H from the \mathbf{B}_0 -field is illustrated. NMR instruments are most often labelled by their working frequency of ^1H which corresponds to a certain \mathbf{B}_0 -field. For example, a 500 MHz NMR unit operates at 11.7 T.

²If, in contrast to this result, nuclei with a magnetic moment behaved equivalent to a classical dipole, every spin orientation with respect to the \mathbf{B}_0 -field would be possible. According to equation 2.3, this would result in an energy continuum instead of discrete energy states and no resonance condition would exist. Hence, NMR would not be feasible because the signals were distributed over a large frequency range.

In most cases the samples contain a large ensemble of spins leading to a bulk magnetization. The magnetisation strength depends on the population distribution which is a function of field strength \mathbf{B}_0 and the temperature. Under the assumption that the spin ensemble is in thermal equilibrium at a temperature close to zero Kelvin, all spins would populate the lowest possible energy state as indicated in figure 2.1. In this case the complete parallel alignment would lead to the largest possible net magnetisation because all spins contribute to the sample magnetisation. In most cases, however, the sample is in thermal equilibrium at room temperature and the thermal energy leads to the population of higher energy levels. This results in a smaller net magnetization because the spins of lower and higher energy levels nullify through antiparallel alignment. This effect is a very important factor in NMR because only the difference of spins in the lower and higher energy state are available for NMR detection. In a standard NMR experiment the sample contains a large number of spins (e.g. $N_0 = 2 \cdot 6.69 \cdot 10^{23}$ for 10 ml water), and the ratio of the probability distribution is obtained by the Boltzmann distribution³:

$$\frac{N_{high}}{N_{low}} = e^{-\frac{\Delta E}{k_B T}} = e^{-\frac{\gamma \hbar B_0}{k_B T}} \approx 1 - \frac{\gamma \hbar B_0}{k_B T} \quad (2.6)$$

Using the Taylor expansion of this equation the population difference ΔN can be expressed as a function of the total spins N_0 :

$$\Delta N = N_0 \frac{1 - e^{-\frac{\Delta E}{k_B T}}}{1 + e^{-\frac{\Delta E}{k_B T}}} \approx N_0 \frac{\gamma \hbar B_0}{2k_B T} \quad (2.7)$$

A sample, containing a large ensemble of spin half nuclei which is immersed in a static magnetic field, will establish a macroscopic net magnetization due to nuclear magnetism. This net magnetisation M_0 equals the sum of all contributing spin magnetic moments and is obtained by combining the equations 2.7 and 2.2^[66]:

$$\vec{M}_0 = \Delta N \gamma \hat{S} = \frac{\vec{B}_0 N_0 \gamma^2 \hbar^2}{4k_B T} \quad (2.8)$$

Based on these introduced fundamentals two important points for hardware engineering are deducible:

- Any hardware designed for NMR has to be operational at the correct Larmor frequency. To observe two different nuclei simultaneously, e.g. ^1H and ^{13}C the RF circuitry has to operate at two distinct frequencies.
- The equation 2.5 indicates the utmost importance of a homogenous magnetic field \mathbf{B}_0 . A large $\Delta \mathbf{B}_0$ leads to a large spectral distribution $\Delta \omega$ resulting in loss of sensitivity (drop of signal peak) and selectivity (spectral overlap).

³By using eq. 2.7 we see that from approximately $13 \cdot 10^{23}$ spins in 10 ml water at 293 K in an 11.7 T field $2 \cdot 10^{18}$ spins contribute to the NMR experiment. This is roughly one spin per million.

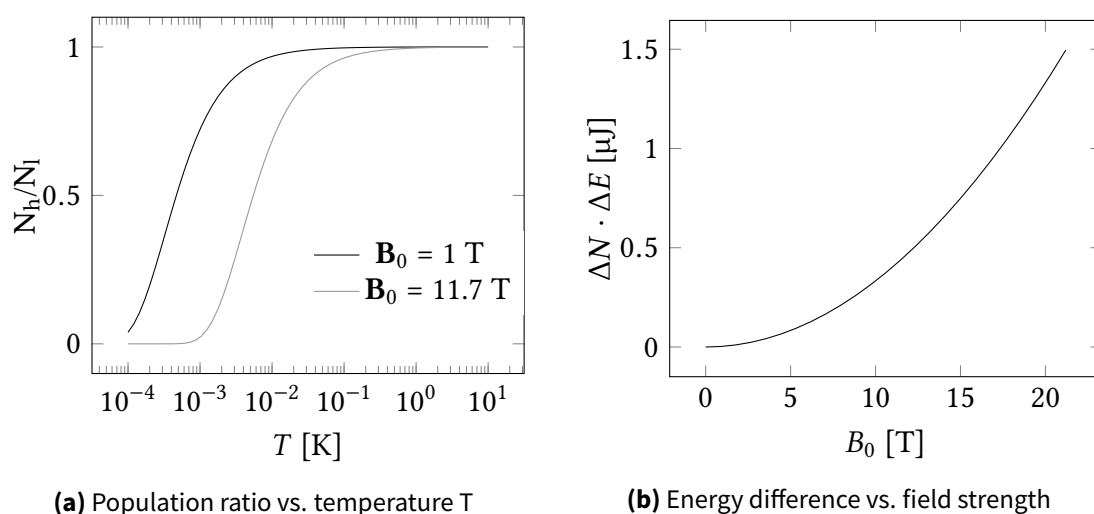


Figure 2.3.: (a) The Boltzmann distribution as a function of the magnetic field strength. (b) The total energy of a NMR sample as a function of magnetic field amplitude(b). Quadratic dependence of the total energy of the spin system in 10 ml water from the \mathbf{B}_0 -field.

2.1.2. Excitation, transverse magnetization and dynamics of magnetization vector and signal amplitude

The general working principle of an actual NMR experiment is described on the basis of the ^1H nuclei but this approach is valid for all other observable spin half nuclei. A sample of water is subjected to a \mathbf{B}_0 -field and a macroscopic longitudinal magnetization $M_z = M_0$ parallel to the \mathbf{B}_0 -field is established. An NMR experiment is conducted by excitation and subsequent measurement of the response. For excitation, an alternating magnetic field \mathbf{B}_1 , which oscillates at the Larmor frequency to obey the resonance condition, is superimposed perpendicular to the \mathbf{B}_0 -field. This "on resonance" condition explains the third term "resonance" in NMR. The \mathbf{B}_1 field, produced by an RF coil, forces the net magnetisation M_0 to flip towards the transverse xy-plane and the flip angle α_{FA} between xy-plane and z-axis is given by:

$$\alpha_{FA} = \gamma B_1 \tau \quad (2.9)$$

The precise controlling of the \mathbf{B}_1 amplitude and the pulse duration τ allows to achieve any desired flip angle. After excitation the transverse magnetization vector M_T rotates within the x-y-plane around the z-axis. This rotating magnetization leads to an alternating electric field which can be transformed to an NMR signal using an RF coil. Dephasing of the transverse magnetization M_T leads to an exponential decay of the measured signal, which is called the "Free induction decay (FID)". The source of this effect is the so-called T_2 -relaxation, a process in which the spins experiences decoherence, hence, it is described as spin-spin relaxation. Simultaneously, the longitudinal magnetization restores exponentially due to T_1 relaxation, a process described as spin-lattice relaxation. A semi-classical model

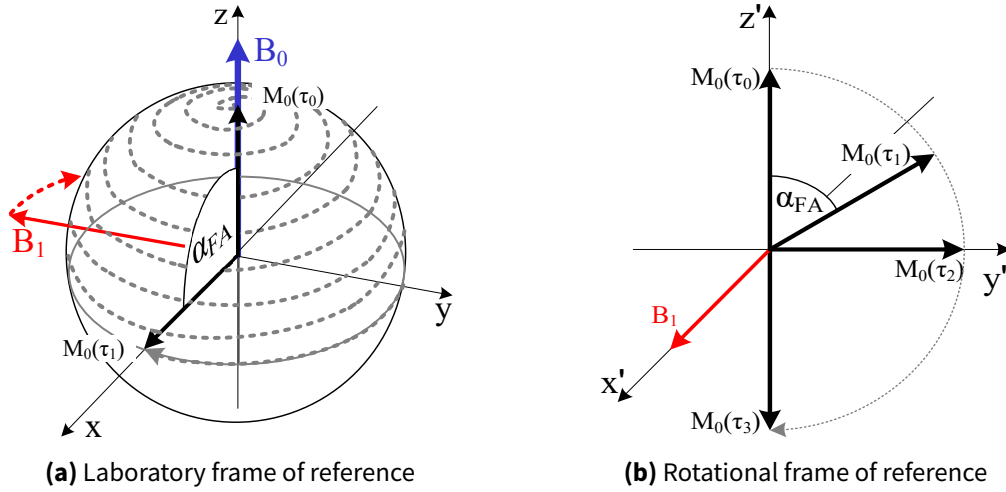


Figure 2.4.: Magnetization trajectories of M_0 during an excitation pulse from laboratory frame of reference and from rotational frame of reference. The schematic in (a) represents the laboratory frame of reference. It illustrates how the magnetization vector starts rotating in the x-y-plane during excitation when \mathbf{B}_01 is applied. The \mathbf{B}_01 vector rotates clockwise if viewed against the orientation of \mathbf{B}_0 , hence the precession follows the left hand rule. In the rotational frame (b) the \mathbf{B}_01 field is fixed and \mathbf{B}_0 vanishes when the larmor condition is exactly met. Then the magnetic vector M_0 is precessing around \mathbf{B}_01 according to the left-hand rule. Magnetization vectors M_0 are depicted for different excitation time durations ($\tau_0 = 0; \tau_0 < \tau_1 < \tau_2 < \tau_3$)

of this dynamics is defined by the Bloch equations (equation 2.10) in which T_2 is the time constant parameter for spin-spin relaxation, and T_1 is the time constant for spin-lattice relaxation.

$$\frac{d}{dt} \begin{pmatrix} M_x \\ M_y \\ M_z \end{pmatrix} = \begin{pmatrix} 0 & \gamma B_z & -\gamma B_y \\ -\gamma B_z & 0 & \gamma B_x \\ \gamma B_y & -\gamma B_x & 0 \end{pmatrix} \begin{pmatrix} M_x \\ M_y \\ M_z \end{pmatrix} - \begin{pmatrix} \frac{M_x}{T_2} \\ \frac{M_y}{T_2} \\ \frac{M_z - 1}{T_1} \end{pmatrix} \quad (2.10)$$

To understand the dynamics after a 90° -pulse, under the assumption that the external field has only components in z-direction, therefore $B_x = B_y = 0$, and neglecting relaxation effects such that $T_1, T_2 = \infty$, a solution for the above equations is given by:

$$M_T(t) = M_0 e^{-i\gamma B_0 t} = M_0 (\cos(\omega_0 t) - i \sin(\omega_0 t)) = M_x(t) + M_y(t) \quad (2.11)$$

$$M_z(t) = 0 \quad (2.12)$$

Equation 2.11 describes the transversal rotation in the complex plane. After the excitation using a 90° pulse M_T equals M_0 and the magnetization vector rotates with the angular frequency ω_0 around the z-axis. To include relaxation effects into the model it is beneficiary, to formulate the Bloch equations in the rotating frame of reference, a coordinate system that rotates with an angular frequency $\Omega = \omega_0$ relative to the resting laboratory frame of reference. Therefore, the external magnetic fields \mathbf{B}_0 and \mathbf{B}_1 have the form $B_x(t) =$

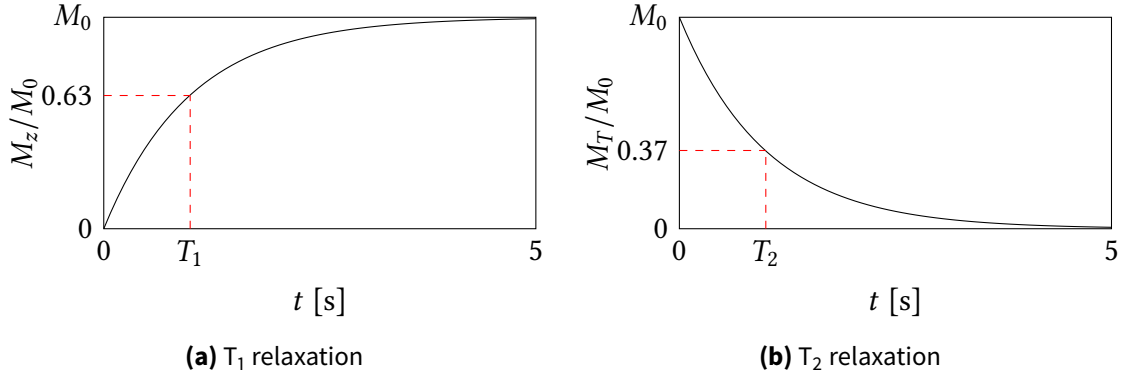


Figure 2.5.: Illustration of T_1 - and T_2 -relaxation effects after a 90° pulse. T_1 -relaxation or spin-lattice relaxation leads to recovery of M_z whereas T_2 -relaxation or spin-spin relaxation leads to a decay of transverse relaxation.

$B_1 \cos \omega_0 t$, $B_y(t) = -B_1 \sin \omega_0 t$ and $B_z(t) = B_0$. We define $\epsilon = \gamma B_1$ and $\Delta = \gamma B_0 - \omega$. In a frame of reference that rotates at Larmor frequency $\omega = \omega_0$ and under the absence of \mathbf{B}_1 -field, the parameters $\epsilon = 0$ and $\Delta = 0$, and the Bloch equations simplify to:

$$\frac{d}{dt} \begin{pmatrix} M'_x \\ M'_y \\ M'_z \end{pmatrix} = - \begin{pmatrix} \frac{M'_x}{T_2} \\ \frac{M'_y}{T_2} \\ \frac{M'_z - 1}{T_1} \end{pmatrix} \quad (2.13)$$

The solution of this equation for the transversal magnetization M'_T is given by:

$$M'_T(t) = M'_T e^{-\frac{t}{T_2}} \quad (2.14)$$

$$M'_z(t) = M_z(t) = M_0(1 - e^{-\frac{t}{T_1}}) \quad (2.15)$$

T_1 -relaxation determines the period of time an excited system needs to recover to full longitudinal magnetization. This effect is of vital importance for acquisition schemes that require recurring excitation pulses because fast repetitions lead to saturation effects. The parameter T_2 determines the time scale of the decay of an FID, and thus the spectral resolution one can obtain. Liquid specimens mostly have T_2 times in the range of seconds leading to frequency resolutions of sub-Hertz. Solids, on the other hand, due to strong dipolar coupling, have T_2 -times in the range of milliseconds or less which leads to very broad spectra. Hence, liquid-state and solid-state NMR are two different NMR fields which require completely different approaches for the experimental setup, for example, Magic-Angle-Spinning (MAS) for solid-state NMR.

Of great importance is the question of how much signal can we obtain from an NMR experiment? For NMR with a sample containing large number of spins, the signal acquisition scheme in NMR is comparable to the working principle of a dynamo. The rotating vector M_T acts similar to a rotating magnet in a dynamo, in which the power output depends on the strength of the magnet and the angular velocity. Similarly, the signal

power in NMR depends on the amplitude of M_{xy} and the angular velocity of M_T which is the Larmor frequency ω . Thus, the signal is proportional to the magnetization and ω :

$$S \propto M_T \cdot \omega \quad (2.16)$$

Maximum signal will be achieved after a 90° excitation where $M_{xy} = M_0$, then we can write for the signal:

$$S \propto M_0 \cdot \omega = \frac{\vec{B}_0 N \gamma^2 \hbar^2}{4k_B T} \cdot \gamma \vec{B}_0 = \vec{B}_0^2 \frac{N \gamma^3 \hbar^2}{4k_B T} \quad (2.17)$$

This equation shows that the increase of \mathbf{B}_0 has two important effects: (i) The bulk magnetization increases linearly with \mathbf{B}_0 which leads to a higher signal. Microscopically this is due to the linear increase of the energy gap resulting in a higher population difference⁴ (ii) The Larmor frequency increases linear with \mathbf{B}_0 leading to a higher electromotive force in the coil due to a larger time gradient dB/dt . On the microscopic scale this is due to the higher energy per spin transition.

Both effects together explain why macroscopically the MR signal scales quadratically with \mathbf{B}_0 , which is the reason for the endeavour towards higher field strengths in MRI and NMR. An alternative strategy to boost the signal can be achieved by increasing the population difference beyond thermal equilibrium. There are various techniques pursuing that approach which are summarized under the term hyperpolarisation.

2.1.3. Nuclear magnetic resonance spectroscopy

The most fundamental properties and aspects of a simple one-dimensional NMR signal are the spectral distribution and linewidth. An NMR acquisition starts by collecting the FID. An example is illustrated in figure 2.6 which shows an FID of diluted ethanol in water. The signal induced in the coil is proportional to the total transverse magnetization $M_T(t)$. After recording the signal, the FID is subjected to a Fourier transformation which facilitates the spectral analysis.

2.1.3.1. Decay time and bandwidth

The FID of a substance with equivalent protons, such as water, is of a decaying waveform. Ideally, the decay is of an exponential nature with the time constant T_2^* , then the result in the frequency domain is a Lorentzian distribution. For small angle excitations, the reciprocal of the time constant T_2^* equals the sum of the reciprocals of the spin-spin-relaxation (T_2), field inhomogeneity (T_i) and radiation damping (T_{rd}) expressed by^[60]:

⁴Often NMR is called an insensitive methodology, which is explained by the small difference of the population densities. However, the small energy gap of the Zeeman level is the fundamental reason which then leads to a small population difference at room temperature.

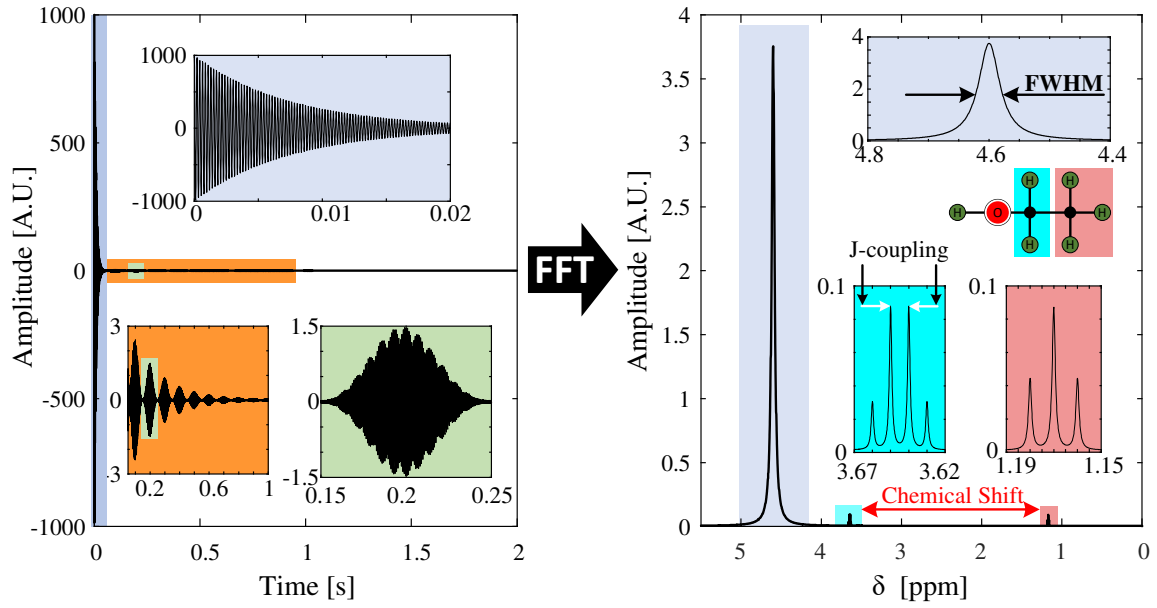


Figure 2.6.: Illustration of the most important features of a typical NMR signal in time and frequency domain. The large graph, with its three insets, on the left side, shows a typical FID of a small fraction of ethanol diluted in water. Most of the vertical signal originates from water showing a rapid decay. A zoom of this part is shown in the blue inset. Signal originating from ethanol with a characteristic beating is highlighted in the orange inset. An enlarged view of one beat period is shown in the green area. The FFT of the entire FID is shown on the right side. The large peak (blue background) originates from water indicating a very high dynamic range. The turquoise and red insets show the spectral part of the methylene and the methyl group, respectively, the distance is called chemical shift. Within these insets individual peaks originate from J-coupling.

$$\frac{1}{T_2^*} = \frac{1}{T_2} + \frac{1}{T_i} + \frac{1}{T_{rd}} = \frac{1}{T_2} + \gamma \Delta B_0 + 2\pi \eta Q \gamma M_0 \quad (2.18)$$

T_{rd} is the signal decay due to radiation damping with the filling factor η and the quality factor Q of the receiver circuit, adapted from the publication by Krishnan et al. [85]. Even though the formula becomes inaccurate for large flip angles due to the term $1/T_{rd}$, the effect of radiation damping becomes clear for a sample that occupies a large amount of coil volume placed in a high Q coil circuit. If normal water is used as solvent, the water signal will decay fast due to radiation damping as indicated in the blue inset in figure 2.6. Hence, in the frequency domain the water will occupy a large bandwidth with a high signal. The time constant T_i describes the decay due to field inhomogeneity. Many specimens in liquid NMR have relaxation time of seconds and field inhomogeneity dominates the signal decay, therefore optimizing for most homogeneous B_0 -field is of utmost importance. One option to quantify the linewidth is to measure the spectral width $\Delta\nu$ at half height of the peak maximum, which is called the "Full Width at Half Maximum" (FWHM).

$$\Delta\nu = \frac{1}{\pi T_2^*} \quad (2.19)$$

This is illustrated in figure 2.6 at the peak of water. As an example, the radiation damping from water leads to a large bandwidth at FWHM. To measure the true T_2 value of a specimen the so-called spin-echo sequence is applied. Exactly at the centre between excitation and acquisition a 180° pulse is applied. In this case, at the acquisition point, the dephasing induced due to field inhomogeneities is reversed such that the signal represents a remanent transversal magnetization which has only T_2 -relaxation.

2.1.3.2. Chemical shift and J-coupling

The ethanol in this example is of low abundance and the radiation damping is negligible. The orange inset shows the ethanol-dominated part of the FID with a signal duration of larger than a second. The large beating with a period of 10 ms comes from the equivalent J-couplings of around 10 Hz. In the frequency domain J-coupling is observable as frequency splitting in both domains, the methylene and methyl group. These two groups are separated by chemical shift. In the classical picture, the chemical shift is caused by the magnetic shielding of a nucleus through the surrounding electrons. An electron in close vicinity to a nucleus induces an opposite magnetic field which leads to a reduced static magnetic field and thus to a shift of the Larmor frequency. This is visible as a peak shift in the NMR spectrum and allows the researcher to get information about the chemical environment.

2.1.4. Magnetic resonance imaging

Magnetic Resonance Imaging is mostly known as a technique that facilitates the generation of monochrome images obtained from NMR signals. Central points to understand the image formation are the contrast mechanism and the technique of spatial encoding. These fundamental principles will be presented in the following text.

2.1.4.1. Spatial encoding

For spatial encoding a third electromagnetic field is superimposed in addition to \mathbf{B}_0 and \mathbf{B}_1 . It consists of three fields of which each of them features a linear gradient in one spatial direction and is switched with a bandwidth in the two-digit kilohertz regime. Most important are the techniques of slice selection, phase and frequency encoding. Slice selection is a fundamental method in 2D MRI that allows to excite only the nuclei in a desired slice⁵. Therefore, a linear gradient G_z is applied and a rectangular shaped RF pulse (in frequency domain) with a defined excitation bandwidth Δf_{exc} is simultaneously applied.

⁵In this explanation, slice selection is chosen to be in z-direction, frequency and phase encoding in x- and y-direction, respectively. The directions, of course, can be arbitrarily exchanged.

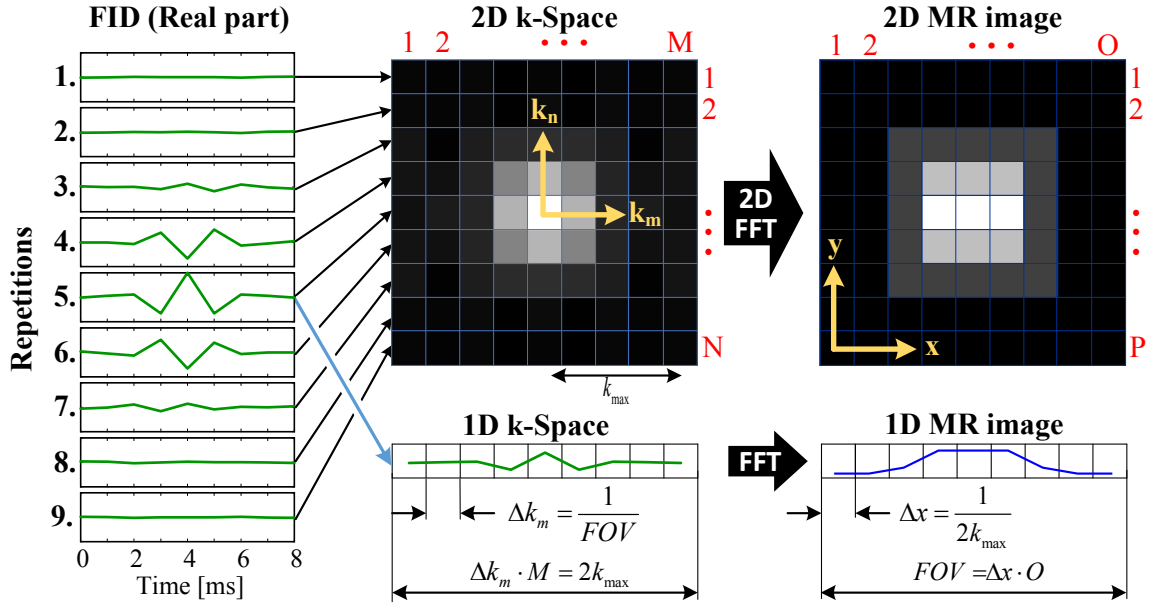


Figure 2.7.: From the FID's to the MR image: A sequence of FID's is used to fill the k-space (the complex matrix $S[m, n]$) of size $M \times N$ which is equal to the size of the final MR image $O \times P$. In the cartesian filling scheme one FID fills one k-space line. If the full k-space data is recorded, this data is subjected to a 2D FFT and the magnitude plot of the transformation yields the familiar MR image.

The linear gradient leads to a location dependency of the Larmor frequency, therefore only those nuclei get excited which resonate within the bandwidth of the RF pulse. The slice thickness Δt can be calculated using the following equation:

$$\Delta z = \frac{\Delta f_{exc}}{\gamma G_z} \quad (2.20)$$

The slice thickness Δz can be controlled by the gradient strength and/or the excitation bandwidth. Spatial encoding within the slice is conducted using phase- and frequency encoding steps. Conceptually, the volume of the slice can be divided in sub-volumes, so-called voxels. Then, the MR signal received from an entire slice is proportional to the sum of the transverse magnetization vectors from all voxels. If two orthogonal gradient fields G_x and G_y are applied before or during the signal acquisition, then the digitized MR signal received from an entire slice equals the sum of the magnetization from all voxels:

$$S[m, n] = \sum_{o=1}^O \sum_{p=1}^P M_T[x_o, y_p] e^{-jk_m x_o} e^{-jk_n y_p} \quad (2.21)$$

According to this equation, the recorded MR signals represent the 2D discrete Fourier transform of an object. To obtain an MR image, MR signals are sequentially recorded and arranged in the so-called k-space matrix, which represents a domain for spatial frequencies.⁶ We are used to describe the shape of an object as a function of space but it is

⁶The reason for the name "k-space" is because "k" is often used as an index to denote spatial frequencies.

2. Theoretical background

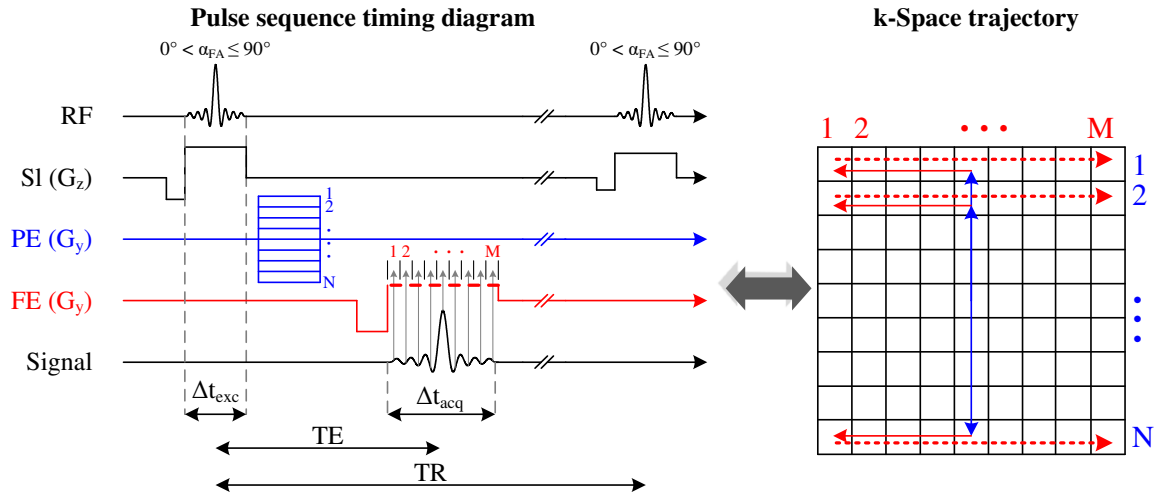


Figure 2.8.: Pulse diagram for a standard gradient echo sequence and the corresponding k-space trajectories. TE and TR are the parameters representing the echo time and repetition time, respectively. Dashed lines indicate the gradient states during signal acquisition. This acquisition scheme is called cartesian filling.

equivalent to describe the shape of an object as a composition of spatial frequencies. Both representations can be transformed into each other, they form a Fourier transform pair. In short, standard MRI is a tool to measure the spatial frequencies of an object and based on the obtained information, an MR image is computed. A very common procedure to fill the k-space is to sequentially acquire the required data points. To form a final MR image this data is subjected to a 2D discrete Fourier transformation as depicted in figure 2.7. In general, the k-space matrix elements $S_{m,n}$ can be filled randomly. One very famous filling scheme, is the sequential acquisition using frequency and phase encoding, the so called cartesian filling. If the frequency encoding is conducted in x-direction the sampling points for the spatial frequency k_m are given by equation 2.22 with Δt the time between two sampling points with $m \in \{1, 2, \dots, M\}$:

$$k_m = \gamma G_x m \Delta t \quad (2.22)$$

This means that the discrete sample points in k-space are reached by varying the time while keeping the gradient constant. The negative frequencies in k-space are reached by applying a negative gradient field. The acquisition duration Δt_{acq} of one FID is given by the number of pixels M divided by the receiver bandwidth Δf_{acq} .

$$\Delta t_{acq} = \frac{M}{\Delta f_{acq}} = M \Delta t_S \quad (2.23)$$

The sampling points for spatial frequency k_n acquired by phase encoding are governed by equation 2.24 with $n \in \{1, 2, \dots, N\}$.

$$k_y = \gamma \Delta G_y n \tau \quad (2.24)$$

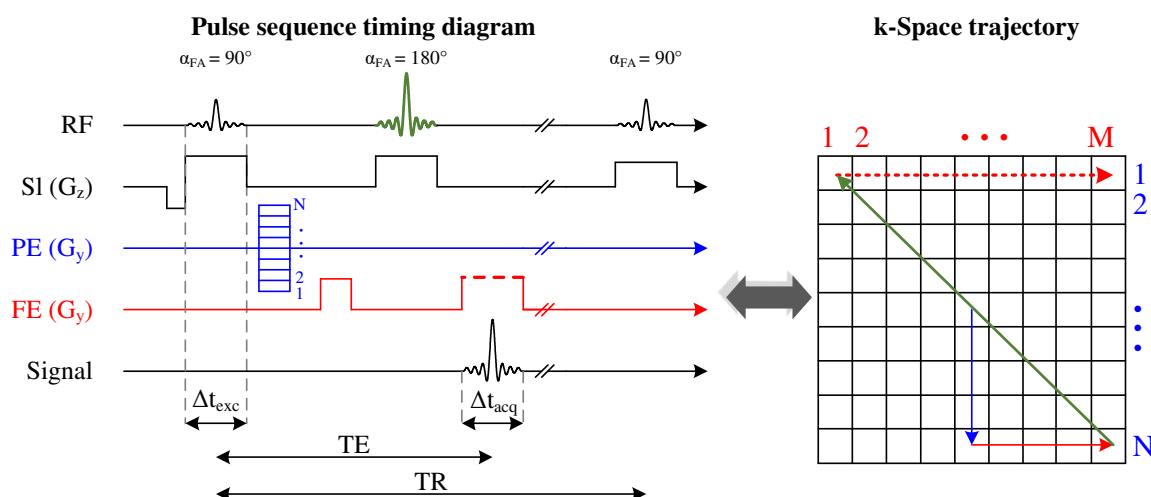


Figure 2.9.: SE pulse sequence diagram and corresponding trajectory of the first acquisition line. The 180° -pulse causes a point reflection at the k-space centre. The phase encoding sequence and the first frequency encoding segment are inverted compared to figure 2.8, because it is applied before the 180° -pulse which inverts the already conducted trajectory.

A standard pulse diagram for a gradient echo (GRE) sequence is depicted in figure 2.8. The echo time TE is defined as the duration from the centre of the excitation pulse to the centre of the echo signal. To fill the k-space N phase encoding steps are required which requires N repetitions. The parameter TR determines the duration between two consecutive excitation pulses; hence the total acquisition time is equal to $N \cdot TR$. A further important parameter is the bandwidth of the excitation pulse $\Delta f_{exc} = 1/\Delta t_{exc}$, which determines the duration of the excitation pulse. The common range is between 1-20 kHz. Reduction of excitation bandwidth enables the application of a lower gradient field at the expense of excitation duration. Very similar is the behaviour of receiver bandwidth, where an increase of receiver bandwidth allows for faster FID acquisition. The shortest possible echo time TE results from:

$$\frac{\Delta t_{exc} + \Delta t_{acq}}{2} < TE_{min} \quad (2.25)$$

There is a large number of different MR acquisition protocols, whereby each of them is optimized for one or more different parameters, for example minimal acquisition time, large SNR, maximal contrast, or for parameter mapping such as \mathbf{B}_0 -field maps. Advanced protocols are tailored by combining fundamental sequence components. All sequences can be fundamentally divided into gradient echo based (GRE) or spin echo based (SE) sequences. The major difference of a SE sequence compared to a GRE sequence is the necessity for a 90° excitation pulse followed by one or more 180° pulses during the sequence which is illustrated in figure 2.9. A 180° pulse has a distinct effect for the k-space trajectory: it leads to a point reflection at the centre of k-space. Apart from that, the gradient switching principles to maneuver through k-space are identical to the presented GRE principles. In 3D MRI the slice selection gradient is replaced by another phase encoding gradient

leading to a 3D k-space matrix that is filled with two phase encoding gradients and one frequency encoding gradient.

2.1.4.2. Contrast weighting

Contrast between different objects in an image is as important as spatial resolution in order to discriminate objects in an image. The larger the difference of the grey scale value of different objects the larger the contrast. The signal acquired from a certain voxel at location (x_o, y_p) is proportional to the FA α_{FA} , T_1 and T_2 ⁷:

$$S[o, p] \propto M_0[x_o, y_p] \sin(\alpha_{FA}) \frac{\left(1 - \exp\left(-\frac{TR}{T_1}\right)\right) \exp\left(-\frac{TE}{T_2^*}\right)}{1 - \cos(\alpha_{FA}) \exp\left(-\frac{TE}{T_2^*}\right)} = C[o, p] \quad (2.26)$$

Two very common methods to obtain contrast in MR images are the so-called T_1 -weighting and T_2 -weighting. For SE-pulses with $\alpha_{FA} = 90^\circ$ equation 2.26 simplifies to:

$$S[o, p] \propto M_0[x_o, y_p] \left(1 - \exp\left(-\frac{TR}{T_1}\right)\right) \exp\left(-\frac{TE}{T_2}\right) = C[o, p] \quad (2.27)$$

T_1 weighting is illustrated in figure 2.10. TR and TE are both short, such that during recording T_2 -relaxation plays a minor role. Due to fast TR more longitudinal magnetization can restore in a material with a smaller T_1 -value, which then appears brighter in the image.

In contrast T_2 -weighting, illustrated in figure 2.11, TR and TE are both long, such that during recording T_1 -relaxation plays a minor role. The large time gap between excitation and acquisition leads to large differences in transverse magnetization due to dephasing, depending on T_2 -relaxation of the specimens. Materials such as water with large T_1 and T_2 times appear bright. In both images, the first scan is skipped, because the magnetization has not reached a steady state condition, which would lead to image artefacts. In non-spoiled imaging sequences, multiple dummy scans are required before steady state condition is reached. Another important weighting scheme is Proton density weighting (PD) in which TE is short and TR is long. Relaxation effects play a minor role in the signal of a voxel and the largest contribution comes from the proton density, which is understandable from equation 2.27: In this case both exponential factors converge towards zero. Most often for T_1 -weighted images GRE-based sequences are used, whereas for T_2 -weighted images SE sequences are applied⁸.

⁷This formula is based on the assumption that there is no residual transverse magnetization. This is true for sequences that destroy transversal magnetization after one FID, which are called spoiled sequences.

⁸With GRE-based sequences only T_2^* -weighted images can be acquired.

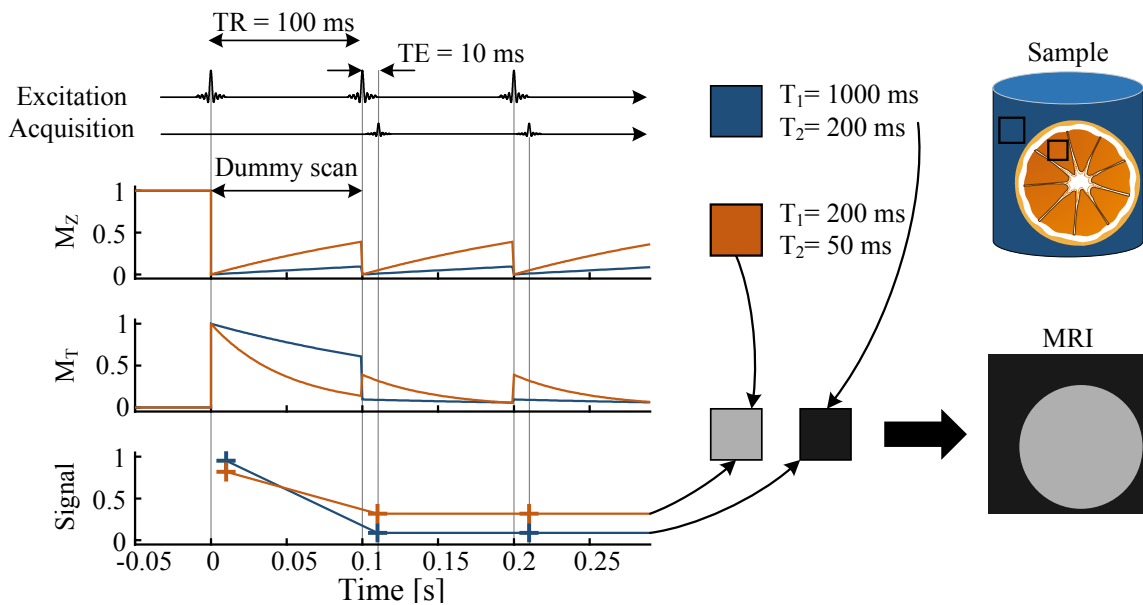


Figure 2.10.: T_1 -weighted image: Short TE and short TR lead to the effect that the transverse magnetization M_T during recording is strongly dependent on the restored longitudinal magnetization M_z .

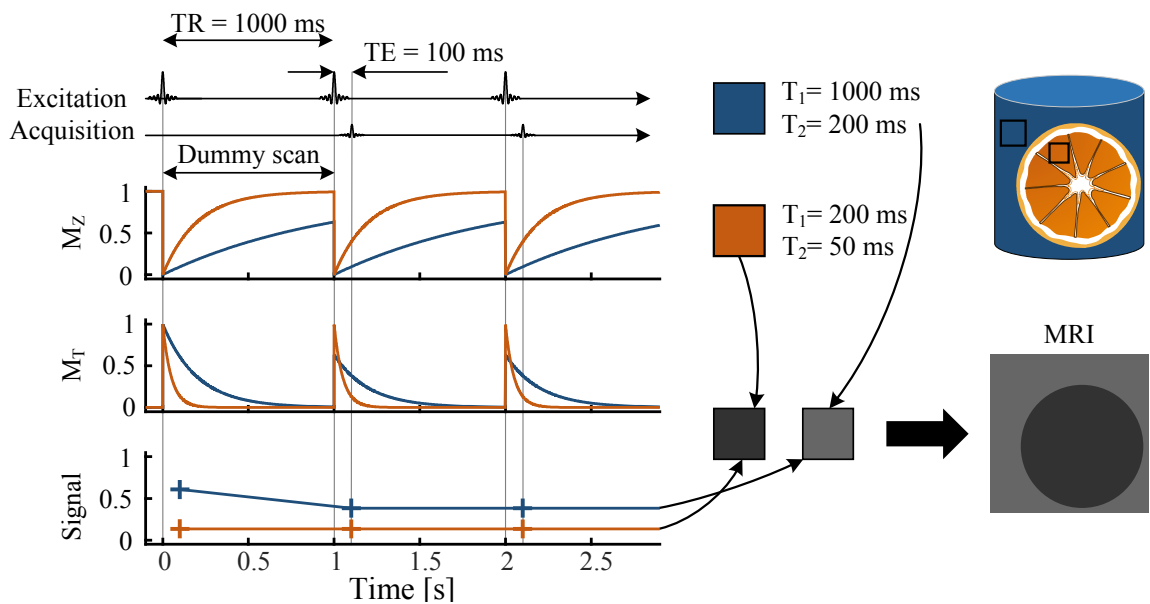


Figure 2.11.: T_2 -weighted image: Long TE and long TR lead to the effect that the transverse magnetization M_T during recording is strongly dependent on the decay of transversal magnetization M_T .

2.1.4.3. Signal-to-noise ratio (SNR) and Contrast-to-noise ratio (CNR)

A very important factor in MRI is to optimize for greatest possible SNR and/or CNR. The signal obtained from a voxel depends on the voxel volume V_{vox} , the number of acquisition points N_i per spatial dimension, the acquisition bandwidth Δf_{acq} , the number of averages of

2. Theoretical background

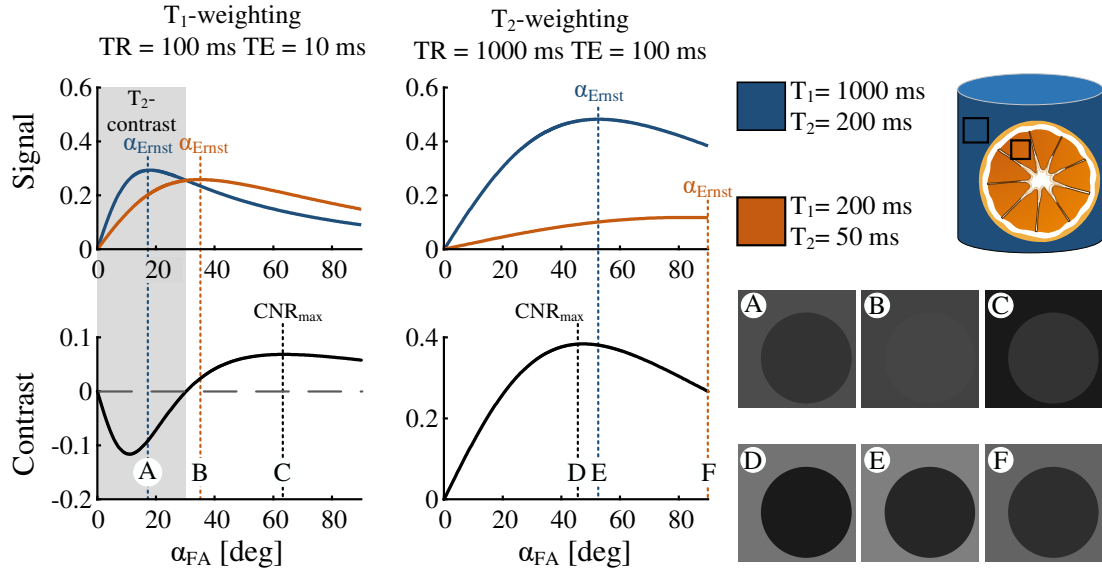


Figure 2.12.: Dependence of signal and contrast amplitude on the FA α_{FA} . The wrong FA can lead to unintentional contrast inversion (A). The correct FA for maximising the signal of one specimen differs oftentimes from the flip angle for largest contrast (B and C; D and E,F).

the entire image N_{avg} and the applied contrast weighting $C[o, p]$ (equations 2.26 and 2.27). The SNR is proportional to:

$$\text{SNR} \propto C[o, p] \frac{V_{vox} \sqrt{N_{avg} N_x N_y N_z}}{\sqrt{\Delta f_{acq}}} \quad (2.28)$$

From figures 2.10 and 2.11 we can see that the signal obtained from different regions is far from the largest possible signal in order to obtain contrast. Whereas for SE sequences the initial flip angle is fixed at 90° , for GRE sequences the adjustment of the flip angle α_{FA} offers one more degree of freedom to adjust for maximal CNR and SNR. The fundamental principle is illustrated in figure 2.12, in which the dependence on the signal from the flip angle is illustrated. A smaller choice for α_{FA} results in less saturation of the longitudinal magnetization, leading to an increase of signal. On the other hand, a smaller flip angle results in less transverse magnetization. Thus, there is flip angle with a signal maximum for each sample and a given TR and TE. The flip angle at which maximum signal is reached is the so-called Ernst angle:

$$\alpha_{Ernst} = \cos^{-1} e^{-\frac{TR}{T_1}} \quad (2.29)$$

If the imaging object contains only one specimen adjusting $\alpha_{FA} = \alpha_{Ernst}$ is important to obtain maximal signal.

As can be seen from equation 2.28, after optimising all parameters for maximal SNR/CNR, the last resort for increasing SNR is to average the image at the expense of total acquisition time. Before an imaging procedure the required limits of all imaging parameters should be established (min. resolution, desired contrast (TE,TR) including receiving bandwidth etc.)

in order to find a good trade-off between all the adjustments. If, afterwards the SNR/CNR is beyond the acceptable limit one can apply averaging. To demonstrate the averaging as last resort it is useful to define the SNR per total acquisition duration T_{acq} which is given by the following equation (under the assumption read encoding is in x-direction):

$$T_{acq} = N_y \cdot N_z \cdot TR \cdot N_{avg} \quad (2.30)$$

Then the SNR per unit acquisition time is computed by:

$$\frac{SNR}{T_{acq}} \propto \frac{V_{vox} \sqrt{N_{avg} N_x N_y N_z}}{N_y \cdot N_z \cdot TR \cdot N_{avg} \sqrt{\Delta f_{acq}}} = \underbrace{\frac{\Delta x \Delta y \Delta z \sqrt{N_x}}{\sqrt{N_y N_z}}}_{\text{FOV \& Resolution}} \underbrace{\frac{1}{TR}}_{\text{Contrast}} \underbrace{\frac{1}{\sqrt{N_{avg}}}}_{\text{Averages}} \quad (2.31)$$

This formula gives a guide on how to optimize for an SNR for an MR acquisition, as read from left to right. First, the required minimum voxel size and the required FOV should be set. The resolution should not exceed the requirements. Additionally, it is most efficient to have the largest number of pixels in frequency encoding direction. If possible, 2D imaging should be preferred, thus reducing the phase encoding directions to one dimension. If more slices are required multi-slice interleaved imaging should be applied. Next, the contrast should be optimized by means of TR for ideal CNR and efficient acquisition time. Changing the flip angle using equation 2.29 may help to reduce TR while keeping the signal constant. The acquisition bandwidth should be as small as possible, however without changing the optimized TE (see equation 2.25). If in this 2D image configuration the SNR is not enough, then the next step is to change to a 3D image instead of conducting averaging on a 2D slice. This has the advantage of boosting the SNR with additional information for free due to a larger FOV compared to plain averaging of the same slice.

2.2. MR hardware & probes

2.2.1. Electromagnetic fields in NMR/MRI

To acquire an NMR spectrum two main fields are required, (i) a large static magnetic field which magnetizes the sample and (ii) an electromagnetic RF field for excitation is required. For advanced NMR (gradient-enhanced NMR) and in particular MRI three gradient fields are required. A fourth field is called the shim-field superimposed to \mathbf{B}_0 to compensate for field inhomogeneities. All four fields are depicted in figure 2.13 and can generally be characterized by their temporal properties and magnitude.

Static \mathbf{B}_0 -field - The static \mathbf{B}_0 -field is constant in a certain NMR/MRI unit has a range from approximately 0.1 T to 20 T⁹. Low fields (up to 1 T) are often produced with permanent magnets, whereas higher fields are produced with superconducting coils cooled with liquid helium. The latter ones are more stable regarding field drift. Ultra high fields 7 T and

⁹There are also earth-field and zero field NMR units which are not considered here.

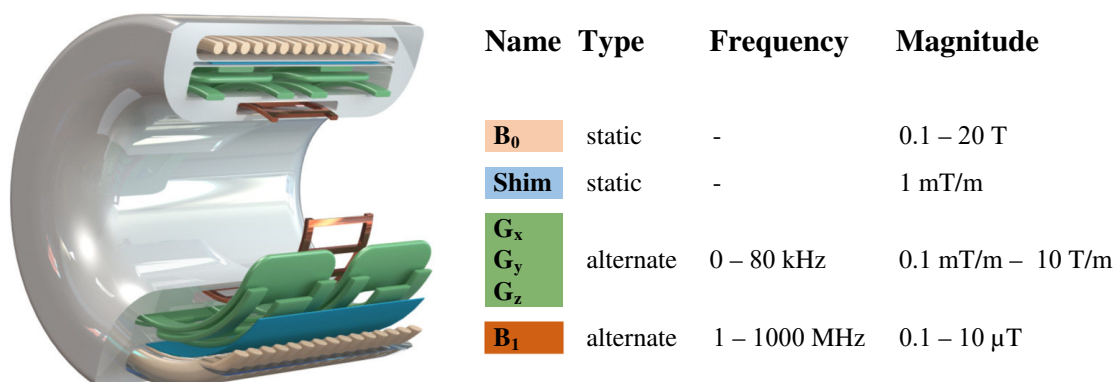


Figure 2.13.: Overview of the applied electromagnetic field and their specific properties in NMR/MRI applications. As an example, on the left, a human MRI scanner with the build-in coils for all four field types.

higher are mostly used in research. Standard human MRI scanners reach up to 7 T. Higher fields are used for small animal scanner and in ultra high field NMR applications.

Static Shim field - A second static field is superimposed to B_0 in order to correct for field inhomogeneities. The static magnetic field B_0 can be represented as a linear combination of orthonormal functions. The usual choice are spherical harmonics. Inhomogeneities can be treated as deviations which can be compensated by a set of coils that produce magnetic fields according to spherical harmonics. For each basis set a certain coil is required, hence high order shims require sophisticated coil systems. In simple NMR systems zero and first order shims are applied, in advanced NMR units up to 5th order shims are applied^[23].

Gradient fields - A gradient coil features a linear field gradient. Typically, three gradient coils are implemented, one for each spatial direction. These fields are used to manipulate the spin systems and the switching times are in the range from tenth of microseconds to hundreds of milliseconds. Two parameters are important to characterise the gradient fields: (i) The gradient strength given in T/m, (ii) the gradient slew rate given in T/(m·s) which is a parameter that describes how fast a gradient can be switched.

RF field - The RF field used for excitation is ideally a homogeneous alternating magnetic field tuned to resonate at the Larmor frequency of the corresponding nuclei. There are a large variety of NMR coils ranging from microscopic applications in NMR/MRI to large macroscopic coils for human MRI. The field strengths are in the μ T range with frequencies in the range of tenth of MHz to one GHz

2.2.2. Magnets, probes and probeheads

In contrast to the human scanners in clinics, as depicted in figure 2.13, the region of interest or the isocenter in NMR/MRI scanners for research and industrial applications is much smaller in size (max. 10 cm), leading to more rigorous geometrical design restrictions. These instruments are divided into two subunits: (i) A large-scale unit, most referred to as "the magnet", that contains the superconducting B_0 -coils (or alternatively a permanent

magnet) and the shim coils. (ii) An exchangeable probe that provides the B_0 coils and all the required electronic interfaces for the RF circuitry. The probehead is fixed onto the probe or exchangeable, depending on the type of probe. Especially for MAS or Solid-State-Probes the probehead is fully integrated. Hereby, the probeheads are the subunits which provide the (pre-tuned) RF coil and, depending on the configuration, the tuning and matching circuit^[105]. The gradient coils are either hardware installed into the magnet unit, or provided as a modular attachment to the probe. Magnet are distinguished according to the bore orientation in horizontal and vertical bore magnets. Horizontal bore magnets are usually used for preclinical MRI studies, whereas vertical bore scanners are used for NMR spectroscopy applications (e.g. chemical analysis) in both, research and industry. At this time, the units with largest B_0 , are vertical bore scanners with a B_0 up to 1 GHz (23.5 T).

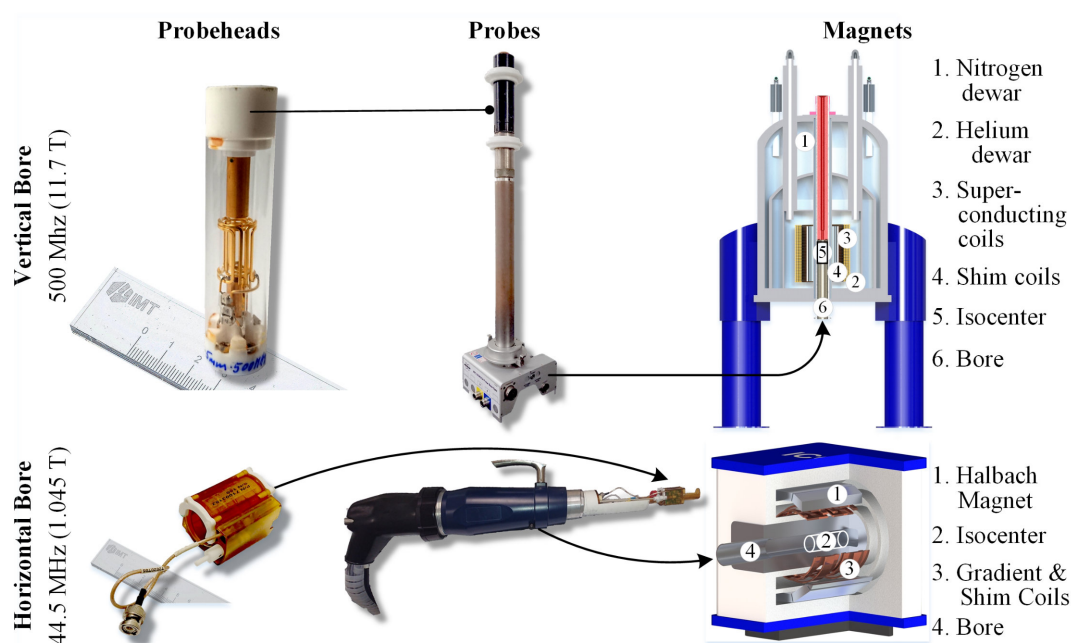


Figure 2.14.: Commercial probeheads, probes and cross-section views of a vertical bore superconducting magnet and a horizontal bore permanent magnet.

Commercially available MR units, which were employed during this research work, are depicted in figure 2.14. These machines are a (i) Bruker Avance III 500 MHz wide bore magnet (vertical) and (ii) a Bruker ICON 44.6 MHz (1.045 T) permanent magnet (horizontal bore). Besides many additional optional features, a probe has three main functions:

- Mechanical fixation of the probehead
- Interface for external tuning and matching
- RF Interface for signal transmission

Depending on the type, many additional features are required such as transmission lines for gradient coils, interfaces for gradient cooling, fluid interfaces in flow probes, temperature control with the necessary interfaces, multi-channel connections, gas lines

for mechanical propulsion (e.g. in MAS) and interfaces for automatic tuning and matching. Although this list may not be complete it encompasses the features of most commercially available probe. Further additional features, such as the integration of feed-throughs for the connection of versatile on-demand items are commercially not available.

2.2.3. RF electronics

2.2.3.1. Tuning/matching and amplification

A central module of each NMR/MRI machinery, the RF transceiver unit, enables the excitation and signal acquisition. All fundamental components involved including the required connections are depicted in figure 2.15.

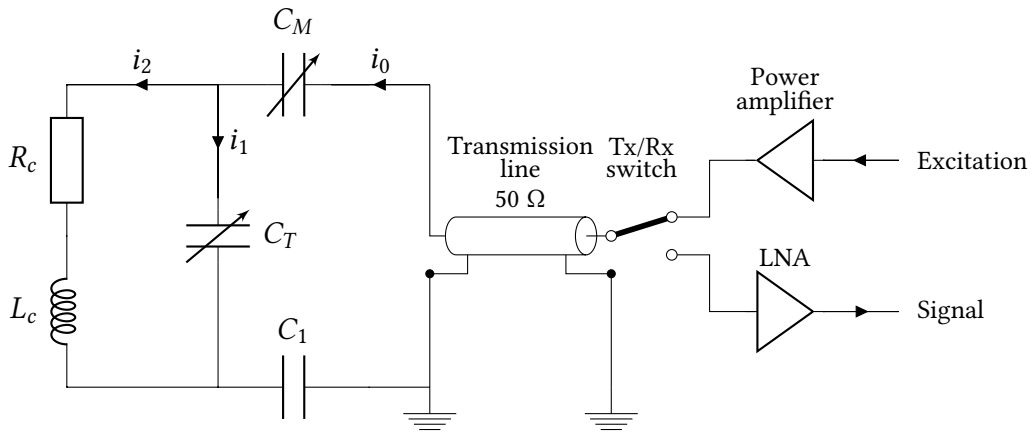


Figure 2.15.: Basic schematics of an RF electronic circuitry implemented in a standard NMR machinery: The inductivity of the coil L_C in combination with the capacitance of the tuning capacitor C_T forms a resonator. Using the capacitance C_M of the matching capacitor enables the impedance matching to 50Ω which matches the impedance of the transmission line. The Tx/Rx switch facilitates the connection to either the power or receiving amplifier during excitation or acquisition.

The core component of the RF transceiver is the RF coil, which is the transducer which facilitates the interaction between the sample magnetization and external control and measurement devices. More precisely this means during excitation a current flow in the coil produces the \mathbf{B}_0 -field which results in flipping the magnetisation vector. During the acquisition the precessing magnetisation induces a voltage across the coil terminals and a current flow which is measurable. Taking into account the resistance of a coil, one can calculate the coil sensitivity with equation 2.32^[12]. The parameters are the current i per magnetic field \mathbf{B}_0 and R represents the high-frequency resistance including skin- and proximity effect.

$$\eta_P = \frac{B_1}{i\sqrt{R}} = \frac{B_1}{\sqrt{P}} \quad (2.32)$$

RF coil optimization strives to increase the magnetic field per unit current. Of great importance is the resistance of the coil, since it reduces the sensitivity. One option to improve the SNR in NMR experiments is to reduce the resistance by means of cooling to cryogenic temperatures. For higher frequencies (in higher fields) the skin effect plays an important role in reducing the sensitivity, because it reduces the resistance by lowering the conductive cross section area.

In current state-of-the-art MR machines, the amplifiers are distant from the RF coils and connected through transmission lines. These transmission lines, so-called coaxial cables, are engineered to achieve a specific characteristic line surge impedance, which in the majority of NMR applications is 50 Ω . Reflections are minimised by impedance matching between components, hence the RF coil impedance has to be transformed to 50 Ω . A basic matching network is illustrated in figure 2.15. A trimmer capacitor C_T is placed parallel to the coil, and a matching capacitor C_M in series to the coil. The normally fixed capacitor C_1 is not generally required, it provides a balanced network. The corresponding equation to the circuit schematic in figure 2.15 is given in equation 2.33.

$$Z = \underbrace{\frac{R(1 - \omega^2 LC_T) + \omega^2 RLC_T}{(1 - \omega^2 LC_T)^2 + (\omega RC_T)^2}}_{Re\{Z\}=50 \Omega} + j \underbrace{\left(\frac{\omega L(1 - \omega^2 LC_T) - \omega R^2 C_T}{(1 - \omega^2 LC_T)^2 + (\omega RC_T)^2} - \frac{1}{\omega(C_M + C_1)} \right)}_{Im\{Z\}=0 \Omega} \quad (2.33)$$

The circuit is tuned and matched when the impedance Z equals 50 Ω and the reactance vanishes, at the desired angular frequency ω . The procedure for tuning and matching, which is described in the following, is visualised in figure 2.16. IN NMR/MRI applications this is the Larmor frequency ω_L . By exchanging the sample, the inductivity L_c of the coil is shifted, which results in a shift of the transfer function. This shift can be corrected by adjusting the capacitance C_T , until $Re\{Z\} = 50 \Omega$ is obtained. As one can observe from equation 2.33, the modification of C_T yields a shift in the reactance. To compensate for this shift, the matching capacitance C_M facilitates the correction for the reactance. A positive side effect is that this configuration forms a resonator circuit and therefore one obtains a first passive preamplifier stage with a low noise figure. This is important because the noise figure of a cascade of amplifiers is dominated by the noise figure of the first stage. The total noise factor F_{tot} of a cascade of N amplifiers is governed by the Friis-formula:

$$F_{tot} = 1 + \underbrace{(F_1 - 1)}_{1^{st} \text{ amp}} + \underbrace{\frac{(F_2 - 1)}{G_1}}_{2^{nd} \text{ amp}} + \underbrace{\frac{(F_3 - 1)}{G_1 G_2}}_{3^{rd} \text{ amp}} + \dots + \underbrace{\frac{(F_N - 1)}{G_1 G_2 \dots G_{N-1}}}_{N^{th} \text{ amp}} \quad (2.34)$$

What can we learn from this equation? The first amplifier stage decreases the total SNR by its noise factor independent from its amplification. The added noise of subsequent amplifier stages diminishes due to the amplification of previous stages. Hence, the overall noise figure is dominated by the noise figure of the first and eventually second stage. In NMR/MRI technology this is realized by using a resonator circuit in combination with a

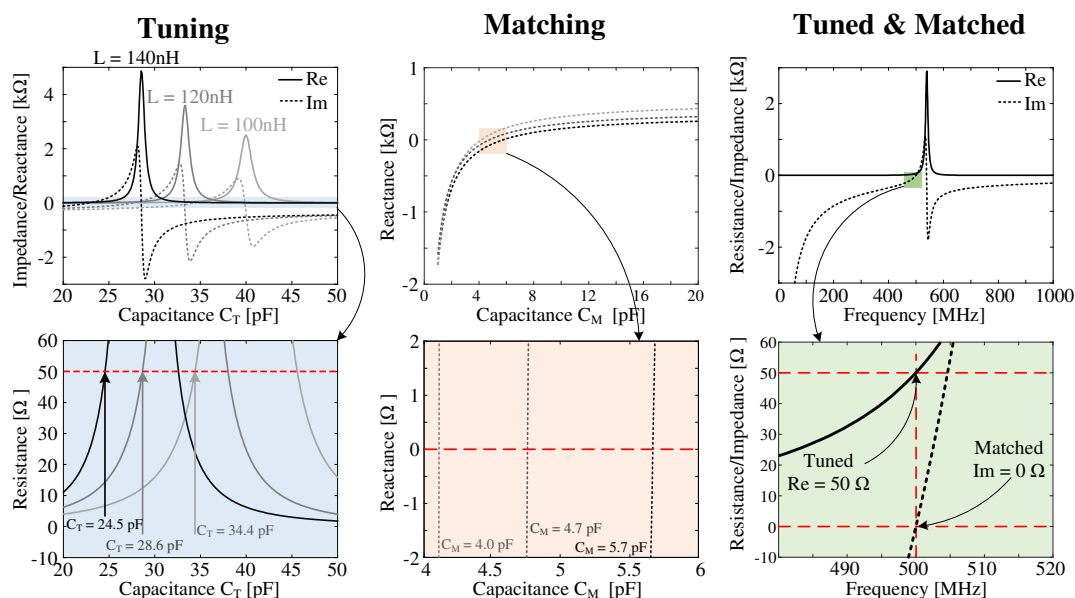


Figure 2.16.: Tuning and matching steps. Left column, top: The impedance and reactance as a function of the tuning capacitance C_T at a Larmor frequency of $f_L = 500$ MHz. Three plots are displayed for three different inductances. Left column, bottom: The tuning capacity C_T is optimal when the resistance equals 50Ω . Middle columns top: Reactance as dependence of matching capacitance C_M . The values for L and C_T are adopted from the left column. The matching is optimal when the reactance vanishes. Right column: Impedance as a function of the frequency. The curve is for a conductivity of $L = 100$ nH, $C_T = 34.4$ pF, and $C_M = 4.0$ pF. The impedance Z at the target frequency is $f_L = 500$ MHz is $Z = 50 \Omega$.

low-noise amplifier (LNA) that acts as a pre-amplifier.

2.2.3.2. Multiresonance technology

In advanced NMR technologies, spectroscopists utilise the options to transmit and/or receive on multiple channels with different frequencies to investigate the interplay of heterogeneous nuclei. In the simplest experiment, the interaction of two nuclei is observed which requires a double resonant circuit. The most important factor for successful multi-nuclear NMR experiments is optimal decoupling of both channels. This can be achieved in two ways: (i) a single coil circuit which achieves decoupling using discrete electronic components (traps) or (ii) two single resonance circuits using geometrically decoupled RF coils. Another type of channel is a lock-channel (most often using deuterium). This channel is used to measure the frequency drift due to \mathbf{B}_0 -field drift or is used as a feedback signal in a control-loop. This is especially important for permanent magnet systems but may also be useful for long-term measurements in superconducting magnets.

2.2.3.3. Shielding

To achieve optimal SNR best possible prevention from coupling of external parasitic signal sources to the RF circuit is essential. Unfortunately, there are many parasitic signal sources in the RF regime from devices such as mobile phones, radio stations etc. Optimal shielding of the signal lines from coil to the amplifier is compulsory. Especially the coupling of parasitic sources to the LC resonator with its amplifying nature needs to be minimal. The concept of Faraday's cage has to be applied such that the resonator is decoupled from the environment through ground planes in the vicinity. This can be achieved by having the NMR experiment enclosed in a metal frame. The outer shield of the coaxial cable is connected to the housing. It is worth mentioning that the housing forms a resonance body and standing waves potentially establish if the required geometric conditions are met. Multiple proper ground connection points are required to avoid standing waves.

2.2.4. Materials and shapes in NMR/MRI

Decent hardware for NMR/MRI applications requires the careful selection of correct materials. All matter interacts with the electromagnetic fields present in NMR applications and only the knowledge of the fundamental physical concepts and consideration of all potential interactions allows for sophisticated and successful hardware design. A brief description of some of the most important aspects for material and shape selection is given in the following section.

Magnetism in materials

Diamagnetism is a type of magnetism which exists in all materials. This type of magnetism weakens the field inside the material and it is based on the opposing magnetic field produced by the orbital motions of the electrons. This can be understood as a result of the Lenz's law. In paramagnetic substances the diamagnetic effect is surpassed by the alignment of the magnetic moment of unpaired electrons to the external field and thus enhancing it. Ferromagnetic substances have, in addition to paramagnetism, the characteristic that the magnetic moments exhibit mutual alignment. Magnetism in matter is a very active research field and much more detailed information can be accessed in current literature^[49]. The magnetic field inside the material can be calculated using the following relation:

$$\mathbf{B} = \mu_0 \mu_r \mathbf{H} = \mu_0 (1 + \chi_V) \mathbf{H} \quad (2.35)$$

Most importantly, the susceptibility for diamagnetic materials ($\chi_v < 0$) and paramagnetism ($\chi_v > 0$) differs in the sign. The susceptibility for ferromagnetic materials is positive, too, but not constant. An example which shows the field distortion created by both types of materials is illustrated in figure 2.17. Platinum, a paramagnetic material focuses the field inside the object which leads to field enhancement inside the material. The opposite effect is visible in a diamagnetic material such as gold. A circular structure leads to the typical dipolar field distortions as illustrated in figure 2.17. An effect which often

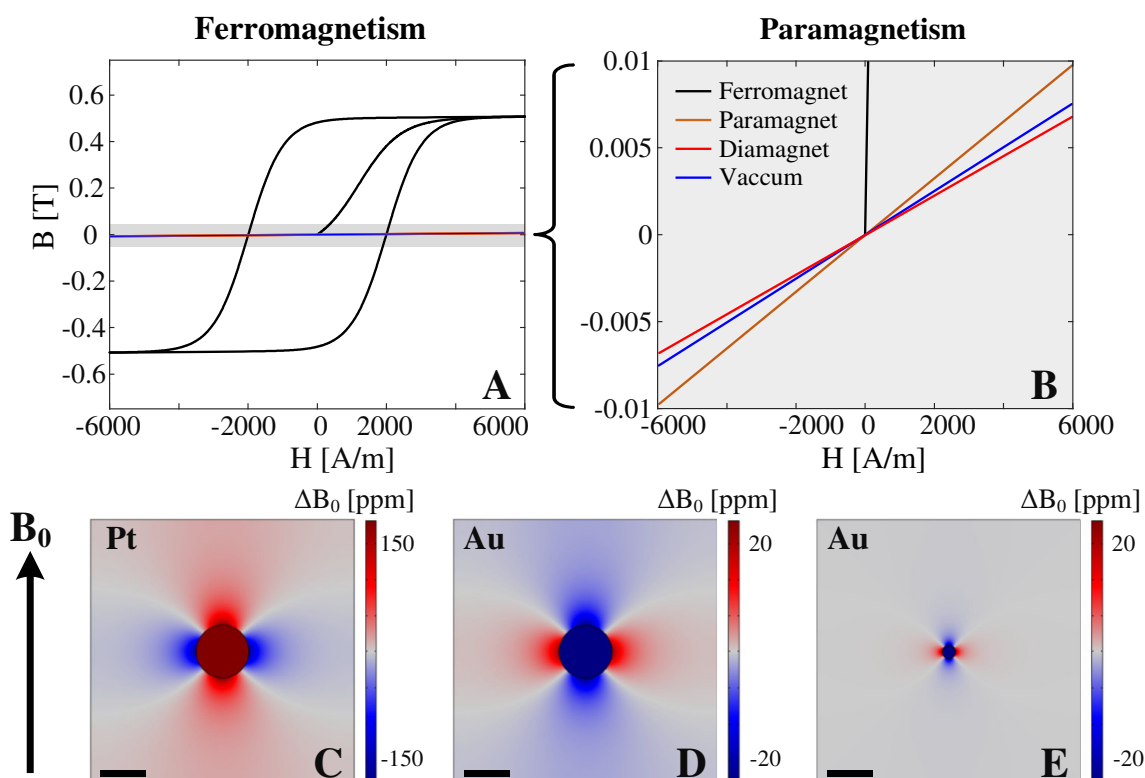


Figure 2.17.: Magnetism in matter. (A) Typical hysteresis curve of a ferromagnet. (B) Magnification to emphasize the larger slope of the B - H -curve which defines paramagnetism and smaller slope for diamagnetism compared to the B - H -curve of vacuum. (C) Field distortion due to a paramagnetic sphere. The magnetic flux is focused inside the sphere. (D) In contrast to (C) magnetic field displacement inside a diamagnetic sphere and the resulting field distortion in close vicinity. (E) Decreasing the object features results in identical field distortions due to linear scaling of electromagnetism. (C)-(D) are 2D FEM-simulations obtained with COMSOL. Scale bar: 2 mm.

occurs in MRI is the image distortion due to trapped air bubbles which is identifiable on the characteristic dipolar appearance. Responsible for this distortion is the paramagnetism of the contained oxygen in air.

The shape and strength of the magnetic field distortions are preserved under dilations due to the scale invariance of electromagnetism. However, the resulting spatial field gradients increase with decreasing feature size; a direct consequence of the fact that smaller feature sizes contain higher spatial frequencies. An MR machine is equipped with a shim system to compensate for field inhomogeneities. Generally, these are made of a set of coils which can be described by an orthogonal set of spherical harmonics. Naturally, the number of shim coils is constrained and compensable field gradients are limited. Features that contain large spatial frequencies, e.g. small features or sharp edges and corners cannot be compensated. Hence, we can derive two main rules to maintain an acceptable B_0 -field homogeneity: Minimisation of large susceptibility differences between the applied materials and the implementation of smooth features.

Another important aspect in magnetic resonance technology and magnetism relates to the occurring forces. In general, an object that exhibits a magnetic moment experiences torque within a magnetic field and translational forces within a gradient field. An expression for the torque of an object which is placed inside the scanner is given by the following equation:

$$\vec{\tau} = \vec{m} \times \vec{B}_0 \quad (2.36)$$

For anisotropic magnetic materials or ferromagnetic materials it is easily understandable that in general the magnetic moment \vec{m} is not aligned with \vec{B}_0 which results in a torque. For isotropic para- or diamagnetic materials the orientation of the induced magnetic moment depends on \mathbf{B}_0 , but also on the shape of the object. Analytical solution for the demagnetization factors can be derived for ellipsoids and needle-like or disc-like structures can be obtained as special cases^[131]. However, this torque due to demagnetization factors is normally for weak magnetisable objects very small and thus negligible. Important aspects of forces can be understood by studying the following equation:

$$\vec{F} = \nabla (\vec{m} \cdot \vec{B}_0) \quad (2.37)$$

The force vanishes if magnetization and the field vector are orthogonal or if the gradient of the magnetic moment or the magnetic field vanishes. For standard MRI applications this means that a translational force exists only at the fringe field of the bore, where a spatial gradient of \mathbf{B}_0 is present. At the magnetic centre, \mathbf{B}_0 is highly homogenous and due to vanishing spatial gradients forces disappear. Forces and torques play a crucial role for MR safety reasons.

Conductive materials

In NMR technology electromagnetism is an immanent part, and the intelligent selection of conductive materials is crucial to build successful hardware. The most important physical principal to consider is the Faraday's law of induction.

$$\oint_{\partial\mathcal{A}(t)} \vec{E} \cdot d\vec{s} = - \int_{\mathcal{A}(t)} \frac{\partial \vec{B}}{\partial t} \cdot d\vec{A} \quad (2.38)$$

All three type of electromagnetic fields which are applied in NMR/MRI are sources of electric vortex fields which lead to currents in conductive structures. According to equation 2.38 any change of magnetic field through a certain area results in an electric field along the boundary. Examples are the transportation through the fringe field of \mathbf{B}_0 , switching of the gradient fields and the alternating RF fields for excitation. Any type of induction in implants are vastly considered adverse effects since the interaction leads to effects such as forces, heating, image artefacts and signal distortions of the implants. In RF engineering for NMR probes induction is also used beneficially. For example, the shielding of the entire signal path, forms a so-called Faraday shield, which includes the RF coil

2. Theoretical background

Table 2.1.: Properties of typical materials used for probehead manufacturing: Magnetic susceptibility χ_V , electric conductivity σ and dielectric permittivity ϵ^a .

Group	Material	χ [ppm]	σ [S/m]	ϵ [1]
Non-metallic	Air	+0.36 ^[152]	-	1.00059 ^[62]
	Carbon fibres	-1.3 to -10.1 ^{[3] b}	1300 ^[164]	6-28 ^{[36] c}
	Fibreglass	-3.1 ^[152]	-	4.1 ^[138]
	PLA	-8.5 ^[152]	$< 2 \cdot 10^{-19}$ ^[139]	2.5 ^[139]
	PMMA	-9.07 ^[152]	$1 \cdot 10^{-7}$ ^[81]	2.7 ^[81]
	PTFE	-10.2 ^[152]	$< 10^{-18}$	2.1 ^[81]
	PUR	-9.13 ^[152]	$1 \cdot 10^{-4}$ ^[81]	6 ^[81]
	Water	-9.05 ^[131]	$5.5 \cdot 10^{-6}$ ^{[90] d}	80 ^[30]
Metallic	Aluminium	20.7 ^[131]	$35 \cdot 10^6$	-
	Brass ^e	-0.09 to -0.19 ^[33]	$18.6 \cdot 10^6$ ^{[81] f}	-
	Copper	-9.63 ^[131]	$59.8 \cdot 10^6$	-
	Nickel	$600 \cdot 10^6$ ^[131]	$14.6 \cdot 10^6$	-
	Platinum	279 ^[131]	$9.44 \cdot 10^6$	-
	Stainless steel	3520 - 6700 ^[131]	$1.4 \cdot 10^6$ ^{[81] g}	-

^a The list provides an approximate information for the order of magnitude and is not intended for specific engineering calculations.

^b Converted to volume susceptibility using $\rho = 1.558 \text{ g/cm}^3$

^c ϵ depends strongly on the wt.% of carbon fibres and the thickness of the fibres.

^d Measurement for ultra-pure water.

^e Considering only brass alloys without iron content.

^f C24000 Zn = 20%, Cu = 80 %

^g Stainless Steel AISI 316

to ensure minimal noise contribution from external electromagnetic sources. Advanced probeheads are completely shielded and properly grounded. A selection of materials and their characteristics with respect to magnetism and conductivity is listed in table 2.1.

Besides the two important material properties regarding NMR interactions, electrical conductivity and magnetic susceptibility, other material properties have to be considered, too, dictated by the requirements of the desired application. Mechanical strength is important for frame parts and the housing as well as for parts that are used for force or torque transmission. Another important aspect is the machinability of selected materials. Whereas metals most often have good machinability, this aspect is very important for the selection of polymers, since not all polymers allow machining with acceptable results. In recent years, research activities enabled many novel prototyping technologies such as 3D printing, which offers new fabrication possibilities for various type of materials such as polymers (ABS or PLA), metals or ceramics. Moreover, many 3D printing devices

have become commercially available to attractive conditions which offers novel, flexible and very fast fabrication possibilities. Further material parameters that may be crucial dependent on the desired application are the thermal properties (thermal conductivity, glass transition temperature), permeability to gases and fluids (e.g. in fluid channels) and chemical properties. The latter point is also important with respect to background signals in NMR. Many polymers contain hydrogen atoms which leads to strong background signal from a substrate containing such polymers. Depending on the application this can be acceptable. In imaging applications this point may not be so crucial due to short relaxation times, however, for MAS application of solid-state materials a correct selection of materials without background signal is crucial. It needs to be emphasized that there are no general rules which materials can be accepted for a certain application regarding the background signal. If possible, the selection of materials with no or low-proton content should be preferred.

2.3. Image postprocessing

Nowadays, the dominant way of presenting, distributing and storing all kind of images is done by digital encoding. One of the main advantages of digitizing images lies in the huge capability of image manipulation after acquisition by means of mathematical concepts. Indeed, digital image processing is a large research field with many areas of applications. Within this section some fundamental basic concepts which are applied in this thesis are presented.

2.3.1. Digital image representation

Digital images in the raster format, so called bitmap images, are matrices that contain the information of the image represented as numerical values (binary) stored in the matrix elements. An example of a digitized image is shown in figure 2.18¹⁰.

More precisely, any arbitrary digital image (2D) can be described by the matrix \mathbf{X} . In this equation the indices i, j, k denote the spatial dimensions such that for a 2D image $k = 1$ for all values. The index l denotes a fourth dimension oftentimes used for encoding color. The exponent n denotes the set of integer numbers the matrix elements can be populated with. A very famous image format is a 24-bit encoded RGB image, then the index $l \in \{1, 2, 3\}$ and $n = 8$, that means the image has three color channels, whereby each channel is encoded with 8 bit.

$$\mathbf{X} = x_{i,j,k,l}, \quad x_{i,j,k,l} \in \{0, \dots, 2^n - 1\} \quad (2.39)$$

¹⁰This image shows an enhanced digital representation of the first known photograph made around 1826 by Joseph Nicéphore Niépce. It is a heliographic image which shows parts of the buildings and countryside as seen from his room in Saint-Loup-de-Varennes, France. The recording duration was approximately 8 hours

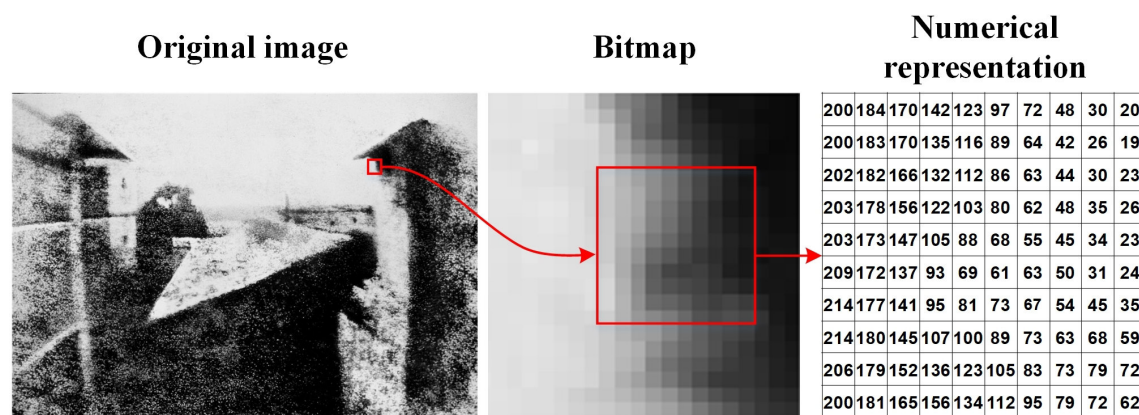


Figure 2.18.: One of the first acquired photographs in digital representation in an 8-bit gray value map. The larger the number the brighter the pixel representation.

Standard gray value magnitude-based MR images have obviously one colour channel often encoded with 8 bit or 16 bit or, in other words, $l = 1$. Advanced MR acquisition techniques make use of the colour channel and encode more information there.

2.3.2. Segmentation by thresholding

Segmentation procedures are processes to define partitions in an image which can be assigned to certain objects. Most often this partitioning process is conducted by binarisation of the image such that the pixels of the background are set to zero (black) and the pixel of the object are set to one (white) or vice versa. This procedure allows to isolate objects from the background and to extract further information such as surface or volume area. For 3D data it is possible to export volume models. A simple thresholding process for a 2D grey colour image with n-bit colour encoding is defined as follows:

$$x_{i,j}^{\text{seg}} = \begin{cases} 1, & \text{if } x_{i,j}^{\text{raw}} \geq t \quad \text{for } 0 \leq t \leq (2^n - 1) \\ 0, & \text{otherwise} \end{cases} \quad (2.40)$$

In this definition t is the threshold parameter to control which pixels are assigned to which partition. This approach becomes more comprehensible with the aid of a histogram as shown in figure 2.19. Here, the binarisation result is shown for two different values for the parameter t . The image, it shows a coin on a homogenous background, has a bimodal intensity distribution, which in general allows to separate pixels by choosing t such that the threshold coincides with the "valley" of the two peaks. The more the bimodal configuration is pronounced, the less the binarised output is affected from varying t within the valley. Stability of binarisation against threshold variation is an important aspect if one uses this approach for further data analysis. In this example, we could calculate the upper surface of the coin by counting all dark pixels if the corresponding area of one pixel is known. In Figure 2.19 the relationship between varying t changes in the obtained result are shown. In general, the variation of the binarisation result with varying t depends on

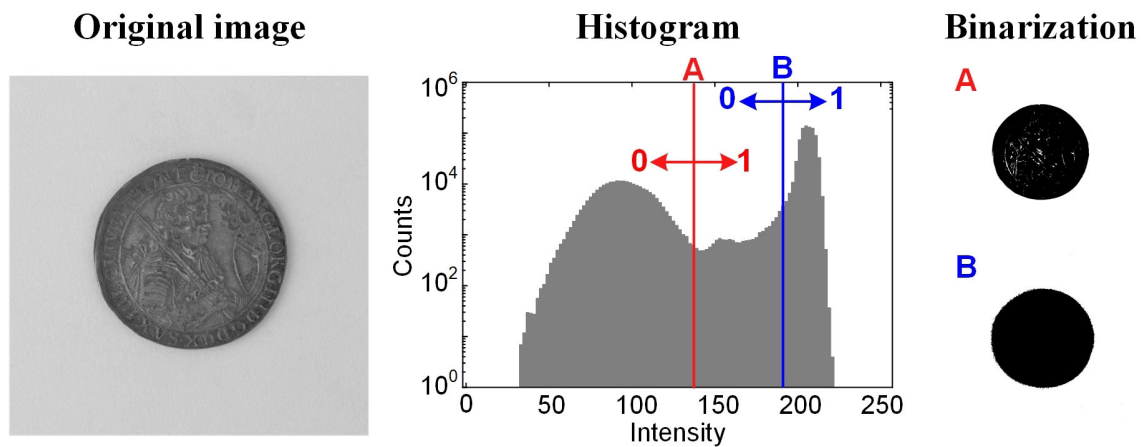


Figure 2.19.: Segmentation using a constant thresholding parameter p for an image with bimodal distribution. A) The parameter $t = 127$ resulting in a binarisation where some pixels are erroneously attributed to the background. B) Increasing the parameter $t = 191$ results in a slightly better binarisation performance. Most pixels, however, are well bimodal distributed and the value of t does not affect the binarisation result to much.

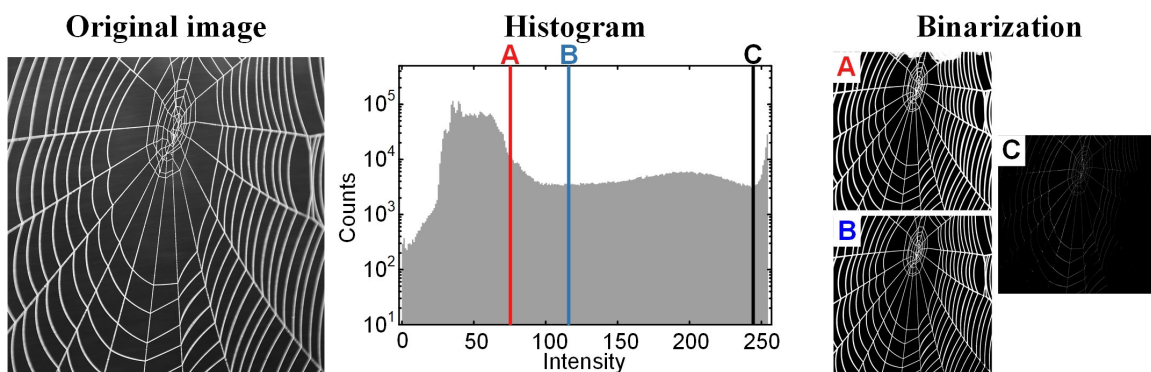


Figure 2.20.: Arbitrarily manual selected thresholds against the optimal threshold computed using Otsus method. A) + C) Parameter selection of $t = 75$ (A) and $t = 245$ (C) result in binarisations where the object is still recognizable, however, the segmentation result clearly varies. In A) parts of the background are attributed to the web, vice versa in C). B) Segmentation result obtained by using $t = 123$ computed using Otsus method (See also figure 2.21)

the characteristic intensity distribution of an image, and despite the manual selection of t may be very straightforward, this procedure has some disadvantages:

- Bad repeatability
- Bad reproducibility
- No selection rules for unimodal distribution

Especially the last item is of great importance. For unimodal distributions there is no simple strategy what threshold should be used. In figure 2.20 an image is displayed in which the two cluster maxima are not clearly distinguishable.

In such cases the results of binarisation depend strongly on the selected threshold t , which consequently yields large output variations as t varies. An important threshold algorithm to compute a correct level also for unimodal distributions was presented by Otsu in 1979^[113]. In brief, Otsu's method is an optimization method which determines the optimal threshold parameter t by minimizing the intra-class variance or, alternatively, maximising the inter-class variance. Here, intra-class variance means the variance within one class and inter-class variance is the variance between classes. Binarisation requires the splitting into two groups and the perfect value for threshold t is found when the intra-class variance is minimised.

Otsu could show that minimising the intra-class variance is equal to the maximising the inter-class variance. The principle is highlighted in figure 2.21 in which both curves, intra-class variance and inter-class variance are displayed as a function of threshold. The mathematical descriptions of Otsu's method is described in the following. Therefore, let's consider a histogram with grey values from $x = 0, x = 1, \dots, x = 2^n - 1$. First, we assume the separation of pixels into two classes $C_0(t)$ and $C_1(t)$ at some threshold value t . Then $P_1(t)$ is the probability to find a pixel in class one and $P_2(t)$ to find a pixel in class two. Furthermore, n_x is the number of pixels with grey value x and N is the total number of pixels.

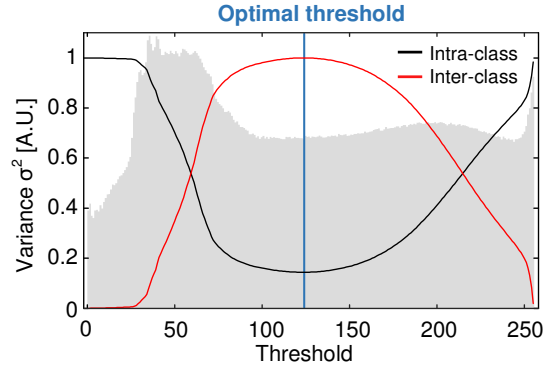


Figure 2.21.: Intra-class and inter-class variance as a dependence on the selected threshold value.

$$P_1(t) = \sum_{x=0}^t p_x = \frac{n_0 + n_1 + \dots + n_t}{N} \quad \text{and} \quad P_2(t) = \sum_{x=t+1}^{2^n-1} p_x = 1 - P_0(t) \quad (2.41)$$

Hence, $p_x = n_x/N$ is the probability that a pixel has the grey value x . The mean grey value of class 1 is obtained by:

$$\mu_1 = \frac{1}{P_1(t)} \sum_{x=0}^t x \cdot p_x = \frac{0 \cdot n_0 + 1 \cdot n_1 + \dots + t \cdot n_t}{n_0 + n_1 + \dots + n_t} = \frac{\sum_{x=0}^t x \cdot n_x}{\sum_{x=0}^t n_x} \quad (2.42)$$

In the same way the the average gray value of μ_2 of class two is calculated. The average gray value of the entire image is given by:

$$\mu_a = \sum_{x=0}^{2^n-1} x \cdot p_x = \frac{1}{N} \sum_{x=0}^{2^n-1} x \cdot n_x \quad (2.43)$$

From here on we can calculate the inter-class variance σ_{inter}^2 by the following equation:

$$\sigma_{inter}^2 = P_1(t)(\mu_1 - \mu_a)^2 + P_2(t)(\mu_2 - \mu_a)^2 \quad (2.44)$$

Alternatively, one can calculate the intra-class variance. The variance within the classes is governed by:

$$\sigma_1^2 = \sum_{x=0}^t p_x (x - \mu_1)^2 \quad \text{and} \quad \sigma_2^2 = \sum_{x=t+1}^{2^n-1} p_x (x - \mu_2)^2 \quad (2.45)$$

The intra-class variance then is given by:

$$\sigma_{intra}^2 = P_1(t)\sigma_1^2(t) + P_2(t)\sigma_2^2(t) \quad (2.46)$$

Otsu showed in his publication that the optimal threshold is obtained by maximising inter-class variance or, equivalently, minimising intra-class variance:

$$t_{opt} : \max \sigma_{inter}^2(t) = \min \sigma_{intra}^2(t) \quad (2.47)$$

The presented segmentation method is an integral part of the MR image analysis process which is presented in chapter 7.1. If the acquired MR images are subjected to post-processing operations, it is important to prepare the image acquisition to obtain the best possible result to simplify the post-processing process. This can be done by following the methods introduced in section 2.1.4, for example, providing images with a homogenous background and a maximal contrast-to-noise-ratio (CNR) which simplifies the segmentation process tremendously. Much more advanced segmentation processes are required, if for example, the background is inhomogeneous or the CNR is low. This, however, was not the case in this work, due to optimisation procedure presented in section 7.1.2.1 and thus is beyond the scope of this thesis.

2.4. Fundamental methods of vibration analysis

Theoretical methods for the analysis of mechanical systems have been published in many textbooks, hence, only a brief introduction to these methods that found application in part I will be presented. One of the main questions in part I concerns the gradient-induced vibration of systems that are embedded in viscoelastic materials. Therefore, the methods to analyse a damped coupled resonator in time domain and the analysis of the image of the Laplace transform are discussed.

2.4.1. Coupled resonator with 2 DOF

A simple coupled resonator with two masses can be modelled using the lumped parameter model illustrated in figure 2.22. The correspondent mathematical model in time domain is governed by equation 2.48.

$$\underbrace{\begin{bmatrix} m_1 & 0 \\ 0 & m_2 \end{bmatrix} \begin{pmatrix} \ddot{x}_1 \\ \ddot{x}_2 \end{pmatrix} + \begin{bmatrix} c_1 + c_2 & -c_2 \\ -c_2 & c_2 + c_3 \end{bmatrix} \begin{pmatrix} \dot{x}_1 \\ \dot{x}_2 \end{pmatrix} + \begin{bmatrix} k_1 + k_2 & -k_2 \\ -k_2 & k_2 + k_3 \end{bmatrix} \begin{pmatrix} x_1 \\ x_2 \end{pmatrix}}_{\mathbf{M}\ddot{\mathbf{x}} + \mathbf{C}\dot{\mathbf{x}} + \mathbf{K}\mathbf{x}} = \begin{pmatrix} F_1(t) \\ F_2(t) \end{pmatrix} \quad (2.48)$$

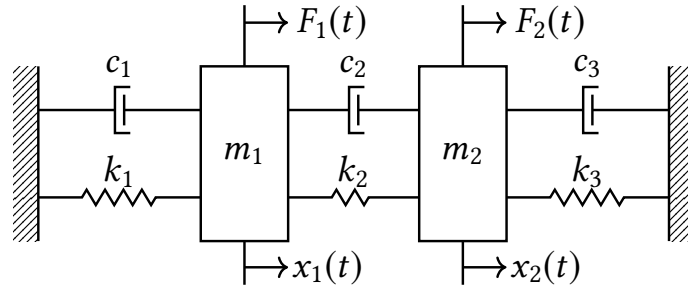


Figure 2.22.: Lumped model for a coupled resonator with the masses m_i , the spring constants k_i , the damping constants c_i , the external forces F_i and the deflection x_i .

This is a typical eigenvalue problem, and solving the characteristic polynomial of the homogenous differential equation without damping, such that $\mathbf{c} = 0$ yields the two natural frequencies (2 DOF). Taking the damping into account yields the resonance frequencies at which maximum deflection will take place. However, we are more interested in the transfer function of the system when a force is applied to the mass m_1 or m_2 and the corresponding deflection x_1 and x_2 of these masses. Therefore, we can write the equations of motion after the Laplace transform:

$$\begin{bmatrix} m_1 s^2 + (c_1 + c_2)s + (k_1 + k_2) & -c_2 s - k_2 \\ -c_2 s - k_2 & m_2 s^2 + (c_2 + c_3)s + (k_2 + k_3) \end{bmatrix} \begin{bmatrix} X_1(s) \\ X_2(s) \end{bmatrix} = \begin{bmatrix} F_1(s) \\ F_2(s) \end{bmatrix} \quad (2.49)$$

Equation 2.49 can now be rewritten as:

$$\underbrace{\begin{bmatrix} G_{11}(s) & G_{12}(s) \\ G_{21}(s) & G_{22}(s) \end{bmatrix}}_{\mathbf{G}(s)} \begin{bmatrix} X_1(s) \\ X_2(s) \end{bmatrix} = \begin{bmatrix} F_1(s) \\ F_2(s) \end{bmatrix} \quad (2.50)$$

$$\mathbf{G}(s)\mathbf{X}(s) = \mathbf{F}(s)$$

From equation 2.50 we can derive the four possible transfer functions for the two-mass system which are displayed in figure 2.23.

Since the matrix $\mathbf{G}(s)$ is symmetric, because $G_{12} = G_{21}$, the transfer function $T_{12} = T_{21}$. Furthermore, we can compute the response of each output as a function of the inputs. The four transfer functions are governed by the equations in 2.51. The solution from this general case allows straightforward simplifications for special cases, as well as the analysis of specific physical systems. Of particular interest is the option to extract information of the vibrational amplitude of x_2 through the readout of x_1 while $F_2(s) = 0$.

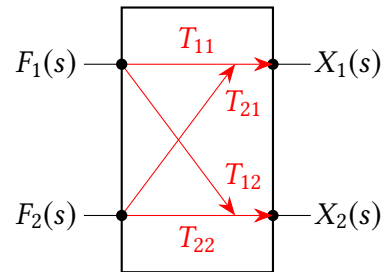


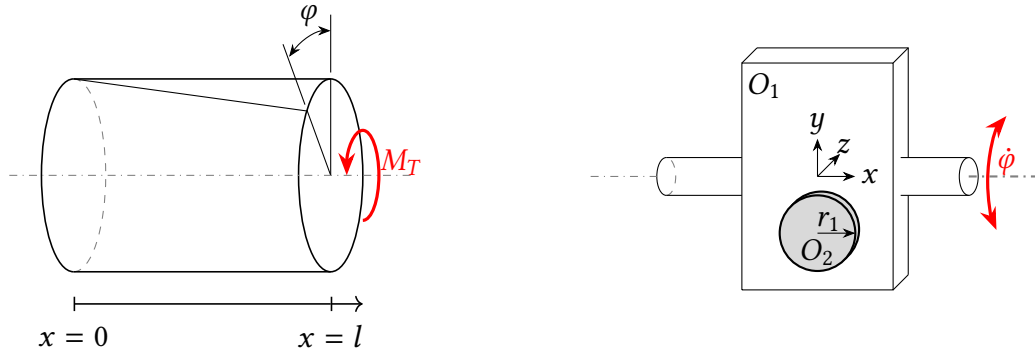
Figure 2.23.: The four possible transfer function pathways for a two-mass system

$$\begin{aligned}
 T_{11} \Big|_{F_2(s)=0} &= \frac{G_{22}}{\det(\mathbf{G}(s))} = \frac{G_{22}}{G_{11}G_{22} - G_{12}G_{21}} \\
 T_{22} \Big|_{F_1(s)=0} &= \frac{G_{11}}{\det(\mathbf{G}(s))} = \frac{G_{11}}{G_{11}G_{22} - G_{12}G_{21}} \\
 T_{12} \Big|_{F_2(s)=0} &= T_{21} \Big|_{F_1(s)=0} = \frac{-G_{12}}{\det(\mathbf{G}(s))} = \frac{-G_{12}}{G_{11}G_{22} - G_{12}G_{21}}
 \end{aligned} \tag{2.51}$$

This model, furthermore, allows to analyse the root loci in dependency of the spring, damping and mass elements.

2.4.2. Basic formulae for torsion

Gradient induced vibration is an effect which bases on the torque product during an MR investigation. A collection of fundamental formulae and concepts will be presented which find application in the experimental setup. This includes especially some fundamentals of rotational mechanics.



(a) Angular spring: The Angular deflection of a beam depends on its length, shear modulus and the torsional constant.

(b) Angular mass: In rotational mechanics the moment of inertia is the equivalent to the mass in translational mechanics.

Figure 2.24.: The equations for rotational mechanics are equal to translational mechanics. The moment of inertia or angular mass is equivalent to the mass and the torsion constant to the spring constant in translational mechanics.

Gradient induced mechanical vibrations are modelled using the laws of rotational dynamics. Fundamentally, the equations of dynamics are equivalent to the previous section, the only difference is in the physical quantities. To analyse gradient-induced vibrations, we are interested in the angular deflection of an object which is governed by the following equation of motion:

$$I\ddot{\varphi} + \Gamma\dot{\varphi} + \mu\varphi = \tau(t) \tag{2.52}$$

Here I denotes the moment of inertia, Γ the rotational friction, μ is the torsion constant and $\tau(t)$ is the time depended applied torque and this equation represents a system with 1

2. Theoretical background

DOF. By replacing the quantities of equation 2.48 with the analogous rotational quantities we obtain the dynamics for the rotational harmonic oscillator. The torsion constant represents a rotational spring, for example, a twisted beam. The static angular deflection φ of a circular beam is illustrated in figure 2.24a and described by the following equation:

$$\varphi = \frac{\tau l}{GI_p} = \frac{2\tau l}{G\pi r_B^4} \quad (2.53)$$

Here, G denotes the shear modulus and thus a material parameter and I_p denotes the second moment of area or more specifically the polar moment of inertia for a circular beam when twisted around its axis (see figure 2.24a). Rearranging this equation allows to compute the torsional stiffness of a beam with the aforementioned torsion constant:

$$\mu = \frac{\tau}{\varphi} = \frac{G\pi r_B^4}{2l} \quad (2.54)$$

This equation can be used as a guideline to find a beam that fulfills the requirements for a certain torsional stiffness.

The moment of inertia is equivalent to the mass in translational mechanics. Here, the configuration which is displayed in figure 2.24b will be analysed. In this situation the total moment of inertia I_{tot} is a sum of the individual moment of inertias of the beam, the object 1 O_1 , a cuboid, and the object 2 O_2 a disc. If the beam is thin its moment of inertia is small compare to the one of O_1 and O_2 , it can be neglected and the total moment of inertia is governed by:

$$I_{tot} = I_{O_1} + I_{O_2} = \frac{1}{12}m_{O_1} \left(l_y^2 + l_z^2 \right) + I_{O_2} \quad (2.55)$$

Here I_{O_1} is the moment of inertia for a cuboid which is rotated around the x-Axis and the rotational axis coincides the center of gravity (COG) of O_1 . Since the rotational axis does not coincide with the COG of the disc O_2 , the moment of inertia is composed of two parts:

$$I_{O_2} = I_{COG} + I_d = \frac{1}{4}m_{O_2} \left(r_1^2 \right) + m_{O_2} \left(\Delta y^2 + \Delta z^2 \right) \quad (2.56)$$

The second addend is obtained by multiplying the mass by the square of the distance between COG and the rotational axis. This is on the basis of the parallel axis theorem or Steiner's theorem. Combining these equation yields the total moment of inertia:

$$I_{tot} = \frac{1}{12}m_{O_1} \left(l_y^2 + l_z^2 \right) + m_{O_2} \left(\frac{1}{4}r_1^2 + \Delta y^2 + \Delta z^2 \right) \quad (2.57)$$

If more objects are mounted onto the cuboid O_1 the total moment of inertia is increased and the computation is straightforward by adding the additional terms.

2.4.3. Beam theory

In this section the fundamentals for simple beams (Euler-Bernoulli-beam) are detailed. Of particular interest is the impact of the boundary conditions on the eigenfrequencies and the vibration modes. In the figure 2.25 three boundary conditions of particular interest for this work are illustrated.

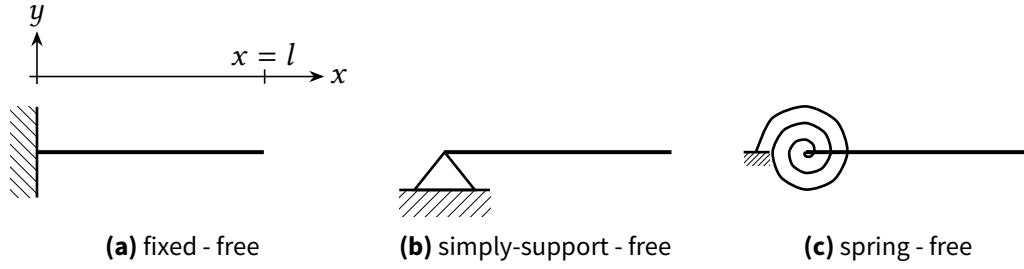


Figure 2.25.: Three different boundary conditions for beam analysis. The conditions in (a) and (b) are called the classical boundary conditions treated in many textbooks. The boundary condition in (c) is a non-classical boundary condition with the spring constant k_S . These examples are not considering gravitational load such that (b) under the absence of external forces is horizontal.

In the following text these boundary conditions are referred to as "fix-free" (a), "simply-free" (b) and "spring-free" (c). To compute the eigenfrequencies and modes of a beam we start with the partial differential equation for the Euler-Bernoulli-beam with the time- and position-dependent deflection $w(x, t)$ of the beam¹¹:

$$\frac{\partial^4 w(x, t)}{\partial x^4} + \frac{\rho A}{EI_y} \frac{\partial^2 w(x, t)}{\partial t^2} = 0 \quad (2.58)$$

A general solution that satisfies equation 2.58 is given by:

$$\begin{aligned} w_k(x, t) &= W_k(x) e^{i\omega_k t} \\ &= (a_1 \cos \kappa x + a_2 \sin \kappa x + a_3 \cosh \kappa x + a_4 \sinh \kappa x) (b_1 \cos \omega_k t + b_2 i \sin \omega_k t) \end{aligned} \quad (2.59)$$

where κ equals:

$$\kappa^4 = \omega^2 \frac{\rho A}{EI_y} \rightarrow \omega = \sqrt{\frac{\kappa^4 EI_y}{\rho A}} \quad (2.60)$$

To compute the coefficients A - D, we have to solve the eigenvalue problem for $W_k(x)$ which depends on the boundary conditions of the beam. The most general form of the linear systems of equations are shown in equation 2.61.

¹¹In the Euler-Bernoulli beam theory, in contrast to the Timoshenko beam theory, the effect of shear deformation is neglected. This yields a higher stiffness of the modelled beams. For long and thin beams, however, the aspect ratio of length to thickness is large enough to neglect this effect.

2. Theoretical background

$$\begin{aligned}
 W_k(x) &= a_1 \cos \kappa x + a_2 \sin \kappa x + a_3 \cosh \kappa x + a_4 \sinh \kappa x = w(x) \\
 W_k^I(x) &= -\kappa a_1 \sin \kappa x + \kappa a_2 \cos \kappa x + \kappa a_3 \sinh \kappa x + \kappa a_4 \cosh \kappa x = \varphi(x) \\
 W_k^{II}(x) &= -\kappa^2 a_1 \cos \kappa x - \kappa^2 a_2 \sin \kappa x + \kappa^2 a_3 \cosh \kappa x + \kappa^2 a_4 \sinh \kappa x = M(x) \\
 W_k^{III}(x) &= \kappa^3 a_1 \sin \kappa x - \kappa^3 a_2 \cos \kappa x + \kappa^3 a_3 \sinh \kappa x + \kappa^3 a_4 \cosh \kappa x = Q(x)
 \end{aligned} \tag{2.61}$$

Here $w(x)$ denotes the deflection of the neutral axis, $\varphi(x)$ the angle, $M(x)$ the torque and $Q(x)$ the force at position x . The four boundary conditions for the "fix-free" beam (figure 2.25a) are $w(0) = 0$, $\varphi(0) = 0$, $M(l) = 0$, $Q(l) = 0$, which results in the homogenous system using $\lambda = \kappa l$:

$$\underbrace{\begin{bmatrix} 1 & 0 & 1 & 0 \\ 0 & 1 & 0 & 1 \\ -\cos \lambda & -\sin \lambda & \cosh \lambda & \sinh \lambda \\ \sin \lambda & -\cos \lambda & \sinh \lambda & \cosh \lambda \end{bmatrix}}_{\mathbf{A}} \underbrace{\begin{bmatrix} a_1 \\ a_2 \\ a_3 \\ a_4 \end{bmatrix}}_{\mathbf{a}} = 0 \tag{2.62}$$

The eigenvalues are the solutions of this characteristic equation:

$$\det(\mathbf{A}) = 1 + \cos \lambda \cosh \lambda = 0 \tag{2.63}$$

The solution set for which all λ_i solve this equation gives the eigenfrequencies ω_i of the beam. One obtains the solution set by using equation ?? with the first three eigenvalues:

$$\omega_i = \lambda_i^2 \sqrt{\frac{EI_y}{l^4 \rho A}}, \quad \lambda_{1,2,3} = \{1.876, 4.694, 7.855, 10.996\} \tag{2.64}$$

The boundary conditions of the "simply-free" beam are given by $w(0) = 0$, $M(0) = 0$, $M(l) = 0$, $Q(l) = 0$ which yields the following systems of equations:

$$\begin{bmatrix} 1 & 0 & 1 & 0 \\ -1 & 0 & 1 & 0 \\ -\cos \lambda & -\sin \lambda & \cosh \lambda & \sinh \lambda \\ \sin \lambda & -\cos \lambda & \sinh \lambda & \cosh \lambda \end{bmatrix} \begin{bmatrix} a_1 \\ a_2 \\ a_3 \\ a_4 \end{bmatrix} = 0 \tag{2.65}$$

From this one obtains the characteristic equations with:

$$\det(\mathbf{A}) = \tan \lambda_i - \tanh \lambda_i = 0 \rightarrow \lambda_{1,2,3} = \{0, 3.927, 7.068, 10.210\} \tag{2.66}$$

The fundamental frequency of the "simply-free" beam is zero or, in other words, vanishes. This is due to the fact that there is no bearing which can support the moment. In the same way, the beam will just fall down if gravity acts. So the fundamental mode cannot exist. Three of the four boundary conditions are identical in all three cases. These are the two boundary conditions for the free end: $M(l) = 0$, $Q(l) = 0$. Furthermore, in all three cases the deflection of the beam at $x = 0$ equals zero: $w(0) = 0$. The third boundary condition in the "spring-free" configuration, represents the transition region which allows to derive the

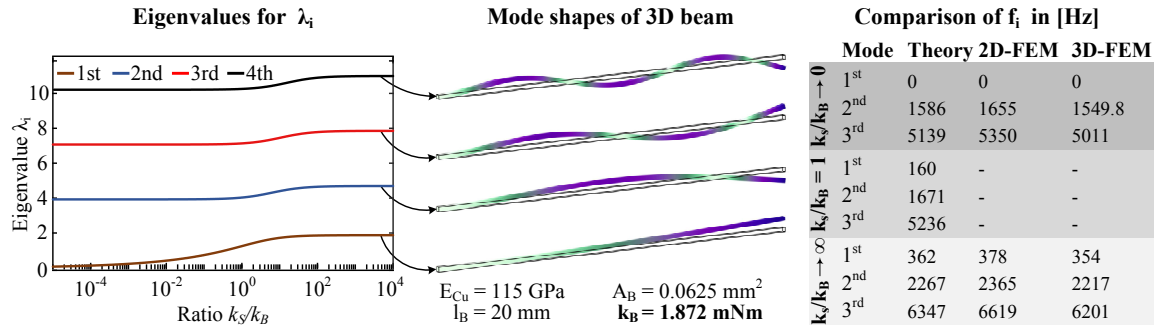


Figure 2.26.: Characteristics of a spring-free beam. *Left:* Dependence of the eigenvalues λ_i on the spring constant of the spring support. *Middle:* Mode shapes of a 3D beam with quadratic cross section area (only vibrations in vertical directions) up to the 4th order. *Right:* Comparison of values obtain from analytical calculations and 2D and 3D FEM-simulation

"fixed-free" for the limits of $k_S \rightarrow \infty$ or "simply-free" configuration for $k_S \rightarrow 0$. This can be analysed by writing down the systems of equation with the boundary condition $M(0) = k_S \varphi(x)$:

$$\begin{bmatrix} 1 & 0 & 1 & 0 \\ -\kappa^2 & 0 & \kappa^2 & 0 \\ -\cos \lambda & -\sin \lambda & \cosh \lambda & \sinh \lambda \\ \sin \lambda & -\cos \lambda & \sinh \lambda & \cosh \lambda \end{bmatrix} \begin{bmatrix} a_1 \\ a_2 \\ a_3 \\ a_4 \end{bmatrix} = \begin{bmatrix} 0 \\ k_S \varphi(0) \\ 0 \\ 0 \end{bmatrix} \quad (2.67)$$

The left side of this inhomogenous equation system is the homogenous part and equals to equation 2.62. In contrast to that induced the spring constant k_S the inhomogenous part on the right side. We can analyse the second row of this matrix which can be rewritten as:

$$-a_1 + a_3 = k_S(a_2 + a_4) \quad (2.68)$$

From this equation we can derive for the limit of $k_S \rightarrow 0$ that $-a_1 + a_3 = 0$, which corresponds to the "simply-free" condition in equation 2.65, whereas by dividing equation 2.68 by $k_S (k_S \neq 0)$ we obtain for the limit of $k_S \rightarrow \infty$ the result $a_2 + a_4 = 0$ which is the condition in equation 2.62.

The general solution to this equation was published by K. R. Chun in 1972^[24]. The spring constant of a beam at the spring support can be wxpressed by:

$$k_B = \frac{EI_y}{l} \quad (2.69)$$

This definition allows to write the characteristic solution by Chung as the ratio of the support spring constant k_S and the beam spring constant k_B :

$$\frac{k_S}{k_B} \frac{1}{\lambda_i} \left(\frac{1}{\cos \lambda_i \cosh \lambda_i} + 1 \right) = \tan(\lambda_i) - \tanh \lambda_i \quad (2.70)$$

2. Theoretical background

For $k_S \rightarrow 0$, which is the condition of the "simply-free" case, this equation becomes $\tan \lambda_i - \tanh \lambda_i = 0$ which corresponds to equation 2.66. At the other limit for $k_S \rightarrow \infty$, dividing by k_S results in $1/\cos \lambda_i \cosh \lambda_i + 1 = 0 \rightarrow 1 + \cos \lambda_i \cosh \lambda_i = 0$ which is the solution for the "fix-free" beam in equation 2.63.

The transition between "simply-free" and "fixed-free" is visualized by plotting the solution of equation 2.70 as a function of k_S/k_B which is displayed in figure 2.26.

This analysis demonstrates, that variations of the spring constant of the support k_S will change the measured resonance frequencies of the beam in those cases, in which both spring constants, k_S and k_B have similar values.

Part I.

Low field probe for MR safety applications

3 | State-of-the-art: MR safety

Part I of this thesis encompasses the development and application of an MR probe to explore effects of gradient-induced MR vibrations. The goal is to derive guidelines for practical implementation to prevent vibration-based incidents. Gradient-induced vibration is a particular phenomenon which belongs to the group of forces within all potential hazards. All potential hazards and the fundamental entities of implants and MR unit are illustrated in figure 3.1.

Prior to the engineering work, a comprehensive and systematic literature review was conducted to investigate the current state-of-the-art of MR safety of neural implants. An additional focus was set on the historical development of MRI and implants, illustrated at the example of Cochlear implants (CI) and Deep brain stimulation devices. This work was published under the title "Should patients with brain implants undergo MRI" in the Journal of neural engineering in 2018^[EF01]¹. On the basis of this published work, an introduction to the state-of-the-art knowledge of MR safety will be given within this chapter. In contrast to the published article, the focus in this monograph is laid on the physical background of the interactions and the developed technical specifications and standards. Starting from a general overview of MR related hazards, the last section details the current state-of-the-art of gradient-induced vibrations. It is described why there is, as of today, a lack of resilient data which highlights the imperative for the research presented in the subsequent chapters.

3.1. Types of MR interactions and hazards

3.1.1. Overview of interactions and hazards

MR interaction means the interplay of the electromagnetic fields of the MR scanner with an external object, for example an implant of a patient. Mostly, these interactions cause undesired side effects constituting a health risk to the patient. A first step to prevent the patient from these adverse events during an MR procedure is to understand the essential causes by finding a scheme that facilitates a general overview. All types of MR interactions can be attributed to two underlying physical phenomenon, magnetization and

¹This work was conducted together with the group of Prof. Thomas Stieglitz and Prof. Ulrike Wallrabe both at IMTEK, University of Freiburg and Prof. Jürgen Hennig, Department of Radiology, Medical Center University of Freiburg.

3. State-of-the-art: MR safety

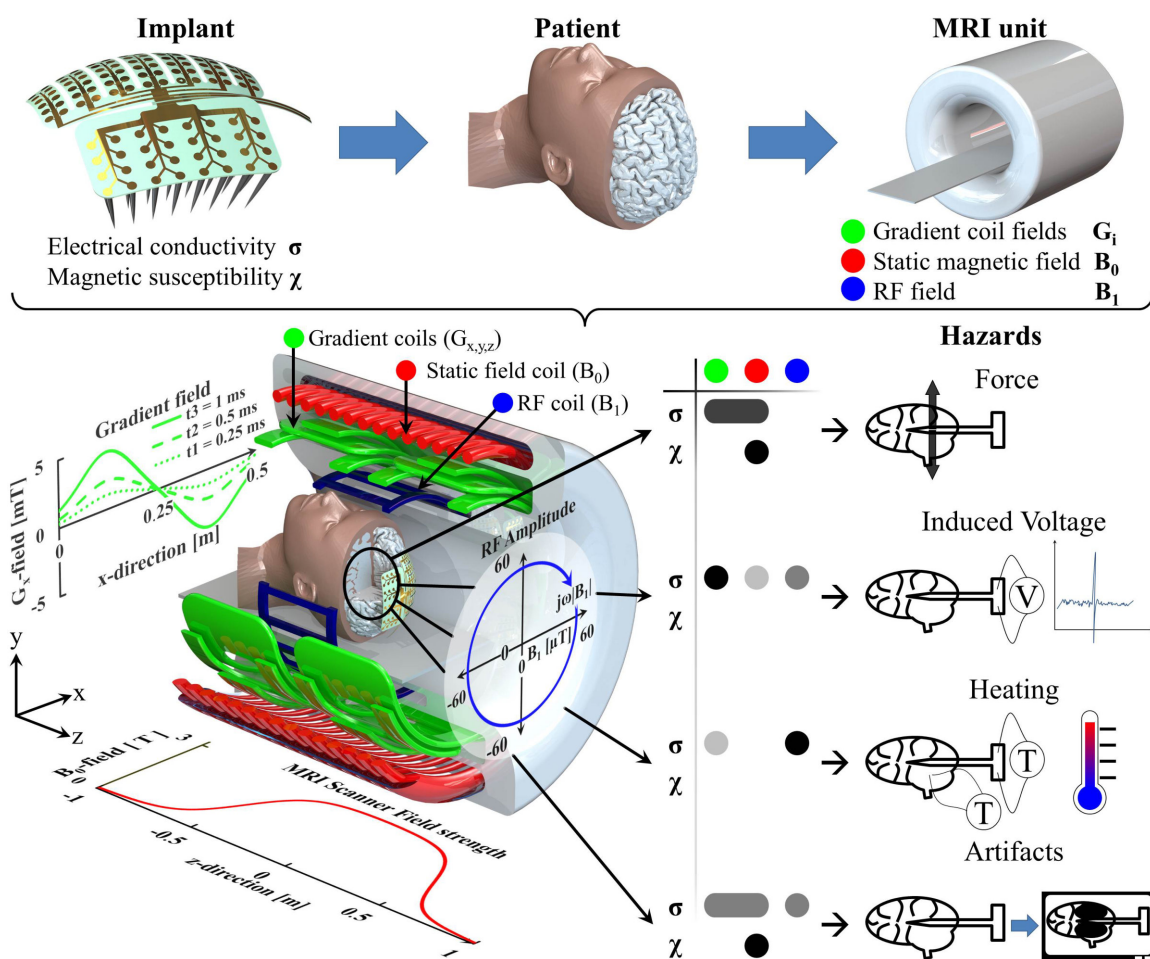


Figure 3.1.: Visualization of the electromagnetic fields of the MR unit, the most important implant characteristics (magnetic susceptibility and electric conductivity) and the interaction between the respective entities which leads to the four groups of hazards. (Adapted from[EF01]).

electromagnetic induction. Using this statement as a guide, we can derive that a material, for example PMMA, which is "not" magnetisable and not conductive, is not prone to MR interactions. Unfortunately, the functional part of many implants requires a certain level of conductance for electrical signalling. In some cases even magnetization is mandatory, for example the permanent magnet in most cochlear implants. Moreover, it is not possible to have materials that are "not" magnetisable, only less magnetisable, since all materials exhibit at least diamagnetic behaviour. Additionally, MR safety is only one of the many other aspects to consider when conducting the implant design. Most often it is inevitable to select certain metals as material of choice. These restrictions lead to the questions if it is most advantageous to group all MR related interactions due to their underlying physical phenomenon magnetism and induction? A more intuitive approach, also for physicians and radiologists, is the viewpoint from the side of resulting hazards, for example MR artifacts. MR image distortions, can have different causes, such as susceptibility induced artefacts and induction-based artifacts. Hence, the underlying physical phenomenon alone

Table 3.1.: A collection of studies grouped by the four main categories with respect to the hazard. Each study is labelled with the underlying physical phenomenon.

Hazard	Incident	Phenomenon
Force	Dislocation of implant ^[77,61]	Magnetism
	MR induced torque and demagnetization ^[43]	Magnetism
	Forces on metallic heart valves ^[25]	Induction
	Torsional moment of metallic parts ^[54]	Induction
Induced voltage	ECG artifacts ^[162]	Induction
	Inhibition of pacemaker ^[99]	Induction
	Unexpected asystole with modern pacemaker ^[51]	Induction
	Wrong detection of ventricular fibrillation ^[100]	Induction
Heating	Heating of small implants ^[29]	Induction
	Permanent neurological deficit ^[64]	Induction
	Heating by gradient switching ^[55]	Induction
	In vivo heating of pacemaker leads ^[91]	Induction
Artifacts	Hair gel artifacts ^[103]	Magnetism
	MRI with CI: Image quality ^[22,92]	Magnetism
	Quantification of susceptibility artifacts ^[98]	Magnetism
	Nonsusceptibility artifacts of metals ^[21]	Induction

is not a good criterion, and it is beneficiary to sort all types of possible incidents into four categories distinguished by the hazard: Force, induced voltage, heating and MR artifacts. In table 3.1 a sorted collection of various studies to specific MR hazards and interactions is presented. All hazardous events fit in this scheme and all publications can be classified according to this scheme whereby each publication is dealing with one or more of the four type of hazards.

The connection between electromagnetic fields, the implant, the underlying physical phenomenon and the hazards is visualised in figure 3.2. On that basis, a fundamental introduction will be given to the individual hazards and the physics behind the phenomena. In the further context I will discuss the interaction between the electromagnetic fields and implants, without specifying any type of implant. The explanations are valid for any type of foreign objects, from advanced active implants to passive objects such as metal splinters.

3.1.2. Force

All types of interactions which lead to motion between implant and tissue are direct hazards for the patient with the potential of severe injuries. Mostly the reason is the delocalisation

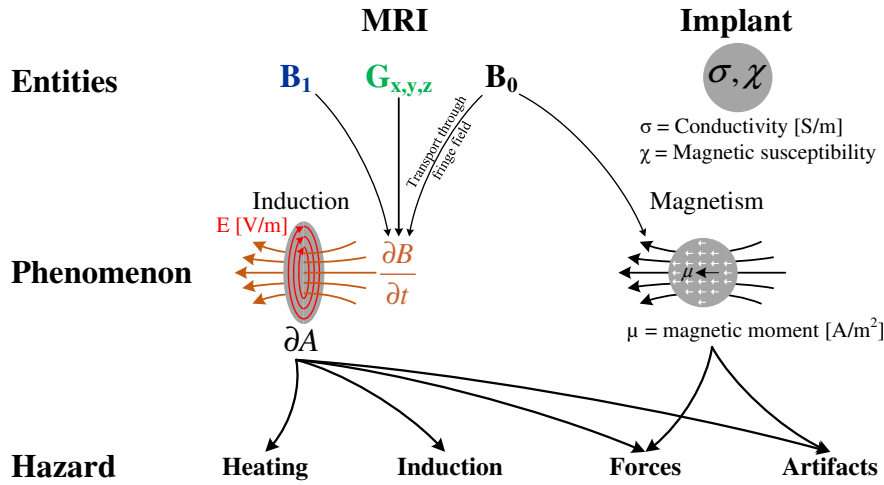


Figure 3.2.: The connection of induction and magnetism with the corresponding hazards. All three electromagnetic fields are time dependent. For \mathbf{B}_1 and the gradient field G_i this is obvious, for \mathbf{B}_0 this is true in the frame of reference of the patient during patient transport. Hence, all three fields are source of induction. Considerable interactions based on magnetism however are only due to the strong \mathbf{B}_0 .

of an implant which may result in tissue inflammation or rupture. Furthermore, the functionality of the implant may be impaired or completely lost due to mechanical defects or displacement of active sites (electrode-tissue interface). Forces that act on certain structural components of the implant are the reason for this displacement. Different types of these forces will be presented in the following text. Therefore, some important formulae are presented to explain fundamental aspects of the interaction with forces. For full derivations I want to refer to the excellent textbook of J.D. Jackson^[70] and for more general formulae with respect to magnetisation based forces in MRI to the excellent publication from J. Schenk^[132]. In general, forces occur if an implant is surrounded by an external magnetic field and any component of the implant exhibits a magnetic moment \vec{m} . There are two sources for a magnetic moment, (i) magnetisation and (ii) circular currents. For isotropic para- or diamagnetic materials (no hysteresis) the magnetic moment \vec{m} , as a result of magnetisation, is computed by:

$$\vec{m} = \iiint \vec{M} dV = \iiint \chi \vec{H} dV = \iiint \chi \frac{\vec{B}_0}{\mu_0} dV = \frac{\chi}{\mu_0} \vec{B}_0 V \quad (3.1)$$

This formula is valid for materials with susceptibility $|\chi| \ll 1$. For paramagnetic materials with $\chi > 0$ the magnetic moment \vec{m} scales linear to \mathbf{B}_0 as well as for diamagnetic materials with $\chi < 0$. In general, the direction of magnetization \vec{m} in any object is dependent on the shape. In addition to shape dependency, for anisotropic or ferromagnetic materials the orientation of the magnetic moment depends on the microscopic structure and/or pre-magnetisation, which is an important aspect when discussing torque. The magnetic moment created by circular current is given by:

$$\vec{m} = \frac{1}{2} \iiint \vec{r} \times \vec{j}(r) dV \quad (3.2)$$

For a circular current loop with current I this simplifies to $\vec{m} = I \cdot A$, and the magnetic moment is proportional to the current and the corresponding enclosed surface. Most often in MRI the circular current is produced through induction, so called eddy-currents. The magnetic moment for a circular area is governed by²:

$$\vec{m}(t) = -\frac{1}{8} \frac{d\vec{B}(t)}{dt} \pi \sigma h r^4 \quad (3.3)$$

Here h denotes the height or thickness of the disc, and r the radius. The change of magnetic field through the cross section of the disc is the source of the magnetic moment which is time dependent. An alternating magnetic field produces an electric vortex field which, in a conductive disc, results in an eddy current that creates a magnetic moment. All three electromagnetic fields of an MR unit are sources for this magnetic moment along with their characteristic time scales. The \mathbf{B}_0 -field is the source of very low frequent or quasi-static eddy currents during patient transportation, the gradient fields produce eddy currents during gradient switching in the Hz - kHz range and the \mathbf{B}_1 -field produces eddy currents in the RF range.

As introduced in chapter 2.2.4, any magnetic moment is a source of a linear force inside a gradient field and a source of torque if the directions of \vec{m} and \mathbf{B}_0 are not parallel. However, especially for weak magnetic objects with an arbitrary shape, where the induced magnetic moment is due to the external magnetic field, the computation of the dipole moment is a cumbersome process. The demagnetization factors can be computed on the basis of ellipsoids and results for needle-like, sphere and disc-like structures are presented by Schenck^[132]. To discuss magnetization based force and torques, the equations for weak magnetic materials are adopted from Schenck^[132] and modified for disc-like structures and presented in table 3.2. All equations, without exception, depend on the scalar and/or cross product, which means that the orientation of the implant with respect to the electromagnetic fields is crucial. The absence of an interaction does not indicate that there is not interaction. Based on these equations one can estimate in which cases the force and torque are at a maximum or vanish completely. There is no linear force at the isocenter since the gradient $\nabla \vec{B}_0$ vanishes. This is true for all objects including ferromagnetic materials. The linear force for weak magnetic materials is at a maximum in the fringe field at the point where the product of gradient and field strength is at a maximum. The reduced fringe field of shielded magnets have stronger gradients, because the distance from earth field to \mathbf{B}_0 is reduced, hence, the expected forces are larger. The linear force due to induction from \mathbf{B}_0 depends on the transportation velocity. This force vanishes if the surface is parallel to the gradient of \mathbf{B}_0 because then follows $\vec{n} \cdot \nabla \vec{B}_0 = 0$. The torque due to magnetism is for weak magnetic materials usually negligible because

²for derivation see appendix A.1

Table 3.2.: A collection of equations which describe the potential forces of an disc-shaped implant due to the electromagnetic fields in an MRI machine. The parameter $C_I = -\frac{1}{8}\pi\sigma tr^4$ is introduced for better overview. The vector \vec{n} denotes the normal vector of the surface of the implant and v_T means transportation velocity from outside to the isocenter.

Forces		Static \mathbf{B}_0	Gradient fields \mathbf{G}_i	RF field \mathbf{B}_1
Force (linear)	χ	$\frac{\chi^V}{\mu_0} \vec{B}_0 \cdot \nabla \vec{B}_0$	-	-
	σ	$C_I (\vec{n} \cdot \nabla \vec{B}_0)^2 v_T$	$C_I (\vec{n} \cdot \dot{\vec{G}}_i) d_{ic} (\vec{n} \cdot \nabla \vec{B}_0)$	$C_I (\vec{n} \cdot \dot{\vec{B}}_1) (\vec{n} \cdot \nabla \vec{B}_0)$
Torque	χ	$\frac{\chi^2 V}{\mu_0} (\vec{n} \cdot \vec{B}_0) \times \vec{B}_0$	-	-
	σ	$C_I (\vec{n} \cdot \nabla \vec{B}_0) v_T \times \vec{B}_0$	$C_I (\vec{n} \cdot \dot{\vec{G}}_i) d_{ic} \times \vec{B}_0$	$C_I (\vec{n} \cdot \dot{\vec{B}}_1) \times \vec{B}_0$

the square of the susceptibility for materials with $|\chi| \ll 1$ becomes very small. On the other hand, considerable torque may occur during the transportation of an implant with high conductivity towards the isocenter. Normally, this torque will be largest when a disc-like structure is inclined by 45° with respect to \mathbf{B}_0 because then $(\vec{n} \cdot \nabla \vec{B}_0) \times B_0$ will be at a maximum. This is also true for gradient-induced vibration which are at maximum if $(\vec{n} \cdot \dot{\vec{G}}_i) \times \vec{B}_0$ is largest. Gradient-induced vibrations of a disc structure vanish completely if (i) the normal of the disc is orthogonal to the gradients ($\vec{n} \cdot \dot{\vec{G}}_i = 0$) or (ii) the normal of the disc is parallel to \mathbf{B}_0 ($\vec{n} \times B_0 = 0$). The torque through induction by \mathbf{B}_1 is non-zero, however, in reality there is effectively no resulting motion at the corresponding frequencies because of the large inertia. Very small objects, on the other hand, may very well resonate at the corresponding frequencies which is even used for NMR signal detection^[129].

Among the common commercial implants, forces are most problematic for Cochlear implants (CI). Most of these implants have a subcutaneous magnet which enables the correct alignment and attachment of the external transmitter. Large torques and forces which lead to dislocation and rupture are reported in the literature^[43,61]. Another aspect which plays a role for CI is the demagnetization of the internal magnet which requires replacement and thus surgery^[147,73]³. Clearly, the majority of hazards due to interactions with the Cochlear implant are based on magnetism. An example for induction based hazards are the interactions of metallic heart valves with the electromagnetic fields leading to impaired cardiac output^[25,34]. A more detailed analysis to gradient-induced vibrations will be presented in section 3.3.

³Every surgery bears a risk for the patient in form of infection, adverse effects of anaesthesia etc. As such, surgery to relocate an implant is an indirect hazard for the patient, which follows as a consequence of adverse MR interactions.

With the support of table 3.2 one can derive some guidelines to avoid or minimise forces and torques in MRI. Clearly, using weak magnetic materials is a method of choice when possible. In order to avoid forces due to induction one can, from the viewpoint of an external object, reduce the area A as much as possible, because forces scale with the power of four with respect to the radius r and linear with the thickness t . Another option is to use materials with lower conductivity. From MR side, all actions that reduce the slew rate (or as such the Larmor frequency ω_L) of any field changes, help to minimize the amplitude of forces.

3.1.3. Induced voltage

Induced voltage is a group of hazards which manifest in different ways. These voltages can lead to direct severe injuries or delayed negative effects due to reduced diagnostic values. All interactions that lead to a voltage between different locations of an implant can be grouped as hazards of induced voltage. In general, active implants are build for recording and/or stimulation by means of interfacing electrodes to various type of excitable tissue such as brain, muscles, sensory systems or peripheral nerves. The electrodes require

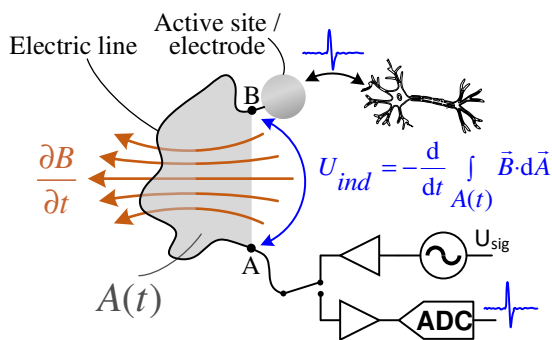


Figure 3.3.: Principle of induced voltage: The rate of change of magnetic flux through the area A embraced by the electric line creates a voltage U_{AB} between the points A and B.

electrical interfacing to external devices for power supply and signal transfer. If implants are inside the MRI, the hazard of induced voltages is the interference of the functional voltage-based signalling with extrinsic voltages formed by induction through the electromagnetic fields of the MRI. These extrinsic voltages lead to signal corruption in recording devices and to undesired excitation in stimulation devices. A general schematic of this phenomenon is illustrated in figure 3.3. The induced voltage depends on the enclosed area of a conductor and the rate of change of the magnetic

field. Similar to the forces, the source of magnetic field change can be the switching of the gradient fields, \mathbf{B}_1 or the fringe field of \mathbf{B}_0 during patient transportation. To analyse the fundamental phenomenon, we evaluate the principle using a simple voltage source with internal resistance as shown in figure 3.4. Under the assumption the electric line forms a circle with one winding, the induced voltage U_{ind} is calculated using the following equation:

$$U_{ind} = -\frac{d}{dt} (\vec{B} \cdot \vec{A}) \quad (3.4)$$

On the basis of figure 3.3 it is deducible that minimizing the enclosed area is an important option to minimise the induced voltage. Another option will be discussed with the aid of

figure 3.4. In this figure, both configurations are visualised, for stimulation and recording electrodes respectively. Induced voltage is equivalent as having an additional voltage source in the electrical feed line. In the ideal case this line has no internal resistance and there is no voltage drop such that $U_A = U_B$. In this case, the voltage of the stimulator output equals the voltage at the active site

which allows perfect control. For recording devices, the voltage from the tissue at B is measured without distortion at A. Due to MR interactions, however, there is an additional voltage U_{AB} which may create such a high voltage level at point B that undesired stimulation occurs. The similar situation exists for recording electrodes where the induced voltage U_{BA} creates a detectable voltage level U_A , but there is no neuronal signal since $U_B = 0$. One option is to use a device that disconnects the parasitic source U_{ind}

from the conductor, such that $U_{AB} \rightarrow 0$. One option is a bandpass filter, such that U_{ind} is blocked and U_{sig} can pass. This requires, however, that the induced voltage has another frequency band than the signal. This is the method of choice for high-frequency, B_1 -induced voltages. Gradient-induced voltages, however, are in the same frequency range than brain signals such that other techniques have to be applied. Pacemakers are most prone to induction-based interactions with severe hazards for the patient in form of erroneous stimulation. Fast movement into the MR may cause pacemaker inhibition^[51,99]. The situation for patients with implantable defibrillator is similar and erroneous sensing of cardiac rhythm^[100] may lead to fatal reactions of the device. Research is conducted, on how to remove interfering gradient-induced signals and to restore the original uncorrupted signals^[162].

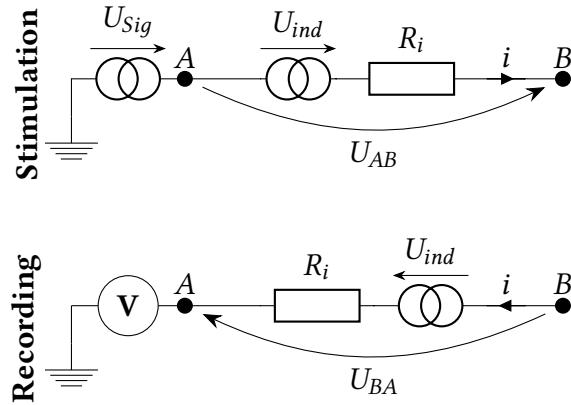


Figure 3.4.: Equivalent circuit for stimulation and recording configuration of an electrode.

3.1.4. Heating

Heating is a direct hazard which may lead to immediate and serious injuries to the patient during an MR procedure. Tissue which is exposed to temperatures above 44 °C degenerates due to disintegration of proteins. Whereas in most parts of the body there are receptors that are sensitive for temperature and enable thermoreception, these receptors are not present in the brain. Consequently, humans do not feel pain in case of excessive heating inside the brain which, in worst case situations, may lead to permanent neurological deficits as previously shown^[64]. But there are also reports of other accidents related to MR heating such as excessive heating due to clothes containing metallic microfibres^[119] or identification bracelets^[71] and more often burns due to ECG electrodes^[32]. Heating is probably the hazard with the most complex physical background. From all the elec-

romagnetic fields in MRI the most contributing one to heating is \mathbf{B}_1 . The complexity of this type of interaction lies (i) in the interaction with different types of materials, (ii) in many situations the wavelength is not negligible. In case of RF heating a certain amount of the transmission power dissipates in tissue or the implant leading to a temperature increase. The amount of absorbed power per mass is called the specific absorption rate (SAR). A widely used formula for SAR is given by equation 3.5^[117,115] where E is the peak magnitude of the electric field.

$$\text{SAR} = \frac{\sigma |\vec{E}|^2}{2\rho} \quad (3.5)$$

This formula is valid under the assumption that $\sigma/\omega\epsilon \ll 1$ as well as $\sigma/\omega\epsilon \gg 1$ ^[101] where ϵ is the permittivity. In other words, the formula holds for low-loss dielectric materials when displacement currents are dominant as well as for highly conductive materials when conduction currents are dominant. For some tissues, however, the magnitude for displacement currents is in the same range than for conduction currents^[44,45,46] such that $\sigma/\omega\epsilon \approx 1$, which requires a more general formula to calculate SAR. A derivation of this calculation was published by Hampe in 2015^[101]. Of great importance in equation 3.5 is the fact that the electric field is the source of heating and not the magnetic field⁴. This is the reason why there is a large focus in RF coil development on reducing the electric fields. In fact, there are two electric fields produced by an RF coil^[154]: (i) A conservative electric field E_c which drives the current through the coil and (ii) a non-conservative field E_i produced by the alternating \mathbf{B}_1 field. The total electric field in a sample is given by the sum of both fields $E_t = E_c + E_i$, hence RF coil designer strive to reduce E_t . However, E_t can only be reduced by reducing E_c since E_i is inherent due to Faraday's law of induction. Fortunately, E_c is dominant for the power loss in samples and the reduction of E_c can tremendously decrease heating inside the sample^[116].

Since the human body consist to a high percentage of water it is prone to heating due to alternating electric fields. Unfortunately, the interaction of (conductive) implants with the present electromagnetic fields are diverse and a general formulation is not possible. Three types of heating in connection with implants are discussed in the following. One type of heating is based on induced eddy currents which heats the implant directly. The alternating \mathbf{B}_1 field creates an electric vortex field which inside a conductive object leads to eddy currents. However, in the two-digit or three-digit MHz regime the calculation of the dissipated power which depends on the amplitude of the induced current becomes more complex. This is due to frequency-dependent skin effect which increases the effective resistance as well as the decrease of effective current due to inductance. A more important effect with respect to long wires are scattered electric fields. Hereby, surface currents are induced into the wire by the RF magnetic fields yielding a scattered electric field with greatest intensity at the tip of the wire^[158,118]. Based on this principle, large local electric

⁴One reason is that the electric dipole moment of molecules is much bigger than the magnetic dipole moment, especially for water, and thus the coupling to the electric field is dominant.

fields resonating at RF frequency lead to strong heating of tissue in direct vicinity to the electrode. This effect becomes even more crucial when the wavelength λ of the RF fields are in the same range as the wire length ($1/2\lambda$, λ , $3/2\lambda$, etc.). Such an example is provided by an experimental result: For identical configurations but various length of the wire, the temperature increased from 37 °C (45 cm) to 72 °C (85 cm)^[80]. Of great importance is the consideration of the reduced wavelength of most soft tissues due to their permittivity ϵ . This reduced wavelength λ_{tissue} is given by equation 3.6^[130]. The range of ϵ of tissues between 10 - 1000 MHz is from 10 up to 400^[10]. As an example, taking a value of $\epsilon = 225$ in a 3 T scanner such that $\lambda_{vacuum} = c/128 \text{ MHz} = 2.34 \text{ m}$ results in a reduced wavelength of $\lambda_{tissue} = 2.34 \text{ m}/\sqrt{225} = 0.16 \text{ m}$. Many implants have components with dimension in this range which makes wavelength dependency an important safety issue.

$$\lambda_{tissue} = \frac{\lambda_{vacuum}}{\sqrt{\epsilon}} \quad (3.6)$$

It is important for accurate RF heating models, to take into account the aspect of heat transfer inside the body. In many publication this is done on the basis of the bioheat transfer equation^[108]. This equation takes into account the heat capacity of tissue and the density as well as heat transfer based on thermal conductivity and blood transfer. An extensive literature review and evaluation of taking these effects into account was conducted by Foster et al. with the conclusion that especially the effect of blood flow variation is mostly unexplored^[42].

How do MR sequence parameters and the magnitude of \mathbf{B}_0 influence SAR? A simplified formula for SAR provides insight into the consequences of varying image sequence parameters and \mathbf{B}_0 strength. Equation 3.5 can be rewritten in the following way (adopted from the book "From picture to proton, ch. 10.2^[104]):

$$\text{SAR} = \frac{\sigma \pi^2 r^2 f_L^2 B_1^2}{2\rho} D = \frac{\sigma \pi^2 r^2 f_L^2 B_1^2}{2\rho} \frac{N \Delta t_{exc}}{T_R} \quad (3.7)$$

Based on this equation we can derive some factors that influence SAR. Reducing the volume size (here the radius r) lowers SAR. Furthermore, SAR scales quadratically with the Larmor frequency f_L , hence increasing \mathbf{B}_0 increases SAR quadratically. The same quadratic dependence holds for \mathbf{B}_1 . D is the duty cycle, which means the fraction of time of one repetition cycle T_R for which RF is present. Hence, increasing T_R lowers SAR, whereas the number N of excitations per cycle increases SAR.

3.1.5. MR artifacts

The fourth hazard, MRI Artifacts, is based on all interactions that lead to distortions and obscuration of the final MR image. The hazard for the patient is of indirect nature resulting from impaired diagnostics which may lead to suboptimal treatment^[4]. There are two main reasons for MR artifacts: (i) Susceptibility based artifacts which arise from distortions of

\mathbf{B}_0 due to magnetism of the implant^[150] and (ii) induction based artifacts which arise from interactions with the gradient fields G_i ^[125] or the RF-field \mathbf{B}_1 ^[21]. Apart from artifacts which are induced by foreign object, there exist various artifacts with manifold reasons such as chemical shift artifacts, partial volume artifacts or distortions as a result of signal processing such as truncation artifacts and ghost artifacts (aliasing)^[15]. Within this section the focus lies on susceptibility and induction-based (\mathbf{B}_1) artifacts of implants.

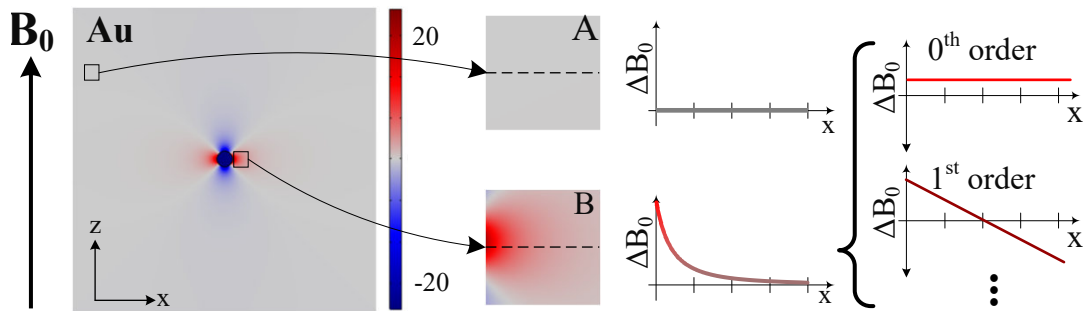


Figure 3.5.: Signal behaviour of different voxel in close and distant vicinity of a circular, diamagnetic object (see figure 2.17). The zeroth-order leads to a signal shift since all spins rotate homogeneously at a different frequency, the first order leads to faster signal decay.

Susceptibility artifacts are common for a wide range of implants especially for CI with a permanent magnet around. The fundamental principle will be discussed with the aid of the illustration in figure 3.5. The spins in a voxel have a Larmor frequency according to the local magnetic field. The computation for image reconstruction is based on the assumption of a homogenous field, hence, spins which rotate with an offset frequency due to local field inhomogeneities lead to signal errors. In MRI, the sum of all spins within a single voxel contribute to the signal intensity of this voxel. If a voxel is undisturbed, such as voxel A in figure figure 3.5, then the signal will be correctly attributed to corresponding voxel of the image. Field distortions with arbitrary field configurations lead to two effects: Wrong mapping of signals and fading of signal. As an example, we investigate voxel B along the central x-axis in which an object induces a local field gradient with a quadratic decay.

To analyse the effect of the resulting signal one can decompose this signal in its polynomial basis. Since in this voxel $\mathbf{B}_{\text{local}} > \mathbf{B}_0$, there is a constant offset, or the zeroth order is not vanishing. This yields a frequency shift and the signal will be, in the final image, assigned to a different wrong voxel. In this wrong voxel the actual and additional erroneous signal will be superimposed, whereas the signal there is no signal in the actual voxel. This type of artifact is called hypo-intense (less signal) and hyper-intense (more signal) signal distortion. The first order distortion leads to the effect that the spins within the voxel experience a faster decoherence and the signal decays faster (T_2^* decay). Higher orders can be analysed equivalently and the underlying principle is equivalent to the field distortions that are corrected by shimming^[23]. The distortion of the final MR image due

to susceptibility artifacts depends strongly on the sequence parameter. For example, SE sequences are a remedy against rapid T_2^* decay, but they do not work against constant frequency offset. The difference $\Delta B_{max} - \Delta B_{min}$ as well as the offset $B_{max} - B_0$ of a voxel can also be interpreted as a certain bandwidth and frequency offset per voxel. Setting the excitation bandwidth and receiving bandwidth accordingly can help to reduce the susceptibility based artifacts. More detailed analytical solutions, with a detailed analysis of different types of magnetism, are presented by Schenck in 1996^[131]

The second type of artifacts is due to B_1 field interactions and occurs when conductive objects are placed inside the B_1 field^[21]. As illustrated in figure 3.6 induced eddy currents establish a secondary magnetic field which is opposing the actual B_1 field. It becomes conceivable from this illustration that the actual magnetic RF field is attenuated in front and rear side of the disc and amplified at the outer rims. This has two effects: (i) A heterogeneous RF field results in a heterogeneous FA which adversely affects all sequences which rely on a homogenous FA (such as SE sequences) and (ii) due to the principle of reciprocity^[67] the sensitivity increases at the outer rims and decreases at the surface of the disc. In many cases this effect lead to typical artifacts where hypo-signals appear at orthogonal to the surface of the disc and hyper-intense signals at the outer rims⁵. From another viewpoint this effect could be seen as refocusing the magnetic flux and clever design of the metallic object allows to focus the B_1 field and to increase SNR. These "magnetic lenses" are known as Lenz lenses^[142].

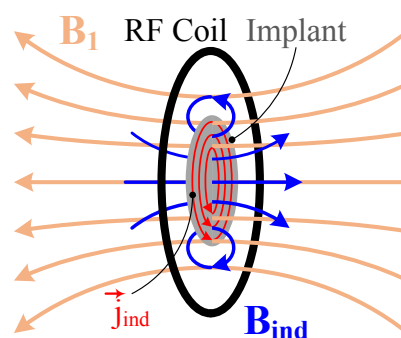


Figure 3.6.: Principle of RF induction artifacts: The alternating B_1 introduces alternating eddy currents in a conductive disc which result in counter field B_{ind} . The resulting magnetic field is a superposition of both fields which attenuates the actual B_1 along the normal vector of the disc and enhances this at the outer rims of the disc.

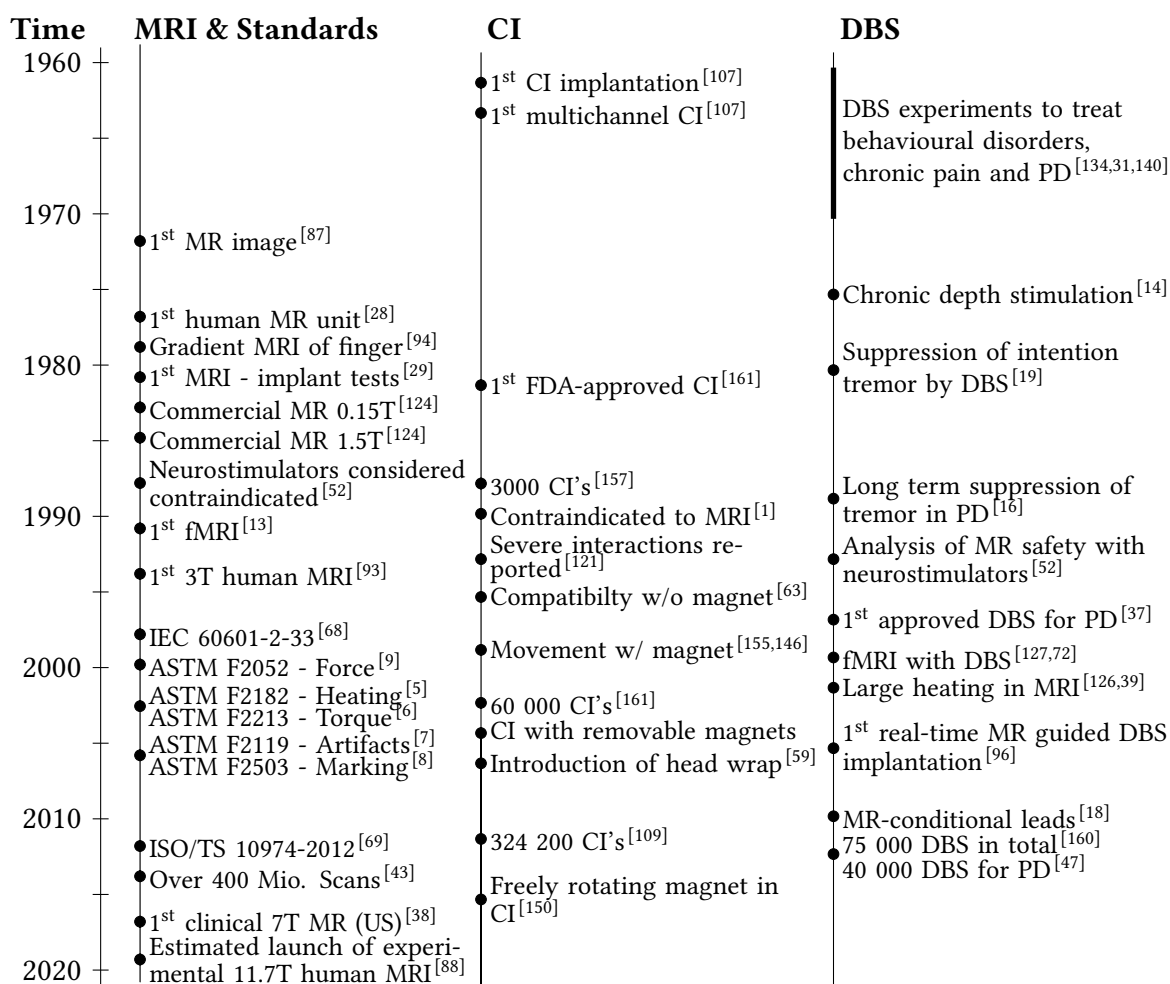
For implants with ferromagnetic materials such as the CI the susceptibility effect is dominant by far^[128,92,26,151,22,150]. For weak magnetic, but highly conductive materials the effect of RF induction is dominant^[21]. It is recommended for the correct analysis of artefacts from materials with larger magnetic susceptibility and conductivity, for example platinum, to clearly distinct both effects by the acquisition of a B_0 map which measures the offset frequency of a voxel. Hence, the B_0 map measures only the effects of B_0 field distortions. For the analysis of inductive artifacts, the acquisition of a B_1 map is recommended.

⁵Generally, the resulting artifact depends, of course, on the local FA and saturation. Hence, by varying TR, TE and FA, also the outer rims can become dark and the region at the surface can become bright.

3.2. Development of MR safety concepts, technical specifications and standards

A short historical overview will be detailed and table 3.3 provides a visual guide. For a long time, the development of MR hardware and implant hardware was completely independent. As a matter of fact, the research of recording the activity from neural or muscle cells goes back until the early 1930's^[48]. Studies for interfacing the brain in living animals did appear approximately 20 years later^[144]. First devices, specifically designed for pacemaking, were presented in the early 1930's and first attempts using completely implantable devices were presented in 1958^[153]. At around the same time, first publications reported on the successful stimulation of the auditory nerve^[107]. In contrast, the first NMR spectrum was published in 1946^[123,17] and it took more than 25 years until 1973 when the first MR images were published^[87]. From there on, it went very fast: The first commercial MR scanner became available only 10 years later^[124] and at around the same time the first FDA-approved CI implant was presented^[161]. Also in the early 1980's the ability of suppressing tremor by DBS stimulation was shown^[19]. At this time, it got obvious that MRI is becoming the modality of choice for soft tissue contrast and it will be inevitable to make MRI available for implant carriers. Consequently, first tests for MR-implant interactions were already conducted even before the first commercial scanner was available^[29]. The independent development of implants and MRI lead to two major issues with respect to MR safety of implants: (i) Design freedom of (active) implants is already very restrictive due to stringent requirements of biocompatibility, longevity and functionality. In addition, the fact that the functionality of all active implants (pacemaker, CI, DBS, etc.) is based on electrical signalling makes it no surprise that the independent development resulted in incompatible techniques. (ii) When it was recognized that implants need to be MR compatible, the type of interactions and resulting hazards were not clear and a systematic approach to solve the emerging challenges had first to be established. Hence, it is no surprise that it took almost 20 years from the first MR safety experiments in the early 1980's to a first official norm which regulates MR safety of MR units as well as the interactions of MR units and implants (DIN EN 60601-2-33/A11:1998-02^[68]). In the US, specific standardized test methods were introduced for heating, artifacts, force and torque as well as the correct labelling of implants. The allocation of hazards presented in chapter 3.1 is built upon these test methods. In 2012 a very detailed technical specification was introduced to standardize the assessment of active implantable medical devices (ISO/TS 10974:2012^[69]). A revised version of this specification was published in 2018. An important aspect is the correct use and labelling of objects according to ASTM F-2503^[8]. All objects which pose no hazard in any MR environment are labelled as "MR safe". It is explicitly pointed out, that only devices qualify for this label which are non-conductive, non-metallic and non-magnetic (see ref.^[8] sec. 3.1.3). Basically all active implants, thence, qualify only for the label "MR conditional",

Table 3.3.: Milestones of the development of MR technology and standards for human-MRI, the development of CI's and DBS. Commercial availability of for CI and MRI in the 80's (DBS in the 90's) and the desire to have a safe integration of these techniques led to technical specifications and standards at the end of the 90's/beginning 2000's. (Table adopted from[EF01]).



which attest safety under defined conditions. Following this definition, it is impossible to have or to strive for "MR safe" active implants.

Having this historical development in mind, it becomes clear that the integration of these technologies is oftentimes difficult. An ideal example is the external magnet of the CI. Inductive coupling was an excellent solution to provide an easy, exchangeable external power supply as well as an audio recording and processing unit. Interfacing the subcutaneous and external components with the aid of a magnet is user-friendly, fast and accurate. However, these thoughts are only valid as long as MR compatibility is not considered, which was certainly the case until the first FDA-approved CI was released. Even though, magnetless CI has been introduced latest by 1997^[156,56] this technology has never become popular. Once a certain technology is established, it requires massive

pressure to modify the approach. From this viewpoint it is extremely important to take into account MR safety as an important issue already in the design and development process.

3.3. Vibration of implant substructures

Most of the research in the field of MR safety is focused on the hazards related to RF heating (DBS, pacemakers), susceptibility-based MR artefacts (CI), induced voltages (ECG, pacemakers) and forces due to magnetism (CI). Little attention is paid to forces resulting from induction such as gradient-induced vibrations. Certainly, an important reason is the assumption, that gradient-induced vibrations have a low-level risk, and are rather considered a non-critical threat. Mostly, however, these assumptions are not backed by sound, reliable data, simply because there exist only few quantitative data.

3.3.1. The fundamental problem

The fundamental process of gradient-induced vibration, lies in the exhibition of a magnetic moment due to induced eddy currents in a conductive structure. This induction originates from any processes associated with a time-variant magnetic field which, inside \mathbf{B}_0 , leads to a torque. Gradient-induced eddy currents have a spectrum within the range of up to the double digit kHz regime^[133]. This range is of great importance because it overlaps exactly with the mechanical resonance of macroscopic and larger microscopic devices. Hence, we have to assume the existence of strong vibration amplitudes due to resonance condition. The spectrum of the gradient-switching during an MR sequence depends on many variables. Most importantly, are the sequence timing parameters and image resolution (including excitation/receiving bandwidth). The latter adjustment controls the amplitude of the applied gradients. The spectrum of the eddy currents and thus the resulting torque is directly correlated to the spectrum of the gradient switching but it depends furthermore on the location of the conductive structure. The local gradient field, as seen by an implant, results from the superposition of the three gradient fields, and constructive or destructive interference may result in a modified spectrum compared to the individual gradient spectra. If we want to predict the mechanical behaviour of an implant during a certain MR sequence, we need to know its transfer function. Assuming a linear system we can then predict the resulting vibration for any excitation. Even more important, however is the question, on how the mechanical transfer function is affected by placing an implant inside the tissue environment. Or more precisely, how strong is the damping of mechanical implants within a viscoelastic environment such as brain matter? Interestingly, until today, there is no clear answer to this question and no quantitative answer to the question on how strong gradient-induced vibrations may be.

3.3.2. Studies about induced torque of implants or implant-like structures

In fact, only few studies explored the effect of induction-based torque in general. To provide an overview, a short synopsis will be given of publications that studied the effects of static and gradient-induced torque. One study, conducted in 2000 by Condon et al.^[25] investigated the static torsional moment of metallic heart valves due to induction during patient transport. In this study they could show that there is significant torque acting on the valves of a cardiac implant resulting in a reduced cardiac output. In 2006 Graf et al.^[54] measured the produced torque acting on a metallic frame during patient transportation with a velocity of 0.2 m/s in a 1.5 T and a 3 T MR scanner. These measurements demonstrated measurable torque on the frames. Moreover, the authors tested the effect of gradient switching and confirmed a perceptible vibration. Quantitative data, however, could not be extracted. A further publication reported about forces on metallic heart valves due to induced torque during transportation through the fringe field. MR contraindication was found for certain valves due to transportation through fringe field. It was indicated, however, that gradient fields and RF fields do not produce large enough Lorentz force's to lead to severe effects^[53]. Another study regarding potential flow irregularities was presented, where they showed adverse effects during movement through the fringe field. Despite there were no experiments conducted with switching gradient fields, these authors highlighted that there is a possibility of adverse effects during gradient switching which may impede functional performance of the heart valves^[34]. Based on that small collection of studies it is obvious that reliable data are missing. As of today, it is not possible to provide a definite statement on the hazardousness of implants in general, let alone the impact of vibrations within tissue. That hazards due to gradient-induced vibration, however, is not only purely hypothetical, proves a case study in which a patient reported on a heating sensation during an MR exam. The reason for this heating sensation in retrospective found to be caused by gradient-induced vibration during an MR imaging sequence with distinct switching parameters^[137].

3.3.3. Studies about mechanical tissue-implant interactions

No studies have been conducted to investigate the effect of gradient-induced vibration of implants in the brain. Especially implants for the brain, however, have to fulfil high standards and comply with a large set of requirements and criteria. Additionally, functional longevity is of utmost importance to minimise complicated and risky surgeries for replacement and correction of implant components. For brain implants correct positioning and the mechanical integration into the viscoelastic brain environment plays a crucial role for long-term functionality. Several studies were conducted which investigated the effect of micromotion between active site and brain tissue with the result that micromotion is an important parameter with a large effect on durability and functionality^[102,50,141,163]. An-

other study by Sridharan et al.^[143] measured the forces on microelectrodes test structures during implantation with up to 1 mN. A great review was presented by Prodanov et al.^[122] in which the mechanical aspects of implant and brain tissue as well as their mechanical interactions are discussed. One focus is laid on the effects of micromotion and the corresponding tissue reaction such as inflammatory effects, which results in change of mechanical properties of brain tissue. Furthermore, micromotion potentially leads to the establishment of adverse tissue formation which results in decrease of functionality of the implant. It is concluded that a basic understanding has been established, however, much more data are needed in order to understand the general processes and to turn this knowledge into the design of improved brain implants.

3.3.4. Studies about gradient-induced force for micro-robot propulsion

The fact that micromotion of foreign objects in association with gradient field in MRI occurs, is proven within another research field. Here the idea is, to use micro-robots to navigate through the body, for example through the cardiovascular system, using the electromagnetic fields of the MRI system as the energy source for the propulsion systems. Such a technology would enable the image acquisition of the internal body, conduct biopsies or enable local drug deposition using minimally invasive techniques to give a few examples^[110]. A first method was proposed in 2006 using a ferromagnetic core which experiences a translational force due to the gradient fields produced by the gradient coils^[97,95]. However there are many challenges to overcome since ferromagnetic particles within the human body, in combination with MRI are certainly hazardous and problematic^[41,114]. Another attempt is to use gradient-induced currents which establish a magnetic moment which allows to produce a torque for propulsion. It is of interest, that the test devices consist of a coil mounted on a tail-like flexible polymer film. The propulsion technique converts the torque produced in the head-coil due to gradient switching to a linear motion due to the elastic tail^[84,82,83]. While this propulsion effect in these applications is desired, there is no reason why this effect may not adversely occur in polymer-based flexible thin-film electrodes^[112]. In this case, the electrode would experience a linear motion which leads to undesired relocation leading to malfunction or data corruption.

3.4. Conclusion

The technologies of MR imaging and active implants have become inter-dependent to an extent, that MR safety of implants constitutes an important topic, for design engineers as well as for clinicians and patients. Many MR issues such as heating pose extremely severe hazards, and therefore gain the required attention. Other MR issues, however, such as gradient-induced vibration still lack reliable data, and definite statements cannot be made. A detailed analysis of the current state-of-the-art was presented in the previous sections,

which is the basis for the research set out in the next chapters. There, a novel methodology will be detailed, which allows to investigate the mechanical tissue-implant interaction with a special focus on the damping of foreign objects within viscoelastic materials such as brain tissue.

4 | Low-field probe for MRI and vibration analysis

In the previous chapter it was found that it is imperative to gain more data on gradient-induced vibrations. The required novel method and experimental setup will be described in the next two chapters. A new method has to be developed to (i) assess quantitatively the mechanical interaction of penetrative implant-like structures with the viscoelastic environment and (ii) measure the produced torque on conductive structures due to gradient switching. Therefore, a novel probe has to be developed which enables the assessment and evaluation of these mechanical interactions. Since most of the information is contained in the transfer function, this device needs to provide a useful interface which allows a rapid evaluation of the transfer function of penetrative structures. Furthermore, the probe should enable the quantitative analysis of the produced torque due to gradient switching on different test specimens. The main requirements are summarized as follows:

- Acquisition of static and dynamic transfer functions with large temporal (up to 10 kHz) and spatial resolution
- Rapid exchangeability of test specimens
- Rapid exchangeability of viscoelastic environments
- Integration of simultaneous MR acquisition and vibration measurements

The probe, needs to be MR compatible to fulfil the corresponding task. For example, a large metallic framework may introduce parasitic vibrations and corrupt the data analysis. Within the next sections, the concept of the probe will be detailed, including its components, the mechanical and electrical interfaces, the required software components and the final benchmark tests. Within this chapter the general functional principle of the entire probe as well as a detailed description of the individual components are described. Most of this work was presented at the 2017 International Conference on Electromagnetics in Advanced Applications (ICEAA) under the title "Optical gauge head to evaluate gradient field induced vibrations of conductive structures during MRI"^[EF09]. The theoretical and experimental analysis of the actual samples will be presented in chapter 5.

4.1. Concept

At first the preconditions will be explained. The experiments are conducted in a 1 T horizontal bore permanent magnet (see figure 2.14). In this MR unit, the gradient coils are hardware installed and not part of the probe and the available space at the isocenter is approximately 5 cm in diameter. The main goal is to evaluate the mechanical behaviour of penetrative implant like-structures. These test structures, in the further text called "sample", are simple circular beams with a length up to 20 mm, which is the maximum possible sample size within this equipment. The sample diameters range from 0.1 mm to 2 mm. All samples are selected from different materials such as polymer-based (ABS or nylon) or metal-based (copper or brass) beams. An important part of the experimental protocol is the measurement of the transfer function of these test structures within air, water and agarose gel. The latter item, agarose gels, yield a viscoelastic environment which resembles the mechanical environment of the brain if prepared with the concentrations. This renders agarose gel as a perfect tool to mimic and study vibrations in brain-like environment^[57,20].

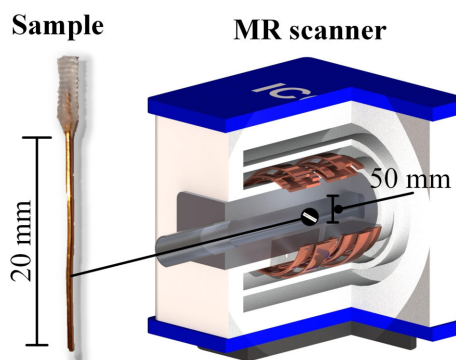


Figure 4.1.: Geometrical restrictions of MR unit

Three different options to measure the vibration of a beam within agarose gel are briefly discussed and the selected approach is described in detail. MEMS-based acceleration sensors are excluded from these considerations, since even the smallest available sensor devices are too bulky to mount it on the tip of a sample, and they largely affect the mechanical behaviour of the samples. There are three options available for the contactless measurement of sample vibration: The measurement using a camera, MR imaging and the measurement of laser beam deflection. The advantages and disadvantages will briefly be discussed to provide a rationale for the selected method.

4.1.1. Measurement using a high-speed camera

Cameras with the correct optical equipment offer image resolution down to 5 μm . Most importantly, this approach allows measuring the deflection of beams directly along their axis. Two major disadvantages, on the other hand, are the complex post-processing approach and the limited temporal resolution. Even most modern, affordable high-speed cameras are limited to approximately 1000 frames per second. At the same time, for most cameras, high temporal resolution comes at the expense of less spatial resolution. Post-processing in this approach is complex, especially in view of object recognition for images with different viscoelastic environments. Image recording requires (i) large storage capacity for raw data and (ii) a sophisticated algorithm to extract the deflection data from the images.

Furthermore, there are high demands on the camera due to MR compatibility and size limitation. In summary the superior number of negative aspects render this approach as not promising to achieve the goal using the available temporal and financial resources.

4.1.2. Measurement using MRI

Direct deflection measurements using MRI offers similar advantages as recording with the camera. It enables the direct measurement of the beam deflection along its axis, without the problem of MR compatibility issues since the technique is naturally inherent. However, the limitations are more restrict compared to the camera. Temporal and spatial resolution of MRI are far beyond the capabilities of standard optical cameras. Advanced acquisition techniques such as the measurement of flow and diffusion could offer the potential to extract mechanical behaviour of the beam. This requires, however, the modification of existing acquisition protocols or even the development of novel sequence schemes which are sensitive to small beam deflections and provide the resolution for a frequency range up to several kHz. In view that the achievable limits of the temporal and spatial resolution are unknown, and considering the weak SNR in NMR/MRI, this approach bears a large risk of failure. Furthermore, the measurement of the free sample vibration in air would not be possible due to the absence of a signal contributing medium¹.

4.1.3. Measurement of laser beam deflection

A third option is to measure the deflection of a laser beam. A similar, commercially available technology, the laser scanning vibrometry which is based on the Doppler effect, is used to measure vibrations of macroscopic and microscopic objects. One large advantage lies in the extremely high temporal and spatial resolution achievable by using this technology. The nowadays available, ultra-fast and precise optical detectors are the foundation for this success. In combination with high-speed data acquisition devices, these detectors enable a sampling rate with a bandwidth up to the MHz range. High speed sampling is most advantageous during the acquisition of vibrations triggered by broad-band excitation because it facilitates the straightforward frequency analysis using the Fourier transform. The disadvantage of this method lies in the fact that a homogenous surface is required for light-beam reflection, hence the beam cannot be observed directly.

Due to the options of high-speed and high-precision sampling, which enables the application of versatile and powerful data processing tools, the decision was made to realize the measurement setup on the basis of the laser-deflection method. The basic

¹A solution to measure free vibration could be the measurement of vibrations using hyperpolarised Xenon. This, however, requires the hardware support for the corresponding Larmor-frequency.

concept of the setup is illustrated in figure 4.2. Here, the fundamental components are visualised which are the Control and acquisition, circuitry, optic and the mechanical setup. Before the detailed analysis is presented, a brief functional explanation will be given.

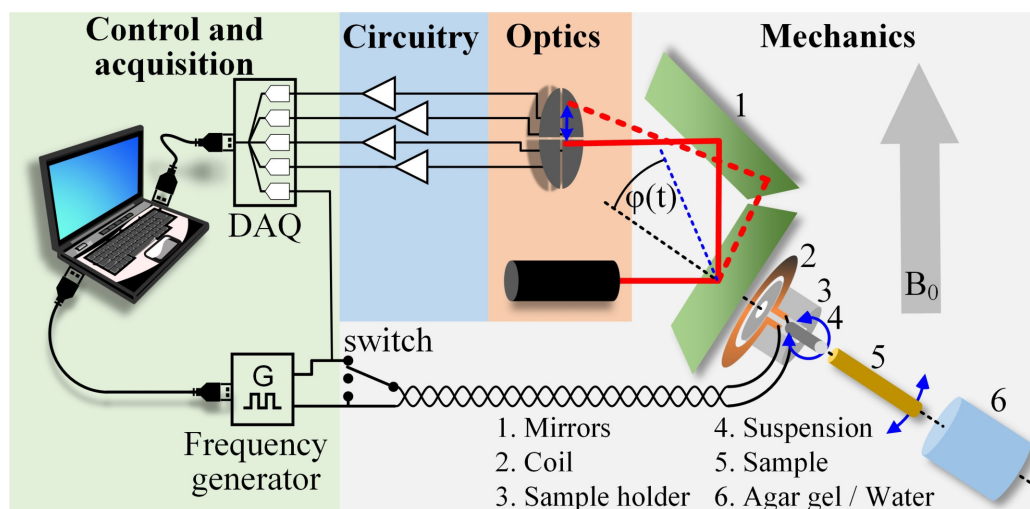


Figure 4.2.: Illustration of the principle concept of the laser deflection measurement setup. A current in the coil produces a magnetic moment which leads to a torque. This torque yields an angular deflection with the angle $\phi(t)$ of the setup, with the axis of rotation of the suspension rod. The deflection of the lower mirror, which is mounted onto the sample holder, leads to a deflection of the laser beam which then is detected using the segmented diode. By exchanging the samples and agar gels, transfer functions of different configurations can be analysed. The fundamental components, control & acquisition protocols and circuitry are detailed in the following sections.

One of the main parts, is the sample holder on which different samples can be mounted. The sample holder is suspended using a torsional beam which enables a rotation around the axis of the suspension rod (blue indicator). Different samples can be attached to the sample holder. Optionally, the attached samples can be immersed within an exchangeable environment such as viscoelastic hydrogels, water or just freely vibrate in air. A planar coil is mounted on top of the sample holder. Inside \mathbf{B}_0 , a current through the coil induces a torque. This current can be externally driven, which allows the precise control of amplitude and frequency. Alternatively, the current path can be shorted and due to gradient switching a gradient-induced current leads to vibration. Furthermore, the current path can be opened. This enables the characterisation using the external current source, and after electrically detaching the coil, the gradient-induced vibration due to a mounted sample can be measured. A mirror on top of the coil enables the reflection of a laser beam, which is used to measure the vibration. This vibration is detected using a segmented photodetector. The laser source and photodetector are both outside \mathbf{B}_0 which guarantees the MR compatible operation of the setup. The signal of the photodetector is amplified, digitized and then further processed using digital signal processing tools. Furthermore, the control of an external frequency generator allows to produce a precise current and thus

torque which enables to implement automatic control routines to measure the transfer function of different beams within different viscoelastic environments.

4.2. Optical unit

4.2.1. Laser module

One of the main components of the probehead is the laser module, equipped with an actuator stage for laser beam positioning. The deployed single-mode laser source emits at 635 nm, has a divergence of smaller than 0.5 mrad^2 and an output power of 0.4 W. The housing material is aluminium, which provides shielding and mechanical stability. The laser-beam profile is displayed in figure 4.3. The relative intensity distribution was measured using an 8-bit camera. The high dynamic range is obtained by varying the exposure time and the intensity matrix I was calculated using the slope of intensity obtained from pictures X with respected to varying exposure times t_k :

$$I_{i,j} = \frac{X_{i,j,k+1} - X_{i,j,k}}{t_{k+1} - t_k}, \quad X_{i,j,t} \in \{5, \dots, 250\} \quad (4.1)$$

The exposure time was logarithmically increased from $t_1 = 0.037 \text{ ms}$ to $t_{18} = 100 \text{ ms}$.

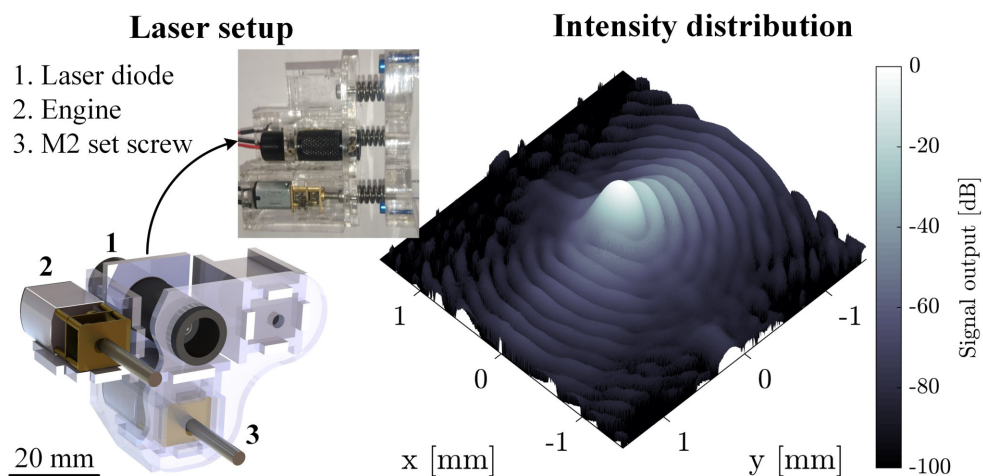


Figure 4.3.: Mechanical setup of laser module and intensity distribution of the laser beam.

The laser was mounted on PMMA-based framework which had two engines integrated for x-y-positioning. These brushless DC motors³ allow straightforward control. The large transmission ration yields slow angular speed for accurate adjustment as well as large torque to drive the M2 screws. Compared to stepper motors, brushless DC motors, in principle, can reach any angular position which allows for very fine precision.

²PICOTRONIC DD635-0.4-3(12x38)-DOE

³G1000 Sol Expert 1:1000 1 - 15 U/min 6 VDC

The minimal translation deflection Δx can be estimated using equation 4.2. Here the number n is the minimum number of rotations per minute. In general, with shorter actuation time any desired position can be achieved. With this setup I could reach minimum translation deflection of $3 \mu\text{m}$. Of course, there are limitations such as minimum latency time of the engine, but for this approach this low-cost solution yielded perfect results.

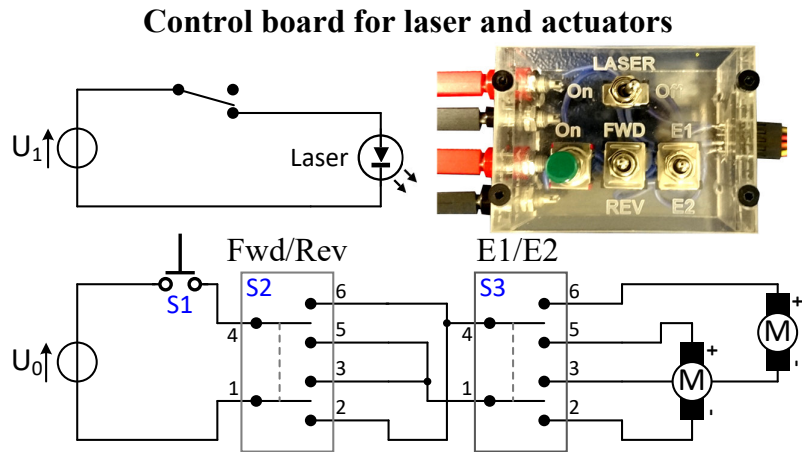


Figure 4.4.: Circuit diagram and image of control board for laser positioning.

$$\Delta x_{min} = \underbrace{\frac{400 \mu\text{m}}{360^\circ}}_{\text{Lead of M2 Min. rpm}} \underbrace{\frac{n \cdot 360^\circ}{60 \text{ s}}}_{\text{rpm}} \Delta t_{min} \quad (4.2)$$

To control the laser and the engines a simple control board was developed which is illustrated in figure 4.4. The two actuators driving the M2 screws are used to adjust the x- and y-direction of the laser beam. Rapid switching to separately control the motors is enabled through the control board, which furthermore allows the user to switch between forward and reverse mode. The push button enables the actuation during short time intervals which enables the user to adjust for small strokes.

4.2.2. Detection unit

4.2.2.1. Specifications and methods of operation

A segmented diode, is used to measure the deflection of a laser beam. The diode is a small gap sensor with a sensitive area of 1 mm^2 and a gap of $16 \mu\text{m}$ as shown in figure 4.5⁴. The diode is operated with a reverse bias voltage $U_{bias} = 3.3 \text{ V}$. The characteristic rise time allows the operation at frequencies up to 1 MHz. There are two modes of operation possible: The first option is to operate the diode within a close-loop circuit in which the diode-signal is used as feedback signal to control the laser point position to impinge at the centre point of the segmented diode. This is realised by active control of one reflection mirror, which is mounted on an actuator. The signal to adjust the actuator is the actual signal. This approach has the big advantage of huge dynamic range for deflection measurements. However, this comes at the expense of complexity for the control circuit. Piezoactuators

⁴First sensor QP1-6 TO

could deliver the required speed, however, they require large driving voltages up to 100 V. This requires (i) high voltage amplifiers with large bandwidth and (ii) an implementation of a stable control circuit which delivers the required bandwidth. The second option is to measure the laser beam deflection as a function of the output of the four diode segments. This approach is straightforward and the signal output from the diode can be directly processed. The disadvantage is the non-linearity of the signal output with respect to the laser position which requires the characterization of the laser beam position vs signal output on the optical bench. The advantage of this approach is the fact that the bandwidth is in first place limited by the photodiode. Limitations by modular second stage amplifiers and digital acquisition devices can easily be updated. Due to this modularity the second approach was selected. Therefore, the transfer function of the laser-beam position and diode output has to be evaluated.

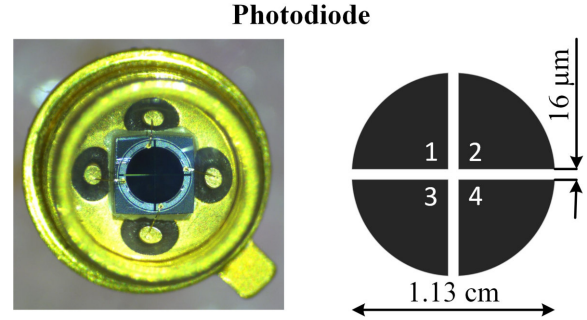


Figure 4.5.: Dimensions of the segmented photodiode

4.2.2.2. Characterisation of transfer function

There is a characteristic signal composition obtained from the four diode outputs, dependent on the laser beam position on the segmented diode. The signal output $S_i(x, y)$ of the i^{th} diode element is a function of the displacement x and y of the laser spot with respect to this diode element. In mathematical terms, the detector output $S_i(x, y)$ is the result of the convolution of the detector surface $A_i(x, y)$ with the intensity distribution $I(x, y)$.

$$S_i(x, y) = A_i(x, y) * I(x, y) = \int_{-\infty}^{\infty} \int_{-\infty}^{\infty} A_i(u, v) I(x - u, y - v) dudv, \quad A_i \in \{0, 1\} \quad (4.3)$$

In this mathematical model, a simple detector surface is emulated with a weighting function $A_i(x, y)$, which equals one where a detector element is existent, else this function equals zero. This is visualized in figure 4.7 where this binary weighting function is displayed as white quarter circles. On the basis of the simulation results, different detector orientations could be tested to find the best orientation for optimal configuration. Since trajectories originating from vertical movement of the laser beam are expected to be of majority, the optimal detector orientation was selected, which delivered sensitivity with the largest field-of-view. This optimal orientation between laser source and detector orientation is shown in figure 4.7, with the main motion along the y -axis. The comparison of simulation to experimental results reveals major differences at the centre and the outer regions. The circle-shaped enhanced signal in the centre, visible in all segments, originates from current leakage between the diode segments. This leakage leads to an increased signal level of approximately -30 dB. Differences

Setup on optical bench

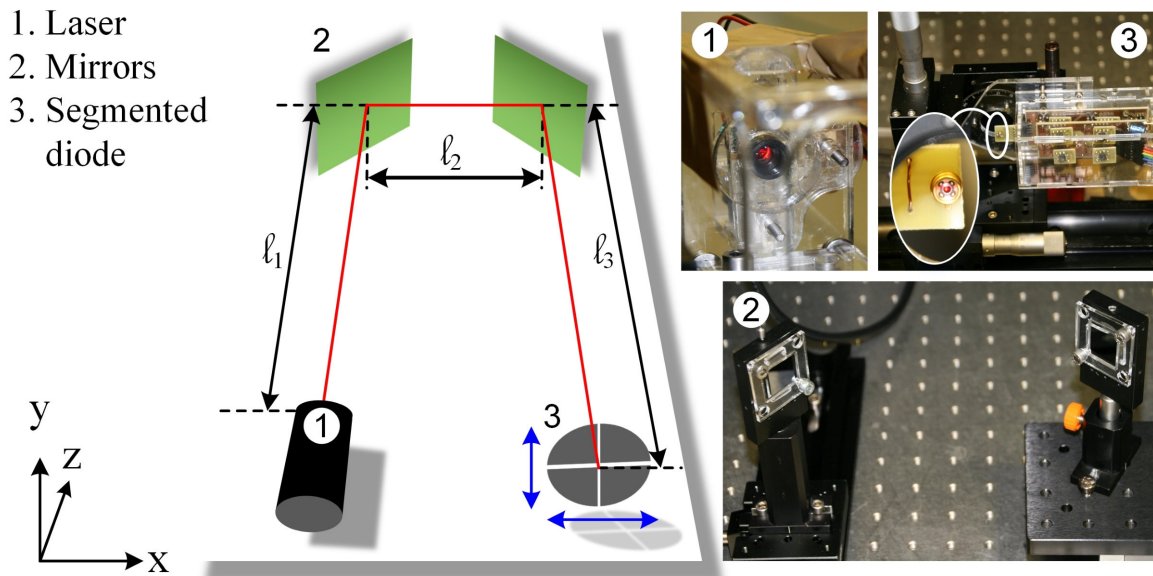


Figure 4.6.: Calibration setup on the optical bench. The laser beam is fix and the detector is moved vertically and horizontally with a field of view of 3 mm in each direction. The signal to each corresponding position is acquired. The total distance $l_{tot} = l_1 + l_2 + l_3$ between laser source and detector surface equals the distance in the final probe configuration. The blue arrows indicate the detector movement during the characterization procedure.

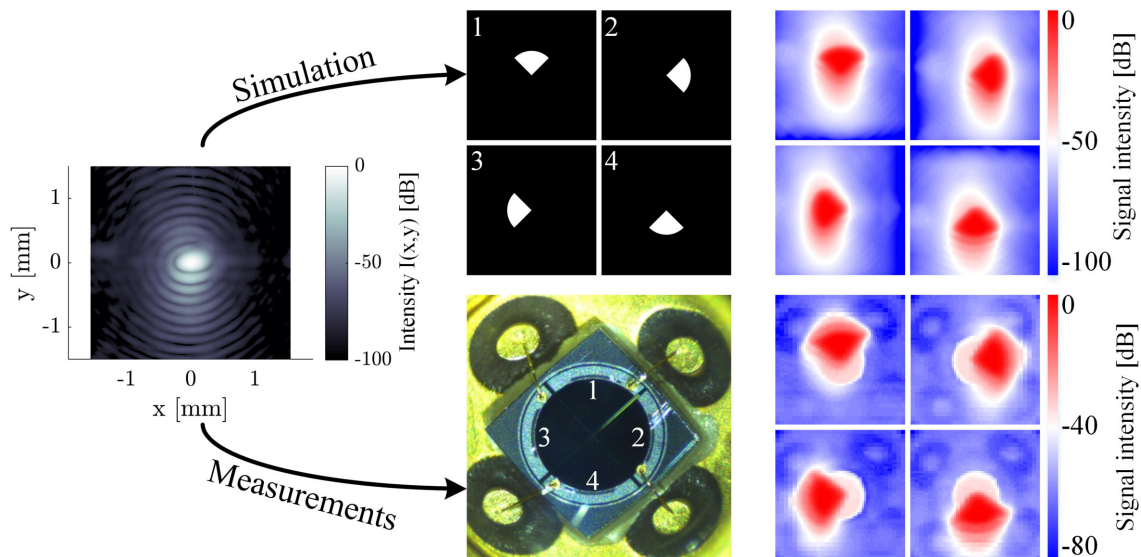


Figure 4.7.: Results of simulated and measured signal output of all four diode segments depending on the laser beam position. Back reflections from the contact pads are clearly visible. All display items have the same scale except the photograph of the photodiode which is slightly enlarged.

between simulation and experiment at the outer regions arise from reflections of light in the real system. In the experimental transfer matrices, the reflections from the contact pads can be clearly identified as regions with increased signal. Hence, using simulation-based transfer matrices for subsequent positioning in the real system would result in large positioning errors. The data for the discrete transfer matrices $S_{i,k,l}$ were acquired manually by vertical and horizontal displacement of the segmented photodiode by ± 1.5 mm in each direction. Here, i stands for detector segment, k for the matrix element in x -direction and l for the matrix element in y -direction. Data recordings were conducted every $50 \mu\text{m}$ within the range of ± 1 mm and every $100 \mu\text{m}$ for remaining positions. This led to a total of 2601 data points per diode segment. The centre reference point was set for equal signal from all segments. Figure 4.8 shows the measured signal as function of vertical displacement. Very high displacement resolutions are obtained within areas where the gradient of the signal is very high. One of these areas is located in the centre of the segmented diode where the slope reaches $80 \text{ mV}/\mu\text{m}$. An ADC with a vertical resolution of 5 mV enables a displacement resolution of 62.5 nm .

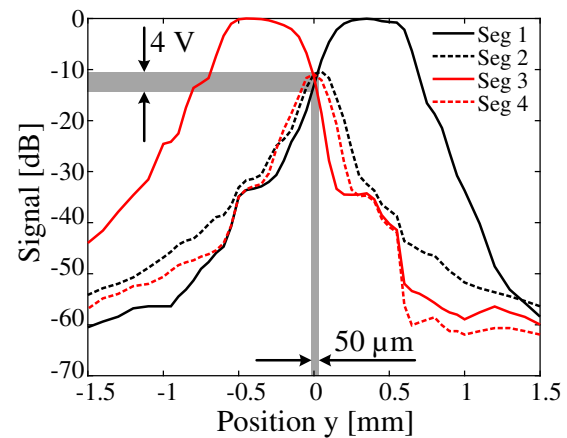


Figure 4.8.: Signal output of the diode elements along the vertical axis at $x = 0$ mm.

4.3. Amplifier circuit

The voltage levels shown in figure 4.8 of the previous section, are in the order of volts. This output voltage is achieved using a two-stage amplifying circuit which translates the photocurrent into a high-voltage signal of $\pm 20 \text{ V}$. A schematic of the electric circuit is displayed in figure 4.9. In this figure the amplifiers are shown for one diode segment. A high voltage output provides a large flexibility to use a wide range of available ADC's. This is due to the fact that most ADC's have a fixed input range, and down conversion using a simple voltage divider is much easier and flexible compared to up conversion. The circuit requires a supply with $\pm 24 \text{ V}$. Three voltage regulators are used to provide the further internal voltage levels. Two of regulators are used to provide the voltage supply for the first stage LNA (OPA381, TI). This amplifier delivers an output of $\pm 1 \text{ V}$ between full and no illumination of the photo detector. To obtain a negative voltage output when no photocurrent is available, the positive input of this LNA is biased with $+1 \text{ V}$ which results in an output of -1 V when there is no illuminance. One segment of the photodetector

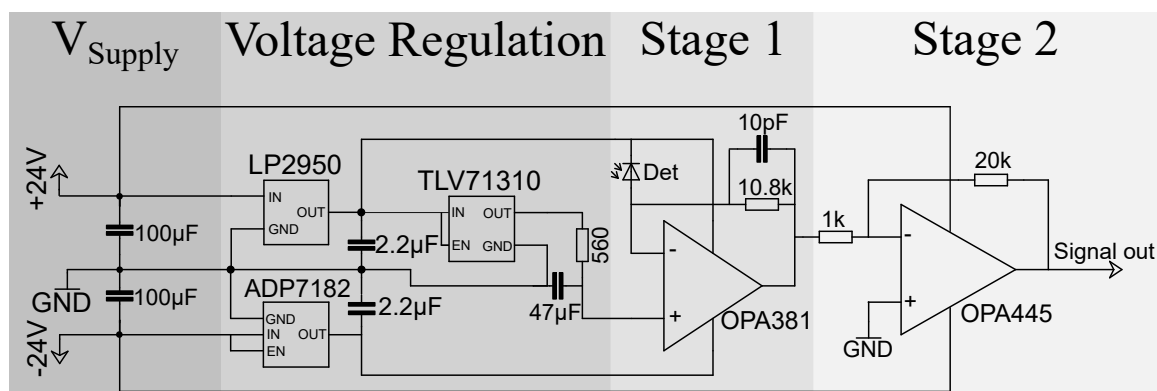


Figure 4.9.: Two-stage amplifier circuit for signal of photodiode. The circuit shows the LNA'S for one segment. The total circuit contains 8 LNA. (Adopted from [EF09] ©2017 IEEE).

delivers $180 \mu\text{A}^5$, and at full illuminance this amplified with $\Delta U = 2 \text{ V}$ using a $25 \text{ k}\Omega$ resistor which results in a voltage output of 1 V . The second stage amplifies this voltage to $\pm 20 \text{ V}$ using a high-voltage amplifier (OPA445, TI). The OPA445 is driven in a 20-fold voltage amplification mode which corresponds to 26 dB. The bandwidth limitation of the circuit, is due to the OPA381. In the driven mode is has a 3dB cut-off at 75 dB amplification at 10 kHz. Larger bandwidths could be achieved by replacing the OPA381 with another high voltage LNA or by using more amplification to the second stage.

4.4. Mechanical design and assembly

4.4.1. Front end

The front end constitutes one of the most important parts, which contains the sample holder with the mirror and exchangeable samples, the agarose gel/water container and the adjustment mirror. Figure 4.10 illustrates the basic components of the front end, which is designed to enable the user to conduct rapid sample and agarose gel exchanges as well as the coarse adjustment of the reflected laser beam. Important for the rapid exchange of components are the side walls with three slots per side wall. A 45° -slot accessible from the bottom enables the rapid installation and mounting of a agarose gel/water container using two screws. The horizontal slot in the middle provides the mechanical adaption for the sample holder. All sample holders consist of the suspension rod, sample interface, sample frame, coil and the mirror. Different sample holders were fabricated using various suspension rods leading to a variation of spring constant. The upper 45° slot of the sidewall allows the installation of the mirror to adjust the back reflection of the laser beam using four adjustment screws. On the right side of figure 4.10 a cross section image of the assembled version is displayed, which shows the laser trajectory and the coil orientation with respect

⁵Some power of the laser beam is absorbed after the beam experiences reflection from two silicon nitride mirrors.

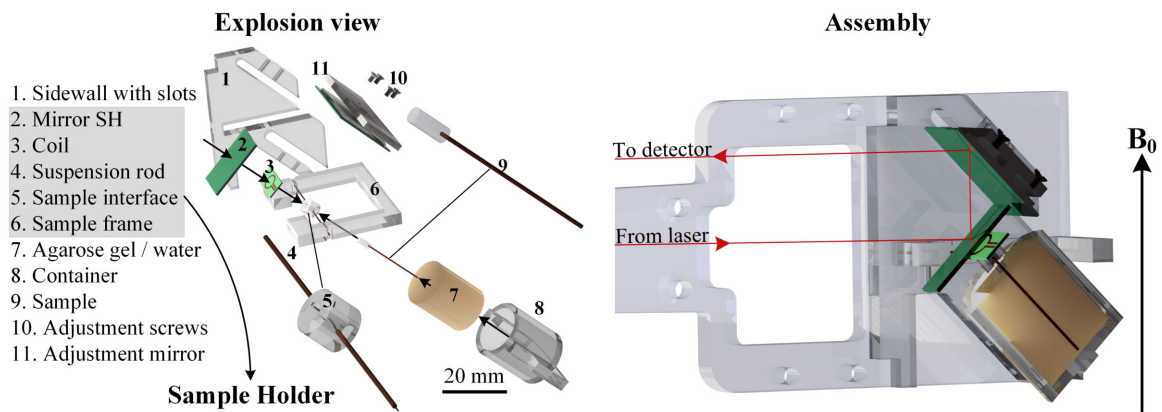


Figure 4.10.: Composition of the front end. Left: Explosion view to expose the functional parts. Right: Cross section of the assembled front end.

to \mathbf{B}_0 . The mounting of the coil at 45° with respect to \mathbf{B}_0 enables the user to test vibrations triggered by MR sequences, as well as testing vibrations triggered by an external current supply. All parts which have larger cross section areas such as the side walls or mirrors are fabricated using "non-magnetic" (low susceptibility) and non-conductive material to avoid parasitic vibrations induced by eddy currents in these components. This is especially important for the mirror installed on the sample holder, because any additional torque created by this mirror would falsify the results. Instead of using conventional metal-based mirrors, squared pieces of silicon nitride wafers were used as reflective surface. A photograph of different sample holders, samples and containers is provided in figure 4.11.

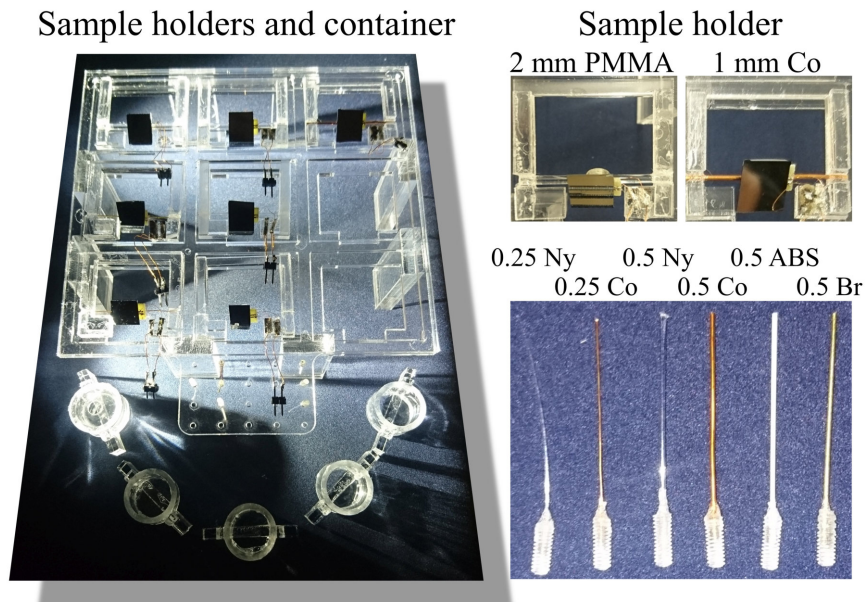


Figure 4.11.: Different type of sample holders, samples and containers arranged on a rack.

A sample holder consists of a mirror, two coil suspension rods, the sample interface and

the sample frame. The sample interface and the sample frame are fabricated through laser cutting of 4 mm PMMA sheets. The coils are obtained using a standard PCB fabrication method and subsequent cutting. In a further step, the sample interface was equipped with two bore holes. An M2 thread is cut into the axial bore hole for mounting of different samples. The other bore hole allows the mounting to the suspension rod. In a next step, the coil, the suspension rod and the mirror are adhesively attached to the sample interface and cured overnight.

Small rods are applied to mimic the shaft of implants. All rods have an equal length of 24 mm. The head parts are M2 threaded rods, which are prepared with a bore hole of 4 mm at one end. The small rods are attached adhesively using two component adhesive and cured overnight. In general, a wide range of different samples can be prepared such as a rod with added weight at the tip.

4.4.2. MRI module

The MRI module is another type of container, which is equipped with an RF coil and a tuning and matching circuit. The outer diameter of the container is reduced with 14 mm

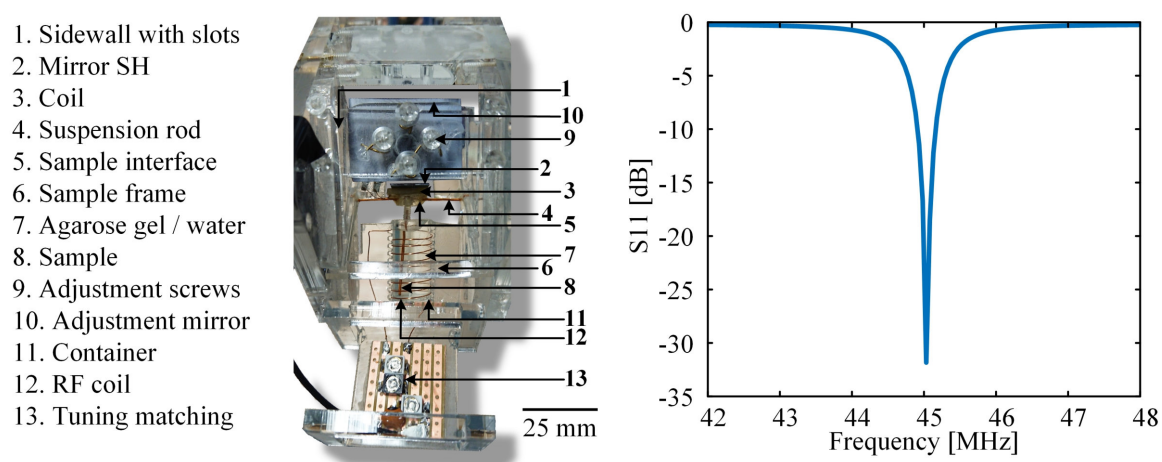


Figure 4.12.: Container with integrated RF coil which enables simultaneous MR acquisition and vibration detection. Tuning and matching capacitors are distant from the coil, to ensure best possible field homogeneity. On the right side are the S11 parameters for the coil without water filling, tuned and matched to 45.03 MHz.

to enable the fabrication of a coil with a smaller diameter. Using 0.5 mm isolated copper wire, a hand-wound RF coil was fabricated using 8 windings, 14 mm diameter and a length of 25 mm. This container is compatible with the sample holder and sidewall slots, and it enables laser-based vibration measurements simultaneously to the standard MR acquisition procedure. To maintain the field homogeneity, it is important to place the capacitors distant to the MR image region. In figure 4.12 most important components, including the RF coil and a S11 measurement, are illustrated and tagged. All materials are MR compatible, to ensure best possible signal integrity. The capacitors, however, yield

large B_0 -field distortions in close proximity to the RF coil. Therefore, they are mounted in safe distance to the region of interest.

4.4.3. Full integration

All components are fully integrated on a framework which is adapted to fit the 1 T permanent scanner. The fully assembled probe is displayed in figure 4.13. The load-bearing

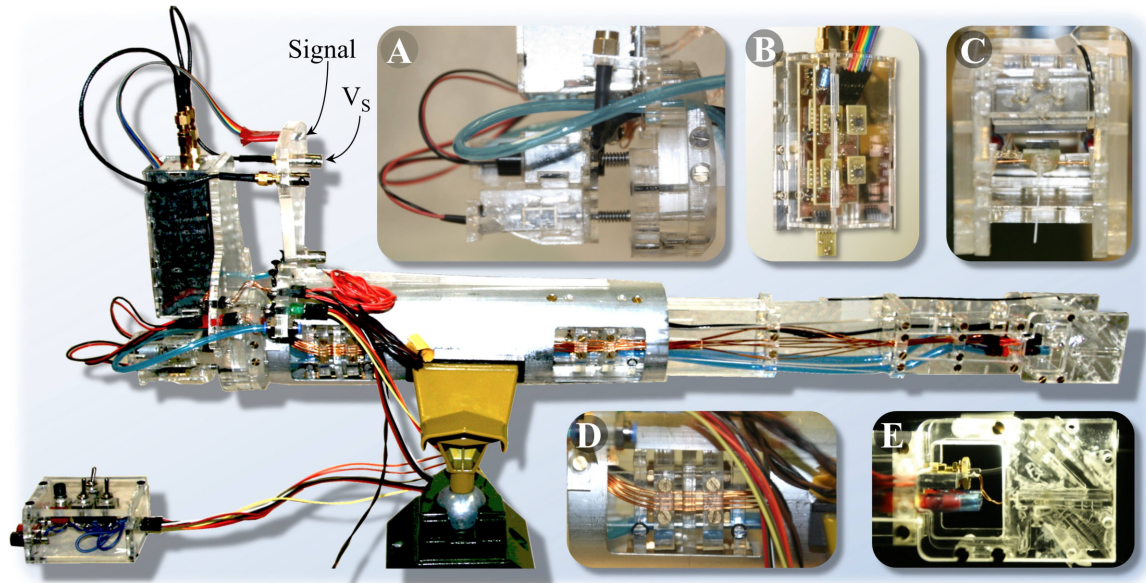


Figure 4.13.: Full assembly of the vibration probe. A) shows the integration of the laser module. B) displays the amplifier stage with the integrated photo diode (circuit without shielding). The two-stage amplifier is realised with a stacked PCB. This module is mounted above the laser module (with shielding). C) Front view of the front end with ABS sample. D) Side view of mechanical frame with exposed view to DC lines and fluid line. E) Side view of the front end with exposed view of interfaces for DC supply, fluid interface, RF connection and sidewall slots.

component is an aluminium tube with 70 mm outer diameter, that matches the MR bore with little slackness to ensure tight fitting when inserting the probe. The laser and amplifier stage are mounted at the rear end of the probe, leaving these components outside the electromagnetic fields, which guarantees proper functioning, also during MR acquisition procedures. Several feed-troughs are integrated for different potential applications such as two fluid lines, 8 DC (or low-frequency) lines and one RF line. The inner frame is mounted on a mechanical low-pass filter using pendulum suspension in x-y-direction and spring suspension in z-direction using elastic polymer rings.

4.5. Software: Control and acquisition interface

Another important engineering process, besides the hardware development, is the development of software components for experimental control, computation of the deflection angle

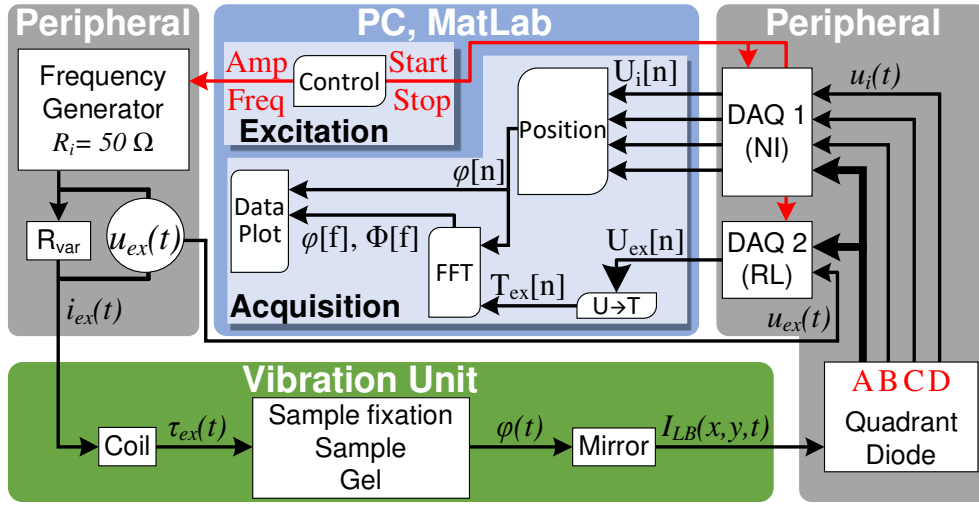


Figure 4.14.: Interfaces between the software components, peripherals and the mechanical setup. The angle ϕ represents the angular deflection of the mechanics, and the angle Φ the phase shift of the signal in the frequency domain. (Adopted and modified from[EF05] ©2019 IEEE).

and post-processing algorithms to determine the transfer function of the beam vibration. The entire signal flow chart including data processing and control structures are presented in figure 4.14. There are three main components illustrated in this flow chart diagram. This is (i) the vibration unit which represents the front end (or the mechanical object being measured), (ii) the peripheral devices (the digital data acquisition devices (DAQ) and the frequency generator) and (iii) the software components realised with MATLAB. Each component transforms an input variable into an output variable. The coil, for example, is a transducer that transforms the applied external current $i_{ex}(t)$ into a torque $\tau_{ex}(t)$ and the sample holder (including the beam) transforms the torque into a measurable deflection $\phi(t)$. The torque is governed by the following equation:

$$\vec{\tau}_{ex}(t) = \hat{i} \sin(2\pi ft + \Phi) \cdot \vec{A}_{coil} \times \vec{B}_0 \quad (4.4)$$

Hence, one can easily control the frequency and amplitude of the torque by controlling the current. Whereas the mechanical aspects are detailed in figure 4.2 and in chapter 5.1, the concepts of the software-based transformations are explained in the following sections. There are in general three types of vibration experiments: Measurement of spring constant, measurement of transfer function and vibration measurements during common MR sequences. The software properties will be explained based on the first two type of experiments, but the acquisition mode during MR acquisitions is very similar. As one can see from figure 4.14, there are two important transformations required in the PC domain. This is (i) the computation of the deflection angle that transforms the digitized diode signals $U_i[n]$ into a deflection angle $\phi[n]$, as well as the computation of the Fourier transform and the subsequent display of the data.

4.5.1. Position computation

An integral part of post-processing is the computation of the discretised angular deflection $\phi[n]$ based on the voltage signals obtained from the segmented diode. The basis for this operation are the transfer or signal matrices $S_i[x,y]$ obtained on the optical bench and

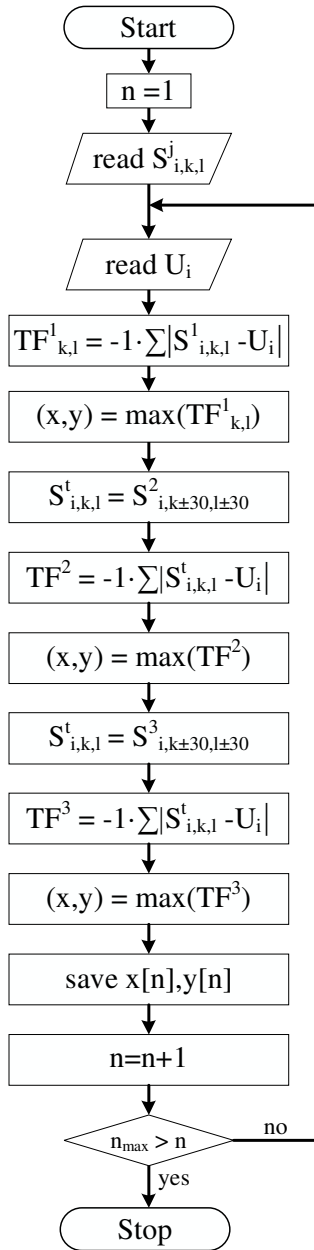


Figure 4.15.: Flow chart for positioning using a refining grid. In this flow chart three iterations are considered.

presented in figure 4.6. As shown in figure 4.8, the resolution can be below 100 nm with a total field of view of 1.5 mm in each direction. After the diode signals are digitized, the general task is to find the position $x[n]$ and $y[n]$ of the laser beam at time point $[n]$ using the four diode signals $U_i[n]$. One possible solution to solve this problem is to find a global two-dimensional polynomial function of n -th order for each signal matrix, which fits the measured results to an acceptable accuracy. This solution, however, was not promising since even up to 8th order polynomial functions did by far not provide the required slope to fit the data points. The second option is a numerical solution. A standard look-up-table (LUT), however is not feasible, since the large FOV in combination with the high-resolution requires large matrices. Besides the computational power, this approach requires many discrete sampling points for calibration. A further problem is the lack of position repeatability during the characterisation measurements on the optical table which yields measurement errors in the LUT. For example, a resolution of 100 nm within a range of $\pm 100 \times 100 \mu\text{m}^2$ and of 1 μm in the rest of the matrix requires a LUT with 4×3.24 million data points. The characterisation as well as the utilisation of such a huge LUT would yield unacceptable processing times. The methodology to overcome the problem of accuracy as well as speed will be explained in two steps. The first step explains how to find the approximate position using the signal matrices $S_i[x,y]$ obtained from the characterisation. In a second step, grid interpolation around this point allows to determine the actual point more accurately. Mathematically, the position (x, y) of the laser beam at a certain time point n is obtained by using equation 4.5. A visualisation of equation 4.5 is given in figure 4.16. To find the location of the laser beam one can utilize the the fact that the absolute value of the difference of U_i and the corresponding matrix $S_{i,k,l}$ yields a transfer matrix $TF_{i,k,l}$ of which all matrix elements approach zero for the entries that equal the input signal. The location of the laser spot is then at

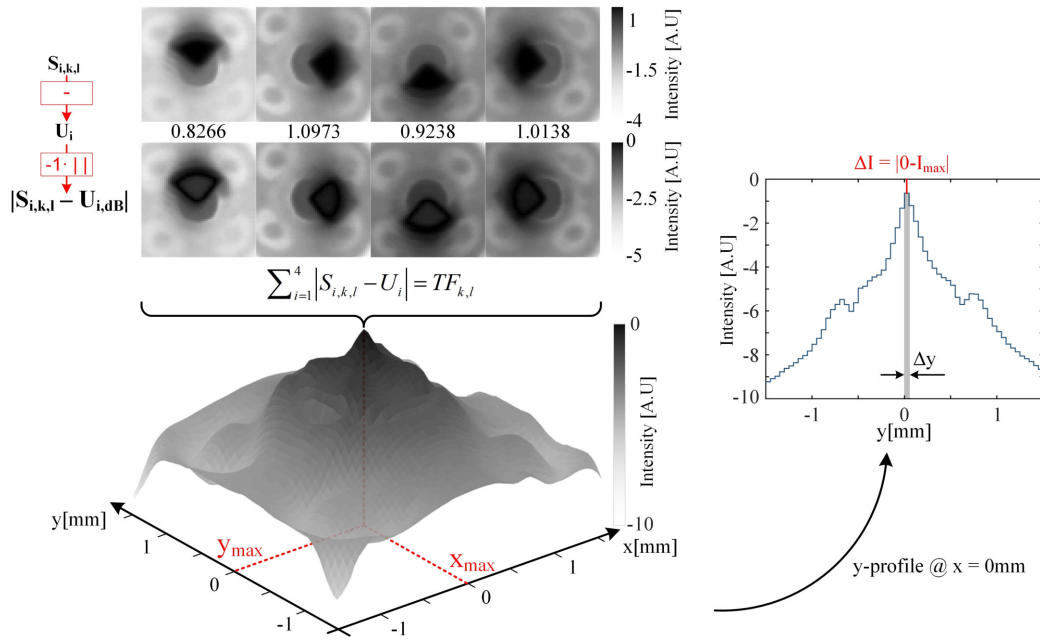


Figure 4.16.: Visualisation of position determination by finding the maximum of the sum of all transfer. Left: All four images in the top row are representations of the signal matrices. The row beneath displays the absolute values of the difference between the elements of the signal matrices with the actual voltage the corresponding diode segment. The sum of all four matrices will be closest to zero at the true position of the actual laser beam. Right: The resolution depends on the grid size of the matrix and the computed intensity will be only be zero in the unlikely event when the true laser position meets a grid point. The offset from zero ΔI , however, can be used as an estimator for the distance of the true location from the discrete grid element.

$$\begin{aligned}
 (x_{max}, y_{max}) &= \arg \max \left(-1 \cdot \left(|S_{1,k,l} - U_1| + |S_{2,k,l} - U_2| + |S_{3,k,l} - U_3| + |S_{4,k,l} - U_4| \right) \right) \\
 &= \arg \max \left(-1 \cdot \left(TF_{1,k,l} + TF_{2,k,l} + TF_{3,k,l} + TF_{4,k,l} \right) \right) \\
 &= \arg \max \left(TF_{k,l} \right)
 \end{aligned} \tag{4.5}$$

the index k, l where the sum of all four matrices $\sum_{i=1}^4 TF_{i,k,l} = 0$. The handling for input parameters which are derived from data that are subject to measurement uncertainties and discretization is very advantageous with this method. Solving a set of linear equations which are overdetermined based on measured data inputs, results most likely in an unsolvable equation system due to an empty solution set. For example, the intersection of two circles which are tangent to each other may vanish because the discretization process relocates them such that the intersections vanishes. Here, the application of equation 4.5 is advantageous, because searching for a maximum value is less restrictive than searching for concrete solution. This makes the algorithm robust against uncertainties and ideal for finding the position based on discretised data. Since the original

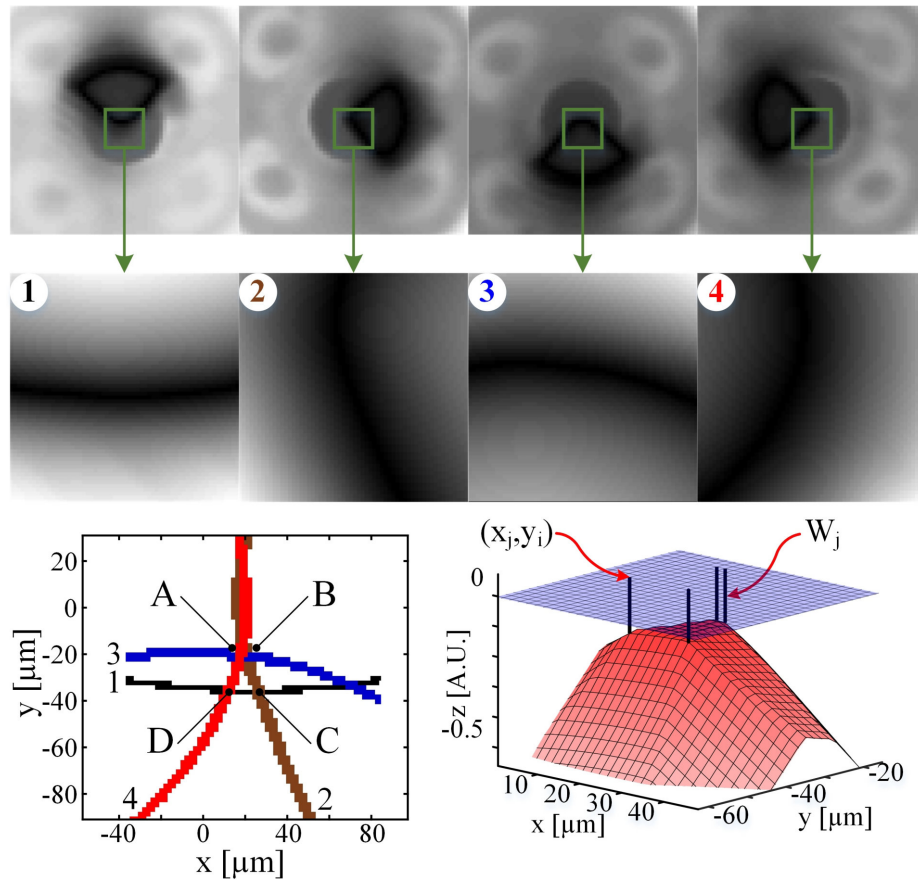


Figure 4.17.: Computation of fine resolution using transfer matrices for one exemplary laser position. Top Row: Global matrices $TF_{i,k,l}$. Second Row: Zoom in potential laser spot position. Bottom left: Lines of maximal values visualized after binarisation of $TF_{i,k,l}$. The intersections obtained from different diode segments leading to the following index combinations: 3,4 \rightarrow A; 2,3 \rightarrow B; 1,2 \rightarrow C; 1,4 \rightarrow D. Bottom right: The four positions are weighted by the distance to the zero plane, which enables the computation of the most probable position.

matrix $S_{i,k,l}$ is only discretised with a resolution of $50 \mu\text{m}$ further processing is required to increase the resolution down to two- or three-digit nanometre range. The straightforward approach is to interpolate the available matrix to obtain a grid with the required resolution. This approach, yielding one large matrix, would lead to many unnecessary additions. For example, a matrix with 3.24 million entries would require $5 \times 3.24 \text{ million} = 16.2 \text{ million}$ operations per time data point, which would result in an unacceptably slow processing speed. The solution is a zoom-in technique, in which the approximate position is computed on a coarse grid and subsequently a new more accurate position is computed using a finer grid of the neighbourhood at the first position. In principle this routine can be repeated n times for any desired resolution. The original grid has 3721 elements with 61 entries in each direction. For faster processing the four-stage process was implemented with 400 nm resolution. An optional fifth iteration step for 100 nm res-

olution is integrated, however, at the expense of longer computation time. Due to the limited measurement accuracy as a result from the characterisation on the optical bench,

Table 4.1.: Combination of indices to compute W_j , x_j and y_j

j	i	i^*
A	3	4
B	2	3
C	1	2
D	1	4

the computation of the position delivers different results if we straightforward search for the maximum value of $TF_{k,l}$ with increased resolution as shown in equation 4.5. This effect is demonstrated in figure 4.17. Here the computation is illustrated at the example for a certain laser position. In this figure, one can see the matrix elements with largest values of each diode segment which represent the potential positions of the laser spot. An ideal measurement would result in an intersection of all four lines at one position leading to $TF_{k,l} = 0$. Due to measurement inaccuracies and discretization, however, the four maxima are located at

different matrix elements k and l . Therefore, the most probable position must be between these points. To compute the most probable point, the intersection points A, B, C, D of each neighbouring diode segment are determined by searching for the location of the maximum position (x_j, y_j) . The difference from zero of the value at each maximum position yields a weighting factor W_j with $j \in A, B, C, D$ which is given by:

$$W_j = \frac{1}{0 - \max(TF_{i,k,l} + TF_{i^*,k,l})} > 0 \quad (4.6)$$

The larger this difference, the less the probability of this point to represent the correct position. Subsequently, the actual position (x, y) is computed using the weighted sum of the four maximum points (x_j, y_j) using the weight W_j :

$$x = \frac{\sum_{j=A}^D x_j W_j}{\sum_{j=A}^D W_j}, \quad y = \frac{\sum_{j=A}^D y_j W_j}{\sum_{j=A}^D W_j} \quad (4.7)$$

In conclusion this presented zoom-in technique to find the position of the laser spot is accurate and fast, with a large dynamic range (FOV: 3 mm, resolution 100 nm). The zoom-in technique reduces the number of operations to approximately $5 \times (5 \times 3721) \approx 93000$. This is approximately 160 times less compared to the 16.2 million operations which were required using the full matrix approach, and hence results in tremendous time saving. The code for computing the location is presented in the appendix A.2.

4.5.2. Timing parameters and computation of Fourier transform

Rapid and precise measurements of the transfer functions for amplitude and frequency sweeps are realized using post-processing techniques. To reduce the size of the raw data also the acquired data was optimized. Transfer functions are measured in the continuous-wave CW mode. The control of external excitation (see equation) allows one to optimally adjust the acquisition duration and sampling rate to minimise the raw data size while acquiring low noise data.

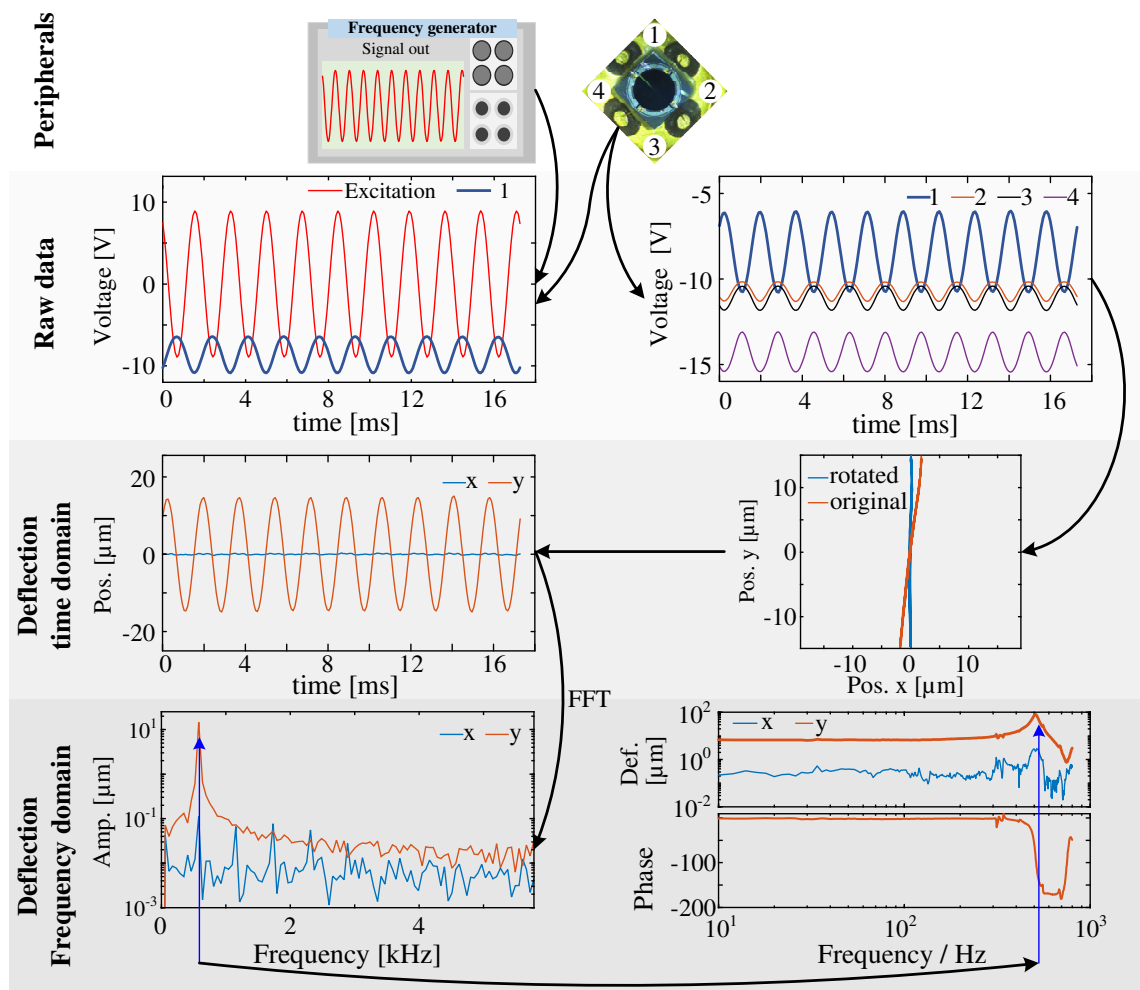


Figure 4.18.: Schematic of the post-processing to obtain the transfer functions using continuous-wave mode. Illustrated is the acquisition of a single frequency data point for the final transfer function. Top: The excitation signal and the photo diode signal are recorded using two different acquisition devices. Synchronisation is obtained by splitting the signal of one diode segment. Second row: Plot of the raw time domain data as recorded with both acquisition devices. Third row: Transformation from voltage signals to position detection. The trajectory of the mechanical vibration is in general not perfectly vertically aligned due to mechanical misalignment. Therefore, the signal is aligned before further post-processing to separate vertical and horizontal mode. Bottom row: The amplitude of the vibration frequency is obtained in the frequency domain using an FFT. The noise floor is below 100 nm which allows precise measurement. The bandwidth here is 6 kHz (max. 24 kHz depending on sampling rate of external DAQ's).

As explained in section 4.5.1 the computation for one position data point requires approximately 100 k operations which yields a processing time of under 0.5 ms. To measure the transfer function in continuous-wave mode, the sample is excited using an externally applied current (see equation 4.4), which enables precise amplitude and frequency adjustments. Timings of excitation and acquisition process per frequency data point are software controlled which allows the acquisition duration of exactly 10 periods

per frequency with 200 data points. The processing pipeline to compute one data point is illustrated in figure 4.18. It takes approximately 125 ms to compute one frequency data point of the transfer function using the presented algorithm, hence it takes approximately 60 s for 500 frequency data points. These values are obtained on a dual-core Intel CPU with 2 GHz (M-5Y10c CPU) with 8 GB RAM. The code is not parallelised. The acquisition is timed in two blocks: A Transient phase with a settling time of 0.5 s, to obtain a stationary vibration after frequency/amplitude switching, followed by an acquisition phase which lasts for $10/f_i$, where f_i represents the i -th frequency. The frequency data points range from 10 Hz up to maximal 10 kHz with steps of 2, 5, or 10 Hz. Hence, the total acquisition duration ranges from one minute (10:10:1000) up to 42 minutes (10:2:10000). The average acquisition duration per transfer function was approximately 3 minutes, which enabled to measure 10 samples an hour including sample exchanges. Before each measurement, the laser spot has to be focused at the centre of the diodes in order to obtain best possible resolution. This is performed after the installation of the fully assembled probe, using the x-y-controller and a live GUI, which displays the current laser position with a precision of 10 μm . The positioning duration is approximately one minute.

4.6. Benchmarking

Benchmark test are conducted to investigate the functionality of the optical detection (computation of trajectory) unit and the RF functionality which are both presented in the following two sections.

4.6.1. Optical detection

A first long duration test was conducted to investigate the long-term behaviour of the optical unit and to measure the difference of using high-resolution detection and low resolution detection. Drifting occurred during the settle time of the linear stage. This behaviour was in agreement with measurement using the CCD camera system. A second test was conducted to measure the reliable field of view for position encoding. It is expected that in the centre area a reliable encoding takes place, however, it has to be tested to what extend the outer regions yield reliable position encoding. This is important because at the outer regions the diode signals are weak and reliable encoding is not guaranteed. The measurement results displayed in figure 4.20 show that within an ellipse oriented along the y-axis reliable encoding is enabled. This surface encompasses the entire FOV of 3 mm along the y-axis and 1.5 mm along the x-axis. This enables the accurate measurements for all samples, especially since the rotational axis of the sample holder is adjusted such that the common trajectory of vibration is along the x-axis. The ellipsoid surface is a result of the laser spot anisotropy, hence, the laser is positioned in this way to achieve maximum FOV along the y-axis. On the basis of this results, the crucial step of centre positioning before each measurement is understandable. The best results are obtained when the laser

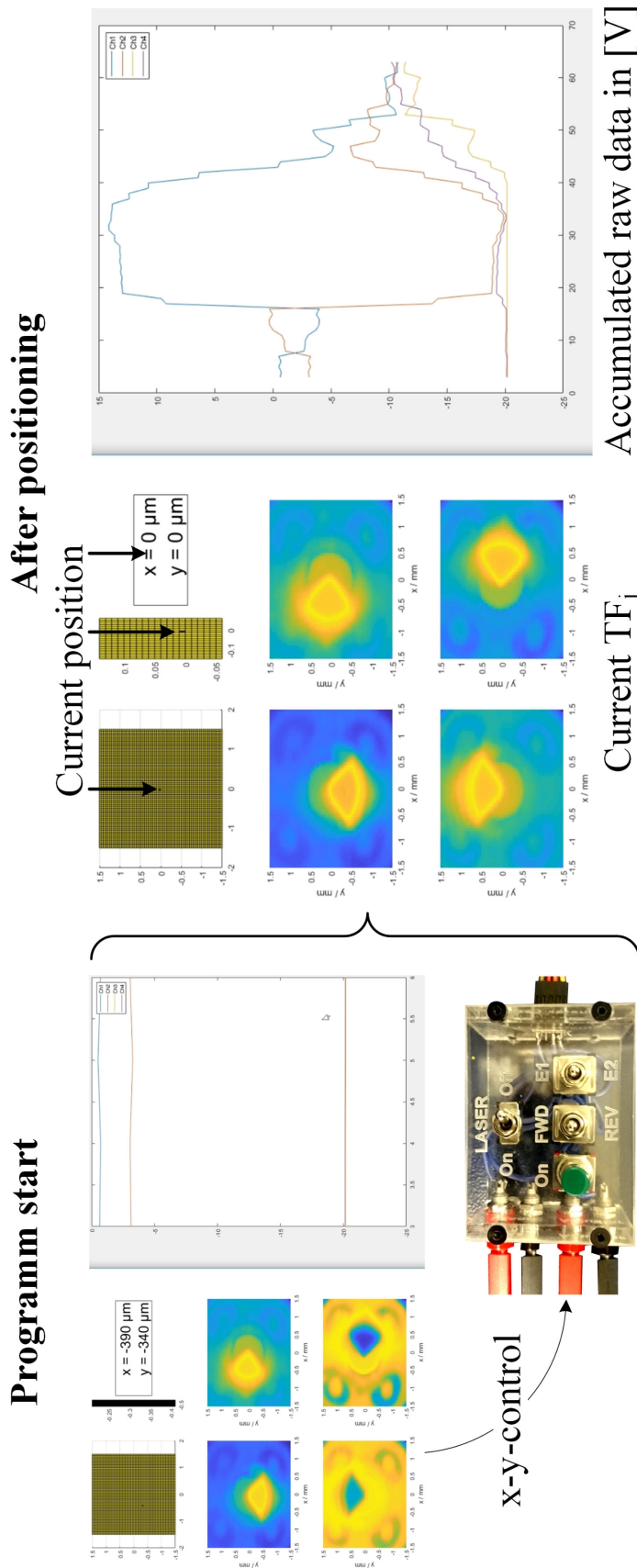


Figure 4.19.: Screenshots from initialisation process. Left: Position at beginning is at (-390,-340). Using the controller one can hover the laser spot towards the high sensitive centre. Right: The laser spot after positioning is exactly at the centre (0,0). The GUI displays the current position of the laser spot on a grid and in numerical values. Furthermore, the current matrix values TF_j of the individual segments are implemented and the history of the raw data. The latter two display items support the troubleshooting in case the current positioning may be impaired through illumination errors (e.g. mirror dirt).

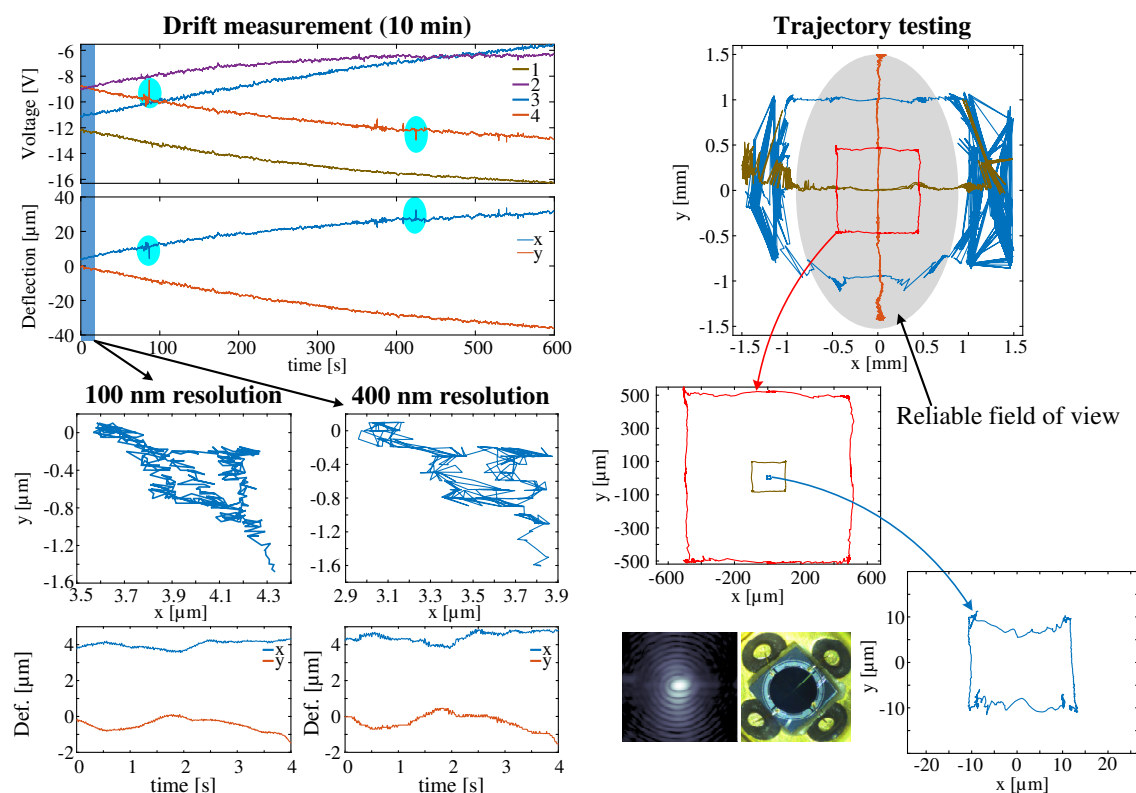


Figure 4.20.: Results of benchmark tests for optical unit. Left: Drift measurement shows the stability of the recording as well as the trajectory computation using the high-resolution grid and the low resolution grid. The drift originates from the mechanical translation stage which settled after approximately 20 minutes. Little spikes (blue ellipses) originate from encoding errors of the DAQ (RedLab 1408). These are not visible with the DAQ from NI. Right: Trajectory test in the entire FOV of 1.5 x 1.5 mm. The grey field illustrates the reliable area of encoding. Outside this field position jumps occur due to ambiguity of weak signal. Along the central y-axis reliable recording is possible for the entire FOV.

spot at the beginning of the measurements is located at the centre to use the full FOV. For most measurements, however, this is important because the samples, especially if placed inside gels, show a drift. This drift does not disturb the measurements as long as the laser spot, taking into account the vibrational deflection, is inside the area of reliable FOV.

4.6.2. MR imaging test

A second test was conducted to test the functionality of the MR imaging hardware. By using CuSO_4 -solution to speed up T1-relaxation acceptable image quality could be reached with an MR image with a resolution of 67 μm isotropic as illustrated in figure 4.21 acquired in 24 minutes. By relaxing the constraints to resolution (e.g from 67 μm to 130 μm), MR images can be acquired within one or two minutes.

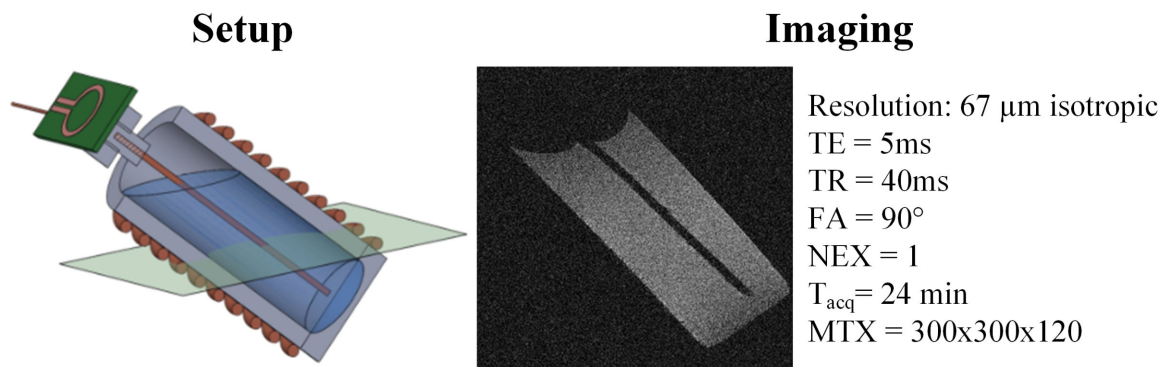


Figure 4.21.: Setup and final MR image acquired during an MR benchmarking test.

4.7. Conclusion

Within this chapter, a fully integrated laser-based vibration measurement system is presented which includes an MR acquisition front end for simultaneous MR and vibration measurements. The modular approach, especially of the front end, enables the user to conduct a rapid sample exchange for both the implant-like samples and the viscoelastic environments. A segmented photodiode, in combination with a two-stage amplifier, is used to provide an amplification bandwidth of the analogue signal of 10 kHz. This covers the range of eigenfrequencies for all considered mechanical, implant-like systems. A large dynamic range is achieved with a FOV of 1.5 x 3 mm and a standard resolution of 400 μm and optionally optional 100 μm . Equipped with this measurement system, an experimental analysis of mechanical vibration of samples inside viscoelastic environment is facilitated. The theoretical analysis and experimental data acquisition and processing are presented within the next chapter.

5 | Vibration analysis of implant sub-structures

The focus in the previous chapter was laid on the probe design and manufacturing. Only few aspects of the samples and viscoelastic environments were introduced. Within this chapter the application is described, which is the theoretical and experimental analysis of mechanical vibrations of implant-like structures in viscoelastic environments. A detailed theoretical analysis provides a fundamental understanding of the expected mechanical behaviour. This analysis is used as an estimator to obtain information about the expected experimental results, which serves, besides the better understanding of the underlying physics, as a fundament for planning the final experiments. The theoretical analysis presented in the first section, is based on analytical and numerical tools in form of FEM simulations. Final conclusions are drawn, on the basis of the experimental results, which supports the better understanding of the behaviour of mechanical systems within the MRI. Most importantly an answer will be given, on how severe vibrations are, which includes the analysis of the damping behaviour. The results which are presented within this chapter are published under title "Gradient-induced mechanical vibration of neural interfaces during MRI" in the journal "IEEE Transactions on biomedical engineering".

5.1. Theoretical analysis and simulation of viscoelastic vibration

5.1.1. Model description

Before starting the description of the detailed analysis, I want to introduce the basic schematics which are used to derive the correct models. Considering penetrative implants and surface electrodes used for stimulation and recording, there are three major fundamental structures which are present in all implants. These common structures are the electrodes for signalling, the substrate for these electrodes and the viscoelastic environment in which the electrodes are embedded. Within this research, the focus is on penetrative devices in brain matter, but the principles are equivalent for or implant types and tissues. A better and more general understanding of such system can be achieved by employing test samples

which mimic these three major components. Variation of important parameters of the test samples allows us to test the developed analytical models. A detailed illustration of an

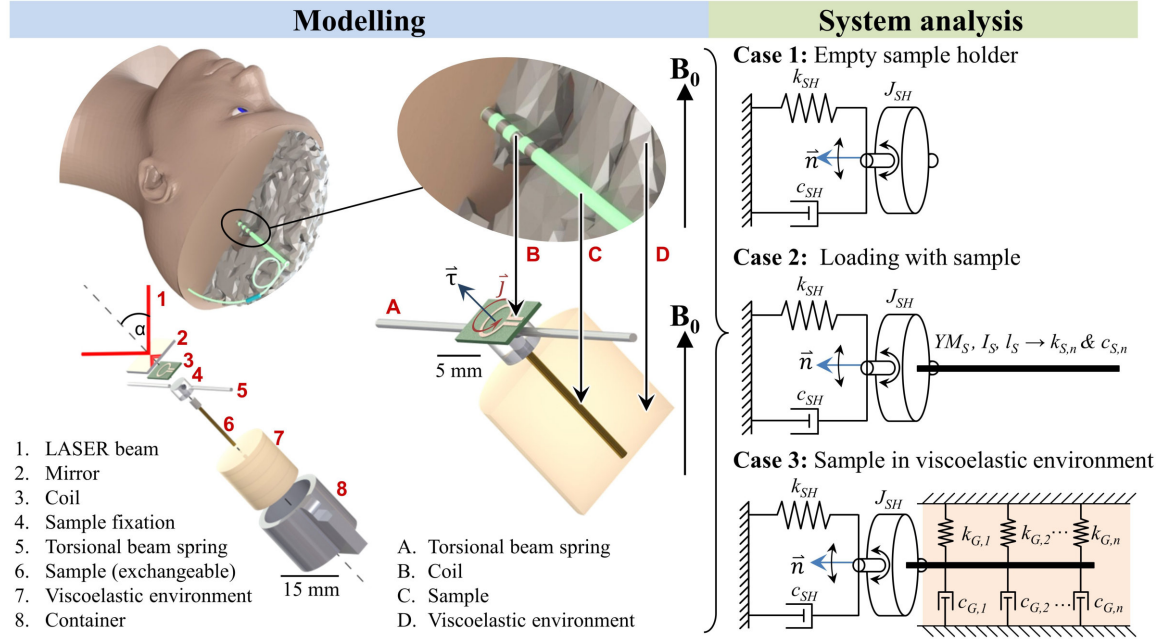


Figure 5.1.: From reality to experimental model: Top left: Location of a DBS electrode inside the human brain. Bottom left: Explosion view of experimental setup. Middle: Mapping of real implant structures and equivalent structures of the measurement model, conductive functional structure, and the viscoelastic environment. Right column: Schematics to derive lumped parameter models for the characterising the sample holder (Case 1), the sample in air (Case 2) and the sample in viscoelastic environment (Case 3). (Adopted from [EF05] ©2019 IEEE).

implant structure and the developed test structures is shown in figure 5.1. The test samples and the corresponding equivalent structure of a real implant are shown at the example of a DBS electrode. The viscoelastic brain environment is emulated using agarose-based gels, the substrate shaft is modelled using an exchangeable beam, and the electrode, which is the transducer for torque, is emulated using a coil. In addition to the real implant, a sample holder is required which facilitates the easy exchange of samples and the integration of the coil and mirror. In table 5.1 all employed testing materials and the corresponding dimensions are listed. On the right-hand side of figure 5.1, simplified lumped-parameter models are displayed which are the basis for the theoretical analysis as well as the experimental planning. Basically, there are three different cases which to determine the values of the individual components. Firstly, the spring constant k_{SH} of the sample holder (index: SH) is characterised, by conducting a quasi-static measurement in which the damping constant with $\lim_{\omega \rightarrow 0} c_{SH}(\omega) = 0$ is negligible. Subsequently, by measuring the eigenfrequency and the Q-factor by means of the transfer function using a frequency sweep, the damping c_{SH} and the angular mass J_{SH} are determined. In case 2, a sample (index: S) is mounted on this sample holder and the modified transfer function is measured. In ideal case this yields the eigenfrequencies of the sample and its damping behaviour. Ultimately in case 3,

Table 5.1.: Properties and materials of sample holder, samples, and test environments. This modular setup lead to a total number of 144 combinations of sub-units (sample holder + sample + environment). Additionally, the sample holders were characterized without load. The measurements furthermore were separated in static and dynamic measurements, leading to a total amount of 296 possible combinations. All samples have a length of 20 mm. The sample with mass, has a weight of approximately 144 mg mounted at the tip.

Sample holder		Sample		Environment	
Ø [mm]	Material	Ø [mm]	Material	Concentration	Material
0.25	Cu ¹	0.25	Cu	–	Air
0.5	Cu	0.25	Cu + mass	–	Water
0.5	Ny ²	0.5	Cu	0.5 %	Agarose
2	PMMA	0.5	Br ³	1 %	Agarose
		0.5	ABS ⁴	2 %	Agarose
		2	Br	4 %	Agarose Oil ⁵

¹Copper ²Nylon ³Brass ⁴Acrylonitrile butadiene styrene

⁵ Conventional sunflower oil, not characterized, approximate viscosity: $\nu = 70\text{mm}^2/\text{s}$

which represents the full model, the mounted beam is immersed in different viscous and viscoelastic environments to analyse the impact on the transfer function and to investigate if critical damping leads to under- or over-damped resonance. The viscoelastic environment or hydrogels (index: G) are modelled using the Kelvin-Voigt model with parallel springs and damping components^[65]. One can simplify the model of case three,

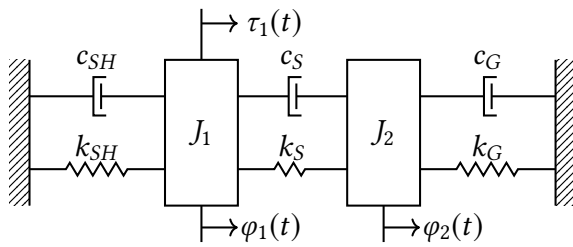


Figure 5.2.: Lumped model derived from case 3. The torque τ_1 is produced by currents in the external coil. The deflection angle φ_2 is of interest, but can only be observed through the deflection of φ_1 . (Adopted from [EF05] ©2019 IEEE).

by taking into account only the first eigenfrequency of the sample. Then the beam is represented by a damped spring-mass oscillator. Furthermore, the viscoelastic-environment is reduced to a single spring-damper element. The resulting model is illustrated in figure 5.2 and the fundamental characteristics of this model are introduced in section 2.4.1. External torque is applied on the sample holder only, where the coil is mounted. In the same way, the deflection of sample holder, the angle $\varphi_1(t)$, is measured

by means of laser beam deflection. The deflection of the sample, the angle $\varphi_2(t)$ is not measured directly, however it is of greatest interest. Therefore, we need the understanding to extract some information about the sample vibration via the the angular deflection $\varphi_1(t)$.

5.1.2. Analysis of static case

A first discussion is about the stationary case. In this case, terms with time derivatives vanish ($J_i \ddot{\varphi}_i(t) = 0$; $c_i \dot{\varphi}_i(t) = 0$) and the model reduces to a spring network. The simplification under these circumstances and the relation from external torque τ and the angular deflection φ_1 are displayed in figure 5.3. The total spring constant k_{tot} is governed by equation 5.1.

$$\frac{\tau_{ext}}{\varphi_1} = k_{SH} + \frac{k_S k_G}{k_S + k_G} = k_{tot} \quad (5.1)$$

From equation 5.1 and figure 5.3 we can derive that there exist three regions for which the spring constant k_{tot} depends mainly on one spring constant. Since we are interested in the effect of the gel on the spring constant, we want a region in the experiments in which the elasticity of the gel is a dominating factor. Ideally, this is reached for $k_S \rightarrow \infty$ and $k_{SH} \rightarrow 0$. In this case the angular deflection is inversely proportional to the spring constant with $\varphi_1 \propto 1/k_G$.

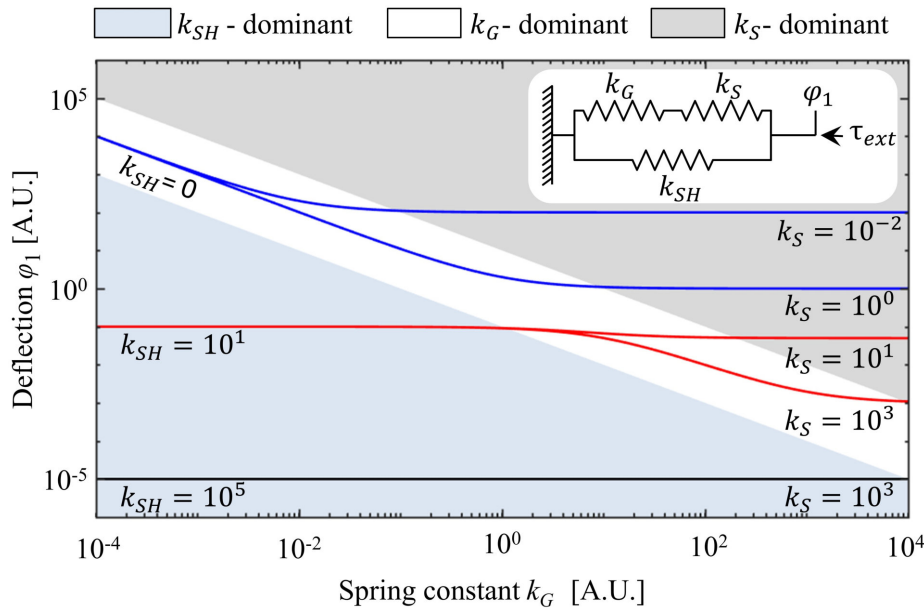


Figure 5.3.: The deflection φ_1 as a dependence of different spring constants k_{SH} , k_S , and k_G . The inset in the top displays the corresponding spring network as a result from figure 5.2. (Adopted from [EF05] ©2019 IEEE).

The important message here is the fact, that for certain combinations of sample holder and samples, one cannot measure differences for k_{tot} by varying the gel, because all the relevant measurement points may be located in one dominant region.

5.1.3. Analysis of transfer function and resonances

The main measurement is the transfer function for constant torque and increasing frequency. Using the lumped model from figure 5.2 and the equations derived in section 2.4.1 we can write the equations of motion for the observable deflection φ_1 and the non-observable deflection φ_2 . The components of the transfer matrix are given by:

$$\begin{aligned} G_{11} &= J_{SH}s^2 + (c_{SH} + c_S)s + (k_{SH} + k_S) \\ G_{22} &= J_Ss^2 + (c_S + c_G)s + (k_S + k_G) \\ G_{12} &= G_{21} = -c_Ss - k_S \end{aligned} \quad (5.2)$$

Then we obtain for the interesting transfer functions T_{11} and T_{12} , for $\tau_2 = 0$ because there is no torque directly on the sample the following equations:

$$\begin{aligned} T_{11}(\omega) \Big|_{\tau_2(\omega)=0} &= \frac{\tau_1(\omega)}{\varphi_1(\omega)} = \frac{G_{22}}{G_{11}G_{22} - G_{12}G_{21}} = \frac{J_S\omega^2 + (c_S + c_G)\omega + (k_S + k_G)}{G_{11}G_{22} - G_{12}G_{21}} \\ T_{12}(\omega) \Big|_{\tau_2(\omega)=0} &= \frac{\tau_1(\omega)}{\varphi_2(\omega)} = \frac{-G_{12}}{G_{11}G_{22} - G_{12}G_{21}} = \frac{c_S\omega + k_S}{G_{11}G_{22} - G_{12}G_{21}} > 0 \end{aligned} \quad (5.3)$$

On the basis of this calculations, we can investigate the behaviour of the transfer function of the sample holder and the sample. In figure 5.4 the corresponding graphs are plotted. One important plot is of the transfer function in the case of no viscoelastic environment ($k_G = c_G = 0$). This case is represented by the blue lines. The measurable T_{11} shows two resonance frequencies, one for the sample and one for the sample holder. The non-measurable T_{12} shows resonances at the identical resonance frequencies. This is understandable from the equations 5.2, because resonances occur at frequencies where the denominator equals zero, hence a pole exists. Since the denominator is identical for

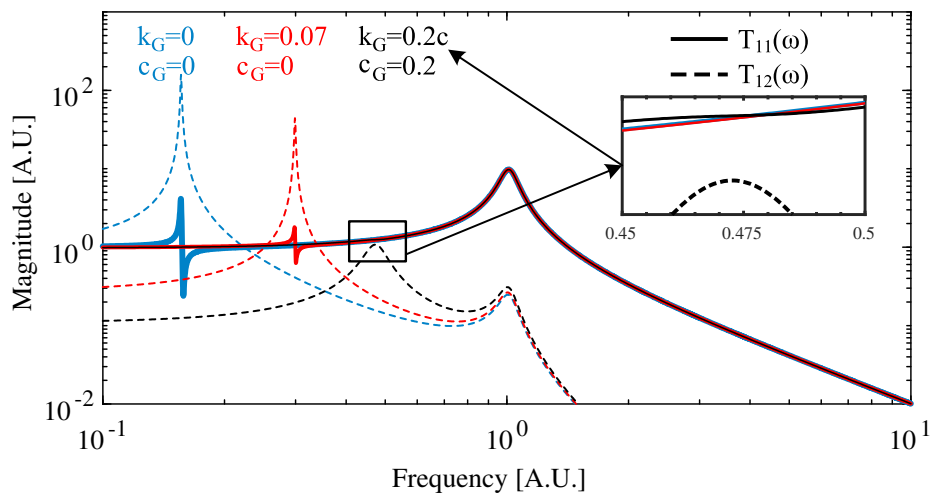


Figure 5.4.: Graphs of the transfer function T_{11} for different values for the spring and damping constants. The other constants in this figure are $J_{SH} = J_S = 1$, $k_{SH} = 1$, $k_S = 0.25$, $c_{SH} = 0.1$ and $c_S = 0.001$.

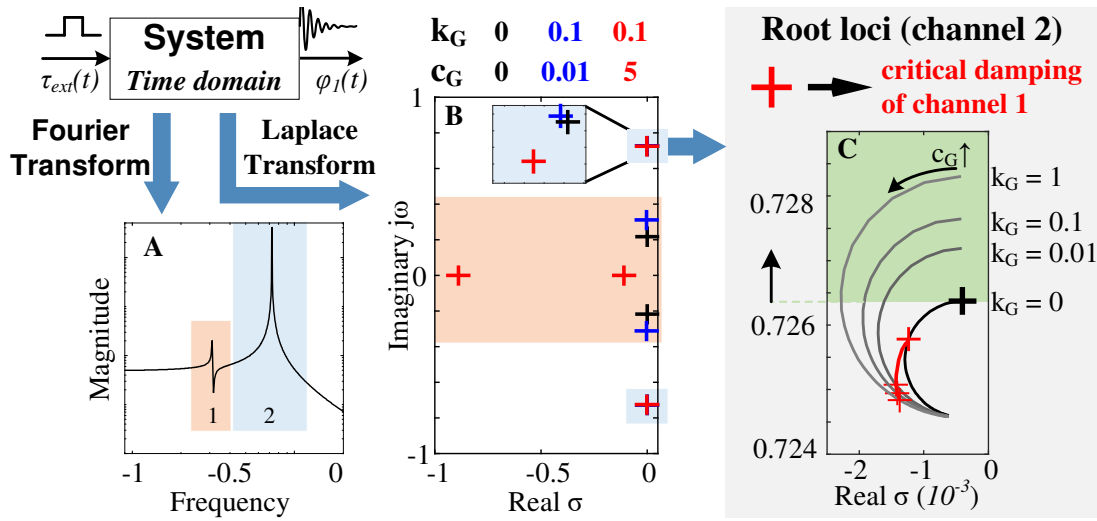


Figure 5.5.: Systems analysis in the image domain after Laplace transformation. (A) shows the result after Fourier transform (measurable T_{11}) of the time domain signal. (B) shows the poles of T_{11} in the Laplace domain. The corresponding peaks of (A) and (B) are highlighted with the orange and blue background. (C) is the magnification of the poles of peak two which is the resonance peak of the sample holder. In the pole is within the green area, hence the resonance frequency increases after insertion of the sample in viscoelastic gel, then the sample resonates underdamped. (Adopted from [EF05] ©2019 IEEE).

both transfer functions, the poles are at the same frequencies. This is the reason that we can investigate the resonance frequency of the sample indirectly by measuring T_{11} . Another important fact is the low-pass behaviour of the sample holder. It is identified best at the resonance of the sample, if it is located at a lower frequency than the resonance peak of the sample holder. If the peaks overlap, the peak is obscured, and if the sample resonance is at a larger frequency it may be invisible due to the fact, that the low pass behaviour decreases the SNR at higher frequencies, since the signal drops. The resonance of the sample holder is increased by using a stiffer sample holder suspension, i.e. by increasing k_{SH} . An important difference when comparing T_{11} and T_{12} , are the zero points that are only visible in T_{11} because the nominator does not approach zero for positive frequencies since $T_{12} > 0$ for $\omega > 0$. The next case considers an ideal elastic gel with no dissipation, which is plotted in red. The resonance frequency of the sample increases, since the spring load on this mass is increased. An increased stiffness reduces the amplitude of the resonance, yet the resonance peak is clearly visible on T_{11} and T_{12} . Considering a more realistic gel which includes damping ($c_G = 0.2$), then the resonance peak of T_{11} seems to disappear. The question arises if we can conclude that the sample resonates overdamped. However, as visible in the small inset, this is not generally true. In T_{12} the resonance is clearly visible, however, in T_{11} this signal may become very weak or flat. In this case we need another possibility to observe the resonance behaviour of the sample to extract information about its physical behaviour within different gels. Using the Laplace transformation from equation 5.2 and 5.3 we can investigate the results of this

equations in the s -plane. The two poles of the measurable transfer function, as described by T_{11} , originate from the resonance frequency of the sample and the sample holder. In figure 5.5 these measurable resonances are marked in the picture section (A) as peak 1 (resonance sample) and peak 2 (resonance sample holder). If peak 1 disappears, and hence is not measurable, we can further investigate the damping condition of the sample by evaluating and comparing peak 2 (frequency of peak maximum and half width) with and without gel environment. The sample resonates overdamped if the poles of peak 2 (orange area in picture section (B)) become real in the s -plane ($j\omega = 0$). This is the case if the damping constant c_G exceeds a certain value. In picture section (C) the root loci of peak 2 are displayed for varying c_G . Increasing c_G always leads to a decrease of the resonance frequency of peak 2, whereas increasing k_G results in an increase of this resonance frequency. Marked in red are the critical points of the damping constant c_G at which peak 1 becomes overdamped. This is not directly measurable, however, the graph shows that in this cases, the resonance frequency of peak 2 is always smaller compared to its resonance frequency without viscoelastic load ($k_G = c_G = 0$). Hence, we can deduce, that if the resonance frequency of peak 2 increases after the sample is immersed in a viscoelastic environment, the sample resonates underdamped. This is represented by the green area of the picture section (C). This important result will play a crucial role in the data analysis in section 5.3.

5.2. Characterisation of viscoelastic gels

Agar gels are used in this experiment to mimic the viscoelastic properties of brain tissue. Materials are characterised as viscoelastic when the deformation under applied forces exhibits viscous and elastic behaviour. This means the material exhibits a restoring force and a friction force. Both forces appear in viscoelastic materials, and one option to characterise a material is to measure the angular deflection under shear stress, which yields the shear modulus G . The viscous and elastic behaviour is characterised using the complex shear modulus $G^* = G' + iG''$ where G' is the storage modulus representing the elastic behaviour, and G'' is the loss modulus representing the loss modulus. Agar gel is used in many brain tissue-based research applications, because the viscoelastic properties of agar gels resemble the properties of the brain^[120]. Four types of agar gels are prepared for the experimental work with concentrations of agar (AGAR AGAR SERVA 11396.02). Therefore, four samples of agar powder of 0.5 g, 1 g, 2 g and 4 g are dissolved in 100 ml of water. Additionally 13-vol % of 1-propanol is added and prepared according to the protocol of Kavitha et al.^[76]. For the analysis with the rheometer (ARES-G2, TA instruments), four gel discs are prepared with 40 mm diameter and 10 mm height. The samples and the measurement results are displayed in figure 5.6. For low frequencies and low strain, the storage modulus is dominant. The shear moduli of the gels are similar to the shear moduli of the brain. Prodanov et al.^[122] reports on post-implantation variation of the

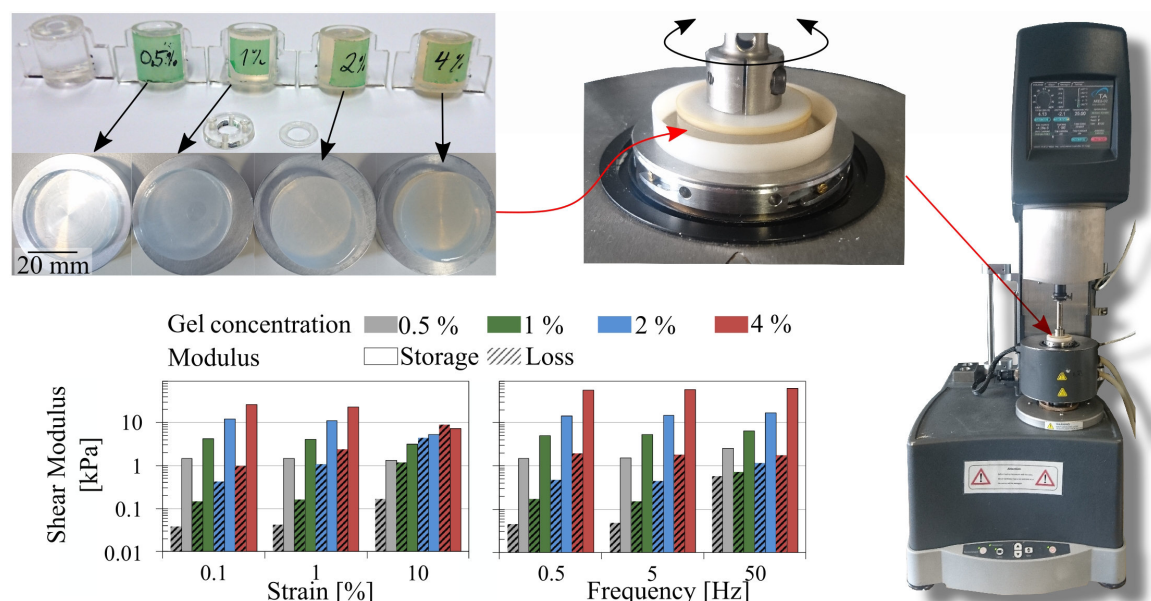


Figure 5.6.: Characterisation of viscoelastic properties of agarose gels: Top left: Four concentrations of agarose gels are prepared with 0.5 %, 1 %, 2 % and 4 %. The top row shows the containers for the vibration probe and the bottom row shows the discs prepared for the rheometer. Four discs are prepared to conduct the measurements on the rheometer (top middle and right). Bottom left: The strain measurements, conducted at 1 Hz, show an increase of loss modulus for large strains. Bottom middle: Frequency sweep of shear modulus conducted at 0.01 % strain rate. At 50 Hz mainly the loss modulus increases. This effect is more pronounced for low concentrated gels. (Bar diagrams adopted from [EF05] ©2019 IEEE).

shear modulus of brain tissue ranging from 0.5-2.6 kPa to 25.7 59.3 kPa after 4 weeks. After reaching the maximum, the shear modulus decreases to values from 0.8 kPa to 7.9 kPa after 6 to 8 weeks. These values are in good agreement with the measured values of the four gels, with storage moduli from 1.5 kPa for the 0.5 %-gel to 55.9 kPa for the 4 %-gel. Therefore, the prepared gels constitute a good choice as a material to mimic the brain tissue during different post-implantation stages.

5.3. Results from viscoelastic vibration tests

In this section the results of the vibration experiments inside the MR unit are presented. First quasi-static measurements were conducted for different sample holders, samples and agar gels to measure the total spring constant. The results are compared to the theoretical predictions. Secondly, the more important measurement of transfer function is presented including the important analysis of resonance behaviour of samples inside the viscoelastic environments. Finally, a worst-case situation on-resonance vibration experiment is presented, triggered by a bad selection of MR imaging parameters.

5.3.1. Static measurements

In the first set of measurements the static behaviour was analysed. Therefore, an amplitude sweep was conducted at a constant frequency of 5 Hz. Based on the experience from the theoretical analysis, not all possible combinations of sample holder, sample and gel yield a measurable difference when increasing the gel stiffness. Therefore, a set of combinations was selected with weak (0.5 Ny), medium (0.5 Cu) and stiff (2 PMMA) sample holders (k_{SH}) as well as weak (0.25 Cu), medium (0.5 ABS), and stiff (0.5 Br) samples (k_S).

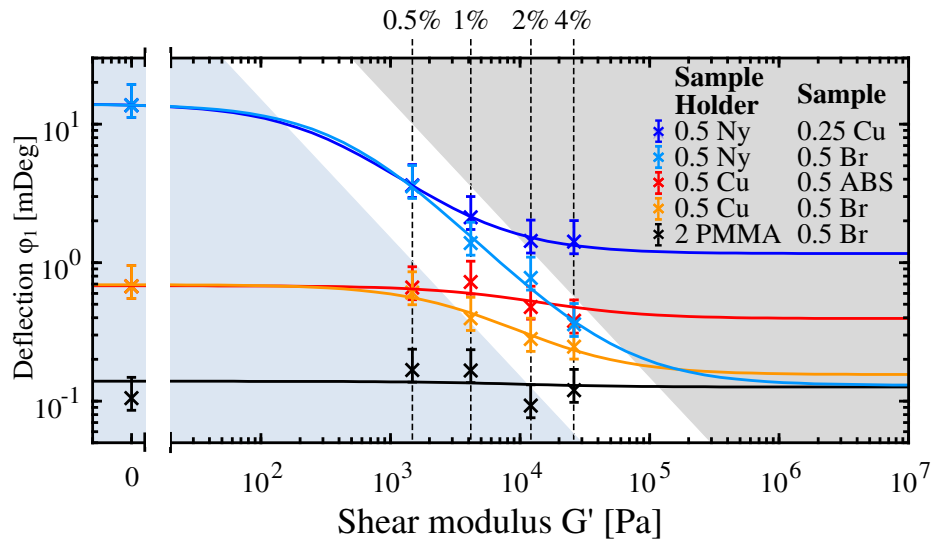


Figure 5.7.: Results of the static deflection measurements for different sample combinations. The applied torque ranges from 0.005 to 5 μNm . To compare the the deflection was normed to a torque of 1 μNm . (Adopted from [EF05] ©2019 IEEE).

The results are plotted in figure 5.7. Measurement uncertainties are taken into account and indicated with the error bars. These measurement errors result from the uncertainty of the angle between the normal of the coil surface and \mathbf{B}_0 -field. The data points are fitted using equation 5.1. It can be seen that for the very stiff sample holder (2 PMMA), the deflection φ_1 is does not dependent on the sample and the gel. On the other hand, for very weak sample holder and sample (0.5 Ny + 0.25 Cu) the the deflection φ_1 depends strongly on the sample, and thus φ_1 is also constant. A strong dependence on the gel is obtained for the combination (0.5 Ny + 0.25 Cu) and (0.5 Cu + 0.5 Br). Moreover, the latter combination yields similar results as the combination (0.5 Cu + 0.5 Cu). Based on that measurements, the main sample holder for the dynamic measurements is the sample holder 0.5 Cu. Its stiffness is weak enough not to be too dominant, while having a self-resonance frequency above the sample resonance.

5.3.2. Dynamic measurements

In this subsection the results from the transfer function measurement are detailed. On that basis, an analysis of the interaction of sample and different viscoelastic environments is presented. Finally, the results of an MR experiment are shown, in which worst-case vibration is triggered by the detailed knowledge of the transfer function.

The first experimental results which are presented, are acquired with the combination of the "0.5 Cu" sample holder with the "0.25 Cu+mass". This combination revealed direct measurable deflection even within the 0.5 % gel. In figure 5.8 the graphs are illustrated in which the data of seven measurements are displayed in the range of 10 to 600 Hz. The Transfer function In the range from 250 to 350 Hz parasitic vibrations were detected which are masked for clarity¹. The black thin line is the transfer function of the sample within air, hence $k_G = c_G \approx 0$. The eigenfrequency of the sample is clearly visible at 42 Hz with an amplitude of 5.4. The grey line results from the transfer function of the sample holder Immersed in water and the resonance frequency drops slightly to 40 Hz with an amplitude of 2.8. A clear change of the damping is seen for the measurement within oil. Here, the resonance is shifted further downwards to 32 Hz with an amplitude of 1.13. If immersed in the 0.5 % gel, the resonance frequency of the sample increases

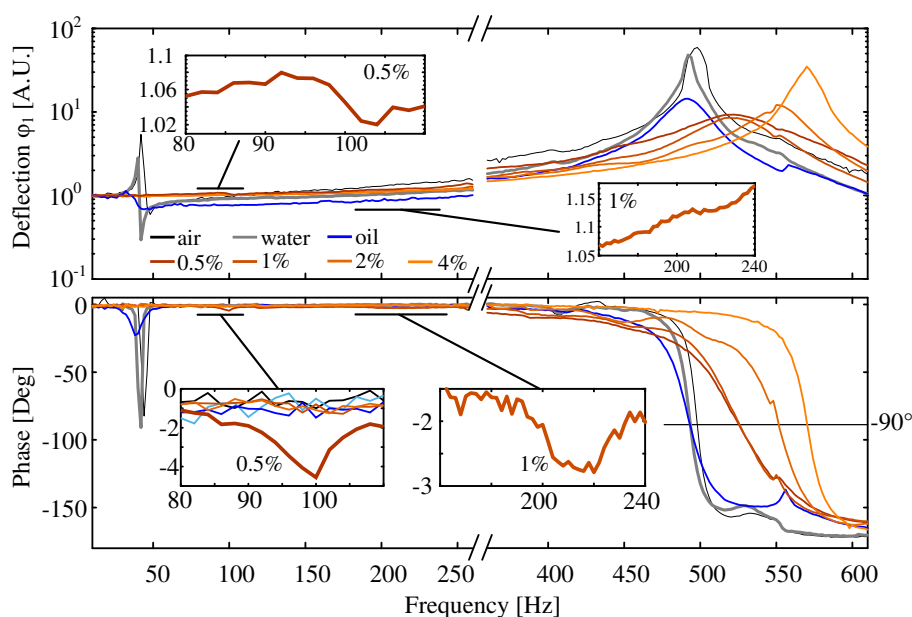


Figure 5.8.: Transfer functions of the combination "0.5 Cu + 0.25 Cu+mass" in air, water and the four gels. On the upper graph the amplitude response is displayed, in the bottom graph the phase response between excitation signal and the deflection. Clearly visible, in air and water, is the direct fundamental sample resonance peak below 50 Hz. The additional spring load of the 0.5% gel yields an increase of resonance frequency to approximately 80 Hz.

¹see ripples at around 300 Hz in figure 5.9

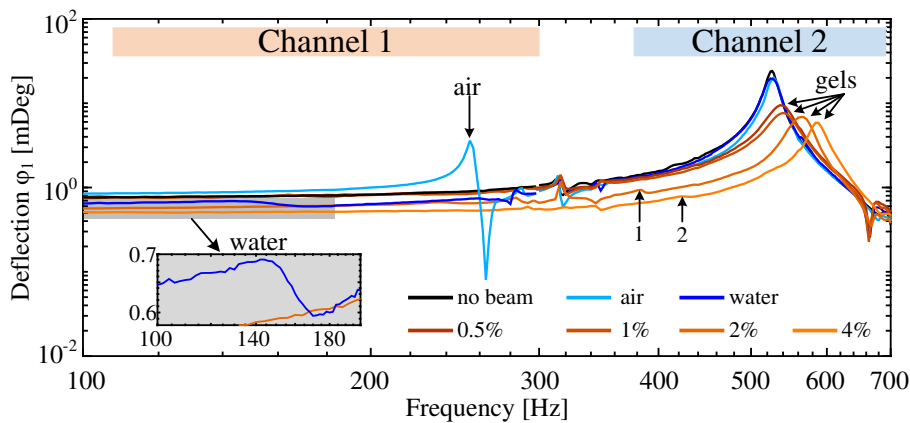


Figure 5.9.: Transfer functions of the combination "0.5 Cu + 0.5 ABS". The light-weight sample resonates in air at approximately 260 Hz. The immersion in water results in strong damping. The increase of the sample holder resonance, is an indicator that the sample resonates underdamped. (Adopted from [EF05] ©2019 IEEE).

to approximately 96 Hz, which is a result of the added spring load (k_G). This is a first direct proof, that the sample resonates underdamped within the 0.5 % gel. The resonance amplitude is relatively weak with 1.08, why detection becomes critical. This is even more pronounced for the resonance in the 1 % gel. Here a small dip is visible in the phase response at approximately 220 Hz along with a small amplitude increase. However, the amplitude resonance is almost invisible due to the amplitude increase of the resonance of the sample holder. Most importantly, a clear effect is also visible on the resonance peaks of the sample holder. Due to encoding error the amplitudes on resonance for air, water and the 4% gel are at the peak region elevated by approximately a factor of two due to large amplitudes. Nevertheless, the resonances are clearly visible and the damping can be analysed using the slope of the phase response at 90° . It is visible that, for water, and oil which has approximately 100 times the viscosity of water, the resonance frequency of the sample holder decreases below 500 Hz. Furthermore, the damping increases. If the sample is placed inside gels the resonance frequency increases with higher gels stiffness. It is notable that the slope at 90° and hence the damping, decreases for higher concentrated gels. This correlates with the observation in figure 5.6, in which the loss modulus G'' only increases with frequency for the lower concentrated gels. It is plausible that the used higher concentrated gels exhibit more elastic behaviour at higher frequencies and lower concentrated gels exhibit rather viscous behaviour at higher frequencies. Therefore, resonant vibrations at higher frequencies are more likely in higher concentrated gels.

In figure 5.9, the graphs are plotted for the combination "0.5 Cu" sample holder with the "0.5 ABS". The deflection angle φ_1 is not normalized to visualise the true deflection angle. Due to the additional spring load the deflection angle φ_1 decreases with increasing gel concentration. In contrast to the previous measurement, the resonance frequency of

the sample is much higher at around 260 Hz. Since the sample is very light, the resonance drops dramatically, if immersed in water, to approximately 140 Hz. The frequency of the sample resonance decreases clearly, if the sample is immersed in water. Based on the argument from figure 5.6 this is a strong indicator that the sample resonant underdamped. Moreover, little amplitude peaks are visible at point 1 for the 2 % gel and point 2 for the 4 % gel. The peaks for the lower concentrated gels may be obscured by the ripples at around 300 Hz. These peaks, however, are small and therefore are not completely reliable.

5.3.3. MRI vibration measurements

All data together demonstrate the possibility of underdamped sample resonance conditions inside the gels. This is of great importance since it indicates that in real MR experiments, penetrative implants have the tendency to exhibit amplitude amplification due to resonance condition. Thus, the timing parameters of an MR sequence play a crucial role in order to

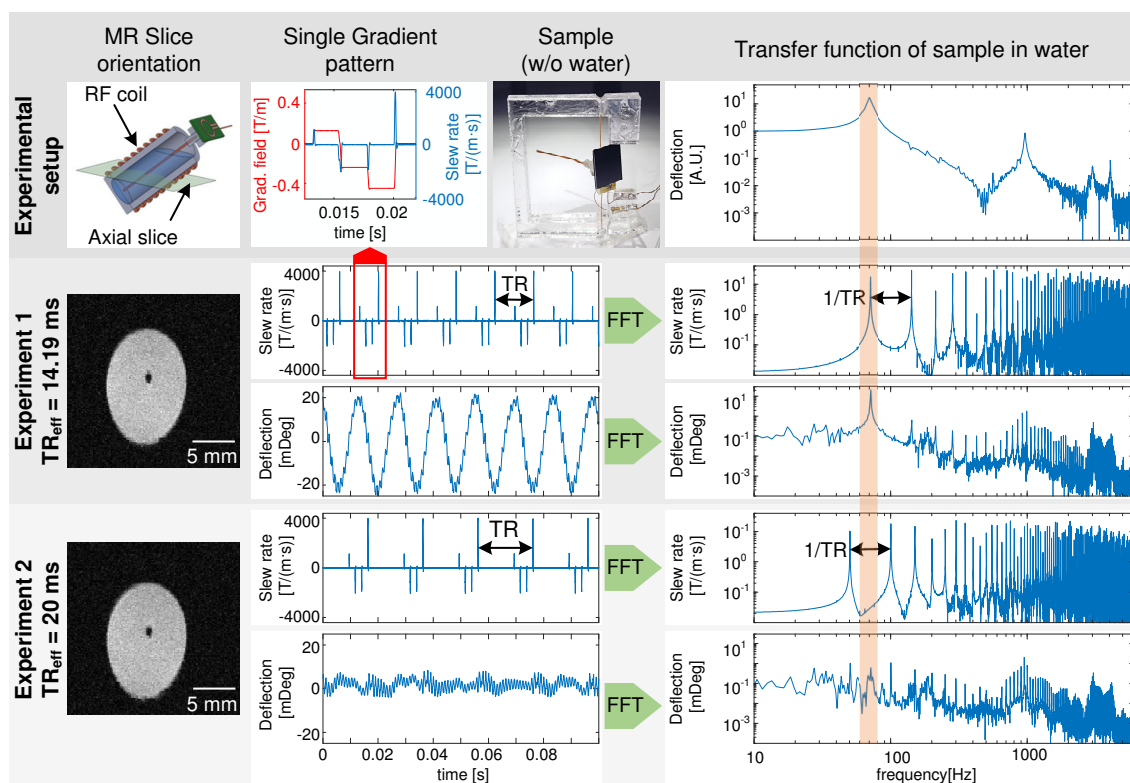


Figure 5.10.: This figure illustrates the effect of different vibration amplitudes due to different timing parameters TR. The top row shows the experimental setup of the sample holder and beam and the RF coil configuration. The Second row shows the MR image and the corresponding vibration during the MR acquisition for TR = 14.18 ms which leads to resonant vibration. The bottom row shows strongly reduced vibration due to different timing parameter TR. (Adopted from [EF05] ©2019 IEEE).

excite or ideally avoid excessive vibration amplitudes during an MR procedure. In a further

experiment this is proven for a sample immersed in water. Therefore, the 0.5 Cu sample was mounted on the 0.5 Cu sample holder. Prior top the MR experiments, the transfer function was measured as shown before, with a first resonance at 70.5 Hz. Once, the resonance condition is known, it is straightforward to manipulate the MR sequence such that the resonance condition is met or avoided. Therefore, I conducted two MR acquisition procedures with identical sequence parameters, except of the repetition time TR. The results are illustrated in figure 5.10. In this figure, the obtained MR images, the deflection in time domain as well as the gradient slew rate which produces the torque are presented, along with the Fourier transform of each time signal. In the time domain we can see that on resonance the timing parameters are such that the sequence is repeated once per period. In other terms for TR = 14.18 ms the following condition is met: $1/TR = 1/14.18 \text{ ms} = 70.5 \text{ Hz}$, which is exactly the resonance of the mechanical system. In the frequency domain it becomes very clear that the first peak. Large vibration can be simply avoided, by setting TR such that the gradient spectrum has a minimum at the resonance frequency of the mechanical system.

Within this section the mechanical response was investigated, which real implants can experience. The torque applied to the sample holder was however artificial, which enabled the precise measurement of the transfer function, but did not answer the magnitude of torque which a real implant may experience. This is conducted in the next section.

5.4. Torque measurements of real electrodes

In this section the torque produced by real electrodes during gradient switching is analysed. This work was conducted in collaboration with the San Diego State University (SDSU)² where the electrodes are fabricated and published elsewhere^[111]. In this collaborative work, we measured the torque induced in these electrodes using the presented vibration setup. Of particular interest is the difference between induced torque in carbon-based electrodes and metal based electrodes. The fundamental equation to describe electrode vibration is governed by equation 5.4.

$$I\ddot{\phi} + \Gamma\dot{\phi} + \mu\phi = \underbrace{\frac{1}{8}\pi\sigma tr^4}_{\text{Implant}} \underbrace{\sin(\alpha)\cos(\beta)}_{\text{Orientation and location}} d_i \underbrace{\dot{G}_i(t)B_0}_{\text{MR environment}} = \tau(t) \quad (5.4)$$

In this equation σ is the conductivity of the electrode material, t and r are the thickness and radius of the electrode, respectively. The angle α represents the angle between the electrode surface and \mathbf{B}_0 , and β is the angle between the surface and the gradient field. A further parameter, d_i , describes the distance between the implant centre and the centre of the gradient element i , and \dot{G}_i is the slew rate of gradient element i . The left side of this equation describes the mechanics which are detailed in the previous chapter. The

²This work was conducted by S. Nimbalkar in the group of Prof. Sam Kassegne.

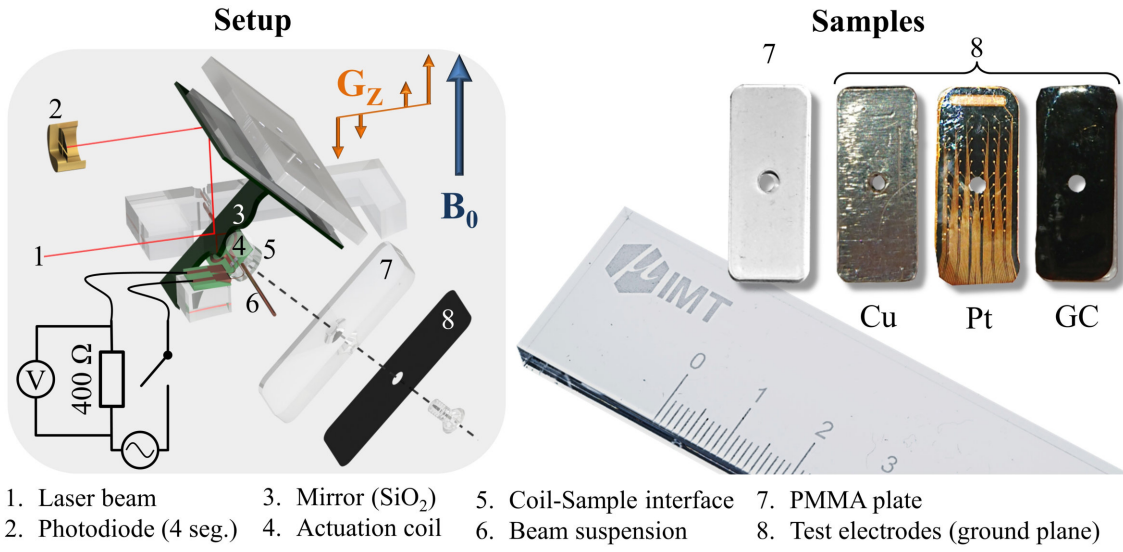


Figure 5.11.: Illustration of TPSR measurement setup and electrodes. Left: Setup including field orientations to measure the TPSR of the electrodes. After mounting the electrodes, an external coil was used to characterise the mechanical transfer function with a known externally applied torque. Then the coil was disconnected and the deflection produced by gradient switching was measured. (Adopted from [EF06])

right side describes the origin of the torque that induces the vibration. As indicated by the description in equation 5.4, there are three main components which contribute to the torque: (i) the conductive layer of the electrode, (ii) its orientation and location inside the MR unit, and (iii) the electromagnetic fields of the MR environment. From the viewpoint of the implant, the induced torque depends on the conductivity, height and surface dimensions of the conductive layer. Therefore, different implants exhibit different torques while orientation, location and sequence are the same. To label implants with a number for their torque response, it is useful to find a classification number which allows the user to estimate largest expected torque independent of the MR unit and sequence. Therefore, the measurements are conducted with an orientation of maximum induction and torque, which means the the surface normal is oriented with 45° with respect to \mathbf{B}_0 and the gradient fields G_i , hence the angles α and β equal 45°. When the torque is measured one can derive a normalised classification number by scaling with the measured distance d_i , the applied slew rate \dot{G}_i and \mathbf{B}_0 . This yields the following relation (see also appendix A.1):

$$\text{TPSR}_{\text{measured}} = \frac{\tau_{\text{measured}}}{\dot{G}_i d_i B_0} \simeq \frac{1}{8} \pi \sigma h r^4 \sin(\alpha) \cos(\beta) = \text{TPSR}_{\text{theo}} \quad (5.5)$$

TPSR is an acronym which means **Torque Per Slew Rate** with the unit [$\text{Nm}/(\text{T}\cdot\text{T/s})$]. This classification number of an implant allows the user to obtain the worst case torque for any MR system. Therefore, the TPSR is multiplied with the characteristic numbers of an MR system, which is the maximum slew rate \dot{G}_{max} , maximal possible distance from isocenter, and the magnitude of \mathbf{B}_0 . The resulting number is the maximal torque which can be

experienced by an implant. Using equation 5.5 facilitates the comparison of measurement and analytical results. This approach is used to characterise the electrodes fabricated at SDSU. Since the largest connected conductive surfaces were the ground planes, and thus, contribute largest to the torque, we extracted the connected ground planes and characterised these components. The setup and electrodes are displayed in figure 5.11. The electrodes from SDSU are PT-based and glassy-carbon (GC) based. All electrodes are 25 x 11 mm, and the Pt-electrode has a PT thickness of 300 nm. The GC electrode has a carbon thickness of 2 μm . As a reference, a high conductive Cu based sample is manufactured and characterised as well. Therefore, a 40 μm thick copper foil (Chomerics CCK-18-101-0200) is applied.

Since the electrode are on a flexible substrate, they are adhesively attached on a stiff PMMA plate to ensure the deflection of the sample holder. All MR related information is known if the torque is measured, thus one can compute the localized force acting on an implant. However, this step was not conducted within this work. As described in the previous chapters, an externally controlled electrode facilitates the characterisation of the mechanical system. Thus, the electrodes, which are to be tested, are attached on a PMMA substrate and mounted on the sample holder. Prior to MR sequence tests, the mechanical system was characterised by measuring the static and dynamic transfer function using the externally driven electrode. Subsequently this electrode is switched off, such that induction is suppressed. In the next step, defined gradient sequences are applied and the deflection is measured. This deflection is caused through induction in the test electrodes. Simultaneously, the gradient signals are recorded and the position of the implant is measured. Since the mechanical transfer function is known, which includes the information of the acting torque, the gradient strength as well as the position and \mathbf{B}_0 is known, too, one can derive the torque produced by the implant.

Of great importance is to take into account the parasitic vibration, induced by acoustic coupling. To distinguish acoustic from induction-based vibration, several test runs are conducted using different empty PMMA plates. This is required because the acoustic coupling results in amplitude differences even at the same location due to little position changes. The results from several scans enable to derive a reliable minimum baseline. Vibrations below this baseline, cannot be distinguished from acoustic coupling, or in other words induction-based vibration in these cases is much smaller than acoustic vibration.

The results from the experiments are shown in figure 5.12. The limit of detection, due to acoustic coupling, in the used MR scanner, is at a critical value for the platinum-based electrode and too large to measure any induction-based vibration for the GC-electrode. This means, both electrodes did not show larger vibration than the non-conductive PMMA sample. The Cu-based reference sample, on the other hand, shows clear induction-based vibrations which allows assigning a TPSR value. The theoretical values, are larger by a

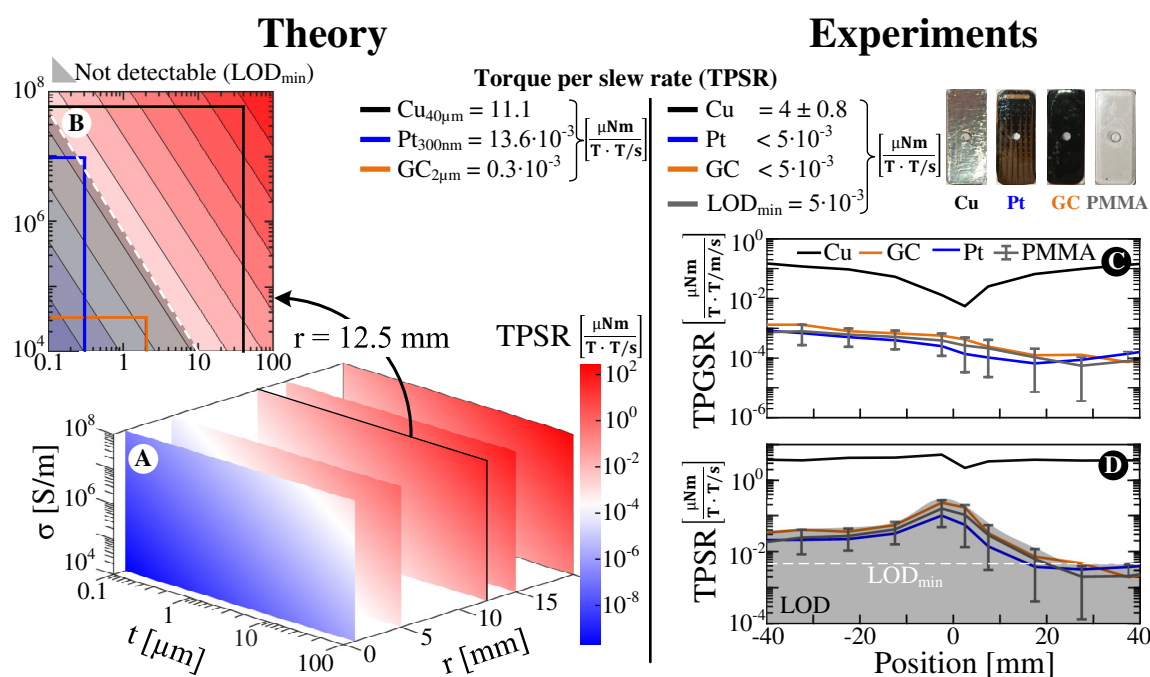


Figure 5.12.: Results of TPSR measurements. The graph (A) shows the TPSR as a function of sample radius r , thickness t and conductivity σ . The target set ranges about ten orders of magnitude for the selected domain. In (B) the slice is shown for the corresponding radius of the test electrodes. The theoretical limit of detection is highlighted as white dashed line. Values below that line, which are inside the grey area, exhibit less induction-based vibration than acoustic coupled vibration. In (C) the values of the torque per gradient slew rate are displayed, which depends on the location. These values are normalized with their corresponding location, which leads to the TPSR shown in (D). The Pt-electrode is at the limit of detection, the GC-electrode is far below it. The copper-based reference sample shows clear induction-based vibration. (Adopted from [EF06])

factor of two to three. One reason is that in the theoretical calculation, self-induction of the eddy currents is not taken into account. Self-induction decreases the eddy currents due to its impedance. Neglecting this effect leads to an overestimation of the TPSR. Another effect is that equation 5.4 is derived using the integral of the Maxwell-Faraday equation. This integral is straightforward for circular discs using polar coordinates, which results in the displayed equation. The test electrodes, however, are of rectangular shape, and for comparison the largest dimension was selected. Hence, the theoretical values represent the expected TPSR for circular discs instead of rectangular electrodes. Considering these two effects the analytical values are a good estimator for the expected order of magnitude, and allow the analysis why vibration above the acoustic could not be detected in all samples.

5.5. Conclusions

In this chapter a novel probe is presented which facilitates the full characterisation of implant vibration. This includes the analysis of the mechanical response of a system, as

well as the electrical response of the conductive structures. In addition, the developed probe shows full MR compatibility, which enables the simultaneous measurement of vibration and MR acquisition. The vibrational measurements of mechanical structures, immersed in brain-like viscoelastic materials, exhibit underdamped vibrations. This is of great importance, since the accidental excitation of such resonances, exposes a risk for fatal incidents. With respect to the characterisation of conductive structures a new classification number is introduced, which provides a labelling of implants independent of the MR unit. Both numbers in combination, the TPSR and the resonance frequencies, represent a label, which furnishes all required information necessary to avoid excessive vibration, and in turn guarantees an MR-compatible acquisition procedure for implant carriers.

Part II.

High field probe for bioengineering applications

6 | Flexible high-field probe for in-situ measurements

High-field NMR systems are advantageous in particular with respect to the SNR. When coil-noise is dominant, which is the case for small volume research scanners, the SNR scales approximately according to: $SNR \propto B_0^{7/4}$. Therefore, a lot of effort is invested for developing systems for high fields. Even though there are powerful hyperpolarisation techniques to increase the signal up to three order of magnitudes, these methods are not applicable in many situations. Especially for the investigation of living biological systems, hyperpolarisation is often difficult, because it requires specific chemical prerequisites of the investigated sample, for example, radicals in DNP. Hence, high field NMR/MRI is currently the only option to boost the signal in these circumstances. Novel, horizontal bore scanners, usually made for animal testing, are nowadays available for up to 15.2 T. These systems support very flexible interfacing to enable manifold research test for animals. Furthermore, these systems are optimised for MRI not NMR, hence they have limited capabilities with respect to spectroscopy. To combine the flexibility of horizontal bore scanners with the high-end image and shimming capabilities of the vertical bore scanners optimised for NMR, a novel type of probehead is required. The focus in this work is to develop a probe which enables augmentation of sample control and sensing. Therefore, the focus is laid on the modularity for integration additional components for research application. In this chapter the design and benchmarking tests as well as two applications are presented. In the second chapter, the focus is laid on the development of an MR compatible seeding substrate for *in-situ* cell analysis.

6.1. Design- and Manufacturing

The target system of the probe design is a Bruker AVANCE III 500 MHz wide-bore system with a bore diameter of 71.8 mm. Within the next chapter the most important design considerations are presented.

6.1.1. Design and construction

6.1.1.1. Mechanical design

The probe design is conducted mainly in SolidWorks, since the majority of parts are of mechanical nature. This is due to the fact that the concept of tuning and matching is adopted from the commercial products. This means that the probe is equipped with a modular interface for pre-tuned exchangeable probeheads. Therefore, per channel, one tuning and one matching capacitor is provided, whereas decoupling of multiple channels is realized on the probehead and hence, no advanced circuitry is required. The connectivity to a commercial gradient system (Micro 5, Bruker) is implemented. In the final design, the probe is equipped with two-channel support and gradient interface. In addition, the frame is manufactured using a hollow framework which integrates the mechanical support and the required feed-through within one system. In figure 6.1 the main components of the target MR unit are illustrated.

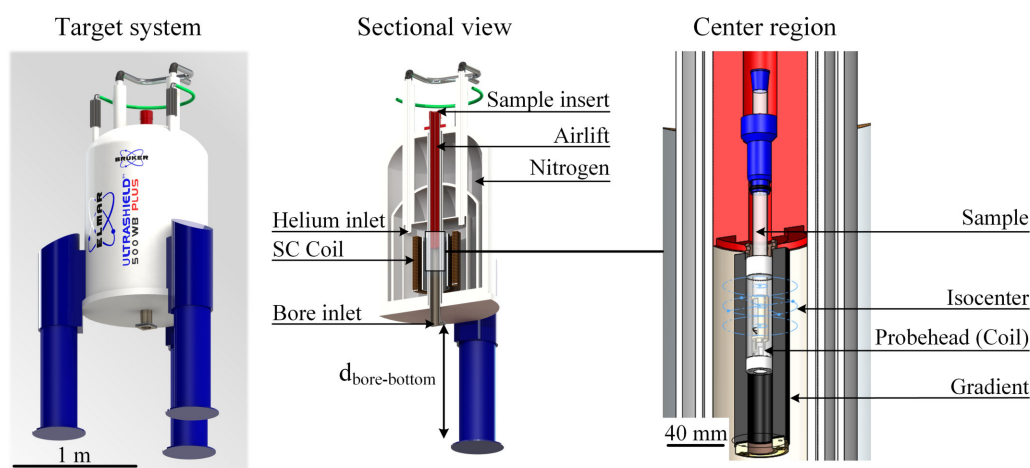


Figure 6.1.: 3D-CAD model of target system. Left: Visualisation and scale of the full model. Middle: Sectional view exposes the inner structure. The sample insert is conducted from top via air lift. The distance between bore entrance and bottom restricts the maximal length of the probe to enable insertion. Right: Center region with isocenter, probehead and gradient. The sample is settled at the bottom of the airlift.

For a proper design, the consideration of geometrical restrictions of the target system are crucial. The minimum length of the probe is given by the distance from the bore entrance to the isocenter. Once the probehead and gradient is mounted, the probehead needs to be placed at exactly the isocenter. The maximal length is given by the distance from the bottom to the bore entrance. An excess in length does not allow the user to insert the probe into the magnet. The outer diameter of the probe requires a tight fit to the diameter of the bore hole, to maintain the functionality of the airlift. Otherwise the sample exchange by the airlift is impeded. To satisfy these geometrical requirements, a

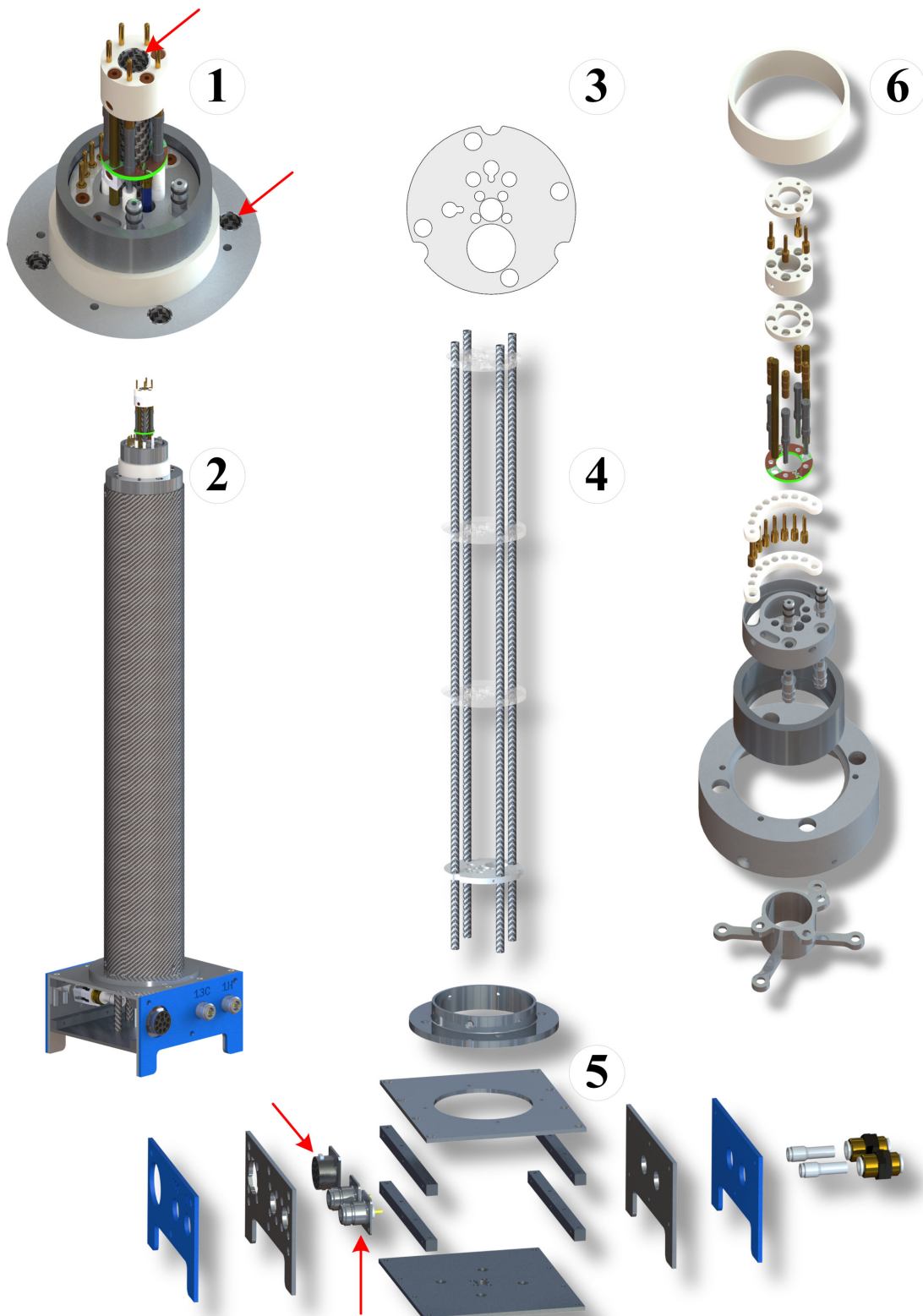


Figure 6.2.: Assembly and explosion view of the two-channel probe. The labels are: (1) Front end, (2) full assembly, (3) intermediate plate, (4) basic frame, (5) base housing and external connection interfaces, (6) explosion view of front end. The red arrows at (1) indicate the feed-throughs from top. The red arrows at (5) highlight the RF and gradient interface.

3D-CAD model is established which enhances the development process and decreases the number of iterations.

The fundamental probe components are illustrated using the explosion view in figure 6.2. Label 1 shows the front end for the coil and gradient interface. The red arrows indicate the central feed-through and one of the outer feed-throughs of the frame. The entire assembled probe is shown under label 2. Under label 3 one copy of the intermediate plate is displayed. It shows the large circle for the gradient power supply, two holes for water cooling lines of gradient, two opening for the RF cable and four small holes for the trimmer rods. The outer for holes are for the frame rods, the inner hole is the central feed-through. The base frame is illustrated under label 4. Notably, the first frame rods were made from carbon fibre and replaced in a later version by brass rods. Additionally, the intermediate plates in the second version are fully covered with copper foil. This approach provides a drastically improved grounding functionality which results in suppression of disturbance signals (see section 6.2). A full explosion view of the base is displayed under label 5. The two red arrows indicate the external RF (N-type) and gradient cable connection. The connector on the rightmost side are the fluid plugs for external water supply. Under label 6 you can see the explosion view of the front end. This front end is designed to enable the mounting of commercially available gradients and RF coils.

6.1.1.2. Materials

All used materials are generally "non-magnetic", whereat a more careful choice of materials and design has to be taken into account at the front end. For example, paramagnetic materials with ($\chi > 300ppm$) are acceptable at the base, but the use of materials at the front end must be restricted to "non-magnetic". Special trimmer capacitors for MR applications are available. Several materials which are applicable at the front end are aluminium, copper, high-quality brass¹, PTFE, PMMA, carbon- and glass-fibre. Of importance is the fact that the conductivity of carbon fibre produces a frequency shift is placed closed to the coil. On the other hand, the conductivity of carbon-fibres is too low if proper grounding is required. The better choice is brass due to its higher conductivity. In the case of non-conductive requirements, for example for the trimmer rods, glass-fibre based materials offer a better choice compared to carbon fibre.

6.1.1.3. Tuning and matching

As described, advanced RF circuitry, such as traps and balancing, is part of the exchangeable probehead. However, to enable tuning and matching after probe insertion into the magnet, a tuning and matching capacitor is installed, which is externally controllable. This approach is common practice for commercial modular probes. The capacitor configuration implemented in this probe is state-of-the-art, however, a short equivalent

¹low-quality brass often has traces of nickel

lumped-parameter-model will be discussed to present the functionality. Additionally, this provides the required information for planning specifically tailored, novel probeheads which are interfaceable with this probe. The probe consists of two trimmer capacitors per

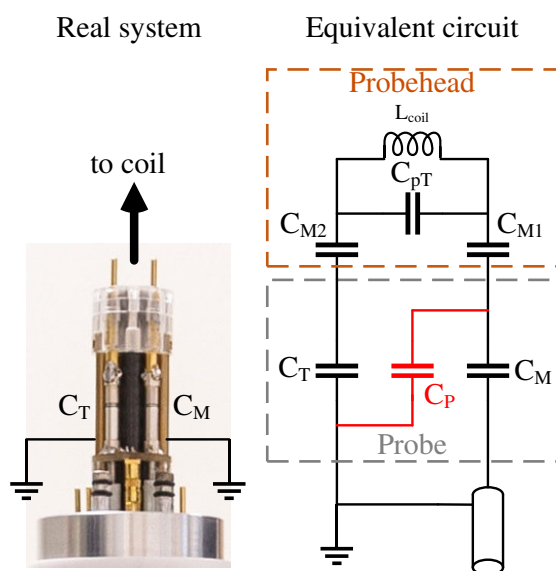


Figure 6.3.: Illustration of the equivalent circuit for tuning and matching. The probehead circuit is exemplary, it can be any RF circuit which is pre-tuned. The capacitors of the probe are C_M for matching and C_T for tuning. The capacitance C_P is of parasitic nature and not realized with a discrete element.

carbon fibre rod. Alternatively, a discrete capacitor with low capacity (< 1.5 pF) can be installed. In this probe, the capacitors C_T and C_M are both sapphire trimmer capacitors which have range from 0.5 to 10 pF (TEMEX TG 092).

RF channel. These trimmers are arranged in series, and as such, would both provide the functionality of a matching capacitor. A lumped-model on that basis will not reproduce the correct electric characteristics and does not allow to emulate realistic behaviour. It is of great importance to take into account the parasitic capacitance which establishes a shunt resistance after the first trimmer capacitor. This principle is visualised in figure 6.3. The shunt resistance parallelises the tuning capacitor C_T with the probehead circuit, which then allows the user to use this trimmer as a tuning capacitor. A functional probe, therefore requires a proper ground at the trimmer capacitors, if they are in serial configuration. Otherwise, no tuning will be possible but only matching will be functional. This is realized by proper ground planes close to the trimmers. In the figure this is seen by the brass rods of the frame and partially the

6.1.1.4. Assembly

Two versions of the probe are fabricated consecutively using the results from initial test for optimisation. The first version consisted of a single proton channel. A gradient interface was incorporated which involves the gradient power supply and the gradient cooling lines. In the commercial gradient a four-terminal temperature sensing is embedded, therefore four lines are integrated in addition to the power supply. The base housing was electrically connected to the MR unit and therefore grounded. All intermediate plates, which are fabricated from PMMA using laser cutting, were installed without a conductive cover. The carbon-fibre frame tubes had an isolation coating. As a result, this assembly had shielding problems, which led to distortion signals. The reason for this behaviour is the insufficient

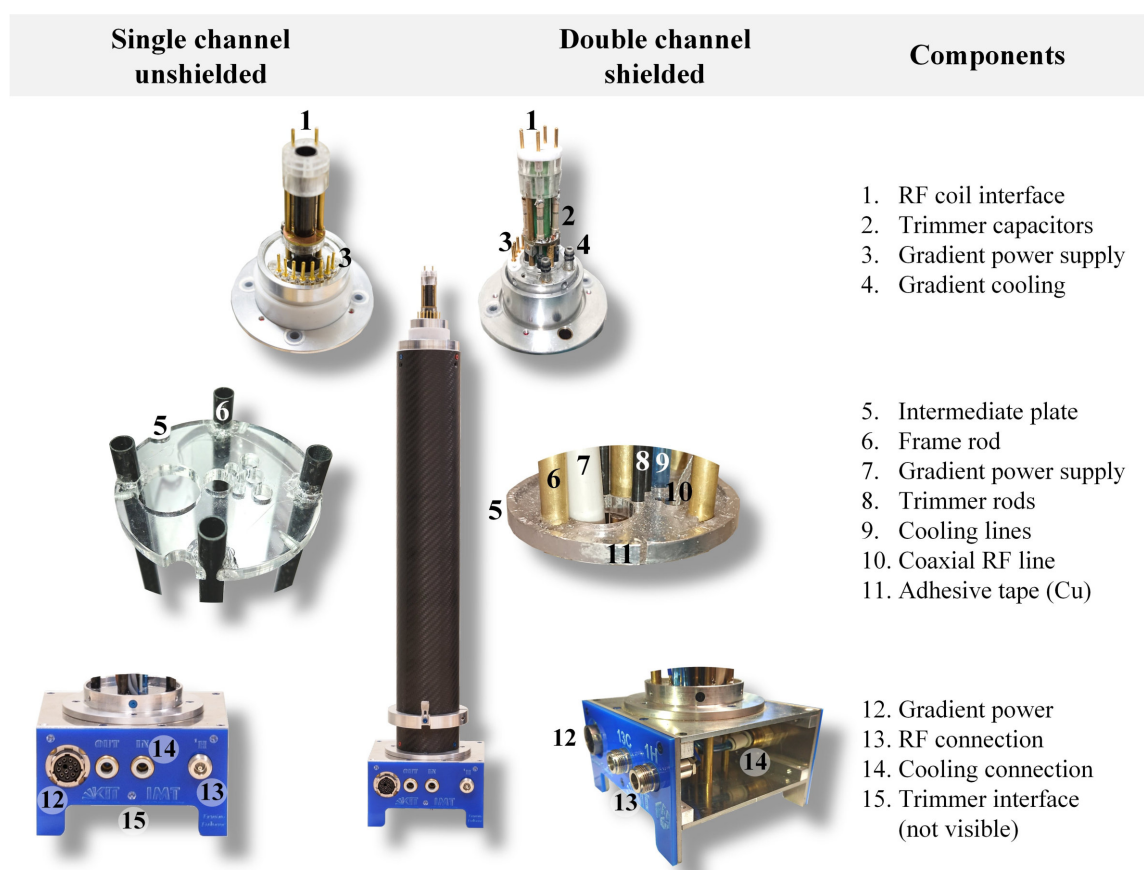


Figure 6.4.: The full probe in the centre is the first assembly with the carbon fibre housing (single channel configuration). Left: Components of the first assembled version with single channel configuration and unshielded. Right: Revised version with second channel

shielding of the RF resonator from the electromagnetic environment. Thus, interfering signals are picked up by the resonating circuit and mixed with the NMR signal.

The distortions signals were however not severe, and benchmarking test for linewidth and MRI could be conducted. A linewidth of 0.5 Hz (see section 6.2) was acceptable and the measured SNR was identical to the commercial probe. The gradient worked seamlessly and no degradation was measurable in comparison to the commercial probe. After these test a revised version has been manufactured taking into account the mentioned deficits. The carbon-fibre tubes are exchanged for better conducting brass tubes and the intermediate plates were covered with adhesive copper tape. The coaxial cable is stripped and the outer shield connected the the grounded frame. All intermediate plates, brass tubes and coaxial cables are connected using solder joints. Components of both versions are illustrated and labelled in figure 6.4. The outer carbon-fibre shell was applied in both cases. Degradation in form of interfering signals could not be observed after this upgrade. The results of the benchmarking tests are illustrated in the following section.

6.2. Benchmarking

In this section the results of the benchmarks tests are presented obtained from measurements using the two probes described in the previous section.

6.2.1. NMR measurements

To investigate the NMR capability 1D/2D-NMR experiments are conducted to test the performance of linewidth and signal performance. The 2D and carbon spectrum were recorded using a 5 mm double resonance coil and the 1D proton spectra were recorded using a 10 mm saddle coil of Bruker. All results are combined in figure 6.5. The spectra are

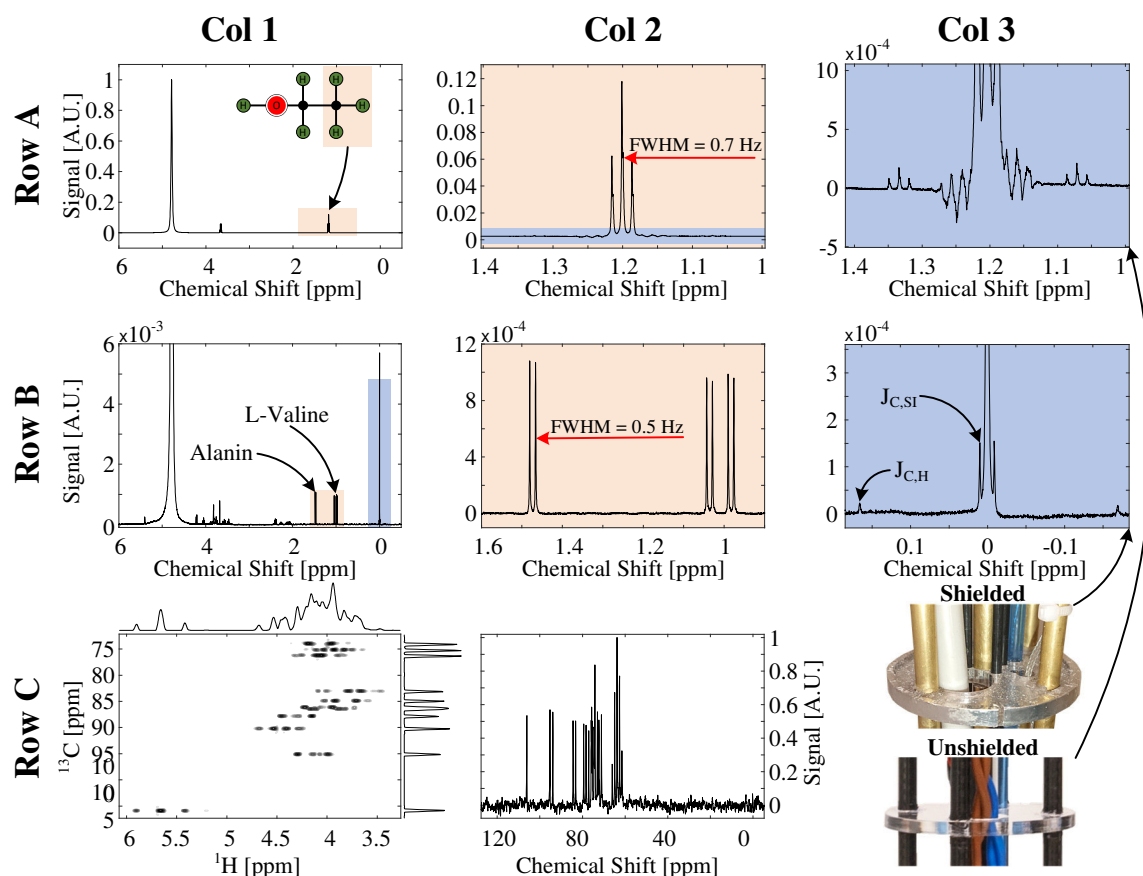


Figure 6.5.: Results from the NMR benchmark tests with unshielded single-channel and double-channel shielded probe. Row A: Spectrum of a 4 % ethanol solution in water obtained with the unshielded single-channel probe. A line width at half maximum was achieved with 0.7 Hz. Distortions are visible at the base of the multiplets. Row B: Experimental results of the mixture containing sucrose, alanine, valine and TSP. A line width of 0.5 Hz was achieved, and silicon and carbon satellites are clearly resolved. No distortion signals are visible. Bottom row: 2D HSQC measurement of sucrose and carbon spectrum of sucrose. At C3 the picture of a unshielded and shielded intermediate plate is displayed. In the shielded version the carbon-fibre tubes are replaced by brass tubes due to better conductivity.

normalised to the largest peak. The probe performance of the single-channel unshielded probe is displayed in row A. This spectrum is obtained from a 4 % aqueous solution of ethanol. A linewidth of 0.7 Hz was achieved. Clearly visible are the signal distortions at the base of the multiplets (A3). With the revised double-channel probe this distortion is removed due to the introduced shielding. The sample used for this experiment consisted of 10 mM sucrose, 10 mM glucose, 10 mM alanine, 10 mM valin and 10 mM TSP as reference dilute in aqueous solution. A linewidth of 0.5 Hz is achieved and clearly visible are the carbon and silicon satellites of the TSP. In addition, a carbon spectrum is presented in C2 obtained from a 1 M sucrose sample. The functionality of both channels was furthermore verified by acquiring a 2D spectrum of the sucrose sample shown in C1.

6.2.2. MR experiments

MR benchmark test were conducted to test the capabilities of the developed probe for applications in MR imaging experiments. Most important are the gradient functionality and the signal integrity.

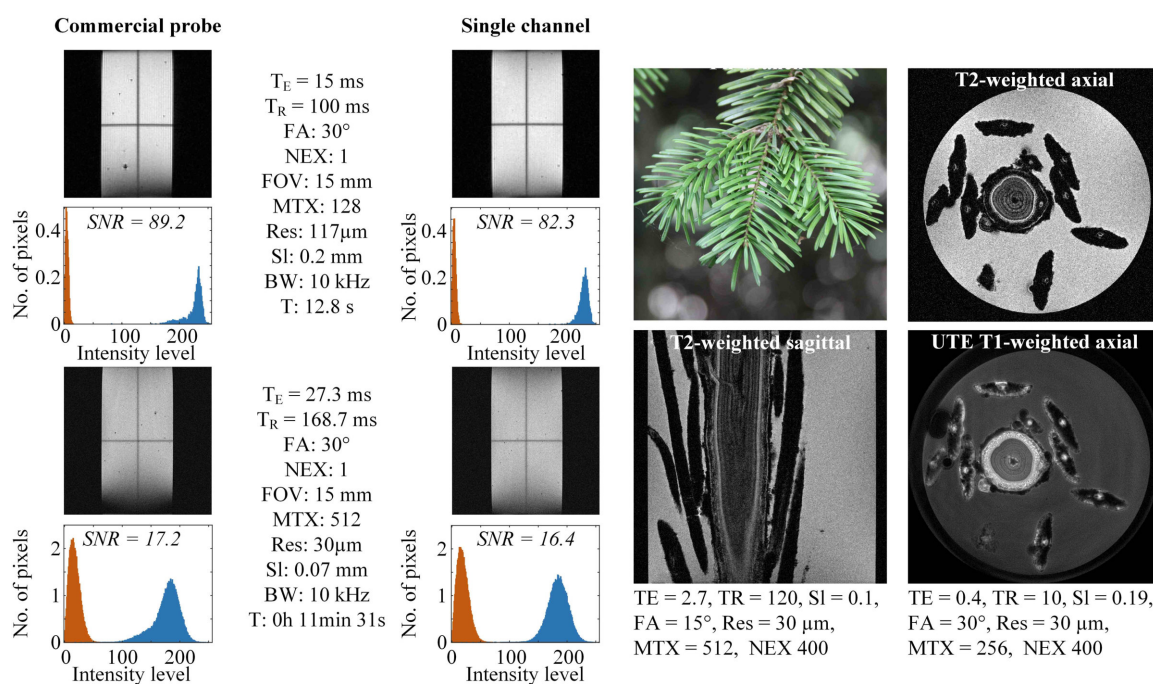


Figure 6.6.: Results of the MRI benchmark tests. On the left column the results of the MRI comparison tests are shown. The corresponding histogram of each MR image is plotted beneath. Orange represents the histogram from the background region and blue the histogram from the signal region. Both histograms are extracted from the vertical central regions of the image, excluding the darkening regions due to orthogonal slices. On the right, MR images acquired from a fir branch are displayed showing the application for different sequence types (GRE and UTE).

To evaluate these capabilities the general functionality was tested, such as leakage for gradient cooling and interfacing to the existing hardware. This interfacing works

seamlessly. To test the signalling, MRI images were acquired for identical parameters using the commercial probe and the developed probe. Results of MRI benchmark test with the single-channel unshielded probe are displayed in figure 6.6, where on the left side the comparison tests are illustrated. The acquired MR signals are comparable, however the SNR for the custom probe is slightly lower by approximately 7 %. The reason is due to the unshielded configuration, which increases the coupling of external disturbance signals (see figure 6.5) and a larger damping of the applied coaxial cable.

The SNR is computed using the following equation, where S_i stands for pixel of the signal region and B_i represents pixel in the background region:

$$SNR = \frac{\bar{S} - \bar{B}}{\sigma_B} \quad (6.1)$$

Therefore, the SNR is computed by measuring the distance of the mean value between signal and background region and divided by the standard deviation of the background signal.

6.3. Experiments

The manufactured probe is distributed in the research group and used for various applications. To demonstrate its applicability two examples are selected and illustrated. The experiments which are shown here, are not conducted by myself, and the presented illustrations are based on images by courtesy of Neil MacKinnon and Lorenzo Bordonali.

6.3.1. Oil droplet measurements

The oil droplet measurement is an experiment in which the abundance of water or oil in the coil region is measured. Alternating oil and water droplets are fed into the ROI using a flow setup. Water inside the RF-coil yields a strong MR signal, whereas oil is recognized due to the absence of an MR signal. The setup and initial results are shown in figure 6.7. These measurements are conducted by Omar Nassar and Neil MacKinnon.

On the left side in figure 6.7 the experimental setup is illustrated. Inserting additional hoses into the feed-throughs facilitates the usage as flow probe. The flow is externally controlled. On the right side of this figure first experimental results are displayed. Each peak represents an individual NMR experiment. While the oil-water droplets flow through the coil, the signal increases and decreases with time, dependent on the current sample inside the coil. This experiment uses the developed probe as a flow through probe using the available feed-throughs for inserting the flow lines. Further, experiments are planned for integrating additional electronics.

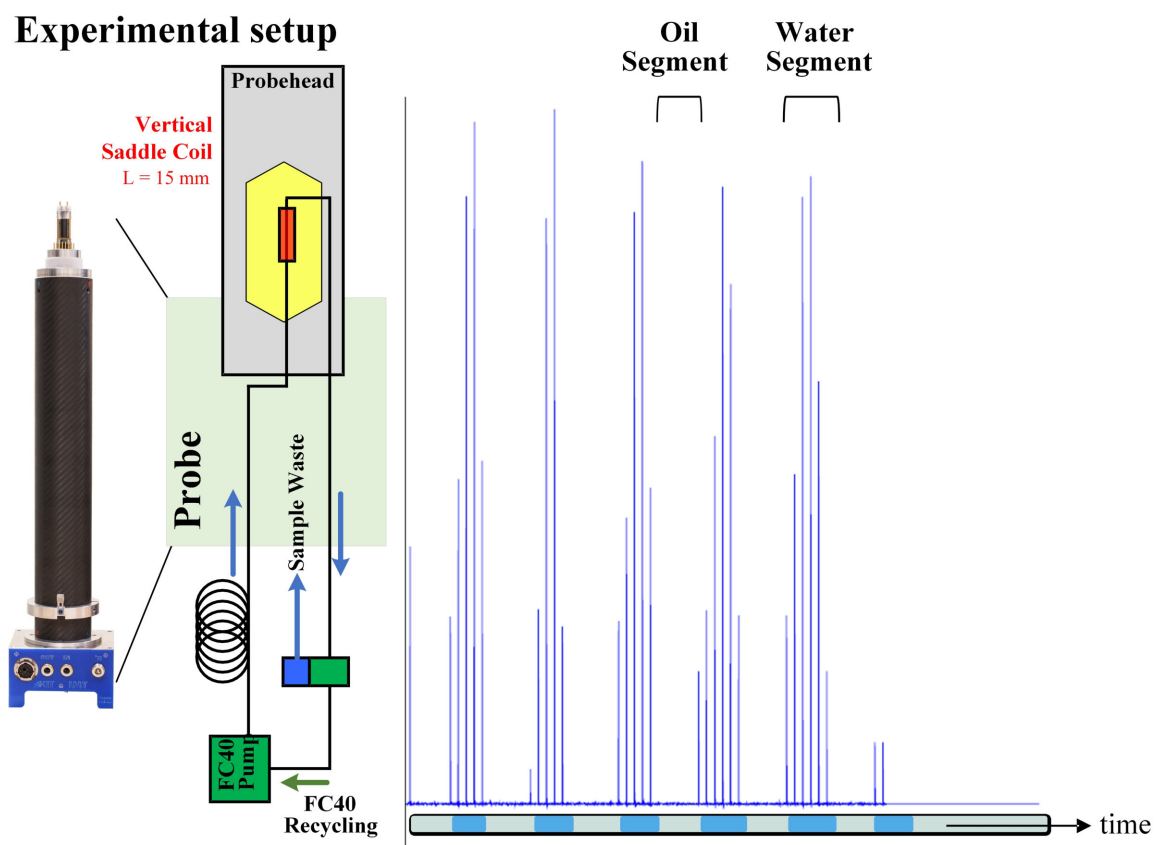


Figure 6.7.: Experimental setup for oil-water droplet measurements. The probe is applied in this configuration as flow probe. Each peak on the right side represents an individual NMR measurement, hence this figure shows many consecutive NMR measurements. The measurement graph is by courtesy of N. MacKinnon.

6.3.2. Hyperpolarisation experiments using parahydrogen (SABRE)

Another experiment uses a modified version of the presented probe with an increased central feed-through. This experiment is lead, designed and manufactured by Lorenzo Bordonali. A custom designed probehead is used to conducted SABRE hyperpolarisation on a microfluidic platform. This probehead is interface with a version of the presented probe. The setup is illustrated in figure 6.8.

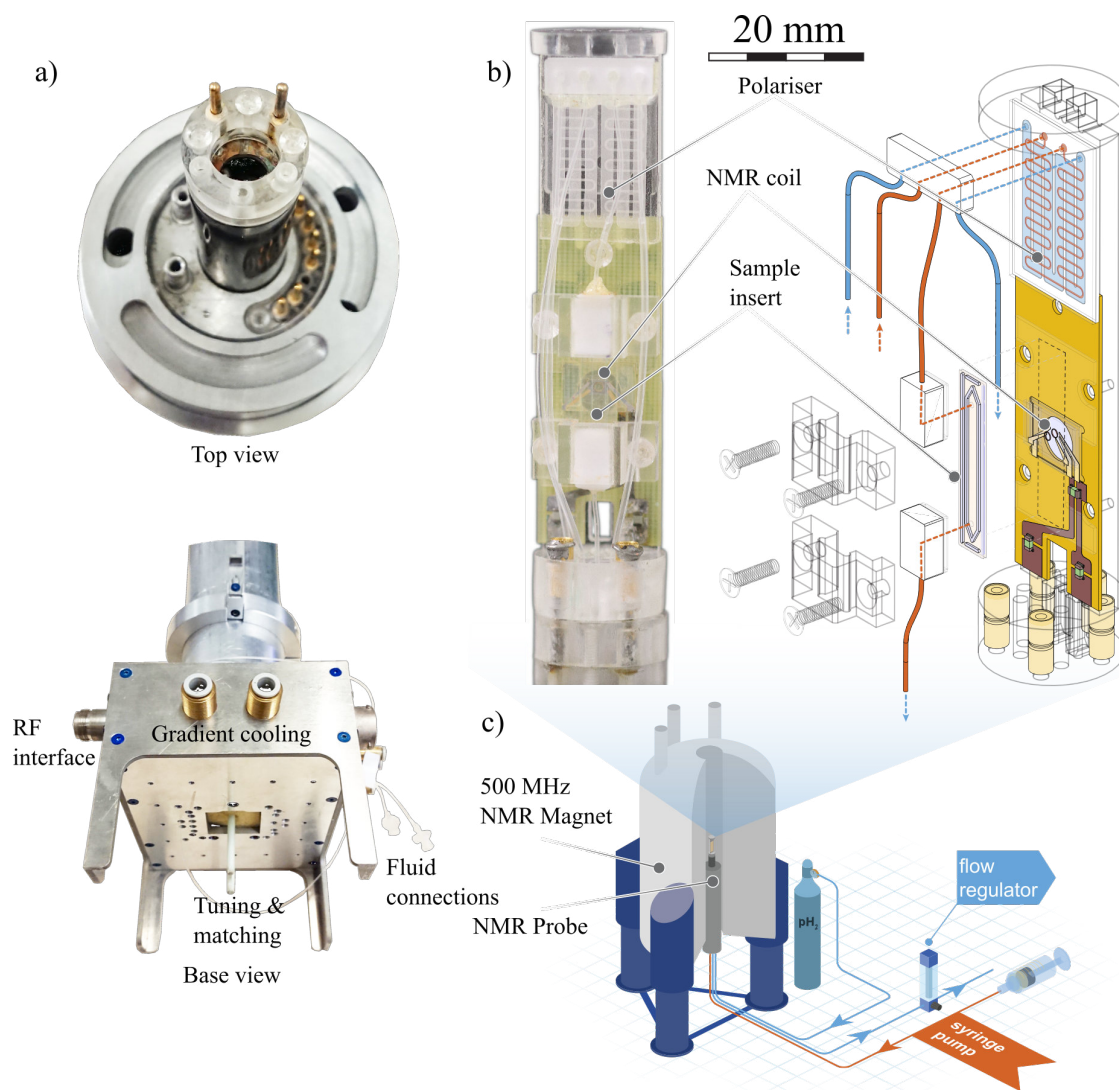


Figure 6.8.: Probe configuration for SABRE experiments in high field. On the left side the assembly of a modified probe version is displayed in which the central feed-through is extended. The subfigures b) and c) are reprinted from [EF04]) and generated by L. Bordonali.

On the left side one can see the used probe for this experiment. From the top view one can see that this probe is set up in a single-channel configuration with a gradient interface. The base shows the RF interface as well as the tuning and matching rods. Additional fluid connections are required for the specific experiment and make use of the central and frame

feed-throughs. On the right hand side the probe head configuration is displayed. This work is published under the title "Parahydrogen based NMR hyperpolarization goes micro: an alveolus for small molecule chemosensing" in Lab-on-a-chip.^[EF04].

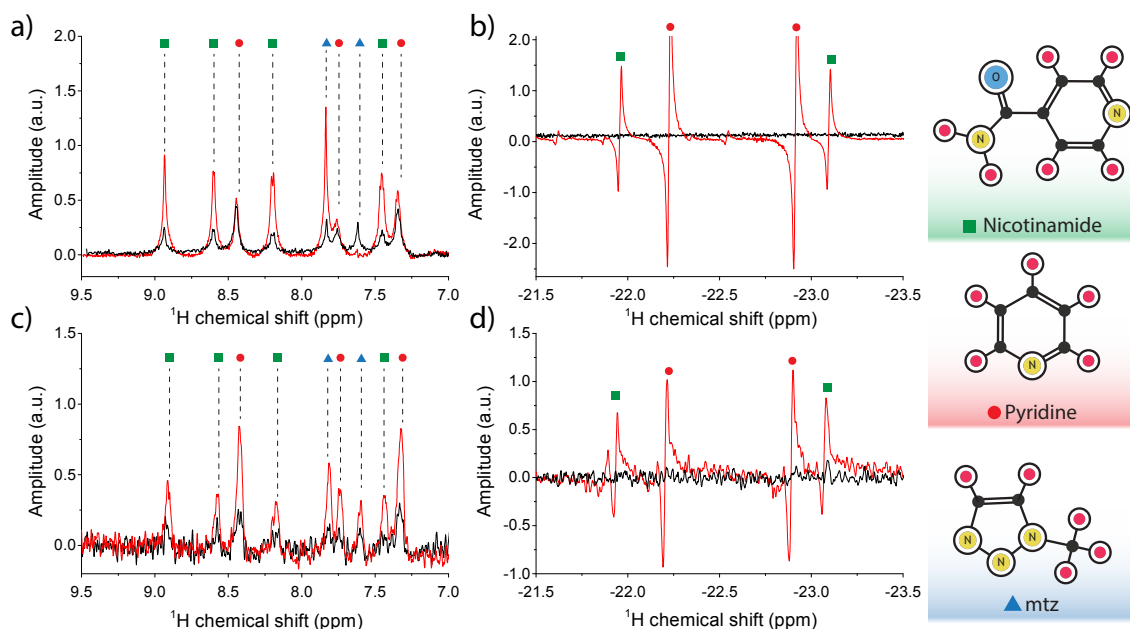


Figure 6.9.: Results of the hyperpolarisation experiment. ^1H spectra are shown in (a) of the analyte signal peaks. Red lines are under flow conditions and black lines are background measurements without flow. This figure is reprinted from [EF04]) and generated by L. Bordonali.

6.4. Conclusions

In this chapter the design and construction, assembly and benchmarking test of a novel probe design is presented. NMR and MRI benchmark test were conducted to evaluate the MR functionality of the probe. This includes measurement of spectral linewidth measurements which yields information of the \mathbf{B}_0 -compatibility as well as SNR test to evaluate the RF electronics compatibility. A redesign in which a proper ground shielding was introduced facilitates to remove any measurable distortion signals. The linewidth with 0.5 Hz is comparable to the commercially available probe. The SNR is slightly weaker, most probably due to cable losses. This can easily be improved by employing a coaxial cable exhibiting less damping, which however, may results in a thicker cable and/or higher costs. Most importantly, the probe finds application in various experimental environments and facilitates the flexibility to enables a rapid approach to design custom tailored NMR experiments. It is proved that the probe works in standard configuration using NMR tubes as well as for sophisticated flow through experiments. This is an important feature also for applications of in-situ biological experiments. Such require the constant supply of nurturing liquids and gases as well as the monitoring of different parameters such as

temperature. All setups of such experiments require the straightforward integration of these supply lines, and exactly this could be shown by similar configurations.

6.5. Outlook

A revised version of the probe is envisaged, which supports an extended feed-through. The design of this probe is concluded, and a first prototype has been manufactured and presented in figure 6.8. A second assembly is planned, with additional RF channels and a revised RF circuitry. The main goal of this probe is a vertical shaft with an increased cross-section area, to enable the mounting of a complete second probe inside. Therefore, the outer probe provides the RF interfacing and the inner probe can be fully tailored and equipped with a variety of signal and transport lines. Images of the 3D virtual model of this probe are displayed in figure 6.10. Orange encoded is a dummy model of such an additional probe. In collaboration with M. Wapler from the IMTEK, University of

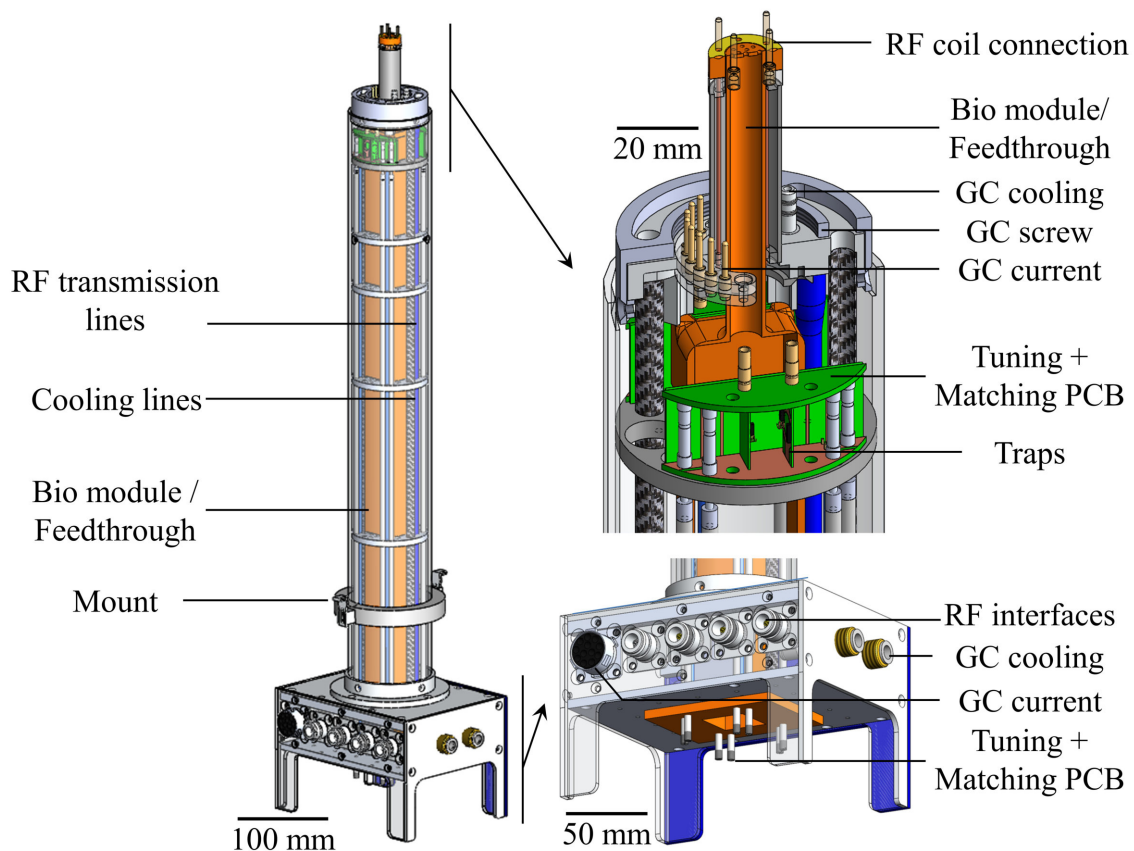


Figure 6.10.

Freiburg, the integration of an additional camera system is envisaged. This camera system, developed at IMTEK, is fully compatible to the MR probe and will allow simultaneous MR and optical imaging. Application areas of such a system are found in the biomedical

research. An example is the nematode *Caenorhabditis elegans* (*C. elegans*), which is often used as a model organism. A major goal is to enable MR imaging of a free-moving, unstressed worm. To obtain enough SNR for acceptable MR image quality, averaging is required. This in return, requires a novel acquisition scheme, which automatically updates the gradient sequence to take into account the moving worm. In other words, the image encoding requires an on-line adaption to the moving coordinate system of the worm. Initial procedures and acquisition protocols have been developed and virtually tested, aiming towards the establishment of optical tracking and real-time adaption of the MR gradient sequence. This work, with main contributions from M. Reischl and M. Jouda has been submitted to PLOS Computational Biology[EF07]. A combination of the integrated camera system, MR probe and this novel acquisition scheme can enable the MR imaging of an unrestrained, moving worm. A publication of the presented probe is planned in Review of Scientific Instruments [EF08].

7 | Evaluation of substrates for in-situ cultivation

An important application of NMR spectroscopy and MRI is the investigation of biological systems. NMR offers a wide spectrum of acquisition tools to investigate such systems on a molecular level using the ability of sophisticated quantitative chemical analysis. This comprehends the investigation of the molecular composition as well as the analysis of the chemical structure of the abundant molecules. MRI is another tool to further investigate the morphology of larger cell compounds and tissues. In form of many specifically tailored pulse sequences the investigation of various tissue properties is facilitated. Two salient approaches are (i) the relaxation-based contrast imaging methods and (ii) diffusion-weighted acquisition schemes. From biological point-of-view, there are two main methods to investigate living organisms. A first approach is to extract tissue from a living organism, so-called tissue-slices^[75,40]. A different approach is to extract stem cells with the potential to proliferate and subsequent culturing on a seeding substrate which results in tissue formation. Common requirements for both methods are the continuous supply and exchange of nurturing fluid as well as humidified gases (mixture of O₂/CO₂) and the temperature control^[74]. In case of cell culturing another important component is the substrate. Manifold seeding substrates are 2D systems, however, tissues normally develop as 3D structures. To better reproduce the *in-vivo* environment there is an increase development towards 3D scaffold systems. There are many 3D scaffold structures, even commercially available such as Matrigel[®], hydrogels and cryogels^[79]. These substrates, however, have several disadvantages. In Matrigels[®], culture variation have been observed due to its poorly chemical definition^[27]. Chemical processing is required to provide important cellular chemical cues^[35]. This increases the risk for entrapped residual chemicals, which then may impede with the reproducibility of the cells. Another important aspect is the degradation of the material which affects its mechanical integrity. If a scaffold is required which provides mechanical stability over a longer period of time, the presented approaches may be insufficient, since these scaffolds suffer from degradation.

To overcome these problems a scaffold on the basis of glassy carbon is introduced. Glassy carbon is a material which offers an excellent cytocompatibility^[148,106,2]. Apart from that, glassy carbon, derived from polymer structures, is a material which is extensively used in

batteries^[135], carbon MEMS and NEMS^[136,159]. The combination of cytocompatibility and process technology renders this material a promising candidate for novel 3D substrates. Moreover, glassy carbon has been employed for neural interfaces due to its conductive properties^[149]. In combination with NMR/MRI analysis, glassy carbon fulfils the requirements for cell culturing as well as the MR compatibility. Due to its low susceptibility, low conductivity and the absence of any protons, it does not (i) interfere with \mathbf{B}_0 and (ii) with \mathbf{B}_1 , and (iii) it does not produce proton background signals. Therefore, glassy carbon renders an ideal substrate material for *in-vitro*, *in-situ* studies for cell culture experiments using NMR/MRI analysis.

To prove the hypothesis, that glassy carbon scaffolds can serve as an MR compatible seeding substrate, a precursor cryogel is converted into a glassy carbon scaffold using pyrolysis. On these scaffolds NSCs are cultured, and after fixation, the cells cluster distribution is analysed using MRI. A precursor gel with known mechanical structures that facilitate cell growth is selected, to obtain an already tested, functional pore network. This work has been published previously by Bäcker et al.^[11]. Subsequently, MRI is employed to investigate the shrinkage of the scaffold and to analyse the preservation of the pore structure. This is done by comparing the pre- and post-pyrolysis scaffolds. In the following sections this procedure is presented in detail. This work is published under the title "3D Carbon Scaffolds for Neural Stem Cell Culture and Magnetic Resonance Imaging" in *Advanced Healthcare Materials*^[EF02]. The major focus in the next sections is laid on the contribution from my side, which is the MR pore size analysis and MR imaging of cells. The pyrolysis was performed by Swati Sharma and the precursor scaffolds were provided by Anne Bäcker^[11], both at IMT, KIT. The cell culturing was conducted by Matthias Kirsch from University of Freiburg, Department of Anatomy and Cell Biology.

7.1. Methods

In this section the fundamental methods are reported, which are used to obtain MR images of cultured NSCs including the porosity analysis of the precursor and carbonised scaffolds.

7.1.1. Cryogel fabrication, pyrolysis and cell culturing

The entire process flow which shows the steps from cryogel fabrication to MR imaging of the cultured cell clusters is illustrated in figure 7.1. Cryogels are obtained by following the protocol of Kumar and Srivastava^[86]. In an initial aqueous solution 1 % chitosan, 6 % agarose and 2 % gelatin are mixed and cross-linked at room temperature and poured into a syringe. Subsequently the mixture is cooled down to $-21\text{ }^\circ\text{C}$ and after 5 hours thawed to room temperature followed by dicing. This obtained scaffold are then pyrolysed at $900\text{ }^\circ\text{C}$. A ramp rate of $3\text{ }^\circ\text{C}/\text{min}$ is applied, followed by cooling down to room temperature naturally. Neurosphere cultures are obtained from adult mice and

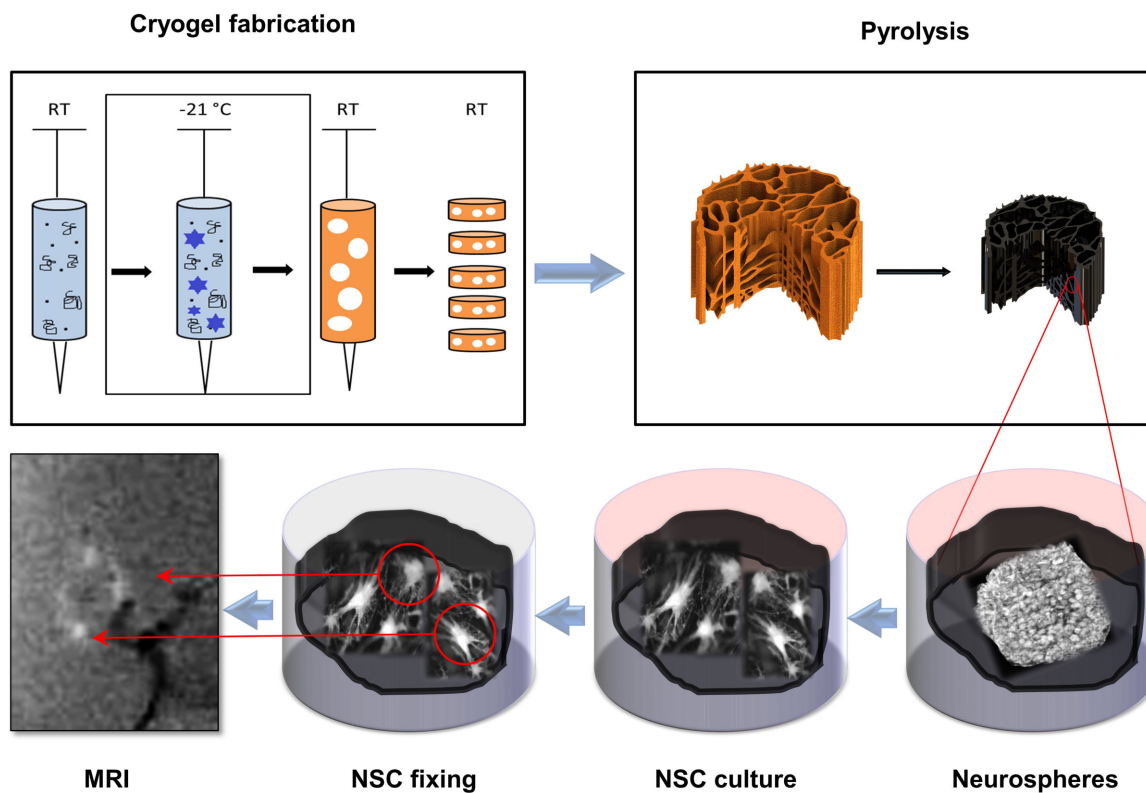


Figure 7.1.: Process flow of the glassy carbon scaffold fabrication, cell culturing fixation and final MR imaging. Image adapted from [EF02] and generated by A. Bäcker, E. Fuhrer and S. Sharma.

subsequently seeded for 5 days in growth medium. Prior to culturing, the carbon scaffolds are sterilised by immersion in isopropanol. After washing with water, the scaffolds are immersed in growth medium. An important step is the placement in an excitator to remove air bubbles from the pores. Afterwards neurospheres are transferred by dissociating with accutase and 250 000 cells in 5 μ l growth medium and seeding on top of the scaffolds. This step is followed by incubation at 37 °C in 5 % CO₂ for 30 min. Then the scaffolds are transferred to individual well plates and cultured for 4 days. A 50 % medium change is conducted after 2 days. Afterwards cell cultures are fixed with para-formaldehyde in phosphate buffer and transferred into glass tubes for MRI. Results from SEM imaging and fluorescence imaging are presented elsewhere^[EF02].

7.1.2. Porosity analysis using MRI

For successful cell culturing, the size and morphology of the scaffold structures play a crucial role. To investigate the impact of pyrolysis on the morphology and porosity, MRI is used as a non-destructive tool, to conduct image-based porosity analysis of identical scaffolds before and after pyrolysis. The acquisition and post-processing protocol is identical for both scaffold types. Therefore, the scaffolds are immersed in an aqueous CuSO₄ solution, which has reduced T1-time. For both scaffold types, a 3D-GRE image protocol is used with

the parameters: TR = 50 ms, TE = 7 ms, BW = 22.5 kHz, FA = 80°, and an isotropic resolution of 30 µm. The matrix size is 230 × 320 × 320 for the cryogel scaffolds and 160 × 320 × 320 for the glassy carbon scaffold. The image analysis is based on extracting the scaffold from the background and to produce a reconstructed virtual 3D model, which is then analysed with respect to volume and surface area. The segmentation procedure uses thresholding based on Otsu's method (see chapter 2.3.2). For robust thresholding it is essential to obtain the image data with large SNR and homogenous background. Furthermore, any air bubbles leading to blackened regions in the MR image will be erroneously labelled as scaffold structure and falsify the data. Therefore, two approaches were applied which will be described in detail. To obtain maximal SNR per acquisition time a CuSO₄ solution was prepared which is tailored for the desired acquisition timing parameters. Subsequently the process to immerse scaffolds in water while avoiding air bubble trapping is presented.

7.1.2.1. Preparation of CuSO₄-solution for maximising CNR

To acquire MR images of the scaffolds, these are immersed in an aqueous solution. Regions that are occupied with scaffold material appear as dark voxels. A thresholding procedure, operated on the obtained MR images, enable the virtual reconstruction of the scaffold. Accurate thresholding is achieved with sufficient SNR, which is optimised using the contrast agent CuSO₄. Most signal is obtained when all polarised protons contribute to the MR signal. This means that for each excitation the entire longitudinal

Table 7.1.: Values for *A* and *B* as published by Kjær et al.^[78] and extrapolated values for **B**₀ = 11.7 T in red.

<i>f_L</i>	<i>T</i> ₁		<i>T</i> ₂	
	<i>A</i>	<i>B</i>	<i>A</i>	<i>B</i>
64 MHz	0.730	0.36	0.921	0.35
90 MHz	0.678	0.44	-	-
270 MHz	0.632	0.32	0.843	0.27
500 MHz	0.536	0.36	0.745	0.25

magnetisation is available and tilted into the horizontal plane. Furthermore, after excitation no significant transverse relaxation takes place. This renders a typical proton density weighted image. For pure water, however, T₁ relaxation can take up to 3s, which makes the repetition, and thus acquisition time, very long. Therefore, the water requires doping with the exact amount of CuSO₄ to guarantee full T₁-relaxation within TR and minimal transverse relax-

ation within TE. Since minimising TE requires an increased bandwidth and thus lowers the SNR, the task is to find the optimal concentration of CuSO₄, that satisfies the demands for full T₁-relaxation within a certain TR and minimal T₂-relaxation for a given TE and bandwidth. In a publication by Kjær et al.^[78], the relaxation times of CuSO₄ depending on **B**₀ and CuSO₄-concentration *c*_{CuSO₄} are published.

$$\frac{1}{T_i} = A \left[\frac{1}{s \cdot \text{mmol/l}} \right] \cdot c_{\text{CuSO}_4} + B \left[\frac{1}{s} \right] \quad (7.1)$$

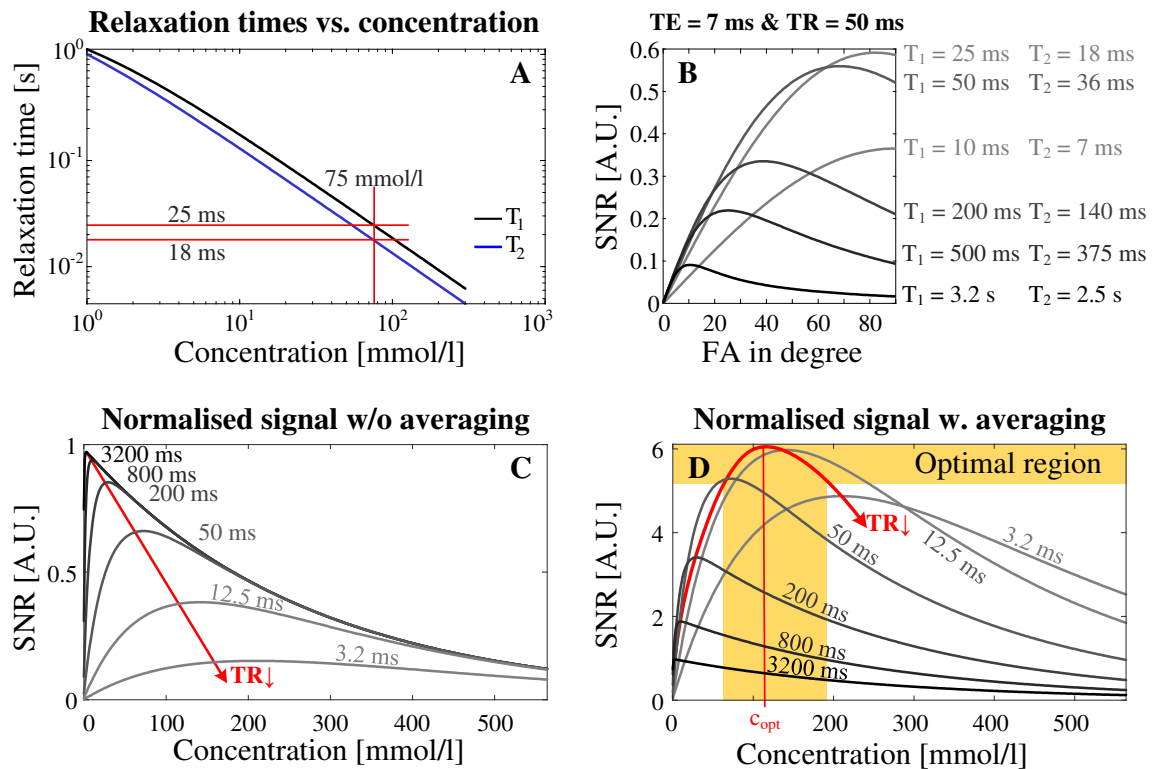


Figure 7.2.: Graphs of signal dependencies to find optimal optimal CuSO_4 -concentration and sequence parameters. A) Dependency of relaxation time of aqueous solution on CuSO_4 -concentration for $B_0 = 11.7$ T. B) Relative SNR for depending on the FA for different T_1/T_2 combinations and short TR. The signal and Ernst angle increase up to an optimal point for approximately $T_1/T_2 = 25$ ms/18 ms. C) Dependence on SNR as a function of concentration for different TR without averaging. If TR is decreased, the maximum SNR appears for higher concentrations of CuSO_4 . D) Taking into account the noise reduction due to averaging, an optimal SNR is reached for a concentration of approximately $c = 125$ mmol/l and TR = 15 ms. A factor of 5-6 in SNR enhancement can be reached compared to pure water imaging.

The inverse relaxation times T_1 and T_2 as a function of CuSO_4 -concentration c_{CuSO_4} (in the further text c) are given by the linear-affine function shown in equation 7.1. In this equation, $i \in \{1, 2\}$ stands for the corresponding relaxation time (T_1 or T_2), and A is the corresponding factor for the linear relation of concentration and relaxation time, and B the corresponding inverse relaxation times for pure water ($c_{\text{CuSO}_4} = 0$). By using the published data, the parameters for A and B are derived, and the correct relaxation times for $B_0 = 11.7$ T are computed. The entire parameter space for optimal SNR, however, is quite large and hardware limitations have to be taken into account. The receiving bandwidth BW and echo time TE, are interdependent and also connected to the number of readout pixels. Further parameters are the repetition time TR, flip angle FA and the number of averages N_{Avg} . The echo time TE should not exceed 10 ms because GRE sequences are prone to susceptibility artefacts, for example from small trapped air bubbles. A minimum matrix size is required to obtain an acceptable resolution for the required FOV. An echo time of TE = 7 ms is

good trade-off, which allows a bandwidth down to 22.5 kHz while enabling the acquisition of 200-350 readout pixels. Having BW, and TE defined, the parameters FA, TR, and c_{CuSO_4} are subsequently optimised. By combining equation 2.26 introduced in chapter 2.1.4.3, and equation 7.1, one can optimise the $CuSO_4$ -concentration which yields an optimal SNR. The equation to optimise SNR is governed by:

$$SNR(c, TR, \alpha_{FA}) = PD \cdot \sin(\alpha_{FA}) \frac{\left(1 - \exp\left(-\frac{TR}{T_1(c)}\right)\right) \exp\left(-\frac{TE}{T_2(c)}\right)}{1 - \cos(\alpha_{FA}) \exp\left(-\frac{TE}{T_2(c)}\right)} \cdot \sqrt{N_{Avg}} \quad (7.2)$$

Considering a normalised Proton density ($PD = 1$) and no averaging ($N_{avg} = 1$), we obtain for $TR \rightarrow \infty$ and $TE \rightarrow 0$ and $\alpha_{FA} = 90^\circ$ a SNR of one, which serves as a reference. The results of this optimisation procedure is illustrated in figure 7.2. In figure 7.2 A the relation of relaxation time and $CuSO_4$ -concentration is shown. The finally selected concentration value and its corresponding relaxation times are indicated with red lines. In figure B the dependence of FA and relaxation times for given parameters TE and TR are illustrated. A higher concentration yields a shorter T_1 and T_2 , which results in an increase of the Ernst angle and signal, until an optimum is reached. The further increase of concentration yields a decay of signal due to rapid transverse relaxation. The results for setting the flip angle $FA = 90^\circ$, while varying TR and concentration, are displayed in figure 7.2 C and D. If averaging is not taken into account, one can see a linear increase of the maxima with concentration. For more realistic SNR, averaging has to be taken into account, which then shows an optimum point for the concentration and the corresponding TR as shown in figure 7.2 D. That optimum is at $c = 125 \text{ mmol/l}$ and $TR = 15 \text{ ms}$, which yields an enhancement of 6^1 . Final acquisitions are conducted using a $CuSO_4$ -concentration of $c = 75 \text{ mmol/l} = 12 \text{ g/l}$, which yields $T_1 = 25 \text{ ms}$ and $T_2 = 18 \text{ ms}$, which is slightly below the optimum. The reason is that a small TR yields a large gradient duty cycle. The selected value offers a good compromise between SNR and moderate gradient duty cycle, especially in the view of longer acquisition durations.

7.1.2.2. Desiccator supported immersion of scaffolds in aqueous solution.

Reliable porosity data analysis requires artefact free MR images. Any air bubbles thwart the automatic MR image-based post-processing and render data analysis impossible. Hence, bubble-free scaffold immersion in aqueous solution is an essential process step. A desiccator was developed which enables the bubble-free filling of aqueous solution into an NMR tube. Therefore, the NMR tube including the sample is placed inside, the desiccator. A vacuum pump (down to 0.1 mbar) is connected to the vacuum line, and the starting of the vacuum pumping automatically closes the lid. After the vacuum is established, the inlet is opened

¹In all calculation residual transversal magnetisation in the subsequent FID is not taken into account due to simplification. Hence, this calculation emulates spoiled sequences, which is of course not applied in the real acquisition, since non-spoiling increases the SNR.

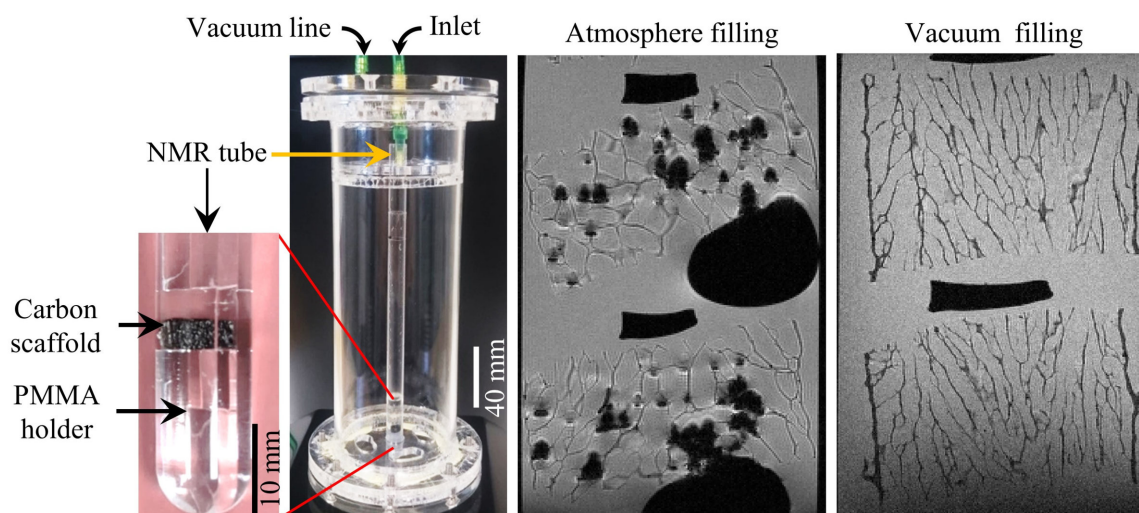


Figure 7.3.: Left: Setup of the desiccator and a carbon scaffold in the NMR sample holder. Right: Two comparative images show resulting MR images of a scaffold immersed in aqueous solution and filled under atmospheric condition and in vacuum. The vast amount of air bubbles appearing as dark spots are clearly visible. Photographs are adapted from [EF02].

and the aqueous solution is sucked into the NMR tube. A small nozzle facilitates a steady and slow inflow. The desiccator and comparative images are shown in figure 7.3.

7.1.3. MRI imaging of fixed cell cultures

MRI imaging of cell clusters are acquired with the scaffolds in buffer solution. Due to the longer relaxation times, the acquisition parameters differ from the acquisition parameters used for porosity analysis. The following parameters are applied: Sequence 3D GRE, TE = 2.75ms, TR = 100 ms, FA = 45°, BW = 100 kHz, Matrix size: 160 × 160 × 320 with an isotropic resolution of 31.25 μm. Prior to imaging, a scaffold was crushed to enable access for optical inspection. This procedure facilitated the confirmation of MR signals that originate from cell clusters, by means of direct comparison of MR images and optical images.

7.1.4. Postprocessing

7.1.4.1. Porosity analysis

The 3D MRI data are exported as DICOM-files which can directly be read from MATLAB and saved as binary matrices. To simplify the processing, a cube occupying a sub-volume of the scaffold is extracted. Therefore, the thresholding based on the histogram is reliable since the distribution is not skewed due to over-representation of bright background pixels. After thresholding of this cube, for which scaffold voxels are labelled with zero and background voxels are labelled with one, an isosurface object is created using Matlab's in-build function *isosurface*. This function creates a triangular mesh connecting the points

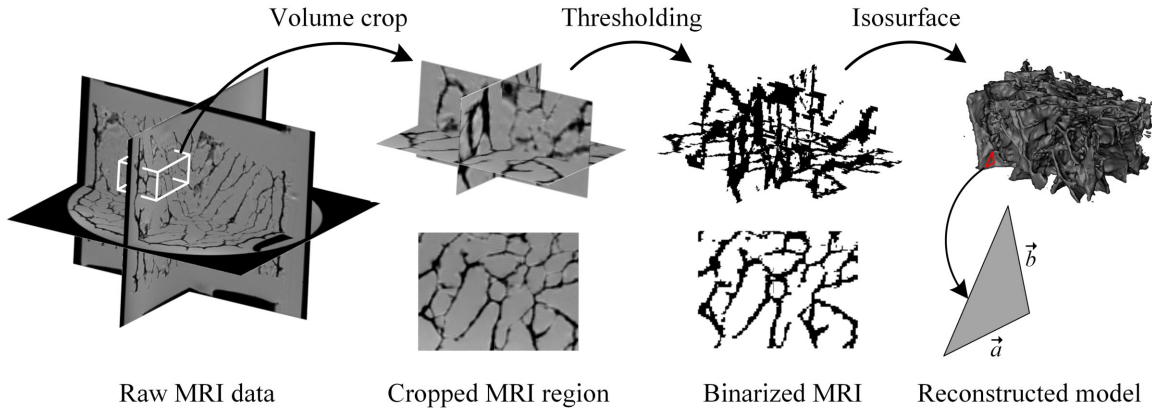


Figure 7.4.: Visualisation of post-processing pipeline to compute porosity data. From the raw 3D MRI data a cube of known dimension is cropped. This matrix is binarised using Otsu’s method. Subsequently, the isosurface is computed which consist of triangular elements. The surface of a single element is computed using the cross product, and the sum of all elements yields the total surface. The process from volume cropping to surface computation is repeated, until the major volume of the scaffold is analysed.

of zero-value, and thus represent the scaffold. The total area of the isosurface object, which represents the surface area A_S of a scaffold, is obtained as the sum of the areas of all triangular faces. To obtain the value for A_S the following equation is applied:

$$A_S = \frac{1}{2} \sum_{i=1}^N |\vec{a}_i \times \vec{b}_i| \quad (7.3)$$

The vectors \vec{a}_i and \vec{b}_i are the edges of element i , as illustrated in figure 7.4, and the final surface is a result of the sum of all N elements. The total volume of the scaffold V_S is the sum of all voxels assigned with zero after thresholding. The total occupied volume of both, void space and material, V_{tot} equals the volume of the cube. Based on this data the surface to volume ratio (SA:V) is given by:

$$SA:V = \frac{A_S}{V_{tot}} \quad (7.4)$$

The porosity ϕ is calculated using the following relation:

$$\phi = \frac{V_S}{V_{tot}} \quad (7.5)$$

In summary, the approach of porosity analysis using local cubes exhibits many advantages. The total volume of the cube is occupied with scaffold material, which ensures a correct histogram, since background pixels are not over-represented compared to a global thresholding routine. The impact on background inhomogeneity on the threshold value becomes less dominant, this effect scales with the size of the cube. Furthermore, the calculation of V_{tot} for an entire scaffold is not easy automatable since the scaffold boundaries are of random nature. Using a volume crop, solves this problem automatically,

since the total volume V_{tot} simply equals the cropped volume. Another important aspect, is the fact that the program sequence is repeated, and many different regions per scaffold are analysed. In principle, this allows to investigate the homogeneity of the scaffold, by comparing the results obtained from different regions. On the other hand, the size of the cube, should not become critically small. This means it should occupy, a certain volume which contains pores to yield reliable data. If, for example, the cropped cube fits into one pore, and not containing any scaffold materials the result is unusable. In this work the cube sizes and locations are implemented manually, however, an automatisisation routine is plausible.

7.1.4.2. 3D reconstruction and virtual inspection

For visual inspection the freeware "3D-slicer" is used. It is a modular software mainly developed for processing DICOM-files and used in clinical medicine. Once the MRI data is loaded, it offers a wide selection of post-processing options, such as volume cropping and geometric transformations, multilevel-segmentation, image-filtering, volume rendering, statistical analysis, model-making and many more. The latter module "model-making" is extensively used for rendering 3D models on the basis of the MR image data. After segmentation, this module computes the isosurface on the basis of the binarised 3D data, and offers various smoothing algorithms. Advanced in-built visualisation tools are available, such as anaglyph 3D rendering, which enables the stereoscopic view while maintaining the colour integrity. Further options for data visualisation, are facilitated with advanced rendering tools which enables settings such as reflection, opacity, and many more. Finally, the 3D model can be exported as an STL-file which allows 3D printing.

7.2. Experimental results

In this section the most important results are presented. In the first part results to the porosity analysis are detailed, in the second part the results of the cell imaging.

7.2.1. Porosity measurements and analysis of scaffold morphology

Before conducting the cell seeding works, MR experiments were conducted to investigate the porosity and morphology of the gel and carbon scaffold before and after pyrolysis. As described in section 7.1.2.1 it is of great importance to obtain a large SNR

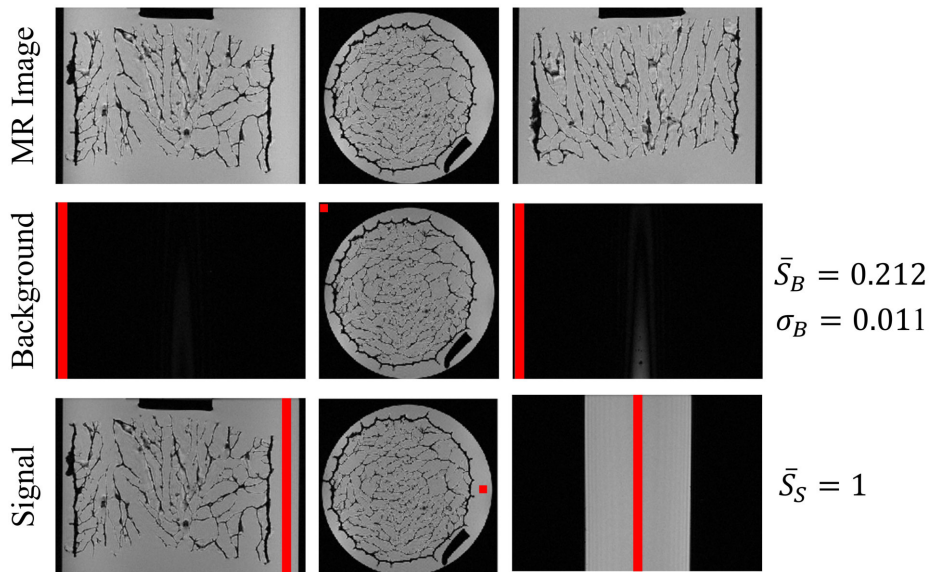


Figure 7.5.: SNR computation for MR images obtained from porosity analysis. First the difference of the mean signal value and the mean background value is determined. The SNR equals then obtained by dividing this difference by the standard deviation of the background signal. The selected regions for background and signal regions are indicated by the red areas. The SNR is: $\text{SNR} = (\bar{S}_S - \bar{S}_B) / \sigma_B = 87.7$

(which equals in that case the CNR) to enable a reliable thresholding process. In figure 7.5 the MR image obtained from an acquisition using an aqueous CuSO_4 -solution

Table 7.2.: Results of porosity ϕ and surface-to-volume ratio SA:V measurements.

Scaffold	ϕ	SA:V
Cryogel	$(83 \pm 4) \%$	6.8 ± 0.5
Carbon	$(58 \pm 6) \%$	11.5 ± 0.5

with a concentration of $c = 12 \text{ g/l}$ is shown. The imaging parameters were: TE = 7 ms, TR = 7 ms, FA = 80° , resolution = $30 \mu\text{m}$ isotropic, Matrix size = $230 \times 320 \times 320$, BW = 22.5 kHz, Averages = 13, total acquisition time = 18.5 h, RF-coil: 10 mm saddle coil. The obtained SNR is 87.7. This result shows the strength of using an optimised CuSO_4 -solution for maximising SNR when possible. To provide a comparison: The high-resolution images in figure 6.5 show an

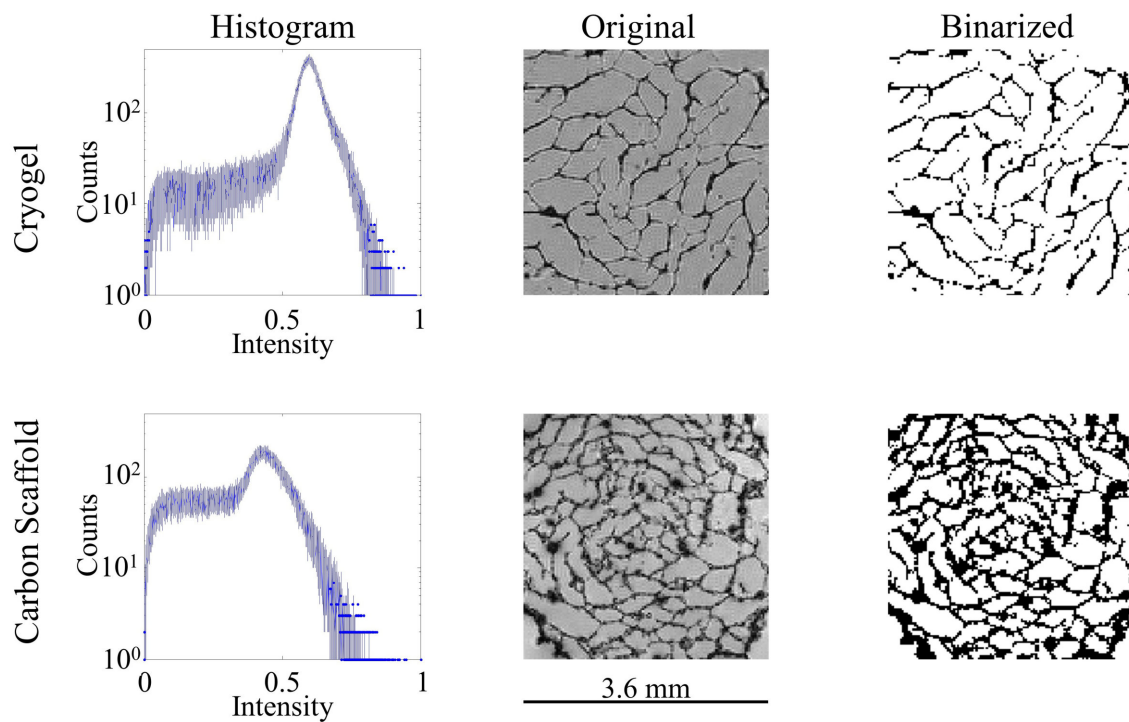


Figure 7.6.: Comparison of the histogram of cryogel and carbon scaffold. Both MR section show the same FOV, therefore the reduction of pore size due to shrinkage resulting from pyrolysis is clearly visible. This shrinkage yields a decrease of porosity and an increase of SA:V. (Adapted from [EF02]).

approximate SNR of 17 which is 5 times less SNR than reported here, but for many applications still acceptable. This means we can obtain an MR image with an SNR of 17, using the 10 mm coil while having an isotropic resolution of $30\ \mu\text{m}$ in under one hour. This comes from the fact that, five times less SNR, allows for 25-fold reduction in averaging. In figure 7.6 results from the binarisation are presented. The histogram of both samples appears with unimodal peaks. This is due to the fact that the applied resolution of $30\ \mu\text{m}$ is in the range of the wall size. Furthermore, the cryogels absorb water which means that reduced signal is also obtained from the walls. Here, the application of Otsu's method for correct thresholding is crucial to obtain reliable results. The investigation was made for two different gels which yield identical results. By comparing the scaffold before and after pyrolysis, the decrease of porosity is obvious. The measurement results of porosity ϕ and surface-to-volume ratio SA:V measurements detailed in table 7.2 confirm this visual perception.

In figure 7.7, reconstructed 3D images and axial, as well as sagittal MR images of the identical scaffold, are presented. The preservation of mechanical structures is clearly visible.

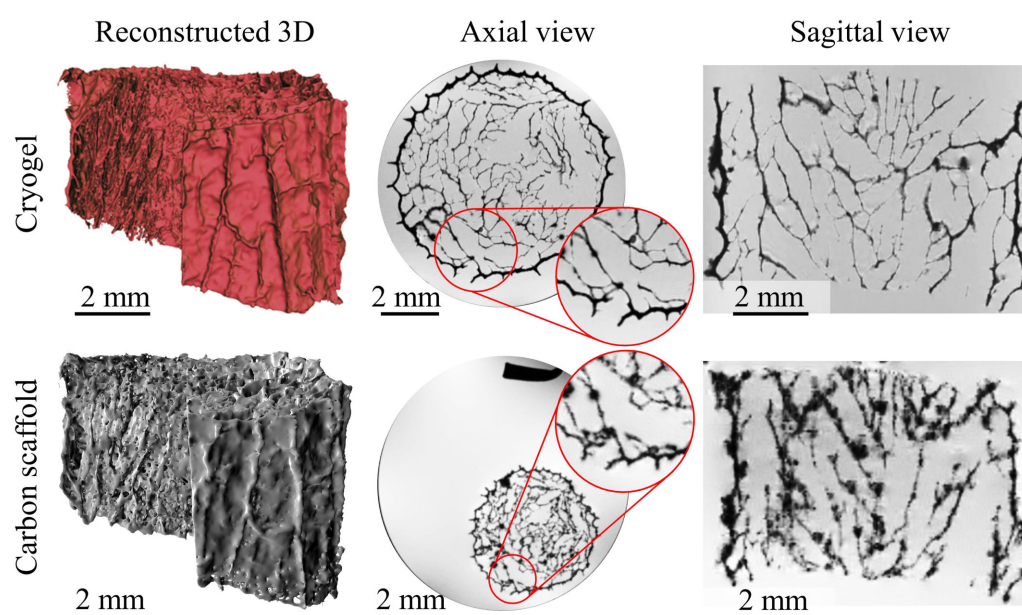


Figure 7.7.: Reconstructed 3D model derived from MR data. The data is from the identical cryogel before and after carbonisation. Upscaling of the carbon scaffold supports the visualisation of the resemblance. The axial view is not rescaled to illustrate the shrinkage. The circular insets show the preservation of morphological details. On the right side a highly interconnected pore network is visible in the sagittal view. To a larger proportion, the channels are oriented in vertical direction. (Adapted from [EF02]).

7.2.2. MR imaging of cell clusters

The scaffold with the cells were poured into an NMR glass tube including the fixation liquid. The breaking of the scaffold facilitates the optical investigation of the cell clusters. This is important, because reliable relaxation data of the cells are not available and the distribution is unknown. To confirm, that the MR signal originate from cell clusters the optical confirmation is required. Once, a reliable MR acquisition protocol is established this step, of course, will then not be required anymore. In figure 7.8 the comparison of optical and MR images is displayed. Identical structures are identifiable, and cell clusters in the MRI are clearly visible. This proves that the methodology of MR imaging of cell clusters cultured on glassy carbon scaffold is functional. In figure 7.9 a slice sequence of a single cluster is presented. Hyper-intense signals and dark regions can be identified. The dark regions originate most probably from regions with high cell density in the cell cluster. In the lower row of figure 7.9, cell cluster distributions are visualised, obtained from two consecutive segmentation processes. In the first step a low value thresholding is conducted and dark pixels are labelled as scaffold material. Subsequently, using a high value thresholding, bright pixels are labelled as cell structures. This principle works in general, however, manual adjustment was required for many regions due to inhomogeneity of the signal and lack of resolution and CNR. If conducted carefully, the cell distribution can be visualised.

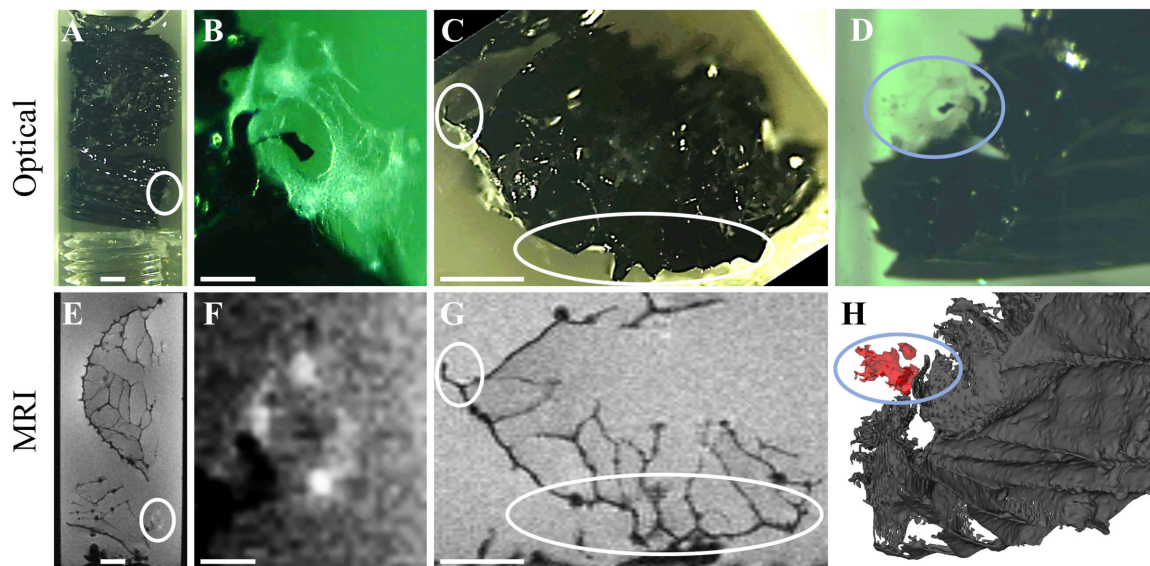


Figure 7.8.: Comparison of optical images and the corresponding MR images of the cells. A) and E) show an entire scaffold broken into two pieces. On the lower right cell clusters can be identified. B) and F) show a zoom of the circles from A) and B). The images in C) and G) provide an illustration of allocation using specific morphological details. D) and H) are comparison of reconstructed 3D image and optical image. Identical cell clusters are clearly visible on both images.

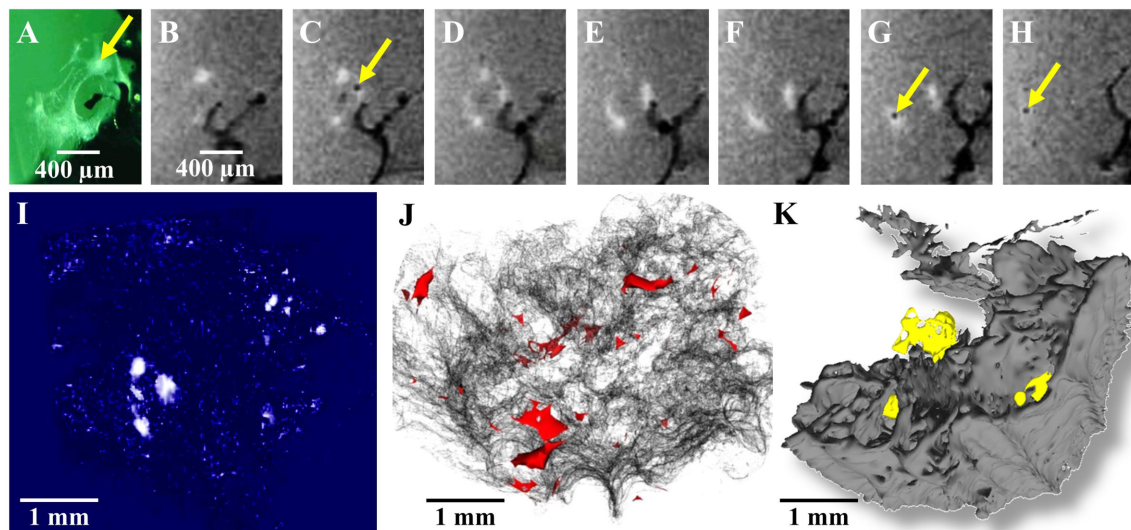


Figure 7.9.: The images from B)-H) are a series of slices from one cell clusters. The yellow arrows indicate high dense cluster material which appears dark in the MRI. In A) the corresponding optical image is shown. The image I), J) and K) show visualise different options of visualisation for cell cluster distribution. (Adapted and modified from [EF02]).

7.3. Conclusions

In this work, the potential application of glassy carbon as a candidate for producing MR compatible 3D-scaffolds for *in-vitro* and *in-situ* research applications has been investigated.

7. Evaluation of substrates for in-situ cultivation

It has been proven that NSCs can be cultured on the derived substrates and furthermore that the cell structures are identifiable using MRI technology. This combination offers indeed a great potential since it is in general possible to integrate the culturing process into an MR observable incubator. By this means, one can analyse the cell proliferation over time and non-destructively. The main advantage of carbon is that it can be derived from a wide range of precursor materials, not only the used cryogel. This offers a wide range of tunability for developing 3D scaffold structures which are compatible to MR investigations.

Part III.

Conclusions and Outlook

8 | Conclusion

In the introduction of this thesis, four main questions are raised and we will return at this point to these four questions, to summarise this work, to discuss the consequences of the key findings and to elaborate potential opportunities for further actions.

8.1. Should patients with brain implants undergo MRI?

The answer should be, without any doubt, a clear yes. Current technology, however, does not provide any unrestricted, arbitrary MR procedures of implant carriers. A literature review was conducted to find a profound answer to this question. Depending on the implant-specific potential health risks, some implants are still completely contraindicated. In chapter 3 the findings of the review work are presented with a focus on the physical principles of the manifold interactions. It is furthermore analysed, if there are types of interactions, with an incomplete fundamental understanding. Prominent interactions which gain large research focus, are the RF heating of stimulation implants such as the devices used for deep brain stimulation (DBS) as well as forces and artefacts produced by Cochlear implants (CI). Another famous type of interaction is the external stimulation that is triggered in pacemakers which can lead to erroneous stimulation. These four interactions are well-known and much research is conducted in combination with the corresponding implant type. This is a consequence of the fact, that all three implant types are technologically matured and commercially available and therefore obtain research interest. The literature review conducted in this work revealed, that gradient-induced vibrations are of minor concern within the research community. A very likely reason is the fact, that no commercial implants are known, that are prone to gradient-induced vibration. Within this work, it is shown, that there is currently no solid information and data available, if there is any possibility for resonant vibrations within viscoelastic environments. This lack of knowledge and data, renders any profound risk analysis impossible. Amplified vibrations have the potential to yield much higher vibration amplitudes compared to the static case. But the lack of any data does not facilitate any reliable statement. The question arose, if there are resonant vibrations within viscoelastic environments and the answer found in this work is a clear "yes".

To conclude the question of this section in a broader frame: Patients with implants should be able to undergo MRI, but this is, as of today, not free of risk. If active implants are tested for MR safety, they are labelled as MR conditional. This label restricts the MR procedure of a patient carrying that implant, and allows the clinician to conduct an MR procedure only under the defined conditions. This includes scanner type, field strength, RF power and many more parameters, and prevents the application of many MR sequences. Especially for non-linear relationships, such as the dependency of wavelength in RF heating, solutions for general test conditions are difficult to derive. The unconstrained use of an implant during MR acquisitions is a major challenge for the future. It is furthermore an important issue, because MR scanners are expensive, and for patients a strong constraint in MR compatibility, means an increased expenditure to receive a proper MR diagnose by finding a conditional MR system. With this in mind, a new classification number has been introduced for gradient-induced vibrations, which strives to satisfy the demands for generality.

8.2. Do penetrative implant-like structures experience resonant vibration in brain-like environment?

The short answer is: yes. A novel probe was developed which is detailed in chapter 4. This probe allows the user to measure the transfer function of implant-like structures within agarose-based hydrogels. These gels resemble the mechanical properties of brain tissue and were fully characterised. The vibration is measured using a segmented diode which facilitates fast (up to 100 kHz¹) and high precision measurements ($\phi < \text{mDeg}$). A tailored sample container is integrated which enables the acquisition of MR images while simultaneously measuring the vibration. This enables to measure the correlation of vibration amplitudes and sequence parameters, especially the repetition time TR. From the vibrational experiments, which are presented in chapter 5, two salient key findings are important: (i) The vibration of implant-like structures is underdamped. Hence, the vibration amplitude depends on the frequency spectrum of the trigger source, the gradient switching. (ii) Worst case on-resonance vibration could be triggered during an MR acquisition using the detailed knowledge of the mechanical transfer function. A five-fold increase of amplitude was observed in this case with slight modification of only the repetition time (TR = 20 ms \rightarrow TR = 14.18 ms). This experiment illustrates the necessity to measure the full transfer function of an implant. Only with that data, resonant excitation can be actively circumvented.

In further experiments the probe was used to analyse the induced torque on real implant structures. The tested electrodes were thin-film platinum-based electrodes and glassy-carbon based electrodes. The measurable torque of the thin-film platinum electrode was critically at the limit-of-detection and the torque of the glassy-carbon electrode was clearly

¹Under the condition that a DAQ is applied that provides the required bandwidth.

beyond this limit. These findings were supported by a theoretical analysis. To further evaluate theoretical and experimental values a dummy electrode was used with a 40 μm copper adhesive tape. This dummy electrode led to clear measurable deflections. A new figure-of-merit, Torque per slew rate (TPSR) is introduced, which provides a general coefficient to label implants. This figure-of-merit allows the user to compute worst-case torque for any MR unit, by multiplying the TPSR with the corresponding B_0 -field, maximal slew rate and dimension of the MR unit. The advantage of such a label, compared to a label with a fixed torque, is its flexibility. Instead of taking the measured torque, and indicate the measurement conditions, the results are normalised with respect to the measurement condition. On that basis, the expected worst-case condition, can simply be derived for any other MR device. This approach enables a much more flexible integration of MR and implant technology.

What do these measurements mean for implant vibrations in the brain? The fact that implant-like structures vibrate underdamped is confirmed, but a quantitative analysis regarding the amplitude of the shaft tip is pending. The next important question concerns the transferability of the results to brain tissue. How accurately can the agarose-based gels resemble the brain tissue? One option is to exchange the gels with preserved brain-tissue to repeat the measurement. This methodology, however, rather than providing new answers, only transfers the question to how transferable are data from conserved brain to the *in-vivo*-situation. It is conceivable to obtain more profound data, by conducting similar experiments on anaesthetised animals. This could also give a deeper insight on the question on how severe vibrations are in general. An important question is if, and how strong, do gradient-induced vibrations deteriorate the implant-tissue interface. How does such a process scale with vibrations amplitudes? This overlaps with research about the impact of mechanical consideration on implant functionality and longevity. With respect to labelling, it is desirable, that the concept of TPSR finds application in labelling implants with respect to gradient-induced vibrations. This depends also on the further research about, how severe, vibrations in soft tissue are. It is worthwhile mentioning, however, that the concept of normalised labelling, can be as well transferred to other types implants or even interactions.

8.3. Can we develop a flexible probe for different applications?

A modular, flexible probe was developed and is presented in chapter 6, hence the answer is yes. State-of-the-art concepts for RF and gradient coil interfacing are applied, in which the final version provides the interface for two RF channels and a three-axis liquid-cooled gradient system. In addition, the probe is upgraded with a novel concept of feed-throughs integrated in the mechanical frame, which provides the user a very flexible and simple

integration of additional interfaces. The MR compatibility and functionality was tested using standard NMR and MRI acquisition schemes. A linewidth of 0.5 Hz was achieved which allows the application in high-resolution solution NMR. 1D spectra were recorded using hydrogen and carbon channel, respectively. Subsequently, 2D HSQC were successfully conducted. The SNR is comparable to the commercial probe, only a slightly weaker SNR performance was observed. The main reason is the applied RF cable, which is smaller in diameter at the expense of a slightly higher damping. Two applications are presented: (i) The measurement of oil-water-droplets realised as a flow-through setup and (ii) the application in hyperpolarisation experiments based on SABRE. Furthermore, the probe is used as a flow-through probe in this application.

The probe finds wide application in the research group for many more applications such as broadband coil measurements or NMR experiments with integrated heating elements. Advanced probehead platforms can be integrated, which allows the user to perform novel types of integrated NMR experiments.

8.4. Can we develop an MR compatible substrate for biomedical research applications?

A novel solution has been presented, in which cryogels are used as precursor scaffolds to derive glassy carbon scaffolds. It could be proven that these scaffolds facilitate (i) proliferation of neural stem cells and (ii) the artefact free MR imaging of the cells. MR image-based morphology and porosity analysis was used to evaluate and confirm the preservation of scaffold structure.

With this work it is proven that 3D glassy carbon scaffold can be used as MR compatible scaffold materials. This approach facilitates the application of *in-situ* cultivation in general. The strength of this approach lies in the fact that it enables the usage of a wide range of precursor materials which can be converted into biocompatible materials. This approach unifies the strength of flexible 3D manufacturing using polymer materials and MR- as well as biocompatibility of glassy carbon material. This offers a new tool to develop tailored 3D scaffold structures for biomedical applications.

Bibliography

- [1] Abrams, H. L. (1989). Cochlear Implants Are a Contraindication to MRI. *JAMA J. Am. Med. Assoc.*, 261(1):46.
- [2] Amato, L., Heiskanen, A., Caviglia, C., Shah, F., Zór, K., Skolimowski, M., Madou, M., Gammelgaard, L., Hansen, R., Seiz, E. G., Ramos, M., Moreno, T. R., Martínez-Serrano, A., Keller, S. S., and Emnéus, J. (2014). Pyrolysed 3D-Carbon Scaffolds Induce Spontaneous Differentiation of Human Neural Stem Cells and Facilitate Real-Time Dopamine Detection. *Adv. Funct. Mater.*, 24(44):7042–7052.
- [3] Araj, S., Moyer, C. A., Kote, G., and Kalnins, I. L. (1978). Diamagnetic susceptibility of carbon fibre reinforced epoxy resin composites. *J. Mater. Sci.*, 13(9):2061–2063.
- [4] Arena, L., Morehouse, H. T., and Safir, J. (1995). MR imaging artifacts that simulate disease: how to recognize and eliminate them. *RadioGraphics*, 15(6):1373–1394.
- [5] ASTM International (2011a). ASTM F2182 - 11a: Standard test method for measurement of radio frequency induced heating near passive implants during magnetic resonance imaging.
- [6] ASTM International (2011b). ASTM F2213 - 06: Standard Test Method for Measurement of Magnetically Induced Torque on Medical Devices in the Magnetic Resonance Environment 1.
- [7] ASTM International (2013a). ASTM F2119 - 07: Standard Test Method for Evaluation of MR Image Artifacts from Passive Implants 1.
- [8] ASTM International (2013b). ASTM F2503 - 13: Standard Practice for Marking Medical Devices and Other Items for Safety in the Magnetic Resonance Environment 1.
- [9] ASTM International (2015). ASTM F2052 - 15: Standard Test Method for Measurement of Magnetically Induced Displacement Force.
- [10] Athey, T., Stuchly, M., and Stuchly, S. (1982). Measurement of Radio Frequency Permittivity of Biological Tissues with an Open-Ended Coaxial Line: Part I. *IEEE Trans. Microw. Theory Tech.*, 30(1):82–86.
- [11] Bäcker, A., Göppert, B., Sturm, S., Abaffy, P., Sollich, T., and Gruhl, F. J. (2016). Impact of adjustable cryogel properties on the performance of prostate cancer cells in 3D. *Springerplus*, 5(1):902.
- [12] Badilita, V., Meier, R. C., Spengler, N., Wallrabe, U., Utz, M., and Korvink, J. G. (2012). Microscale nuclear magnetic resonance: a tool for soft matter research. *Soft Matter*, 8(41):10583.

- [13] Bandettini, P. A. (2012). Twenty years of functional MRI: The science and the stories. *Neuroimage*, 62(2):575–588.
- [14] Bechtereva, N. P., Bondartchuk, A. N., Smirnov, V. M., Meliutcheva, L. A., and Shandurina, A. N. (1975). Method of electrostimulation of the deep brain structures in treatment of some chronic diseases. *Stereotactic and Functional Neurosurgery*, 37:136–140.
- [15] Bekiesińska-Figatowska, M. (2015). Artifacts in Magnetic Resonance Imaging. *Polish J. Radiol.*, 80:93–106.
- [16] Benabid, A., Pollak, P., Hoffmann, D., Gervason, C., Hommel, M., Perret, J., de Rougemont, J., and Gao, D. (1991). Long-term suppression of tremor by chronic stimulation of the ventral intermediate thalamic nucleus. *Lancet*, 337(8738):403–406.
- [17] Bloch, F., Hansen, W. W., and Packard, M. (1946). The Nuclear Induction Experiment. *Phys. Rev.*, 70(7-8):474–485.
- [18] Bottomley, P. A., Kumar, A., Edelstein, W. A., Allen, J. M., and Karmarkar, P. V. (2010). Designing passive MRI-safe implantable conducting leads with electrodes. *Med. Phys.*, 37(7Part1):3828–3843.
- [19] Brice, J. and McLellan, L. (1980). Suppression of Intention Tremor by Contingent Deep-Brain Stimulation. *Lancet*, 315(8180):1221–1222.
- [20] Budday, S., Sommer, G., Birkl, C., Langkammer, C., Haybaeck, J., Kohnert, J., Bauer, M., Paulsen, F., Steinmann, P., Kuhl, E., and Holzapfel, G. A. (2017). Mechanical characterization of human brain tissue. *Acta Biomater.*, 48:319–340.
- [21] Camacho, C. R., Plewes, D. B., and Henkelman, R. M. (1995). Nonsusceptibility artifacts due to metallic objects in MR imaging. *J. Magn. Reson. Imaging*, 5(1):75–88.
- [22] Carlson, M. L., Neff, B. A., Link, M. J., Lane, J. I., Watson, R. E., McGee, K. P., Bernstein, M. A., and Driscoll, C. L. W. (2015). Magnetic Resonance Imaging With Cochlear Implant Magnet in Place. *Otol. Neurotol.*, 36(6):965–971.
- [23] Chmurny, G. N. and Hoult, D. I. (1990). The Ancient and Honourable Art of Shimming. *Concepts Magn. Reson.*, 2(3):131–149.
- [24] Chun, K. R. (1972). Free Vibration of a Beam With One End Spring-Hinged and the Other Free. *J. Appl. Mech.*, 39(4):1154.
- [25] Condon, B. and Hadley, D. M. (2000). Potential MR Hazard to Patients With Metallic Heart Valves: The Lenz Effect. *J. Magn. Reson. Imaging*, 12(1):171–176.
- [26] Crane, B. T., Gottschalk, B., Kraut, M., Aygun, N., and Niparko, J. K. (2010). Magnetic Resonance Imaging at 1.5 T After Cochlear Implantation. *Otol. Neurotol.*, 31(8):1215–1220.
- [27] Cushing, M. C. and Anseth, K. S. (2007). Hydrogel Cell Cultures. *Science (80-)*, 316(5828):1133–1134.
- [28] Damadian, R., Goldsmith, M., and Minkoff, L. (1977). NMR in cancer: XVI. FONAR image of the live human body. *Physiological Chemistry and Physics*, 9:97–100.

- [29] Davis, P., Crooks, L., Arakawa, M., McRee, R., Kaufman, L., and Margulis, A. (1981). Potential hazards in NMR imaging: heating effects of changing magnetic fields and RF fields on small metallic implants. *Am. J. Roentgenol.*, 137(4):857–860.
- [30] De Sousa, F. F., Da Silva, L. D. P., and Freitas, K. H. G. (2017). Electrical and dielectric properties of water. *Sci. Plena*, 13(01):1–6.
- [31] Delgado, J. (1969). *Physical control of the mind: toward a psychocivilized society*. Harper & Row, New York, USA.
- [32] Dempsey, M. F., Condon, B., and Hadley, D. M. (2001). Investigation of the factors responsible for burns during MRI. *J. Magn. Reson. Imaging*, 13(4):627–31.
- [33] Deutsches Kupferinstitut (2019). Kupfer-Zink-Legierungen (Messing CuZn). <https://www.kupferinstitut.de/de/werkstoffe/eigenschaften/kupfer-zink-messing.html>. Accessed on 24.03.2019.
- [34] Edwards, M.-B., Mclean, J., Solomonidis, S., Condon, B., and Gourlay, T. (2015). In vitro assessment of the lenz effect on heart valve prostheses at 1.5 T. *J Magn Reson Imaging*, 41(1):74–82.
- [35] El-Sherbiny, I. M. and Yacoub, M. H. (2013). Hydrogel scaffolds for tissue engineering: Progress and challenges. *Glob. Cardiol. Sci. Pract.*, 2013(3):38.
- [36] Elimat, Z. M., Hamideen, M. S., Schulte, K. I., Wittich, H., de la Vega, A., Wichmann, M., and Buschhorn, S. (2010). Dielectric properties of epoxy/short carbon fiber composites. *J. Mater. Sci.*, 45(19):5196–5203.
- [37] FDA (1997). FDA Approval - P960009 Medtronic® Activa™ Tremor Control System. https://www.accessdata.fda.gov/cdrh_docs/pdf/p960009.pdf. Accessed on 16.01.2018.
- [38] FDA (2017). FDA clears first 7T Magnetic Resonance Imaging Device. <https://www.fda.gov/NewsEvents/Newsroom/PressAnnouncements/ucm580154.htm>. Accessed on 10.11.2017.
- [39] Finelli, D. a., Rezai, A. R., Ruggieri, P. M., Tkach, J. a., Nyenhuis, J. a., Hrdlicka, G., Sharan, A., Gonzalez-Martinez, J., Stypulkowski, P. H., and Shellock, F. G. (2002). MR imaging-related heating of deep brain stimulation electrodes: in vitro study. *AJNR. Am. J. Neuroradiol.*, 23(10):1795–802.
- [40] Flint, J. J., Lee, C. H., Hansen, B., Fey, M., Schmidig, D., Bui, J. D., King, M. A., Vestergaard-Poulsen, P., and Blackband, S. J. (2009). Magnetic resonance microscopy of mammalian neurons. *Neuroimage*, 46(4):1037–1040.
- [41] Folio, D. and Ferreira, A. (2017). Two-Dimensional Robust Magnetic Resonance Navigation of a Ferromagnetic Microrobot Using Pareto Optimality. *IEEE Trans. Robot.*, 33(3):583–593.
- [42] Foster, K. R., Ziskin, M. C., Balzano, Q., and Bit-Babik, G. (2018). Modeling Tissue Heating From Exposure to Radiofrequency Energy and Relevance of Tissue Heating to Exposure Limits. *Health Phys.*, 115(2):295–307.
- [43] Freden Jansson, K.-J., Hakansson, B., Reinfeldt, S., Taghavi, H., and Eeg-Olofsson, M. (2014). MRI Induced Torque and Demagnetization in Retention Magnets for a Bone Conduction Implant. *IEEE Trans. Biomed. Eng.*, 61(6):1887–1893.

- [44] Gabriel, C., Gabriel, S., and Corthout, E. (1996a). The dielectric properties of biological tissues: I. Literature survey. *Phys. Med. Biol.*, 41(11):2231–2249.
- [45] Gabriel, S., Lau, R. W., and Gabriel, C. (1996b). The dielectric properties of biological tissues: II. Measurements in the frequency range 10 Hz to 20 GHz. *Phys. Med. Biol.*, 41(11):2251–2269.
- [46] Gabriel, S., Lau, R. W., and Gabriel, C. (1996c). The dielectric properties of biological tissues: III. Parametric models for the dielectric spectrum of tissues. *Phys. Med. Biol.*, 41(11):2271–2293.
- [47] Gardner, J. (2013). A history of deep brain stimulation: Technological innovation and the role of clinical assessment tools. *Soc. Stud. Sci.*, 43(5):707–728.
- [48] Gelfan, S. and Bishop, G. H. (1932). Action Potentials From Single Muscle Fibres. *Am. J. Physiol. Content*, 101(4):678–685.
- [49] Getzlaff, M. (2007). *Fundamentals of Magnetism*. Springer, Berlin Heidelberg, Germany.
- [50] Gilletti, A. and Muthuswamy, J. (2006). Brain micromotion around implants in the rodent somatosensory cortex. *J. Neural Eng.*, 3(3):189–195.
- [51] Gimbel, J. R. (2009). Unexpected asystole during 3T magnetic resonance imaging of a pacemaker-dependent patient with a 'modern' pacemaker. *Europace*, 11(9):1241–1242.
- [52] Gleason, C. A., Kaula, N. F., Hricak, H., Schmidt, R. A., and Tanagho, E. A. (1992). The Effect of Magnetic Resonance Imagers on Implanted Neurostimulators. *Pacing Clin. Electrophysiol.*, 15(1):81–94.
- [53] Golestanirad, L., Dlala, E., Wright, G., Mosig, J. R., and Graham, S. J. (2012). Comprehensive analysis of lenz effect on the artificial heart valves during magnetic resonance imaging. *Prog. Electromagn. Res.*, 128(May):1–17.
- [54] Graf, H., Lauer, U. A., and Schick, F. (2006). Eddy-current induction in extended metallic parts as a source of considerable torsional moment. *J. Magn. Reson. Imaging*, 23(4):585–590.
- [55] Graf, H., Steidle, G., and Schick, F. (2007). Heating of metallic implants and instruments induced by gradient switching in a 1.5-Tesla whole-body unit. *J. Magn. Reson. Imaging*, 26(5):1328–1333.
- [56] Graham, J., Lynch, C., Weber, B., Stollwerck, L., Wei, J., and Brookes, G. (1999). The magnetless Clarion® cochlear implant in a patient with neurofibromatosis 2. *J. Laryngol. Otol.*, 113(05):458–463.
- [57] Green, M. A., Bilston, L. E., and Sinkus, R. (2008). In vivo brain viscoelastic properties measured by magnetic resonance elastography. *NMR Biomed.*, 21(7):755–764.
- [58] Gross, D., Hauger, W., and Wriggers, P. (2018). *Technische Mechanik 4: Hydromechanik, Elemente der Höheren Mechanik, Numerische Methoden*. Springer, Berlin Heidelberg, Germany.
- [59] Gubbels, S. P. and McMenomey, S. O. (2006). Safety Study of the Cochlear Nucleus® 24 Device with Internal Magnet in the 1.5 Tesla Magnetic Resonance Imaging Scanner. *Laryngoscope*, 116(6):865–871.

- [60] Guéron, M. and Leroy, J. (1989). NMR of water protons. The detection of their nuclear-spin noise, and a simple determination of absolute probe sensitivity based on radiation damping. *J. Magn. Reson.*, 85(1):209–215.
- [61] Hassepass, F., Stabenau, V., Arndt, S., Beck, R., Bulla, S., Grauvogel, T., and Aschendorff, A. (2014). Magnet Dislocation: An Increasing and Serious Complication Following MRI in Patients with Cochlear Implants. *RöFo - Fortschritte auf dem Gebiet der Röntgenstrahlen und der Bildgeb. Verfahren*, 186(07):680–685.
- [62] Hector, L. G. and Schultz, H. L. (1936). The Dielectric Constant of Air at Radiofrequencies. *Physics (College. Park. Md)*, 7(4):133–136.
- [63] Heller, J. W., Brackmann, D. E., Tucci, D. L., Nyenhuis, J. a., and Chou, C. K. (1996). Evaluation of MRI compatibility of the modified nucleus multichannel auditory brainstem and cochlear implants. *Am. J. Otol.*, 17(5):724–9.
- [64] Henderson, J. M., Tkach, J., Phillips, M., Baker, K., Shellock, F. G., and Rezai, A. R. (2005). Permanent Neurological Deficit Related to Magnetic Resonance Imaging in a Patient with Implanted Deep Brain Stimulation Electrodes for Parkinson’s Disease: Case Report. *Neurosurgery*, 57(5):E1063.
- [65] Holm, S. (2019). *Waves with Power-Law Attenuation*. Springer, Cham, Switzerland.
- [66] Hoult, D. and Richards, R. (1976). The signal-to-noise ratio of the nuclear magnetic resonance experiment. *J. Magn. Reson.*, 24(1):71–85.
- [67] Hoult, D. I. (2000). The principle of reciprocity in signal strength calculations? A mathematical guide. *Concepts Magn. Reson.*, 12(4):173–187.
- [68] International Electrotechnical Commision (2015). IEC 60601-2-33 Medical electrical equipment.
- [69] International Organization for Standardization (2012). ISO/TS 10974:2012 - Assessment of the safety of magnetic resonance imaging for patients with an active implantable medical device.
- [70] Jackson, J. (1998). *Classical Electrodynamics*. John Wiley & Sons, New York, USA, 3 edition.
- [71] Jacob, Z. C., Tito, M. F., and Dagum, A. B. (2010). MR Imaging–related Electrical Thermal Injury Complicated by Acute Carpal Tunnel and Compartment Syndrome: Case Report. *Radiology*, 254(3):846–850.
- [72] Jech, R., Urgošík, D., Tintěra, J., Nebuželský, A., Krásenský, J., Liščák, R., Roth, J., and Růžička, E. (2001). Functional magnetic resonance imaging during deep brain stimulation: A pilot study in four patients with Parkinson’s disease. *Mov. Disord.*, 16(6):1126–1132.
- [73] Jeon, J. H., Bae, M. R., Chang, J. W., and Choi, J. Y. (2012). Reversing the polarity of a cochlear implant magnet after magnetic resonance imaging. *Auris Nasus Larynx*, 39(4):415–417.
- [74] Kamberger, R. (2017). *Manufacturing Methods for Magnetic Resonance Microscopy Tools with Application to Neuroscience*. PhD thesis, Karlsruher Institut für Technologie (KIT). 43.22.01; LK 01.

- [75] Kamberger, R., Göbel-Guéniot, K., Gerlach, J., Gruschke, O., Hennig, J., LeVan, P., Haas, C., and Korvink, J. (2018). Improved method for MR microscopy of brain tissue cultured with the interface method combined with Lenz lenses. *Magn. Reson. Imaging*, 52:24–32.
- [76] Kavitha, M. and Reddy, M. R. (2012). Characterization of tissue mimicking phantoms for acoustic radiation force impulse imaging. In *2012 IEEE Int. Conf. Imaging Syst. Tech. Proc.*, pages 553–557. IEEE.
- [77] Kelly, W. M., Paglen, P. G., Pearson, J. A., San Diego, A. G., and Soloman, M. A. (1986). Ferromagnetism of intraocular foreign body causes unilateral blindness after MR study. *AJNR. Am. J. Neuroradiol.*, 7(2):243–5.
- [78] Kjær, L., Thomsen, C., Henriksen, O., Ring, P., Stubgaard, M., and Pedersen, E. J. (1987). Evaluation of Relaxation Time Measurements by Magnetic Resonance Imaging. *Acta radiol.*, 28(3):345–351.
- [79] Knight, E. and Przyborski, S. (2015). Advances in 3D cell culture technologies enabling tissue-like structures to be created in vitro. *J. Anat.*, 227(6):746–756.
- [80] Konings, M. K., Bartels, L. W., Smits, H. F., and Bakker, C. J. (2000). Heating Around Intravascular Guidewires by Resonating RF Waves. *J. Magn. Reson. Imaging*, 12(1):79–85.
- [81] Kopeliovich, D. (2019). Substances & Technologies. www.substech.com. Accessed on 24.03.2019.
- [82] Kosa, G., Jakab, P., Hata, N., Jolesz, F., Neubach, Z., Shoham, M., Zaaroor, M., and Szekely, G. (2008). Flagellar swimming for medical micro robots: Theory, experiments and application. In *2008 2nd IEEE RAS EMBS Int. Conf. Biomed. Robot. Biomechatronics*, pages 258–263. IEEE.
- [83] Kósa, G., Jakab, P., Székely, G., and Hata, N. (2012). MRI driven magnetic microswimmers. *Biomed. Microdevices*, 14(1):165–178.
- [84] Kosa, G., Shoham, M., and Zaaroor, M. (2007). Propulsion Method for Swimming Microrobots. *IEEE Trans. Robot.*, 23(1):137–150.
- [85] Krishnan, V. and Murali, N. (2013). Radiation damping in modern NMR experiments: Progress and challenges. *Prog. Nucl. Magn. Reson. Spectrosc.*, 68(9):41–57.
- [86] Kumar, A. and Srivastava, A. (2010). Cell separation using cryogel-based affinity chromatography. *Nat. Protoc.*, 5(11):1737–1747.
- [87] Lauterbur, P. C. (1973). Image Formation by Induced Local Interactions: Examples Employing Nuclear Magnetic Resonance. *Nature*, 242(5394):190–191.
- [88] Le Bihan, D. and Schild, T. (2017). Human brain MRI at 500 MHz, scientific perspectives and technological challenges. *Supercond. Sci. Technol.*, 30(3):033003.
- [89] Levitt, M. (2001). *Spin Dynamics: Basics of Nuclear Magnetic Resonance*. Wiley, Chichester.
- [90] Light, T. S., Licht, S., Bevilacqua, A. C., and Morash, K. R. (2005). The Fundamental Conductivity and Resistivity of Water. *Electrochem. Solid-State Lett.*, 8(1):E16.

- [91] Luechinger, R., Zeijlemaker, V. a., Pedersen, E. M., Mortensen, P., Falk, E., Duru, F., Candinas, R., and Boesiger, P. (2005). In vivo heating of pacemaker leads during magnetic resonance imaging. *Eur. Heart J.*, 26:376–383.
- [92] Majdani, O., Rau, T. S., Götz, F., Zimmerling, M., Lenarz, M., Lenarz, T., Labadie, R., and Leinung, M. (2009). Artifacts caused by cochlear implants with non-removable magnets in 3T MRI: Phantom and cadaveric studies. *Eur. Arch. Oto-Rhino-Laryngology*, 266(12):1885–1890.
- [93] Mansfield, P., Coxon, R., and Glover, P. (1994). Echo-Planar Imaging of the Brain at 3.0 T. *J. Comput. Assist. Tomogr.*, 18(3):339–343.
- [94] Mansfield, P. and Maudsley, A. A. (1977). Medical imaging by NMR. *Br. J. Radiol.*, 50(591):188–194.
- [95] Martel, S., Mathieu, J. B., Felfoul, O., Chanu, A., Aboussouan, E., Tamaz, S., Pouponneau, P., Yahia, L., Beaudoin, G., Soulez, G., and Mankiewicz, M. (2007). Automatic navigation of an untethered device in the artery of a living animal using a conventional clinical magnetic resonance imaging system. *Appl. Phys. Lett.*, 90(11):114105.
- [96] Martin, A. J., Larson, P. S., Ostrem, J. L., Keith Sootsman, W., Talke, P., Weber, O. M., Levesque, N., Myers, J., and Starr, P. A. (2005). Placement of deep brain stimulator electrodes using real-time high-field interventional magnetic resonance imaging. *Magn. Reson. Med.*, 54(5):1107–1114.
- [97] Mathieu, J.-B., Beaudoin, G., and Martel, S. (2006). Method of Propulsion of a Ferromagnetic Core in the Cardiovascular System Through Magnetic Gradients Generated by an MRI System. *IEEE Trans. Biomed. Eng.*, 53(2):292–299.
- [98] Matsuura, H., Inoue, T., Konno, H., Sasaki, M., Ogasawara, K., and Ogawa, A. (2002). Quantification of susceptibility artifacts produced on high-field magnetic resonance images by various biomaterials used for neurosurgical implants. Technical note. *J. Neurosurg.*, 97(6):1472–5.
- [99] Mattei, E., Censi, F., Mancini, M., Napolitano, A., Genovese, E., Cannata, V., Burriesci, G., Falsaperla, R., and Calcagnini, G. (2014). Currents induced by fast movements inside the MRI room may cause inhibition in an implanted pacemaker. In *2014 36th Annu. Int. Conf. IEEE Eng. Med. Biol. Soc.*, pages 890–893. IEEE.
- [100] Mattei, E., Censi, F., Triventi, M., Mancini, M., Napolitano, A., Genovese, E., Cannata, V., Falsaperla, R., and Calcagnini, G. (2015). Wrong detection of ventricular fibrillation in an implantable cardioverter defibrillator caused by the movement near the MRI scanner bore. In *2015 37th Annu. Int. Conf. IEEE Eng. Med. Biol. Soc.*, pages 7200–7203. IEEE.
- [101] Matthias Hampe (2013). Specific Absorption Rate in Human Tissues: Accurate and Approximated Values. *Int. Symp. Electromagn. Compat. (EMC Eur. 2013 2-6 Sept. 2013, Brugge, Belgium)*, (11):143–148.
- [102] Maynard, E. M., Fernandez, E., and Normann, R. A. (2000). A technique to prevent dural adhesions to chronically implanted microelectrode arrays. *J. Neurosci. Methods*, 97(2):93–101.
- [103] McKinstry, R. C. and Jarrett, D. Y. (2004). Magnetic Susceptibility Artifacts on MRI: A Hairy Situation. *Am. J. Roentgenol.*, 182(2):532–532.

- [104] McRobbie, D. W., Moore, E. A., Graves, M. J., and Prince, M. R. (2006). *MRI from Picture to Proton*. Cambridge University Press, Cambridge, UK, 2 edition.
- [105] Mispelter, J., Lupu, M., and Briguet, A. (2006). *NMR Probeheads for Biophysical and Biomedical Experiments: Theoretical Principles and Practical Guidelines*. Imperial College Press, London, UK.
- [106] Mitra, J., Jain, S., Sharma, A., and Basu, B. (2013). Patterned growth and differentiation of neural cells on polymer derived carbon substrates with micro/nano structures in vitro. *Carbon N. Y.*, 65:140–155.
- [107] Mudry, A. and Mills, M. (2013). The Early History of the Cochlear Implant. *JAMA Otolaryngol. Neck Surg.*, 139(5):446.
- [108] Nadobny, J., Szimtenings, M., Diehl, D., Stetter, E., Brinker, G., and Wust, P. (2007). Evaluation of MR-Induced Hot Spots for Different Temporal SAR Modes Using a Time-Dependent Finite Difference Method With Explicit Temperature Gradient Treatment. *IEEE Trans. Biomed. Eng.*, 54(10):1837–1850.
- [109] National Institutes of Health (2018). Cochlear Implants. <https://www.nidcd.nih.gov/health/cochlear-implants>. Accessed on 18.01.2018.
- [110] Nelson, B. J., Kaliakatsos, I. K., and Abbott, J. J. (2010). Microrobots for Minimally Invasive Medicine. *Annu. Rev. Biomed. Eng.*, 12(1):55–85.
- [111] Nimbalkar, S., Castagnola, E., Balasubramani, A., Scarpellini, A., Samejima, S., Khorasani, A., Boissenin, A., Thongpang, S., Moritz, C., and Kassegne, S. (2018). Ultra-Capacitive Carbon Neural Probe Allows Simultaneous Long-Term Electrical Stimulations and High-Resolution Neurotransmitter Detection. *Sci. Rep.*, 8(1):6958.
- [112] Ordonez, J., Schuettler, M., Boehler, C., Boretius, T., and Stieglitz, T. (2012). Thin films and microelectrode arrays for neuroprosthetics. *MRS Bull.*, 37(06):590–598.
- [113] Otsu, N. (1979). A Threshold Selection Method from Gray-Level Histograms. *IEEE Trans. Syst. Man. Cybern.*, 9(1):62–66.
- [114] Pané, S., Puigmartí-Luis, J., Bergeles, C., Chen, X.-Z., Pellicer, E., Sort, J., Počepcová, V., Ferreira, A., and Nelson, B. J. (2018). Imaging Technologies for Biomedical Micro- and Nanoswimmers. *Adv. Mater. Technol.*, 1800575:1800575.
- [115] Panych, L. P. and Madore, B. (2017). The physics of MRI safety. *J. Magn. Reson. Imaging*, 47(1):28–43.
- [116] Park, B., Webb, A. G., and Collins, C. M. (2009). A method to separate conservative and magnetically-induced electric fields in calculations for MRI and MRS in electrically-small samples. *J. Magn. Reson.*, 199(2):233–237.
- [117] Park, S., Kamondetdacha, R., Amjad, A., and Nyenhuis, J. (2005). MRI safety: RF-induced heating near straight wires. *IEEE Trans. Magn.*, 41(10):4197–4199.
- [118] Park, S. M., Kamondetdacha, R., and Nyenhuis, J. a. (2007). Calculation of MRI-induced heating of an implanted medical lead wire with an electric field transfer function. *J. Magn. Reson. Imaging*, 26(5):1278–1285.

- [119] Pietryga, J., Fonder, M., Rogg, J., North, D., and Bercovitch, L. (2013). Invisible Metallic Microfiber in Clothing Presents Unrecognized MRI Risk for Cutaneous Burn. *Am. J. Neuroradiol.*, 34(5):E47–E50.
- [120] Pomfret, R., Miranpuri, G., and Sillay, K. (2013). The Substitute Brain and the Potential of the Gel Model. *Ann. Neurosci.*, 20(3):118–122.
- [121] Portnoy, W. M. and Mattucci, K. (1991). Cochlear Implants as a Contraindication to Magnetic Resonance Imaging. *Ann. Otol. Rhinol. Laryngol.*, 100(3):195–197.
- [122] Prodanov, D. and Delbeke, J. (2016). Mechanical and Biological Interactions of Implants with the Brain and Their Impact on Implant Design. *Front. Neurosci.*, 10(February).
- [123] Purcell, E. M., Torrey, H. C., and Pound, R. V. (1946). Resonance Absorption by Nuclear Magnetic Moments in a Solid. *Phys. Rev.*, 69(1-2):37–38.
- [124] Raimond, J.-M. and Rivasseau, V. (2007). *The Spin*. Birkhäuser, Basel, Switzerland.
- [125] Reese, T., Heid, O., Weisskoff, R., and Wedeen, V. (2003). Reduction of eddy-current-induced distortion in diffusion MRI using a twice-refocused spin echo. *Magn. Reson. Med.*, 49(1):177–182.
- [126] Rezai, A. R., Finelli, D., Nyenhuis, J. A., Hrdlicka, G., Tkach, J., Sharan, A., Rugieri, P., Stypulkowski, P. H., and Shellock, F. G. (2002). Neurostimulation systems for deep brain stimulation: In vitro evaluation of magnetic resonance imaging-related heating at 1.5 tesla. *J. Magn. Reson. Imaging*, 15(3):241–250.
- [127] Rezai, A. R., Lozano, A. M., Crawley, A. P., Joy, M. L. G., Davis, K. D., Kwan, C. L., Dostrovsky, J. O., Tasker, R. R., and Mikulis, D. J. (1999). Thalamic stimulation and functional magnetic resonance imaging: localization of cortical and subcortical activation with implanted electrodes. *J. Neurosurg.*, 90(3):583–590.
- [128] Romner, B., Olsson, M., Ljunggren, B., Holtås, S., Säveland, H., Brandt, L., and Persson, B. (1989). Magnetic resonance imaging and aneurysm clips. Magnetic properties and image artifacts. *J. Neurosurg.*, 70(3):426–31.
- [129] Rugar, D., Zuger, O., Hoen, S., Yannoni, C. S., Vieth, H.-M., and Kendrick, R. D. (1994). Force Detection of Nuclear Magnetic Resonance. *Science (80-.)*, 264(5165):1560–1563.
- [130] Sammet, C. L., Yang, X., Wassenaar, P. a., Bourekas, E. C., Yuh, B. a., Shellock, F., Sammet, S., and Knopp, M. V. (2013). RF-related heating assessment of extracranial neurosurgical implants at 7T. *Magn. Reson. Imaging*, 31(6):1029–1034.
- [131] Schenck, J. F. (1996). The role of magnetic susceptibility in magnetic resonance imaging: MRI magnetic compatibility of the first and second kinds. *Med. Phys.*, 23(6):815.
- [132] Schenck, J. F. (2000). Safety of strong, static magnetic fields. *J. Magn. Reson. Imaging*, 12(1):2–19.
- [133] Schmitt, F. (2013). The Gradient System. In *Proc. Intl. Soc. Mag. Res. Med*, volume 21, pages 1–13.

- [134] Sem-Jacobsen, C. W. (1965). Depth electrographic stimulation and treatment of patients with parkinson's disease including neurosurgical technique. *Acta Neurologica Scandinavica*, 41(S13):365–376.
- [135] Sharma, S., Kamath, R., and Madou, M. (2014). Porous glassy carbon formed by rapid pyrolysis of phenol-formaldehyde resins and its performance as electrode material for electrochemical double layer capacitors. *J. Anal. Appl. Pyrolysis*, 108:12–18.
- [136] Sharma, S. and Madou, M. (2012). Micro and nano patterning of carbon electrodes for bioMEMS. *Bioinspired, Biomim. Nanobiomaterials*, 1(4):252–265.
- [137] Shellock, F. (2000). *Magnetic Resonance Procedures: Health Effects and Safety*. CRC Press, Boca Raton, USA.
- [138] Shin, S., Lim, D. G., Kang, T., Chun, H., and Cho, J. K. (2012). Thermal and electrical properties of glass fiber reinforced o-cresol novolac epoxy composites cured with allylated phenol novolac hardener. *Polym. Int.*, 61(9):1411–1416.
- [139] Shinyama, K. and Fujita, S. (2004). Study on the electrical properties of a biodegradable plastic. In *Proc. 7th Int. Conf. Prop. Appl. Dielectr. Mater. (Cat. No.03CH37417)*, volume 2, pages 707–710. IEEE.
- [140] Sironi, V. A. (2011). Origin and Evolution of Deep Brain Stimulation. *Front. Integr. Neurosci.*, 5(August):1–5.
- [141] Sohal, H. S., Jackson, A., Jackson, R., Clowry, G. J., Vassilevski, K., O'Neill, A., and Baker, S. N. (2014). The sinusoidal probe: a new approach to improve electrode longevity. *Front. Neuroeng.*, 7(April):10.
- [142] Spengler, N., While, P. T., Meissner, M. V., Wallrabe, U., and Korvink, J. G. (2017). Magnetic Lenz lenses improve the limit-of-detection in nuclear magnetic resonance. *PLoS One*, 12(8):1–17.
- [143] Sridharan, A., Rajan, S. D., and Muthuswamy, J. (2013). Long-term changes in the material properties of brain tissue at the implant–tissue interface. *J. Neural Eng.*, 10(6):066001.
- [144] Strumwasser, F. (1958). Long-term recording' from single neurons in brain of unrestrained mammals. *Science*, 127:469–470.
- [145] Sundararajan, D. (2017). *Digital Image Processing - A Signal Processing and Algorithmic Approach*. Springer, Singapore.
- [146] Teissl, C., Kremser, C., Hochmair, E. S., and Hochmair-Desoyer, I. J. (1998). Cochlear implants: in vitro investigation of electromagnetic interference at MR imaging–compatibility and safety aspects. *Radiology*, 208(3):700–708.
- [147] Teissl, C., Kremser, C., Hochmair, E. S., and Hochmair-Desoyer, I. J. (1999). Magnetic resonance imaging and cochlear implants: compatibility and safety aspects. *J Magn Reson Imaging*, 9:26–38.
- [148] Teixidor, G. T., Gorkin, R. A., Tripathi, P. P., Bisht, G. S., Kulkarni, M., Maiti, T. K., Battacharyya, T. K., Subramaniam, J. R., Sharma, A., Park, B. Y., and Madou, M. (2008). Carbon microelectromechanical systems as a substratum for cell growth. *Biomed. Mater.*, 3(3):034116.

- [149] Vomero, M., Zucchini, E., Delfino, E., Gueli, C., Mondragon, N., Carli, S., Fadiga, L., and Stieglitz, T. (2018). Glassy Carbon Electroocortigraphy Electrodes on Ultra-Thin and Finger-Like Polyimide Substrate: Performance Evaluation Based on Different Electrode Diameters. *Materials (Basel)*, 11(12):2486.
- [150] Wagner, F., Wimmer, W., Leidolt, L., Vischer, M., Weder, S., Wiest, R., Mantokoudis, G., and Caversaccio, M. D. (2015). Significant Artifact Reduction at 1.5T and 3T MRI by the Use of a Cochlear Implant with Removable Magnet: An Experimental Human Cadaver Study. *PLoS One*, 10(7):e0132483.
- [151] Walton, J., Donnelly, N. P., Tam, Y. C., Joubert, I., Durie-Gair, J., Jackson, C., Mannion, R. A., Tysome, J. R., Axon, P. R., and Scoffings, D. J. (2014). MRI Without Magnet Removal in Neurofibromatosis Type 2 Patients With Cochlear and Auditory Brainstem Implants. *Otol. Neurotol.*, 35(5):821–825.
- [152] Wapler, M. C., Leupold, J., Dragonu, I., Von Elverfeld, D., Zaitsev, M., and Wallrabe, U. (2014). Magnetic properties of materials for MR engineering, micro-MR and beyond. *J. Magn. Reson.*, 242:233–242.
- [153] Ward, C., Henderson, S., and Metcalfe, N. H. (2013). A short history on pacemakers. *Int. J. Cardiol.*, 169(4):244–248.
- [154] Webb, A. G., editor (2016). *Magnetic Resonance Technology*. New Developments in NMR. The Royal Society of Chemistry, Cambridge, UK.
- [155] Weber, B. P., Goldring, J. E., Santogrossi, T., Koestler, H., Tziviskos, G., Battmer, R., and Lenarz, T. h. (1998). Magnetic resonance imaging compatibility testing of the Clarion 1.2 cochlear implant. *Am. J. Otol.*, 19(5):584–90.
- [156] Weber, B. P., Neuburger, J., Battmer, R. D., and Lenarz, T. (1997). Magnetless cochlear implant: relevance of adult experience for children. *Am. J. Otol.*, 18(6 Suppl):S50–1.
- [157] Wilson, B. S. and Dorman, M. F. (2008). Cochlear implants: A remarkable past and a brilliant future. *Hear. Res.*, 242(1-2):3–21.
- [158] Yeung, C. J., Susil, R. C., and Atalar, E. (2002). RF safety of wires in interventional MRI: Using a safety index. *Magn. Reson. Med.*, 47(1):187–193.
- [159] Zakhurdaeva, A., Dietrich, P.-I., Hölscher, H., Koos, C., Korvink, J., and Sharma, S. (2017). Custom-Designed Glassy Carbon Tips for Atomic Force Microscopy. *Micromachines*, 8(9):285.
- [160] Zekaj, E., Saleh, C., Menghetti, C., and Servello, D. (2013). Does magnetic resonance imaging induce tissue damage due to DBS lead heating? *Acta Neurochir. (Wien)*, 155(9):1677–1678.
- [161] Zeng, F.-G. (2004). Trends in Cochlear Implants. *Trends Amplif.*, 8(1):1–34.
- [162] Zhang, S. H., Tse, Z. T. H., Dumoulin, C. L., Kwong, R. Y., Stevenson, W. G., Watkins, R., Ward, J., Wang, W., and Schmidt, E. J. (2016). Gradient-induced voltages on 12-lead ECGs during high duty-cycle MRI sequences and a method for their removal considering linear and concomitant gradient terms. *Magn. Reson. Med.*, 75(5):2204–2216.

- [163] Zhang, W. (2014). Mechanical simulation of neural electrode -brain tissue interface under various micromotion conditions. *J. Med. Biol. Eng.*, 34(4):386.
- [164] Zhu, J.-H., Zhu, M., Han, N., Liu, W., and Xing, F. (2014). Electrical and Mechanical Performance of Carbon Fiber-Reinforced Polymer Used as the Impressed Current Anode Material. *Materials (Basel)*, 7(8):5438–5453.

Publications

Journal articles

Published

- [EF01] Erhardt, J. B.*, **Fuhrer, E.***, Gruschke, O. G., Leupold, J., Wapler, M. C., Hennig, J., Stieglitz, T., Korvink J. G.*, *Should patients with brain implants undergo MRI?*, Journal of Neural Engineering, 15(4), 041002, **2018**
(*These authors contributed equally)
- [EF02] **Fuhrer, E.**, Bäcker, A., Kraft, S., Gruhl, F. J., Kirsch, M., MacKinnon, N., Korvink, J. G., Sharma, S., *3D Carbon Scaffolds for Neural Stem Cell Culture and Magnetic Resonance Imaging.*, Advanced Healthcare Materials, 7(4), 1700915, **2018**
- [EF03] Jouda, M., **Fuhrer, E.**, Silva, P., Korvink, J. G., MacKinnon, N., *Automatic adaptive gain for magnetic resonance sensitivity enhancement.*, Analytical chemistry, 91, 2376-2383, **2019**
- [EF04] Bordonali, L., Nordin, N., **Fuhrer, E.**, MacKinnon, N., Korvink, J. G., *Parahydrogen based NMR hyperpolarisation goes micro: an alveolus for small molecule chemosensing.*, Lab on a Chip, 19, 3, 503-512, **2019**
- [EF05] **Fuhrer, E.**, Jouda, M., Klein, C. O., Wilhelm M., Korvink, J. G., *Gradient-induced mechanical vibration of neural interfaces during MRI.*, IEEE Transactions on biomedical engineering, accepted: 07.06.2019, early access.
- [EF06] Nimbalkar S.*, **Fuhrer, E.***, Silva, P., Nguyen T., Sereno M., Kassegne S., Korvink, J. G., *Glassy Carbon Microelectrodes Minimize Induced Voltages, Mechanical Vibrations and Forces and Artifacts in Magnetic Resonance Imaging.*, Microsystems & Nanoengineering, accepted: 29.08.2019
(*These authors contributed equally)

Submitted

- [EF07] Reischl M.*, Jouda, M.*, MacKinnon N., **Fuhrer, E.**, Bakhtina N., Bartschat A., Mikut R., Korvink, J. G. *Motion prediction enables simulated MR-imaging of freely moving model organisms.*, PLOS Computational Biology, submitted: 30.03.2019
(*These authors contributed equally)

In preparation

- [EF08] **Fuhrer, E.**, Jouda, M., Wapler, M. C., Korvink, J. G., *A modular NMR probe system enables augmented interfacing for advanced experimental setups in high-field.*, Review of Scientific Instruments.

Proceedings

- [EF09] **Fuhrer, E.**, Jouda, M., Gruschke, O. G., Korvink, J. G., *Optical gauge head to evaluate gradient field induced vibrations of conductive structures during MRI.*, International Conference on Electromagnetics in Advanced Applications (ICEAA), 1555 -1558, Verona, Italy, **2017**, DOI: 10.1109/ICEAA.2017.8065581
- [EF10] Erhardt, J. B., Leupold, J., **Fuhrer, E.**, Gruschke, O. G., Wapler, M. C., Hennig, J., Korvink, J. G., Stieglitz, T., *Influence of Pt/Ir electrode thickness on magnetic resonance imaging susceptibility artefacts.*, Biomedical Engineering / Biomedizinische Technik, 60, S193, Hann **2015**, DOI: 10.1515/bmt-2015-5009

Conference contributions

Oral presentations

- [EF11] **Fuhrer, E.**, Gruschke, O. G., Wapler, M. C., Fakhrabadi, M., Müller, M., Göbel, K., LeVan, P., Stieglitz, T., Wallrabe, U., Hennig, J., Korvink, J. G. *Can patients with brain implants undergo MRI?*, Biomedical Engineering / Biomedizinische Technik DGBMT, Hannover, Germany, **2014**.
- [EF12] Jouda, M., **Fuhrer, E.**, Silva, P., Korvink, J. G., MacKinnon, N., *Automatic adaptive gain (AGAIN): a digital technique to enhance NMR sensitivity.*, ENC, Asilomar, US, **2019**
- [EF13] **Fuhrer, E.**, Zakhurdaeva, A., Karsten, R. E. H., Olinga, P., Salentijn G. IJ., Grajewski M., Patra, B., Sharma, M., Mager, D., Verpoorte, E., Utz, M., Korvink, J. G., *Automatic adaptive gain (AGAIN): a digital technique to enhance NMR sensitivity.*, Euromar, Nantes, France, **2018**
- [EF14] **Fuhrer, E.**, Gruschke, O. G., Leupold, J., Erhardt, J. B., Göbel, K., Wapler, M. C., Stieglitz, T., Wallrabe, U., Hennig, J., Korvink, J. G. *Susceptibility artefacts of thin film platinum electrodes.*, ICMRM, Munich, Germany, **2015**.
- [EF15] **Fuhrer, E.**, Gruschke, O. G., Erhardt, J. B., Leupold, J., Wapler, M. C., Stieglitz, T., Hennig, J., Korvink, J. G. *Susceptibility artifact characterisation of electrode materials and geometries for neuronal implants.*, Euromar, Prague, Czech Republic, **2015**.
- [EF16] Erhardt, J. B., Leupold, J., **Fuhrer, E.**, Gruschke, O. G., Wapler, M. C., Hennig, J., Korvink, J. G., Stieglitz, T., *Influence of Laser Structured Pt/Ir Brain Implant*

Electrodes with Trapezoidal Cross Section on MRI Artefact Size, Material Research Society Fall meeting, Boston, US, **2015**.

- [EF17] Erhardt, J. B., Kleber, C., Leupold, J., **Fuhrer, E.**, Asplund, M., Hennig, J., Korvink, J. G., Stieglitz, T., “*MRI artefact comparison of electrode structures made of Pt/Ir and the conducting polymer PEDOT*”, ESMRMB, Edinburgh, UK, **2015**.
- [EF18] Meissner, M. V., **Fuhrer, E.**, Kiss, S. Z., Ryan, H. B., MacKinnon, N., While, P. T., Korvink, J. G. *Low Expense General Operation probe (LEGO)*, ENC, Boston, US, **2014**.

A | Appendix

A.1. Derivation of equations for MR interactions

Translative force due to magnetism

A simplified formula can be used to estimate the maximal mass susceptibility χ_m which an object may exhibit to be MR conditional. Therefore one can express the maximal allowed force according to the ASTM-standard F2052 - 15^[9].

$$F_g \geq F_m \quad (\text{A.1})$$

This means the maximum allowed magnetic force must be smaller or equal the gravitational force of an object. We can rewrite this equation in the following way:

$$\rho V g \geq \frac{\chi V}{\mu_0} \vec{B}_0 \nabla \vec{B}_0 \quad (\text{A.2})$$

Here, $g = 9.81 \text{ m/s}^2$ denotes the gravitational acceleration, ρ the density and V the volume of an object. The magnetic susceptibility χ is the volume susceptibility. Rearranging of equation A.2 yields:

$$\frac{\mu_0 g}{\vec{B}_0 \nabla \vec{B}_0} \geq \frac{\chi}{\rho} = \chi_{mass} \quad (\text{A.3})$$

From this equation we can derive some important points. At any location where the gradient of the \mathbf{B}_0 -field vanishes, the translational force vanishes, because $\nabla \vec{B}_0 \rightarrow 0$. Theoretically, at these locations the mass susceptibility can be infinitely large. At the bore centre, even ferromagnetic material would be allowed, simply because the force vanishes. In reality, however, torque plays a similar important role, and this will be at a maximum at the isocenter, hence the vanishing force is rather an anecdote with no practical aspect. Yet, an important fact is that for the maximal allowed susceptibility, the product of field strength and spatial gradient at the fringe field is crucial. Hence, the field strength of \mathbf{B}_0 , is not the only critical value, but also the gradient $\nabla \vec{B}_0$ of the fringe field.

Forces based on eddy currents

In chapter 5.4 the equation 5.4 for computing the gradient-induced torque is presented, which is derived from Faraday's Law of induction. The derivation of the torque, induced by gradient-switching, is given for the quasi-static case (neglecting of self-induction of eddy-currents). The torque $\vec{\tau}(t)$ which is produced by a magnetic moment $\vec{\mu}(t)$ inside an external magnetic field \vec{B}_0 is given by equation A.4.

$$\vec{\tau}(t) = \vec{\mu}(t) \times \vec{B}_0 \quad (\text{A.4})$$

Gradient-induced eddy currents produce a magnetic moment $\vec{\mu}(t)$ which is calculated using Faraday's law of induction. In the following equation \vec{B} denotes an arbitrary magnetic field.

$$\oint_{\partial A} \vec{E} \cdot d\vec{l} = - \int_A \frac{\partial \vec{B}}{\partial t} \cdot d\vec{A} \quad (\text{A.5})$$

\vec{E} is the electric field along the contour l . For small deflections we can consider the angle α between normal vector of the surface A and the magnetic field B as constant, thus one can rewrite:

$$\oint_{\partial A} \vec{E} \cdot d\vec{l} = - \cos(\alpha) \frac{\partial \vec{B}}{\partial t} \int_A d\vec{A} \quad (\text{A.6})$$

To calculate the magnetic flux change $\dot{\Phi}$ through a circular disc with surface A , we integrate the right term of that equation written in polar coordinates:

$$\begin{aligned} - \cos(\alpha) \frac{\partial \vec{B}}{\partial t} \int_A d\vec{A} &= - \cos(\alpha) \frac{\partial \vec{B}}{\partial t} \int_0^{r_s} \int_0^{2\pi} r dr d\varphi \\ \dot{\Phi} &= - \cos(\alpha) \frac{\partial \vec{B}}{\partial t} \pi r_s^2 \end{aligned} \quad (\text{A.7})$$

Integration of the left term of equation A.5 yields the electric potential V_E as a function of the radius r . Within a conductive disc with conductivity σ , the electromotive force drives a current with the current density J :

$$V_E = \oint_l \vec{E} \cdot d\vec{l} = \int_0^{2\pi} r d\varphi = \vec{E} 2\pi r = \frac{J}{\sigma} 2\pi r \quad (\text{A.8})$$

Using the relation $V_E = \dot{\Phi}$ yields the current density $j(r)$ as a function of time, changing magnetic field $\frac{\partial \vec{B}}{\partial t} = \dot{\vec{B}}$, electric conductivity σ and the radius r :

$$j(r) = -\cos(\alpha)\frac{1}{2}\dot{B}r\sigma \quad (\text{A.9})$$

The induced eddy-current generates a magnetic moment $\vec{\mu}$. In general a magnetic moment is equal to a current I encompassing an area A . Therefore, we can write:

$$\vec{\mu} = I \cdot A \rightarrow d\mu = j(r)dzdrdA \quad (\text{A.10})$$

In this equation z represents the direction towards the height h of a disc, and r the radius. The total magnetic moment $\vec{\mu}$ is obtained by integration of the current density $j(r)$ over dz , dr and dA . By combining equation A.9 and equation A.9 one has to solve the following integral:

$$\begin{aligned} \mu &= \int_0^{r_s} \int_0^{2\pi} \int_0^h \int_0^{r_s} j(r)drdzrdrd\varphi \\ &= -\frac{1}{2}\dot{B}\sigma \int_0^{r_s} \int_0^{2\pi} \int_0^h \int_0^{r_s} r^2drdzd\varphi dr \end{aligned} \quad (\text{A.11})$$

The result for the magnetic moment $\vec{\mu}$ dependent on \vec{B} and r is given by:

$$\vec{\mu}(\vec{B}, r) = -\frac{1}{8}\dot{B}\pi\sigma hr^4 \quad (\text{A.12})$$

The torque $\tau(t)$ is given by inserting equation A.12 into equation A.4 which yields:

$$\begin{aligned} \vec{\tau}(t) &= -\frac{1}{8}\dot{B}(t)\pi\sigma hr_s^4 \times \vec{B}_0 \\ &= -\frac{1}{8}\dot{B}(t)\pi\sigma hr_s^4 \cos(\alpha) \sin(\alpha)\vec{B}_0 \end{aligned} \quad (\text{A.13})$$

This is the equation which is presented in the technical specification ISO/TS 10974:2012^[69], chapter 12.1.

Furthermore, we can use the identity $\dot{\vec{B}}(t) = \dot{G}_x(t)x$, to calculate the field change at any point along the x-direction (similarly in y- or z-direction) during the gradient switching. Additionally, spring and mass elements of the mechanical system can be considered which then yields a more general mathematical model:

$$J_1\ddot{\Phi} + c_1\dot{\Phi} + k_1\Phi = -\frac{1}{8}\dot{G}_x x \pi \sigma h r_s^4 \times \vec{B}_0 \quad (\text{A.14})$$

A.2. Matlab code for laser vibration

Matlab code applied in vibration setup

The following program example is used for measuring the transfer function. In the header (4-13) the experiment parameters are set which are then used for creating the folder. Important external parameters are then directly available. In the section excitation parameters the frequency range and steps for the transfer function measurements are set. The block duration is the total acquisition duration for one frequency point, whereby the the number of periods (line 31) are acquired at the end of the block. This ensures a settling time for the measured frequency point. The actual acquisition takes place between line 104 and 132. After switching the excitation frequency, a delay is triggered to ensure steady-state-condition of the current vibration. In line 124 the data is acquired from the physical devices and eventually transferred to the RAM (lines 127 - 130). In line 134 - 136 the data is stored as .mat-file in a separate folder.

```

1 clearvars -except deviceObj
2 close all
3
4 Foldmeas = '00_Measurement_and_Transfer/Measurement_electrodes_SDSU_4/';
5 %Experimental paramaters
6 Ex.Measurement = 'freq/';           % in Ohm
7 Ex.Sample_Holder = '05Cu_';        %
8 Ex.Beam = '_PMMA3';                % empty oder sample
9 Ex.Environment = '_air';           % empty, air, water, 05%, 1% 2% 4%
10 Ex.Resistor = '_400Ohm';
11 Ex.Res_num = 400;
12 Ex.freq = '_170_0.5_210Hz';       % start_step_stop frequency
13 Ex.Volt = '_2V';
14
15 directory = [Foldmeas Ex.Measurement Ex.Sample_Holder Ex.Beam Ex.Environment Ex.↔
              Resistor Ex.freq Ex.Volt];
16 filename = 'y1_tot.mat'
17 f = fullfile(directory, filename); %Check if directory exist
18 if 7==exist(f, 'dir')
19 disp('Folder exist already. Should measurement proceed? Press enter')
20 while keypressed ~= 13 % 13 is the equivalent to the "enter" key.
21 keypressed = getkey;
22 end
23 end
24
25 %Excitation parameters -----
26 Start_freq =170;                   % in Hertz
27 delta_freq = 0.5;
28 Stop_freq =210;
29 amp = 2;                           % in Volt
30 Block_duration = 1;                % in s
31 Periods = 10;
32
33 %Variation vector -----
34 freq = [Start_freq; delta_freq; Stop_freq];
35
36 %Initialization Devices

```

```

37
38 %Set up tek control-----
39 % Create a VISA-USB object.
40 if exist('deviceObj') == 0
41 interfaceObj = instrfind('Type', 'visa-usb', 'RsrcName', 'USB0::0 x0699::0 x0347::C037186↔
    ::0::INSTR', 'Tag', '');
42
43 %Create the VISA-USB object if it does not exist otherwise use the object that was ↔
    found.
44 if isempty(interfaceObj)
45 interfaceObj = visa('tek', 'USB0::0 x0699::0 x0347::C037186::0::INSTR');
46 else
47 fclose(interfaceObj);
48 interfaceObj = interfaceObj(1);
49 end
50
51 %Create a device object.
52 deviceObj = icdevice('tek_afg3000.mdd', interfaceObj);
53
54 %Connect device object to hardware.
55 connect(deviceObj);
56 end
57
58 %Configure property value(s).
59
60 set(deviceObj.Waveform(1), 'Shape', 'sin');
61 set(deviceObj.voltage(1), 'amplitude', amp);
62 set(deviceObj.output(1), 'state', 'on');
63 set(deviceObj.frequency(1), 'Freq', freq(1));
64 %-----
65
66 %Setup of acquisition devices-----
67 %Check for devices
68 if exist('s1') == 0
69 devices= daq.getDevices;
70 s1 = daq.createSession('ni')
71 s2 = daq.createSession('mcc')
72 end
73
74 channel_on = exist('ch');
75
76 %Initialize NI card-----
77 if channel_on == 0
78 ch = addAnalogInputChannel(s1, 'Dev1', 0, 'Voltage');
79 ch = addAnalogInputChannel(s1, 'Dev1', 1, 'Voltage');
80 ch = addAnalogInputChannel(s1, 'Dev1', 2, 'Voltage');
81 ch = addAnalogInputChannel(s1, 'Dev1', 3, 'Voltage');
82 s1.Rate = 100000;
83 end
84 %-----
85
86 %Initialize MCC card
87 if channel_on ==0
88
89 ChannelRange = [-10 10];
90 %Ch 1
91 ch = addAnalogInputChannel(s2, 'Board0', 0, 'Voltage');
92 ch.Range = ChannelRange;
93 ch1.TerminalConfig = 'Diff';
94 %Ch 2
95 ch = addAnalogInputChannel(s2, 'Board0', 1, 'Voltage');
96 ch.Range = ChannelRange;

```

A. Appendix

```
97 ch1.TerminalConfig = 'Diff';
98
99 s2.Rate = 24000;
100 end
101
102 %Acquisition control-----
103 for i= 1:length(freq)
104
105 %Set tekronix control
106 set(deviceObj.frequency(1), 'Freq', freq(i));
107
108 pause(block_duration-10*1/freq(i));
109
110 %Acquisition of NI device
111 s1.NumberOfScans = round(Periods*1/freq(i)*s1.Rate,0);
112 s1.NotifyWhenDataAvailableExceeds = round(Periods*1/freq(i)*s1.Rate,0);
113 lh = addlistener(s1,'DataAvailable',@savedata_ni);
114
115 %Acquisition of MCC device
116 s2.NumberOfScans = round(Periods*1/freq(i)*s2.Rate,0);
117 s2.NotifyWhenDataAvailableExceeds = round(Periods*1/freq(i)*s2.Rate,0);
118 lh = addlistener(s2,'DataAvailable',@savedata_mcc);
119
120 %start acquisition
121 startBackground(s1);
122 startBackground(s2);
123
124 wait(s1)
125 wait(s2)
126
127 alltime_ni(i) = {time_ni};
128 alltime_mcc(i) = {time_mcc};
129 alldata_ni(i) = {data_ni};
130 alldata_mcc(i) = {data_mcc};
131 end
132
133 %% Save file -----
134 f = fullfile(directory, filename)
135 mkdir(directory)
136 save(f, 'alltime_ni', 'alldata_ni', 'alltime_mcc', 'alldata_mcc', 'amp', 'freq', 'Ex')
137
138 %% Close Tek instrument-----
139 % Disconnect device object from hardware.
140 set(deviceObj.output(1), 'state', 'off');
141 % Delete objects.
142 %delete([deviceObj interfaceObj]);
143
144 %functions-----
145 function savedata_ni(src, event)
146 time_ni = event.TimeStamps;
147 data_ni = event.Data;
148 assignin('base', 'data_ni', data_ni);
149 assignin('base', 'time_ni', time_ni);
150 end
151
152 %Transfer MCC data
153 function savedata_mcc(src, event)
154 time_mcc = event.TimeStamps;
155 data_mcc = event.Data;
156 assignin('base', 'data_mcc', data_mcc);
157 assignin('base', 'time_mcc', time_mcc);
158 end
```

Matlab code to compute transfer function

If the raw data is acquired a second script is used to compute the transfer function offline. Therefore the raw data is loaded, and downsampled to reduce computation time. This is important because redundant computation of laser point location is time costly. Then the raw data and the corresponding transfer matrices are transferred to the function *coordinate_cal* which returns the location of the laser beam for each requested time point (74 - 82). From the first low-frequent, quasi-static data point the y-axis of the vibration is calculated. Due to mechanical misalignments, the coordinate system of the vibration is not identical to the coordinate system of the photodetector. Therefore, using a low frequency component with no resonant vibrations, the eigenvectors are computed and the corresponding transfer function between the two coordinate systems is established (100 - 114). Then the amplitude per frequency point is computed using the FFT (from line 199). After computing the amplitude function the phase function is computed (from line 131). The data is afterwards saved as .mat-file.

```

1 clear all
2 close all
3
4 %Intial settings-----
5 savedata = 'y'; %Should data be saved 'y' = yes
6 High_res = 'n'; %enables resolution down to 0.1 um
7 dpx = 30; %The less the faster but Error might increase with smaller number
8 thres_min = 0.003;
9 Periods = 10; %Number of samples for 10 periods
10 SamplePerPeriod = 20;
11 NS = Periods*SamplePerPeriod+1;
12
13 %Load data and downsample 10 sample per period with oversample averaging-----
14 Folder1 = 'Measurement_files/freq/';
15 Folder2 = '05Cu_05Cu_soldmass_1gel_400_Ohm_10_2_800Hz10V/';
16 Folder = [Folder1 Folder2];
17 File = 'y1_tot.mat';
18 File_tot = [Folder File];
19
20 load (File_tot)
21
22 %Preallocation of cell array
23 data_ni = zeros(4,NS,length(freq));
24 data_mcc = zeros(2,NS,length(freq));
25 data_trans = zeros(4,NS);
26
27 %Convert to +- 20V (required if using NI-Device as input device with +- 10V input)
28 conv_fac = [4.122619 4.079314 4.096344 4.094712];
29 %Downsample ni data
30 tic
31
32 for i=1:length(freq)
33 %Downsample Ni data
34 time_red_ni(:,i) = linspace(0,alltime_ni{1,i}(end),NS);
35 data_ni(1,:,i) = interp1(alltime_ni{1,i},alldata_ni{1,i}(:,1)*conv_fac(1),time_red_ni←
(:,i),'pchip');
36 data_ni(2,:,i) = interp1(alltime_ni{1,i},alldata_ni{1,i}(:,2)*conv_fac(2),time_red_ni←
(:,i),'pchip');

```

A. Appendix

```
37 data_ni(3, :, i) = interp1(alltime_ni{1, i}, alldata_ni{1, i}(:, 3) * conv_fac(3), time_red_ni ↔
    (:, i), 'pchip');
38 data_ni(4, :, i) = interp1(alltime_ni{1, i}, alldata_ni{1, i}(:, 4) * conv_fac(4), time_red_ni ↔
    (:, i), 'pchip');
39
40 %Downsample MCC data
41 time_red_mcc(:, i) = linspace(0, alltime_mcc{1, i}(end), NS);
42 time_ch2 = alltime_mcc{1, i} + ((alltime_mcc{1, 2}(2) - alltime_mcc{1, 2}(1)) * (1/2));
43 data_mcc(1, :, i) = interp1(alltime_mcc{1, i}, alldata_mcc{1, i}(:, 1), time_red_mcc(:, i), '↔
    pchip');
44 data_mcc(2, :, i) = interp1(time_ch2, alldata_mcc{1, i}(:, 2), time_red_mcc(:, i), 'pchip');
45
46 end
47 toc
48 %-----
49
50 %% Load detector matrices and Specifiy calculationmatrix -----
51 load('Det_LUT_50um')
52 load('Det_LUT_10um')
53 load('Det_LUT_2um')
54 load('Det_LUT_04um')
55 if strcmp(High_res, 'y')
56 load('Det_LUT_01um')
57 end
58
59 %Make logarithm of transfer matrices
60 Data_zero = log10(Data_zero);
61 Data_zero_ip_2 = log10(Data_zero_ip_2);
62 Data_zero_ip_3 = log10(Data_zero_ip_3);
63 Data_zero_ip_4 = log10(Data_zero_ip_4);
64 if strcmp(High_res, 'y')
65 Data_zero_ip_5 = log10(Data_zero_ip_5);
66 end
67
68 %% Call function to calculate x & y position -----
69 for i=1:length(freq)
70
71 data_trans = data_ni(:, :, i)';
72
73 if strcmp(High_res, 'y')
74 [x_raw, y_raw] = coordinate_cal(dpx, thres_min, data_trans, Data_zero, X, Y, Data_zero_ip_2, ↔
    X_ip_2, Y_ip_2, Data_zero_ip_3, X_ip_3, Y_ip_3, Data_zero_ip_4, X_ip_4, Y_ip_4, ↔
    Data_zero_ip_5, X_ip_5, Y_ip_5);
75
76 elseif strcmp(High_res, 'n')
77 [x_raw, y_raw] = coordinate_cal(dpx, thres_min, data_trans, Data_zero, X, Y, ↔
    Data_zero_ip_2, X_ip_2, Y_ip_2, Data_zero_ip_3, X_ip_3, Y_ip_3, Data_zero_ip_4, ↔
    X_ip_4, Y_ip_4);
78
79 else
80 error('Please specify desired resolution')
81 end
82
83 x_raw = x_raw * 1000; %Conversion from mm to um
84 y_raw = y_raw * 1000; %Conversion from mm to um
85
86 coordinate_data_x_raw(:, i) = x_raw;
87 coordinate_data_y_raw(:, i) = y_raw;
88
89 %Find origin for vibration at certain frequency
90 x0(i) = sum(x_raw) / length(x_raw);
91 y0(i) = sum(y_raw) / length(y_raw);
```

```

92
93 coordinate_data_x(:,i) = coordinate_data_x_raw(:,i) - x0(i);
94 coordinate_data_y(:,i) = coordinate_data_y_raw(:,i) - y0(i);
95
96 end
97 %-----
98
99 %Calculate rotation matrix
100 [maxval_tot,idxmax] = max( abs(sqrt( (coordinate_data_x(:,1).^2 + coordinate_data_y←
    (:,1).^2 )    ));
101 [minval_tot,idxmin] = min( abs(sqrt( (coordinate_data_x(:,1).^2 + coordinate_data_y←
    (:,1).^2 )    ));
102
103 alpha = asind(coordinate_data_x(idxmax,1)/coordinate_data_y(idxmax,1));
104
105 %Calculated rotated values
106 for i=1:length(freq)
107 x_final(:,i) = coordinate_data_x(:,i)*cosd(alpha)-coordinate_data_y(:,i)*sind(alpha);
108 y_final(:,i) = coordinate_data_x(:,i)*sind(alpha)+coordinate_data_y(:,i)*cosd(alpha);
109 end
110 %-----
111
112 %Determination of amplitude and phase transfer function
113 for i= 1:length(freq)
114
115 %Amplitude transfer function
116 FFT_x(:,i) = 2*fftshift(fft(x_final(:,i)))/length(x_final(:,i));
117 FFT_y(:,i) = 2*fftshift(fft(y_final(:,i)))/length(y_final(:,i));
118
119 if i==1
120 [minval,idxmin] = max(abs(FFT_y(:,i)));
121 end
122
123 Amp_x(i) = abs(FFT_x(idxmin,i));
124 Amp_y(i) = abs(FFT_y(idxmin,i));
125
126 %Measurement of phase transfer function -----
127 %Phase_difference MCC vs NI
128
129 phase_corr = 1/(2*24000)*(2*pi*freq(i))*180/pi;
130 Phase_diff_offset = phdiffmeasure(data_mcc(1,:,i),data_ni(1,:,i));
131
132 Phase_corr_i(i) = phase_corr;
133 Phase_diff_offset_i(i) = Phase_diff_offset;
134
135 %Measure Phase difference between excitation and vibration signal X
136 Phase_diff= phdiffmeasure_vib(data_mcc(2,:,i),x_final(:,i))-Phase_diff_offset+←
    phase_corr;
137
138 Phase_diff(Phase_diff < -180) = 360+Phase_diff(Phase_diff < -180);
139 Phase_diff(Phase_diff > 180) = -360+Phase_diff(Phase_diff > 180);
140
141 Phase_diff_x(i) = Phase_diff;
142
143
144 %Measure Phase difference between excitation and vibration signal Y
145 Phase_diff= phdiffmeasure_vib(data_mcc(2,:,i),y_final(:,i))-Phase_diff_offset+←
    phase_corr;
146
147 Phase_diff(Phase_diff < -180) = 360+Phase_diff(Phase_diff < -180);
148 Phase_diff(Phase_diff > 180) = -360+Phase_diff(Phase_diff > 180);
149

```

```

150 Phase_diff_y(i) = Phase_diff;
151
152 end
153
154 savefile = 'final_data'
155 Fullfile = [Folder savefile]
156 save(Fullfile, 'freq', 'coordinate_data_x', 'coordinate_data_y', 'x0', 'y0', 'x_final', '←
    y_final', 'Amp_x', 'Amp_y', 'Phase_diff_x', 'Phase_diff_y', 'time_red_ni')

```

Matlab code to compute laser location

The function *coordinate_cal* computes the location of the laser point for the time data point i . It requires the input of the raw data vector, as well as the transfer matrices. The in-built option for high-resolution or low-resolution computation requires a variable parameter input. The output are the corresponding location x_i and y_i at time point i . This code list shows the code up to the third iteration. The fourth iteration is identical to the third and hence not displayed due to save space. At line 210 the most probable point is computed using the weightings W and the different intersection points.

```

1 The function [xi,yi] = coordinate_cal(varargin)
2
3 %% Assign variables-----
4 if nargin < 15 || nargin > 18 || nargin == 16 || nargin == 17
5 error ('Please check number of input arguments')
6 end
7
8 dpx =          varargin{1,1};
9 thres_min =    varargin{1,2};
10 data =         varargin{1,3};
11
12 Data_zero =    varargin{1,4};
13 X =            varargin{1,5};
14 Y =            varargin{1,6};
15
16 Data_zero_ip_2 =  varargin{1,7};
17 X_ip_2 =       varargin{1,8};
18 Y_ip_2 =       varargin{1,9};
19
20 Data_zero_ip_3 =  varargin{1,10};
21 X_ip_3 =        varargin{1,11};
22 Y_ip_3 =        varargin{1,12};
23
24 Data_zero_ip_4 =  varargin{1,13};
25 X_ip_4 =        varargin{1,14};
26 Y_ip_4 =        varargin{1,15};
27
28 if nargin == 18
29 Data_zero_ip_5 =  varargin{1,16};
30 X_ip_5 =         varargin{1,17};
31 Y_ip_5 =         varargin{1,18};
32 end
33 %-----
34
35 %Offset channels-----
36 Ch_1 = -19.927; % Det_1

```

```

37 Ch_2 = -19.927; % Det_2
38 Ch_3 = -19.962; % Det_3
39 Ch_4 = -19.9684; % Det_4
40
41 %Preallocate Vectors xi and yi
42 xi = zeros(length(data(:,1)),1);
43 yi = xi;
44
45 %-----
46 Det1_meas = log10(data(:,1)+ 20 - (Ch_1 + 20));
47 Det2_meas = log10(data(:,2)+ 20 - (Ch_2 + 20));
48 Det3_meas = log10(data(:,3)+ 20 - (Ch_3 + 20));
49 Det4_meas = log10(data(:,4)+ 20 - (Ch_4 + 20));
50
51 %% ----- Running loop -----
52
53 for i=1:length(data(:,1))
54 %for i=89:89
55
56 %% Calculate 1st position -----
57 LP_pos_hold_1 = abs( Data_zero(:,1) - Det1_meas(i) )*-1;
58 LP_pos_hold_2 = abs( Data_zero(:,2) - Det2_meas(i) )*-1;
59 LP_pos_hold_3 = abs( Data_zero(:,3) - Det3_meas(i) )*-1;
60 LP_pos_hold_4 = abs( Data_zero(:,4) - Det4_meas(i) )*-1;
61
62 LP_pos_hold = LP_pos_hold_1 + LP_pos_hold_2 + LP_pos_hold_3 + LP_pos_hold_4;
63
64 [max_val,max_idx] = max(LP_pos_hold(:));
65 [ind_y ind_x]=ind2sub(size(LP_pos_hold),max_idx); % Conversion of max_val to indice
66
67 xpos = X(1,ind_x);
68 ypos = Y(ind_y,1);
69 %-----
70
71 %% Calculate 2nd interpolated position -----
72 %Find index of position in second matrix -----
73 ind_x = find(abs(X(1,ind_x)-(X_ip_2(1,:))) < 1e-10);
74 ind_y = find(abs(Y(ind_y,1)-(Y_ip_2(:,1))) < 1e-10);
75
76 cut_x = [ind_x-dpx:ind_x+dpx];
77 cut_y = [ind_y-dpx:ind_y+dpx];
78
79 %Cut Matrix adjust in case border condition is met -----
80 if cut_x(1) < 1
81 cut_x = [1:1+2*dpx];
82 end
83 if cut_y(1) < 1
84 cut_y = [1:1+2*dpx];
85 end
86 if cut_x(end) > length(Data_zero_ip_2(:,1,1))
87 cut_x = [length(Data_zero_ip_2(:,1,1))-2*dpx:length(Data_zero_ip_2(:,1,1))];
88 end
89 if cut_y(end) > length(Data_zero_ip_2(1,:,1))
90 cut_y = [length(Data_zero_ip_2(1,:,1))-2*dpx:length(Data_zero_ip_2(1,:,1))];
91 end
92 %-----
93
94 LP_pos_hold_1_ip_2 = abs( Data_zero_ip_2 (cut_y,cut_x,1) - Det1_meas(i) )*-1;
95 LP_pos_hold_2_ip_2 = abs( Data_zero_ip_2 (cut_y,cut_x,2) - Det2_meas(i) )*-1;
96 LP_pos_hold_3_ip_2 = abs( Data_zero_ip_2 (cut_y,cut_x,3) - Det3_meas(i) )*-1;
97 LP_pos_hold_4_ip_2 = abs( Data_zero_ip_2 (cut_y,cut_x,4) - Det4_meas(i) )*-1;
98 X_red_ip = X_ip_2 (cut_y,cut_x);

```

A. Appendix

```
99 Y_red_ip = Y_ip_2 (cut_y, cut_x);
100
101 LP_pos_hold_ip_2 = LP_pos_hold_1_ip_2 + LP_pos_hold_2_ip_2 + LP_pos_hold_3_ip_2 + ←
    LP_pos_hold_4_ip_2;
102
103 [max_val, max_idx] = max(LP_pos_hold_ip_2 (:));
104 [ind_y ind_x] = ind2sub(size(LP_pos_hold_ip_2), max_idx); % Conversion of max_val to ←
    indice
105
106 xpos = X_red_ip(1, ind_x);
107 ypos = Y_red_ip(ind_y, 1);
108
109 %-----
110
111 %% Calculate 3rd interpolated positions for intersections-----
112
113 %Find index of position in second matrix & define cut section-----
114 ind_x = find(abs(X_red_ip(1, ind_x) - (X_ip_3(1, :))) < 1e-10);
115 ind_y = find(abs(Y_red_ip(ind_y, 1) - (Y_ip_3(:, 1))) < 1e-10);
116 cut_x = [ind_x-dpx:ind_x+dpx];
117 cut_y = [ind_y-dpx:ind_y+dpx];
118
119 %Cut Matrix adjust in case border condition is met----
120 if cut_x(1) < 1
121 cut_x = [1:1+2*dpx];
122 end
123 if cut_y(1) < 1
124 cut_y = [1:1+2*dpx];
125 end
126 if cut_x(end) > length(Data_zero_ip_3(:, 1, 1))
127 cut_x = [length(Data_zero_ip_3(:, 1, 1))-2*dpx:length(Data_zero_ip_3(:, 1, 1))];
128 end
129 if cut_y(end) > length(Data_zero_ip_3(1, :, 1))
130 cut_y = [length(Data_zero_ip_3(1, :, 1))-2*dpx:length(Data_zero_ip_3(1, :, 1))];
131 end
132 %-----
133
134 %Prepare interpolation matrix
135 LP_pos_hold_1_ip_3 = abs(Data_zero_ip_3(cut_y, cut_x, 1) - Det1_meas(i)) * -1;
136 LP_pos_hold_2_ip_3 = abs(Data_zero_ip_3(cut_y, cut_x, 2) - Det2_meas(i)) * -1;
137 LP_pos_hold_3_ip_3 = abs(Data_zero_ip_3(cut_y, cut_x, 3) - Det3_meas(i)) * -1;
138 LP_pos_hold_4_ip_3 = abs(Data_zero_ip_3(cut_y, cut_x, 4) - Det4_meas(i)) * -1;
139 LP_pos_hold_tot = LP_pos_hold_1_ip_3 + LP_pos_hold_2_ip_3 + LP_pos_hold_3_ip_3 + ←
    LP_pos_hold_4_ip_3;
140 X_red_ip = X_ip_3(cut_y, cut_x);
141 Y_red_ip = Y_ip_3(cut_y, cut_x);
142
143 %Calculate intersection points-----
144 %IS 12-----
145 Lap_tot_ip_12 = LP_pos_hold_1_ip_3 + LP_pos_hold_2_ip_3;
146 [val12, idx12] = max(Lap_tot_ip_12 (:));
147 [y12 x12] = ind2sub(size(LP_pos_hold_1_ip_3), idx12);
148
149 %IS 14-----
150 Lap_tot_ip_14 = LP_pos_hold_1_ip_3 + LP_pos_hold_4_ip_3;
151 [val14, idx14] = max(Lap_tot_ip_14 (:));
152 [y14 x14] = ind2sub(size(LP_pos_hold_2_ip_3), idx14);
153
154 %IS 23-----
155 Lap_tot_ip_23 = LP_pos_hold_2_ip_3 + LP_pos_hold_3_ip_3;
156 [val23, idx23] = max(Lap_tot_ip_23 (:));
157 [y23 x23] = ind2sub(size(LP_pos_hold_3_ip_3), idx23);
```

```

158
159 %IS 34-----
160 Lap_tot_ip_34 = LP_pos_hold_3_ip_3 + LP_pos_hold_4_ip_3;
161 [val34,idx34] = max(Lap_tot_ip_34(:));
162 [y34 x34] = ind2sub(size(LP_pos_hold_4_ip_3),idx34);
163
164 %Detemine x & y positions -----
165 %Point 12
166 xI_12 =X_red_ip(1,x12);
167 yI_12 =Y_red_ip(y12,1);
168
169 %Point 14
170 xI_14 =X_red_ip(1,x14);
171 yI_14 =Y_red_ip(y14,1);
172
173 %Point 23
174 xI_23 =X_red_ip(1,x23);
175 yI_23 =Y_red_ip(y23,1);
176
177 %Point 34
178 xI_34 =X_red_ip(1,x34);
179 yI_34 =Y_red_ip(y34,1);
180
181 %If one point is outside the 200um box the waiting is based on the 2 um
182 %matrix and the rest of the loop is skipped
183 if (xI_12 > 0.2 || xI_14 > 0.2 || xI_23 > 0.2 || xI_34 > 0.2 || yI_12 > 0.2 || yI_14 > 0.2 || yI_23 < ->
    > 0.2 || yI_34 > 0.2 || xI_12 < -0.2 || xI_14 < -0.2 || xI_23 < -0.2 || xI_34 < -0.2 || yI_12 < ->
    < -0.2 || yI_14 < -0.2 || yI_23 < -0.2 || yI_34 < -0.2)
184
185 %Detemine x & y positions and value of max-----
186 %Point 12
187 val12 = LP_pos_hold_tot(y12,x12);
188 W12 = round(1000/(0-val12));
189
190 %Point 14
191 val14 = LP_pos_hold_tot(y14,x14);
192 W14 = round(1000/(0-val14));
193
194 %Point 23
195 val23 = LP_pos_hold_tot(y23,x23);
196 W23 = round(1000/(0-val23));
197
198 %Point 34
199 val34 = LP_pos_hold_tot(y34,x34);
200 W34 = round(1000/(0-val34));
201
202
203 xi(i) = (W12*xI_12+W14*xI_14+W23*xI_23+W34*xI_34)/(W12+W14+W23+W34);
204 yi(i) = (W12*yI_12+W14*yI_14+W23*yI_23+W34*yI_34)/(W12+W14+W23+W34);
205
206 %-----
207 continue
208 end
209
210 %% Final determination -----
211 %-----
212 xi(i) = (W12*xI_12+W14*xI_14+W23*xI_23+W34*xI_34)/(W12+W14+W23+W34);
213 yi(i) = (W12*yI_12+W14*yI_14+W23*yI_23+W34*yI_34)/(W12+W14+W23+W34);
214
215 end

```

A.3. 3D anaglyph of scaffolds and cell clusters

3D anaglyph of Cryogel

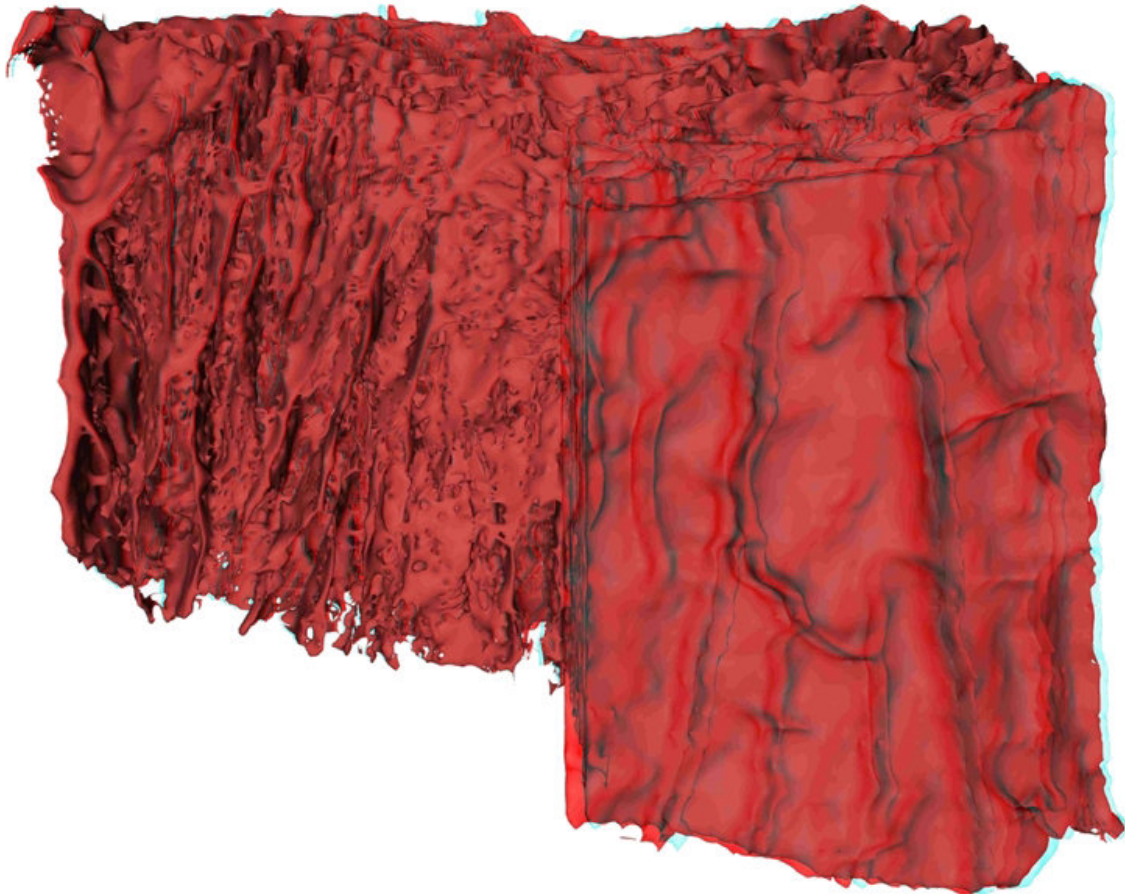


Figure A.1.: 3D anaglyph image of reconstructed Cryogel. (Adapted and modified from [EF02]).

3D anaglyph of Carbon scaffold

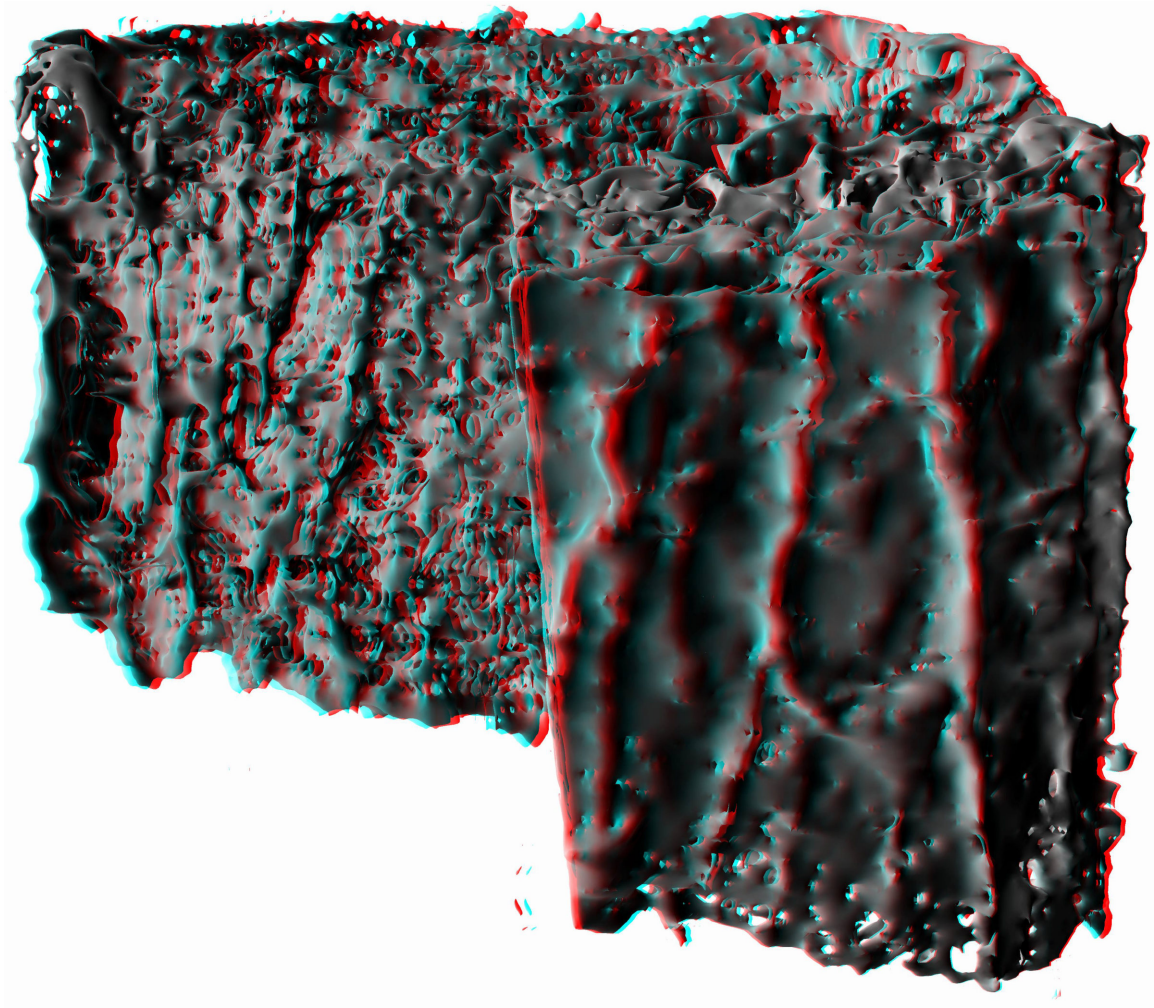


Figure A.2.: 3D anaglyph image of reconstructed Carbon scaffold. (Adapted and modified from [EF02]).

3D anaglyph of Cell cluster distribution

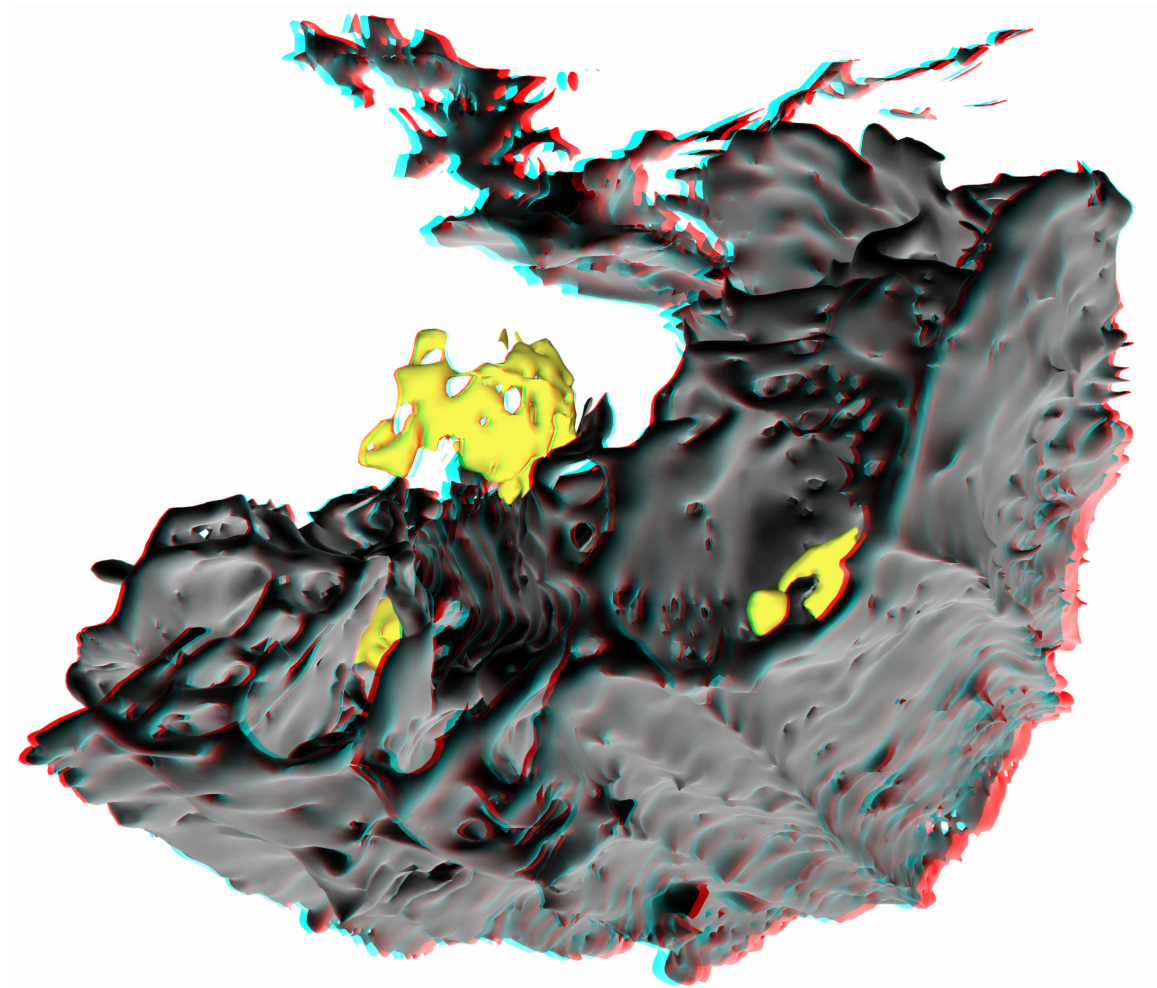


Figure A.3.: 3D anaglyph of cell cluster distribution. (Adapted and modified from [EF02]).

List of Figures

2.1 Spin orientations	6
2.2 Zeeman splitting and Larmor frequency	7
2.3 Boltzmann distribution	9
2.4 Magnetization trajectories	10
2.5 T_1 and T_2 -relaxation	11
2.6 NMR spectroscopy	13
2.7 Illustration of k-space	15
2.8 Pulse sequence of GRE sequence	16
2.9 Pulse sequence of SE sequence	17
2.10 T_1 -weighted imaging	19
2.11 T_2 -weighted imaging	19
2.12 SNR and CNR	20
2.13 Electromagnetic fields in NMR/MRI	22
2.14 Probe and Magnets	23
2.15 Hardware electronics	24
2.16 Tuning and Matching steps	26
2.17 Magnetism in matter	28
2.18 Digital Image	32
2.19 Segmentation	33
2.20 Segmentation using Otsus method	33
2.21 Otsus method	34
2.22 Lumped model of coupled resonator	36
2.23 Transfer function of two port	36
2.24 Torsion constant and moment of inertia	37
2.25 Boundary conditions	39
2.26 Characterisits of a spring - free beam	41
3.1 MR hazards	46
3.2 Physics and hazards in MRI	48
3.3 Principle of induced voltage	51
3.4 Equivalent circuit for stimulation and recording configuration of an electrode.	52
3.5 Principle of susceptibility artifact	55
3.6 Principle of B_1 artifacts	56

4.1	Preconditions of sample and scanner	64
4.2	Principle concept of vibration probe	66
4.3	Laser module	67
4.4	Control module	68
4.5	Photodiode	69
4.6	Calibration setup	70
4.7	Calibration results	70
4.8	Limit of detection	71
4.9	Amplifier circuit	72
4.10	Front end	73
4.11	Sample holder and samples	73
4.12	RF module	74
4.13	Complete vibration probe	75
4.14	Hard- and software interfaces	76
4.15	Limit of detection	77
4.16	Position computation	78
4.17	Position computation on fine grid	79
4.18	From raw data to transfer function	81
4.19	Initialisation	83
4.20	Trajectory benchmarking	84
4.21	MR imaging with Low-Field probe	85
5.1	From reality to experimental model	88
5.2	Simplified lumped model of measurement setup	89
5.3	Static deflection	90
5.4	Computed transfer function	91
5.5	Laplace transform	92
5.6	Characterisation of agarose gels	94
5.7	Results of static deflection measurements	95
5.8	Direct sample resonance in gel	96
5.9	Transfer function of ABS sample	97
5.10	Combined MR acquisition and vibration measurement	98
5.11	Setup of TPSR measurements	100
5.12	Results of TPSR measurements	102
6.1	3D CAD model of target system	108
6.2	Explosion view of two-channel probe	109
6.3	Parasitic capacitor	111
6.4	Assembled probe	112
6.5	NMR Benchmark tests	113
6.6	MRI benchmark tests	114

6.7	Experimental setup for oil droplet measurements	116
6.8	Experimental setup for SABRE	117
6.9	Results of the hyperpolarisation experiment	118
6.10	Redesign probehead	119
7.1	Process flow of scaffold fabrication	123
7.2	Optimisation of CuSO ₄ -concentration	125
7.3	Desiccator supported vacuum filling.	127
7.4	From MRI to porosity data.	128
7.5	SNR of MR images for porosity analysis	130
7.6	Histogram and binarisation of scaffolds	131
7.7	Morphology comparison of scaffolds	132
7.8	Comparison of optical and MR images of cell clusters.	133
7.9	Detailed images of cell clusters	133
A.1	3D anaglyph of Cryogel	170
A.2	3D anaglyph of Cryogel	171
A.3	3D anaglyph of Cryogel	172

List of Tables

2.1	Physical properties of typical materials used for probehead manufacturing	30
3.1	Table of case studies	47
3.2	Forces and Torque	50
3.3	Milestones of MRI, CI and DBS.	58
4.1	Indices to compute W_j	80
5.1	List of test items	89
7.1	Different values for A and B	124
7.2	Porosity results	130

Acknowledgements

The time has come for the most important chapter of his thesis, in which I want to give my sincere gratitude to all the people that gave me the support to make this entire work a success. My profound gratitude goes to...

- ... my PhD advisor Prof. Dr. Jan G. Korvink, who gave me the opportunity to establish the probe work over the years. It took me some time to develop the skills to build the devices presented in this work, and you gave me the support and time required to fulfil our plans. Especially, I acknowledge the time you spend with the PhD students, always with an open ear and ready to present solutions.
- ... Prof. Dr. Jürgen Hennig for the examining my thesis as co-referent. It was always a pleasure meeting you on conferences and having awesome conversations. And of course, special thanks for let me being part of the legendary christmas partys of the Department of radiology.
- ... Mazin Jouda my group leader at IMT. After becoming the group leader you always had instant time for more than fruitful conversations. I really enjoyed discussing ideas, but most importantly I want to thank you for sharing your large expertise with all the electronics "stuff".
- ... Oliver Gruschke, my group leader in Freiburg and Karlsruhe. Thank you for guiding me through a large period of my thesis and especially through the transition from Freiburg to Karlsruhe.
- ... all of my colleagues from the MR group at IMT. Many thanks to Neil MacKinnon for enduring and of course answering my countless questions about NMR. Many thanks also to Lorenzo Bordonali for a lot of technical advice and also the hiking trips and to Dario Mager for the help in all situations and of course the climbing experience. I want to thank Omar Nassar for taking over and further developing the probe, Shyam for all the informations in and around the group
- ... all of my colleagues from Voxalytic. Many thanks to Ronald Kampmann for helping me with the white light interferometer as well as his awesome skill on the grill as well as to Li Zhao an dAli Moazenzadeh.
- ... my former room colleagues Mehrdad Alinaghian, Emil Mamleyev and of course Pedro Freire da Silva for many interesting and helpful discussions.

- ... all my former colleagues from Freiburg. Special thanks to you Robert Kamberger and Angelina Müller for having you as companions and an awesome studying time. Also to Jens Höfflin for guiding me in my first steps in the field of NMR hardware.
- ... to all the colleagues from the Department of Radiology from the Uniklinik Freiburg. Especially to Jochen Leupold for always having time for discussions and giving me useful advices about MRI. Many thanks also to Katharina Katharina Göbel-Guéniot, Pierre LeVan and the entire team of the radiology group.
- ... to all my collaborators over the years. Very special thanks goes to Christopher Klein for helping me with all the details and measurements regarding viscoelastic materials and the multiple uncomplicated hand-over of the measurement card. Many thanks to Johannes Erhardt and Thomas Stieglitz for our fruitful collaboration and our successful review paper. I want to thank Surabhi Nimbalkar for our very successful collaboration on the electrode measurements. It was really a pleasure to meet you in Karlsruhe. Many thanks also to Sam Kassegne for taking the lead in this collaboration. Many thank also to M. Wapler and our collaboration in the review work and the probe work.
- ... BLBT-team with Johanna Schön and Bettina Schug. You always had an immediate solution to all occurring bureaucratic difficulties in combination with a good advices.
- ... an das gesamte Werkstatt-Team des IMT. Es ist immer jemand da wenn man Hilfe benötigt. Besonders danken möchte ich Alexandra Moritz für ihren fachkundigen Rat und ihre Bereitschaft alles herzustellen was mir in den Sinn kam. Vielen Dank auch an Andre Wolfschläger der mir immer ein gute Ansprechpartner war und viele der notwendigen Bauteile hergestellt hat. Ohne das gesamte Team der Werkstatt wären meine Aufbauten nicht möglich gewesen.
- ... meiner gesamten Familie die mich in all den Jahren ohne Einschränkungen unterstützt haben. Ganz herzlichen Dank meiner Schwester Michaela mit Martin, Lilli, Moritz und Carla. Mein größter Dank gilt meinen Eltern Karola und Gerhard ohne die mein Studium und diese Arbeit nicht zustandegekommen wäre.
- ... meiner Freundin Swati Sharma. Ohne dich wäre diese Dissertation in dieser Form nicht zustandegekommen. Nicht nur deine Unterstützung in direktem Bezug zur Arbeit, sondern vor allem auch außerhalb der Arbeit ermöglichten es mir auch mal einfach abzuschalten, was die Grundlage ist soweit zu kommen. Vielen herzlichen Dank.